INTERPLAY BETWEEN MICROSTRUCTURE/MORPHOLOGY AND THE OPTO-ELECTRONIC PROPERTIES OF MATERIALS FOR ORGANIC PHOTOVOLTAICS

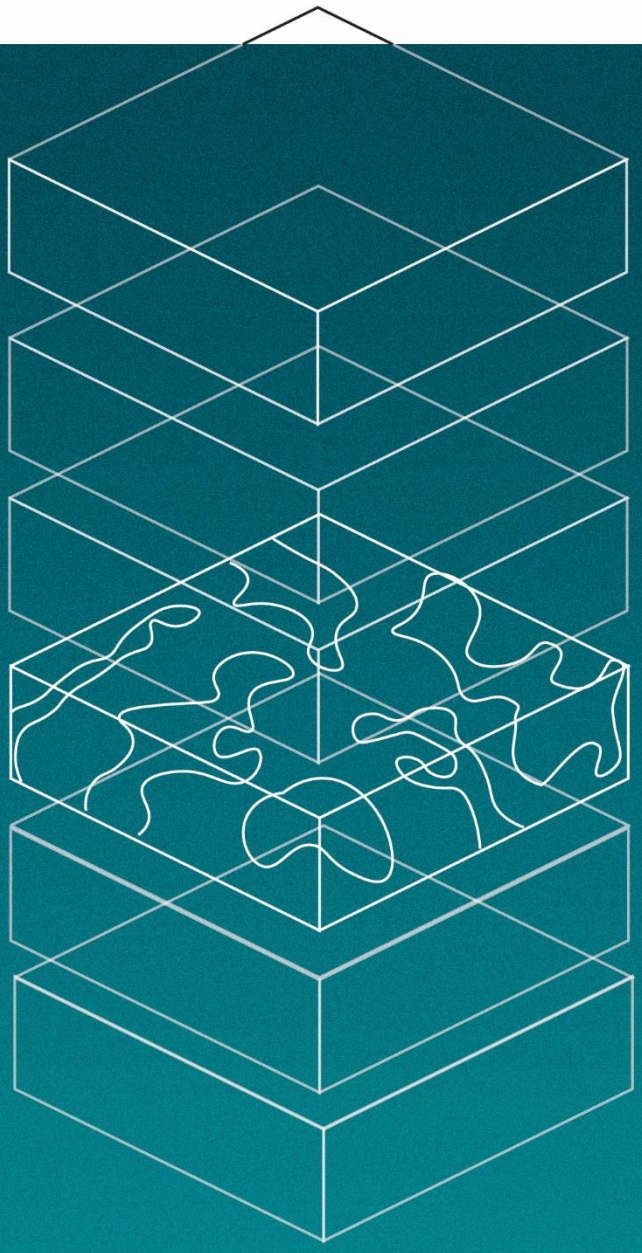

Written by

Sara Marina Barbier

PhD Thesis 2021

eman ta zabal zazu

Universidad del País Vasco

Euskal Herriko Unibertsitatea

SARA MARINA BARBIER

INTERPLAY BETWEEN MICROSTRUCTURE/MORPHOLOGY AND THE OPTO-ELECTRONIC PROPERTIES OF MATERIALS FOR ORGANIC PHOTOVOLTAICS

SUPERVISOR: JAIME MARTIN PÉREZ

TESIS DOCTORAL OCTUBRE 2021

eman ta zabal zazu

Universidad del País Vasco

Euskal Herriko Unibertsitatea

INTERPLAY BETWEEN MICROSTRUCTURE/MORPHOLOGY AND THE OPTO-ELECTRONIC PROPERTIES OF MATERIALS FOR ORGANIC PHOTOVOLTAICS

PhD Thesis

Sara Marina Barbier

Supervisor: Jaime Martin Pérez

Polímeros y Materiales Avanzados: Física, Química y Tecnología

Universidad del País Vasco/ Euskal Herriko Unibertsitatea (UPV/EHU)

Donostia - San Sebastian

2021

SARA MARINA BARBIER: INTERPLAY BETWEEN MICROSTRUCTURE/MORPHOLOGY AND THE OPTO-ELECTRONIC PROPERTIES OF MATERIALS FOR ORGANIC PHOTOVOLTAICS, OCTOBER, 2021.

Dedicado a mis padres y hermanos

RESUMEN

Debido a su bajo coste de producción, su inocuidad para el medio ambiente y sus propiedades mecánicas, se espera que las celdas solares orgánicas (CSO) basadas en polímeros constituyan una importante fuente de energía renovable a corto plazo. Su gran ventaja radica en la diversidad de materiales orgánicos que pueden diseñarse fácilmente. Además, los dispositivos resultantes son flexibles, semitransparentes y fáciles de fabricar mediante procesos de alto rendimiento a baja temperatura, cualidades importantes para su comercialización como complemento en ventanas generadoras de energía integradas en edificios o invernaderos en aplicaciones agrovoltaicas.

La captación de luz se desarrolla en la capa activa de las CSO, que está constituida por una mezcla de material donor de electrones y una molécula aceptora de electrones. Mientras que los polímeros semiconductores son el material donor por excelencia, en los últimos años las moléculas pequeñas (SMA, por sus siglas en inglés) han sustituido a los fullerenos en el papel de moléculas aceptoras de electrones. Esto se debe a un crecimiento considerable de los valores de eficiencia de fotoconversión que, en la actualidad, superan el 18% a escala de laboratorio. Similar a la unión p-n de las celdas inorgánicas de silicio, la morfología más eficiente en estos sistemas ha demostrado ser aquella en la que el polímero (donor) y la molécula aceptora forman una morfología con separación de fases a escala nanométrica denominada heterounión volumétrica (HUV). La morfología optima consiste en dominios puros de los componentes, necesarios para un transporte de cargas efectivo a los electrodos, y una fase entremezclada formada por ambos componentes, responsable de la separación de cargas.

Debido a la flexibilidad sintética de las moléculas pequeñas y de los copolimeros semiconductores tipo “push-pull”, el desarrollo en la síntesis de nuevos materiales ha crecido considerablemente. Esto ha llevado a un aumento significativo de los estudios centrados principalmente en lograr mayores eficiencias de fotoconversión mediante la síntesis de nuevos materiales. En consecuencia, la creciente variedad de materiales orgánicos ha empujado el campo hacia la optimización de los parámetros de procesado basados en una aproximación de prueba y

error en lugar de estrategias derivadas del conocimiento. Debido a su gran complejidad, el desarrollo óptimo de estos dispositivos fotovoltaicos requiere (1) una determinación precisa y exhaustiva de la microestructura en estado sólido de los polímeros semiconductores y los materiales aceptores, así como (2) el control minucioso del efecto de las variables de procesado sobre cada uno de los componentes. Por otro lado, es necesario conocer (3) la composición de los dominios donor y aceptor en la HUV, para así, (4) establecer la relación entre la microestructura, la morfología de la capa activa y el rendimiento de los dispositivos solares orgánicas.

Esta tesis recoge un amplio marco de trabajo que incluye la relación microestructura-procesado-morfología-rendimiento de un sistema modelo basado en el polímero semiconductor PBDB-T y la molécula pequeña ITIC. En primer lugar, la tesis aborda las cuestiones críticas que rodean la microestructura de estado-solido de los distintos componentes de la HUV. En el primer capítulo, resolvemos el enigma que rodea a los polimeros de alto-rendimiento estableciendo un nuevo modelo microestructural para materiales poliméricos denominado "semi-paracristalinidad" que explica las excelentes prestaciones de esta nueva familia de polimeros. En relación al aceptor, estudiamos y aprendemos a controlar su complejo polimorfismo revelando así que el empaquetamiento de la fase cristalina de baja temperatura puede ser una característica importante para lograr elevadas eficiencias. Con la intención de extender el alcance de nuestros resultados, estudiamos la sensibilidad de los parámetros de procesado y establecemos la relación entre la microestructura y ciertas propiedades optoelectrónicas y de transporte de carga.

La siguiente sección, se centra en estudiar la composición de los dominios de polímero (donor) y aceptor en la HUV de células solares reales. Con la ayuda de una novedosa metodología basada en calorimetría de barrido rápido (flash), cuantificamos la composición de las fases entremezcladas del sistema modelo P3HT:fullereno mediante la determinación de la temperatura de transición vítrea (T_g) de la mezcla. En este sentido, cabe destacar que partiendo de un concepto fundamental de la física de mezclas de polímeros como es la dependencia de la T_g con la composición de la mezcla, hemos desarrollado un método sencillo y rápido para determinar una de las características clave de la capa activa de las celdas fotovoltaicas.

Finalmente, el control preciso logrado sobre la microestructura de los componentes individuales y la elección astuta de los disolventes y aditivos de procesado, nos permite delinear el impacto de tales características en relación morfología-función del dispositivo de la célula solar. Así, aprendemos a modificar la microestructura de los componentes individuales en la capa activa y resolvemos los efectos de estas variaciones sobre el funcionamiento del dispositivo solar.

Esta tesis doctoral se centra en un sistema particular de polímero:SMA. Sin embargo, sus resultados amplían la percepción actual de la estructura en estado sólido de los polímeros de alto rendimiento y la relación entre la microestructura, la morfología, el procesamiento en solución y el transporte de cargas en los dispositivos más eficientes de la actualidad. Establecemos que es necesario un conocimiento exhaustivo de las propiedades físicas inherentes de los materiales orgánicos y su microestructura en estado-solido, para poder desarrollar dispositivos óptimos y realizar una transición eficiente de la escala laboratorio hacia una escala industrial.

ABSTRACT

Owing to their low production cost, environmental benignity and mechanical properties, polymer-based organic solar cells (OSCs) are expected to become an important source of renewable energy in the short term. Their great advantage lies in the diversity of organic materials that can be easily designed and functionalized. In addition, the resulting devices are flexible, semi-transparent and easy to manufacture using high-throughput processes at low-temperature, which are important qualities for their commercialisation as building-integrated energy generating windows or greenhouses in agrovoltaics applications.

Light harvesting takes place in the active layer of the OSC, which consists of a blend of electron donor material and an electron acceptor molecule. While semiconducting polymers are the preferred choice as donor materials, in recent years small molecules (SMA) have replaced fullerenes in the role of electron-withdrawing molecules. This is caused by a considerable growth in power conversion efficiency values, which now exceed 18% on a laboratory scale. Similar to the p-n heterojunction of inorganic silicon solar cells, the most efficient morphology in these systems has proved to be one in which the polymer (donor) and acceptor molecule form a nanoscale phase-separated morphology called bulk heterojunction (BHJ). The optimal morphology consists of pure domains of the components, necessary for effective charge transport to the electrodes, and an intermixed phase formed by both components, responsible for charge separation.

The synthetic flexibility of small molecule and push-pull semiconductor copolymers has led to a significant increase in the development of materials engineering. his has led to a substantial growth in studies focusing mainly on achieving higher photoconversion efficiencies through the synthesis of new materials. Consequently, the growing library of organic materials has pushed the field towards optimisation of processing parameters based on a trial-and-error approach rather than knowledge-derived strategies. Due to their high complexity, optimal device development requires (1) precise and comprehensive determination of the solid-state

microstructure of semiconducting polymers and acceptor materials, as well as (2) careful control of the effect of processing variables on the individual components. Furthermore, it is necessary to know (3) the composition of the donor and acceptor domains in the BHJ, in order to (4) establish the relationship between the microstructure, the morphology of the active layer and the performance of the organic solar devices.

This thesis gathers a comprehensive framework that includes the microstructure-processing-morphology-performance relationship of a model system based on the semiconducting polymer PBDB-T and the small molecule ITIC. First, the thesis addresses the critical issues regarding the solid-state microstructure of the different BHJ components. In the first chapter, we solve the enigma surrounding high-performance polymers by establishing a new microstructural model called "semi-paracrystallinity" that explains the excellent performance of this new family of polymers. Regarding the acceptor, we study and learn to control its complex polymorphism, thus revealing that low temperature crystalline phase packing can be an important feature to achieve high efficiencies. In order to extend the scope of our results, we study the sensitivity of the processing parameters and establish the relationship between the microstructure and certain optoelectronic and charge transport properties.

The next section focuses on studying the composition of the polymer (donor) and acceptor domains in the BHJ of real solar cells. By using a novel methodology based on flash scanning calorimetry, we quantify the absolute composition of the intermixed phases of the P3HT:fullerene model system by determining the glass transition temperature (T_g) of the blend. In this regard, it is worth noting that based on a fundamental concept of polymer blend physics, namely the dependence of T_g on the composition of the blend, we have developed a simple and fast method to determine one of the key characteristics of the active layer of photovoltaic cells.

Finally, the precise control achieved over the microstructure of the individual components and the judicious choice of processing solvents and additives allows us to delineate the impact of such features on the morphology-function relationship of the solar cell device. Thus, we learn to

modify the microstructure of the individual components in the active layer and we resolve the influence of these modifications on the performance of the solar device.

This PhD dissertation targets a particular polymer:SMA system. Nevertheless, its findings extend the current understanding of the solid-state microstructure of high-performance polymers and the interplay between microstructure, morphology, solution processing and charge transport in state-of-the-art devices. We establish it is necessary to gain a detailed understanding of the inherent physical properties of organic materials and their microstructure in the solid-state in order to develop optimal devices and make an efficient transition from the laboratory scale to the industrial scale.

LIST OF CONTRIBUTIONS

1. The Importance of Quantifying the Composition of the Amorphous Intermixed Phase in Organic Solar Cells.

Marina, S.; Kaufmann, N. P.; Karki, A.; Gutiérrez-Meza, E.; Gutiérrez-Fernández, E.; Vollbrecht, J.; Solano, E.; Walker, B.; Bannock, J. H.; de Mello, J.; Silva, C.; Nguyen, T.-Q.; Cangialosi, D.; Stingelin, N; Martín, J.

Advanced Materials **2020**, 32, 2005241. (Impact Factor: 30.849)

2. Polymorphism in Non-Fullerene Acceptors Based on Indacenodithienothiophene

Marina, S.; Scaccabarozzi, A. D.; Gutierrez-Fernandez, E.; Solano, E.; Khirbat, A.; Ciammaruchi, L.; Iturrospe, A.; Balzer, A.; Yu, L.; Gabirondo, E..; Monnier, X.; Sardon, H.; Anthopoulos, T. D.; Caironi, M.; Campoy-Quiles, M.; Müller, C.; Cangialosi, D.; Stingelin, N.; Martin, J.

Advanced Functional Materials **2021**, 31, 2103784. (Impact Factor: 18.808)

3. Semi-paracrystallinity in semi-conducting polymers.

Marina, S.; Gutierrez-Fernandez, E.; Gutierrez, J.; Gobbi, M.; Ramos, N.; Solano, E.; Rech, J.; You, W.; Hueso, L.; Tercjak, A.; Ade, H.; Martin, J.

Submitted

4. Identifying the solid-state microstructure of semiconducting polymers

Marina, S.; Gutierrez-Fernandez, E.; Gutierrez, J.; Solano, E.; Rech, J.; You, W.; Hueso, L.; Tercjak, A.; Martin, J.

In preparation

5. The impact of selective donor/acceptor structural ordering in organic solar cell devices

Marina, S.; Harillo, A.; Campoy-Quiles, M.; Martin, J.

In preparation

LIST OF COLLABORATIONS

1. Synthesis of Self-Healable Waterborne Isocyanate-Free Poly(hydroxyurethane)-Based Supramolecular Networks by Ionic Interactions.

Boisson, A.; Olazabal, I.; Aguirresarobe, R. H.; **Marina, S.**; Martín, J.; Irusta, L.; Taton, D.; Sardon, H.

Polymer Chemistry **2019**, 10, 2723-2733. (Impact Factor: 5.342)

2. Diffusion-Limited Crystallization: A Rationale for the Thermal Stability of Non-Fullerene Solar Cells.

Yu, L.; Qian, D.; **Marina, S.**; Nugroho, F. A. A.; Sharma, A.; Hultmark, S.; Hoffmann, A. I.; Kroon, R.; Benduhn, J.; Smilgies, D.-M.; Vandewal, K.; Andersson, M. R.; Langhammer, C.; Martín, J.; Gao, F.; Müller, C.

ACS Applied Materials and Interfaces **2019**, 11, 24, 21766-21774. (Impact Factor: 8.758)

3. Synthesis and Characterization of Fully Biobased Copolyether Polyols.

Basterretxea, A.; Lopez de Pariza, X.; Gabirando, E.; **Marina, S.**; Martín, J.; Etxeberria, A.; Mecerreyes, D.; Sardon, H.

Industrial & Engineering Chemistry Research **2020**, 59, 23, 10746-10753. (Impact Factor: 3.573)

4. Direct-writing of organic field-effect transistors on plastic achieving 22 MHz transition frequency.

Passarella, B.; Scaccabarozzi, A. D.; Giorgio, M.; Perinot, A.; **Marina Barbier, S**.; Martín, J.; Caironi, M.

Flexible and Printed Electronics **2020**, 5, 034001. (Impact Factor: 3.082)

5. Reduction of the Lattice Thermal Conductivity of Polymer Semiconductors by Molecular Doping.

Zapata-Arteaga, O.; Perevedentsev, A.; **Marina, S.**; Martín, J.; Reparaz, J. S.; Campoy-Quiles, M.

ACS Energy Letters **2020**, 5, 9, 2972-2978. (Impact Factor: 19.05)

6. Physical Aging and Glass Transition of the Rigid Amorphous Fraction in Poly(L-lactic acid).

Monnier, X.; Cavallo, D.; Righetti, M. C.; Di Lorenzo, M. L.; **Marina, S.**; Martín, J.; Cangialosi, D.

Macromolecules **2020**, 53, 20, 8741-8750. (Impact Factor: 5.918)

7. Suppressing Co-Crystallization of Halogenated Non-Fullerene Acceptors for Thermally Stable Ternary Solar Cells.

Hultmark, S.; Kumar Paleti, S. H.; Harillo, A.; **Marina, S.**; Nugroho, F. A. A.; Liu, Y.; Ericsson, L. K. E.; Li, R.; Martín, J.; Bergqvist, J.; Langhammer, C.; Zhang, F.; Yu, L.; Campoy-Quiles, M.; Moons, E.; Baran, D.; Müller, C.

Advanced Functional Materials **2020**, 30, 2005462. (Impact Factor: 18.808)

8. Photophysical and structural modulation of poly(3-hexylthiophene) nanoparticles via surfactant-polymer interaction.

Gutiérrez-Fernández, E.; Ezquerra, T. A.; Rebollar, E.; Cui, J.; **Marina, S.**; Martín, J.; Nogales, A.

Polymer **2021**, 218, 123515. (Impact Factor: 4.43)

9. Physical aging behaviour of a Glassy Polyether.

Monnier X.; **Marina S.**; Lopez de Pariza X.; Sardon H.; Martin J.; Cangialosi D.

Polymers **2021**, 13, 954. (Impact Factor: 4.329)

10. Decoupling thermal and electronic transport in conjugated polymers

Rodríguez-Martínez, X.; Saiz, F.; **Marina, S**.; Chen, H.; Gómez, A.; Guimerà, R.; Martin, J.; McCulloch, I.; Rurali, R.; Reparaz, J. S.; Campoy-Quiles, M.

Submitted

CONTENTS

ABBREVIATIONS

χ	Flory–Huggins interaction parameter
μ_{eff}	effective mobility
AFM	Atomic force microscopy
BHJ	Bulk heterojunction
CB	chlorobenzene
CF, $CHCL_3$	chloroform
CCL	crystalline coherence length
C_P	specific heat
D18	poly[(2,6-(4,8-bis(5-(2-ethylhexyl-3-fluoro)thiophen-2-yl)-benzo[1,2-b:4,5-b']dithiophene))-alt-5,5'-(5,8-bis(4-(2-butyloctyl)thiophen-2-yl)dithieno[3',2':3,4;2",3":5,6]benzo[1,2-c][1,2,5]thiadiazole)]
O-DCB	1,2-ortodichlorobenzene
DCM, CH_2CL_2	dichloromethane
DIO	1,8-diiodooctane
DMA	dynamical mechanical analysis
DSC	Differential Scanning Calorimetry
DOPC	degree of paracrystallinity
E_G	band gap
EQE	external quantum efficiency
ETL	electron transporting layer
FF	fill factor
FSC	Fast Scanning Calorimetry
FWHM, ΔQ	Full width half maximum
G	paracrystalline parameter or distortion lattice parameter
GIWAXS	Grazing Incidence Wide-Angle X-ray scattering

GISAXS	Grazing Incidence Small-Angle X-ray scattering
ΔH_m	melting enthalpy
HOMO	highest occupied molecular orbital
HTL	hole transporting layer
IDT-BT	indacenodithiophene-co-benzothiadiazole
IP	in-plane
IPA	Isopropanol
ITIC	3,9-bis(2-methylene-(3-(1,1-dicyanomethylene)-indanone))-5,5,11,11-tetrakis(4-hexylphenyl)-dithieno[2,3-d:2',3'-d']-s-indaceno[1,2-b:5,6-b']dithiophene
ITIC-2F	3,9-bis(2-methylene-((3-(1,1-dicyanomethylene)-6,7-difluoro)-indanone))-5,5,11,11-tetrakis(4-hexylphenyl)-dithieno[2,3-d:2',3'-d']-s-indaceno[1,2-b:5,6-b']dithiophene
ITIC-M	3,9-bis(2-methylene-((3-(1,1-dicyanomethylene)-6/7-methyl)-indanone))-5,5,11,11-tetrakis(4-hexylphenyl)-dithieno[2,3-d:2',3'-d']-s-indaceno[1,2-b:5,6-b']dithiophene
ITIC-TH	3,9-bis(2-methylene-(3-(1,1-dicyanomethylene)-indanone))-5,5,11,11-tetrakis(5-hexylthienyl)-dithieno[2,3-d:2',3'-d']-s-indaceno[1,2-b:5,6-b']dithiophene
ITO	indium tin oxide
J-V	current-voltage
J_{SC}	Short-circuit current density
KWW	Kohlrausch-Williams-Watts law
LUMO	lowest unoccupied molecular orbital
MoO_3	Molybdenum oxide
M_w	molecular weight
NFA	Non-Fullerene Acceptor

OFET	organic field effect transistors
OPP	out-of-plane
OPV	Organic photovoltaics
OSC	organic solar cell
OXCMA	mono-adduct of the *o*-xylenyl C_{60}
OXCBA	bis-adduct of the *o*-xylenyl C_{60}
PBDB-T	poly[(2,6-(4,8-bis(5-(2-ethylhexyl)thiophen-2-yl)-benzo[1,2-b:4,5-b']dithiophene))-alt-(5,5-(1',3'-di-2-thienyl-5',7'-bis(2-ethylhexyl)benzo[1',2'-c:4',5'-c']dithiophene-4,8-dione)]
PBDB-T-2F, PM6	poly[(2,6-(4,8-bis(5-(2-ethylhexyl-3-fluoro)thiophen-2-yl)-benzo[1,2-b:4,5-b']dithiophene))-alt-(5,5-(1',3'-di-2-thienyl-5',7'-bis(2-ethylhexyl)benzo[1',2'-c:4',5'-c']dithiophene-4,8-dione)]
PBDB-T-2CL, PM7	poly[(2,6-(4,8-bis(5-(2-ethylhexyl-3-chloro)thiophen-2-yl)-benzo[1,2-b:4,5-b']dithiophene))-alt-(5,5-(1',3'-di-2-thienyl-5',7'-bis(2-ethylhexyl)benzo[1',2'-c:4',5'-c']dithiophene-4,8-dione)]
PBNDT-FTAZ	poly(benzodithiophene-alt-dithienyl difluorobenzotriazole)
PBTTT	poly[2,5-bis(3-tetradecylthiophen-2-yl)thieno[3,2-b]thiophene]
PCBM	[6,6]-Phenyl-C61-butyric acid methyl ester
PCE	Power conversion efficiency
PCL	poly(ε-caprolactona)
P3DDT	poly(3-dodecylthiophene)
PEDOT:PSS	poly(3,4-ethylenedioxythiophene) polystyrene sulfonate
PEO	poly(ethylene oxide)
PL	photoluminescence
PLOM-S	Polarized Light Optical Microscopy and Spectroscopy
PTAA	poly[bis(4-phenyl)(2,4,6-trimethylphenyl)amine

PTB7	poly [[4,8-bis[(2-ethylhexyl)oxy]benzo[1,2-b:4,5-b']dithiophene-2,6-diyl][3-fluoro-2-[(2-ethylhexyl)carbonyl]thieno[3,4-b]thiophenediyl]]
PSD	power spectral density
PVDF	poly(vinylidene fluoride)
RRA-P3HT	regiorandom poly(3-hexylthiophene)
RR-P3HT	regioregular poly(3-hexylthiophene)
R-SoXS	resonant soft X-ray scattering
ΔS_m	entropy
T_A	annealing temperature
T_A	annealing time
T_C	crystallization temperature
T_G	glass transitions temperature
$T_{G,ON}$	onset glass transition temperature
T_M	melting temperature
UPS	Ultraviolet photoelectron spectroscopy
UV-VIS	ultraviolet visible
V_{OC}	open-circuit voltage
W	heat flow
O-XY	*orto*-xylene
Y6	2,2'-((2Z,2'Z)-((12,13-bis(2-ethylhexyl)-3,9-diundecyl-12,13-dihydro-[1,2,5]thiadiazolo[3,4-e]thieno[2",3'':4',5']thieno[2',3':4,5]pyrrolo[3,2-g]thieno[2',3':4,5]thieno[3,2-b]indole-2,10-diyl)bis(methanylylidene))bis(5,6-difluoro-3-oxo-2,3-dihydro-1H-indene-2,1-diylidene))dimalononitrile
ZnO	zinc oxide

This is the INTRODUCTION. Here you will find the necessary information to understand the content of my work. You will learn basic concepts of organic electronics and its application in photovoltaic technology which will allow you to understand the importance of my research.

1. Introduction

1.1. Motivation

Organic solar cells, which include polymer solar cells, are part of the third generation photovoltaics which take advantage of the inherent properties of polymers and soft organic materials for light harvesting. Currently, the bulk heterojunction (BHJ), which consist of a mixture of a donor and an acceptor semiconducting organic materials, is the most efficient architecture for active layers of polymer solar cells. The great strength of this technology lies in the diversity of organic materials that can be designed and easily functionalized. Moreover, the resulting devices can be flexible, semi-transparent, easy-to-manufacture using high- throughput processes at low temperature and eco-friendly, which are important qualities for building-integrated energy generating windows or greenhouses in agrovoltaics applications among others.[1] To date, polymer solar cells have reached power conversion efficiencies up to 19%.[2] However, its commercialisation is still far from reality due to many factors that make its implementation challenging. For example, organic materials with complex molecular structures are susceptible to multiple degradation pathways. The rapid development of the field has generated a vast number of organic molecules with added complexities, making it difficult to develop in-depth studies of their degradation pathways and solid-state microstructure. Moreover, the lack of morphological stability of the BHJ layer remains a major drawback. Likewise, changes at the interfaces between the BHJ and the inorganic charge transporting layers may lead to instability.[3] Consequently, devices with simultaneously high efficiency and long lifetime have not yet been achieved.

The field is currently aimed at improving the scaling efficiency and long device lifetime for OSC commercialization. However, the rapid development experienced during the past years, has progressed via a trial-and-error approach with limited understanding of the materials' structure–property relation and the connection with device operation. Hence, we first have to understand the fundamental properties of the materials that comprise the photovoltaic layer. This will allow us to design more efficient devices based on stable materials, with improved spectral

response and transport properties. As a result, we will able to understand and manipulate the BHJ morphology responsible for the generation and transport of charges (**Figure 1.1**).

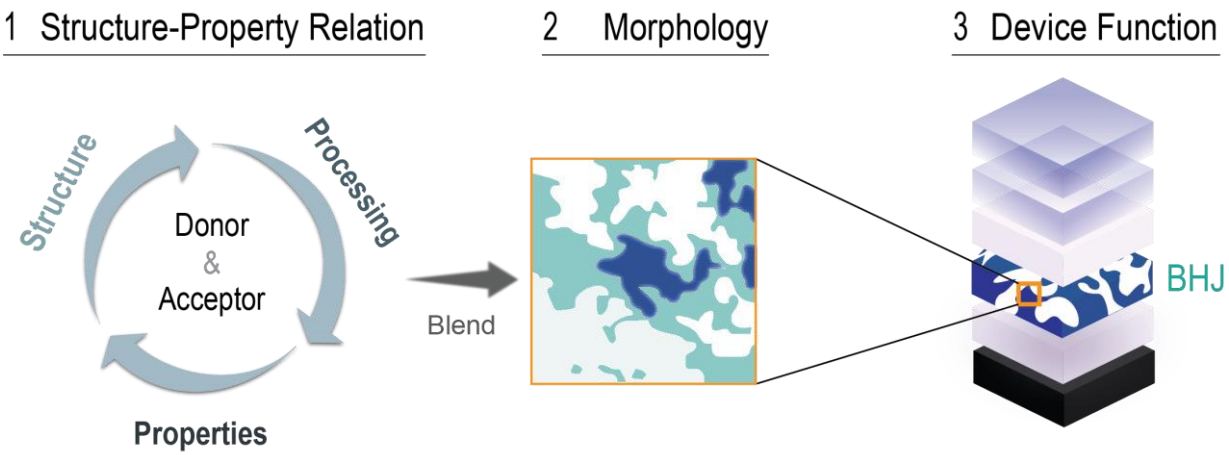

Figure 1.1 This scheme represents the investigation objects of this thesis. First, dealing with physical properties and solid-state microstructure of donor and acceptor materials. Then, regarding the composition of the phases in a BHJ layer and, finally, with device fabrication and characteristics.

1.2. Organic semiconductors

The application of organic materials in photovoltaic devices and other exciting technologies wouldn't be possible without the discovery of Alan Heeger, Alan MacDiarmid and Hideki Shirakawa in 1977.[4] They introduced the possibility of synthesizing organic materials with semiconducting behaviour. Since then, the opportunity to combine the mechanical properties of polymers, such as flexibility, solution processability and chemical versatility, with electrical conductivity made a profound contribution to the research of new materials, processes and device applications. For example, the field of bioelectronics takes advantage of the intrinsic properties of these materials providing a meaning to the interface between the traditional electronics and biology.[5] Other applications of flexible electronics, such as light emitting diodes (OLEDs), thin film transistors (OFETs) or photovoltaic (OPV) devices, offer innovative ways of interacting with the environment which were previously unavailable.[6]

Conventional (commodity) polymers such as polyethylene, are electrically insulating. The molecular structure of these materials consist of tetrahedral sp_3 hybridised carbons. This orbitals bond to adjacent atoms through symmetric, strong and localised σ-bonds each having a pair of electrons i.e. they do not have mobile charges. On the other hand, semiconducting organic molecules owe their electrical, magnetic and optical characteristics to the conjugation of their backbone, which is a regular succession of single and double carbon-carbon bonds (**Figure 1.2**a). Thank to this configuration organic materials adopt sp_2 orbital hybridisation. This means that the three identical sp_2-hybridised orbitals lay in the xy plane and form the planar rigid structure of the backbone forming σ-type bond. The fourth unhybridised p_z orbital projects out of plane and forms π-bonds with neighbouring p_z orbitals (**Figure 1.2**b). Interestingly, the π-electrons are less tightly bound and are delocalized, meaning that electrons can move from atom to atom. In saturated structures the gap between highest occupied molecular orbital (HOMO) and lowest unoccupied molecular orbital (LUMO) is very large and, therefore, the material shown insulating properties. As the conjugation of the molecule increases, the gap is reduced allowing efficient charge transport. The energy barrier formed between the two energy levels is called band gap.[7]

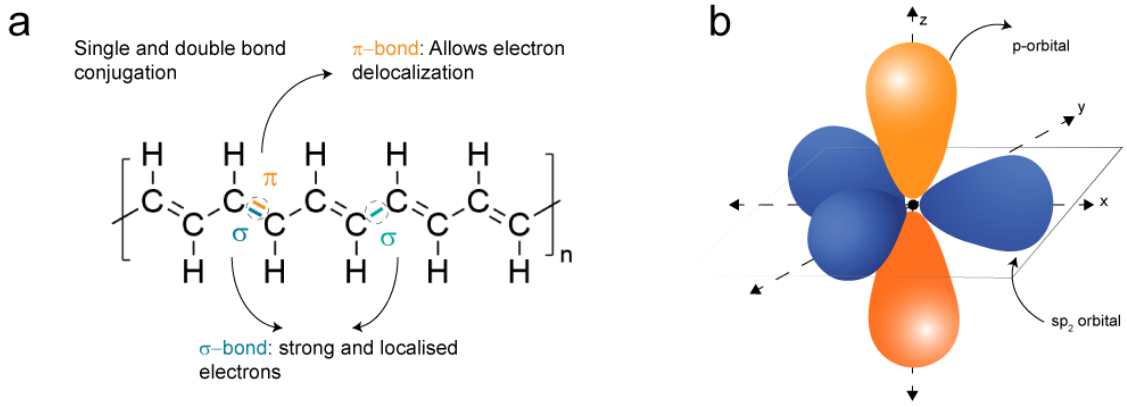

Figure 1.2 Molecular structure of polyacetylene (a) and illustration of the sp2-hybridization (b).

The electron at the π orbital must overcome this barrier to generate charge transport. Excitation energies of conjugated π electrons are usually in the visible range and they are, therefore, addressed as being optically active.[8] Therefore, the excitation can occur by doping the

semiconductor material chemically and electro-chemically but also with light, making them interesting for photovoltaic applications.[9–11] Doping refers to chemical oxidation or reduction. In p-type doping the materials is oxidized by retiring an electron while in n-type the molecule is reduced by the addition of an electron. In the case of photo-doping, in a p-type materials an electron in the HOMO level is excited, this level becomes empty and the organic compound becomes positively charged. At this point the positive charge exerts an attractive Coulomb force. This reduces the excitation energy, which now falls below the gap energy. The state thus formed can be regarded as a coupled electron-hole pair and is called an exciton.[8]

Although molecular orbital overlapping is crucial for charge transport properties, device scale dimensions require the overlap of π-molecular orbitals between adjacent molecules for interchain charge hopping and hence overall charge transport in the film.[12] Packing in organic materials is developed through weak Van der Waals intermolecular forces resulting in lower structural order and defects responsible for limit charge transport. Carrier mobility depends on effective control over the microstructure[13] i.e. the orientation of the conjugated backbone, the degree of packing of the chains in the π-stacking direction and also the energetic disorder due to structural defects.[14] Several works regarding charge transport properties in regioregular-P3HT polymer concluded that π–π interchain stacking between the face-to-face stacked polymer chains is crucial for overall charge transport in polymer films.[12,13] However, the high-mobilities obtained in polymers with much complex microstructures (i.e. some of them even considered amorphous) revealed that crystallinity may not be a fundamental requirement for charge transport. Nevertheless the presence of well-connected aggregates with short-range order is needed.[14]

Organic semiconductor materials have typically been classified according to their molecular structure into small molecules and polymers. Polymers are chains of repeating units (or monomers) that can vary in length and molecular weight, while small molecules are single units with a well-defined shape and molecular weight.

1.3. Materials for polymer solar cells

Organic materials for organic electronic applications have been intensively studied and developed over the past-century. They have been used in commercial applications such as organic thin-film transistors (OTFTs), organic light-emitting diodes (OLEDs), plastic bioelectronics and organic photovoltaic cells (OPVs).[15] The rapid development in molecular design of polymer semiconductors and acceptor for OPVs has been strongly motivated by obtaining high-mobility polymer donor materials with narrower band gaps for efficient light absorption, and novel acceptors with strong absorption and high LUMO (lowest unoccupied molecular orbital) energy levels for proper alignment with donors HOMO (highest unoccupied molecular orbital) energy level to facilitate charge separation. In addition, the progress made towards semiconducting organic materials based OPV devices relies not only on their mechanical and electrical properties but also on the possibility of developing thin films cast from solution using wet processing techniques such as spin coating, doctor-blading,[16] inkjet printing and roll-to-roll printing.[17]

1.3.1. Donor semiconducting polymer materials

From an engineering viewpoint, the major breakthrough in semiconducting polymers design came with the evolution from homopolymers to copolymers (**Figure 1.3**). Although the polymers used at the early stage of OPV field were mainly wide-bandgap alkyl or alkoxy substituted poly(p-phenylene vinylene) (PPV), polythiophene homopolymers emerged as a turning point in the improvement of the efficiency of organic devices.[18–20] To date, the archetypical wide-band gap polymer (>1.9 eV) P3HT remains attractive donor for commercial organic solar cells due to its low cost, ease of manufacture and high stability, together with its regioregularity conferring high mobilities.[21] While mixed with fullerenes depicted low efficiencies due to the limited matching absorption spectrum, it has recently been shown that mixing with a suitable non-fullerene acceptor results in efficiencies of nearly 10%.[22,23]

The performance of these polymer was overcome with the design of donor−acceptor (D−A) (known as “push−pull”) copolymers.[24] This strategy consist in developing alternating

copolymers of donor i.e. electron-donating, and acceptor i.e. electron-withdrawing moieties (**Figure 1.3**). Interestingly, the energy-levels of these low-bandgap polymers can be easily tune modifying the donor or acceptor groups independently, being the HOMO of the copolymer dominated by the HOMO of the donor and the LUMO by that of the electron deficient unit.[25] Regarding, PTB-based polymers, consisting of donor benzodithiophene (BDT) and acceptor thienothiophene (TT) moieties, succeeded with the copolymer PTB7 associated to its enhanced light absorption, hole mobility (1×10^{-3} $cm^2 \cdot Vs$)[26] and more planar structure comparing with P3HT.[27]

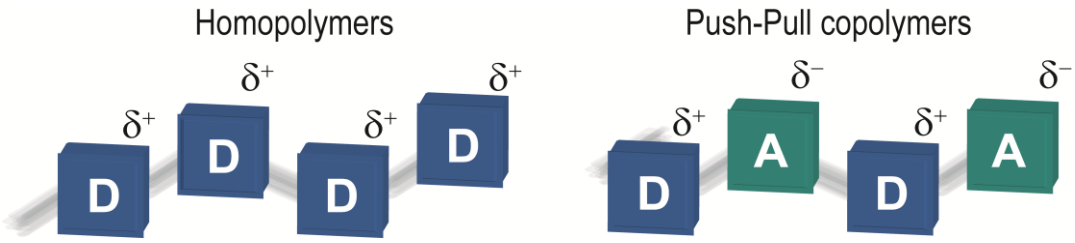

Figure 1.3 Donor homopolymers (such as P3HT) and push-pull copolymers form from alternating copolymers from electron-rich and electron-deficient moieties.

Most successful solar cell devices are currently achieved using PBDB-T (also known as PBDTBDD, PBDTBDD-T or PCE12) and its fluorinated (PM6, PBDB-T-2F, PBDB-T-SF and PCE13) and chlorinated (PM7, PBDB-T-2Cl and PCE14) congeners as donor materials. PBDB-T was first synthesised by Qian et al.[28] and, despite lacking impressive efficiencies mixed with fullerenes (up to 6.67%), its strong aggregation in solution was shown to play an important role in the development of suitable domain sizes.[29,30] In fact, the PBDB-T:$PC_{61}BM$ system exhibited an outstanding fill factor (FF) of 72%. Although the efficiency was restricted to the absorption range of the mixture, the FF value implied the existence of a highly efficient charge generation process in the BHJ.[31] This medium-band-gap polymer (HOMO = -5.23 eV; LUMO = -3.18eV, 1.9–1.5 eV) is mainly composed of two building blocks: 2-alkylthiophene-substituted benzo [1,2-b:4,5-b0] dithiophene (BDT) and 1,3-bis(thiophen-2-yl)-5,7-bis(2-ethylhexyl)benzo-[1,2-c:4,5-c0]dithiophene-4,8-dione (BDD) units, which conferee the polymer excellent planarity and well

delocalized HOMO wave function over the whole conjugated backbone.[28] Its halogenated derivatives were synthesised long after,[32,33] coinciding with one of the major breakthroughs in the field. Hou et al.[34] reported a PCE of 11.21% when PBDB-T was blended with the novel non-fullerene acceptor ITIC.[35] By comparing with the blend of its fullerene counterpart, the PBDB-T:ITIC blend showed a much wider response to sunlight absorption due to the complementary absorptions of both components in the visible range, and a better alignment of the molecular energy levels.[34]

To modulate the optoelectronic properties of polymers and achieve more efficient absorptions, many molecular design strategies have been developed, including the judicious selection of substituents. Fluorination is one of the most effective approaches to alter the properties of organic semiconductors in terms of energy level reduction due to their electron-withdrawing nature, while maintaining a large band gap.[36,37] Moreover, its differences in inter and intrachain interactions due to the effective resonance (π) electron-donating group, can lead to an enhanced backbone planarity and aggregation.[36,38] Chlorination is also a viable route for molecular optimization toward developing high-performing polymers. Interestingly, apart from rendering more cost-effective easy-to-make synthetic procedures, few works have shown that polymers display even deeper HOMO levels. [39–41] Currently, a small modifications in the fused-ring acceptor unit has led to the introduction of the A-D-A copolymer D18 which depicted PCEs exceeding the 18% threshold.[42]

In classical device performance models, it is accepted that the ideal morphology (e.g., in a system such as P3HT:PC[61]BM) consists of polymer crystals.[43,44] These polymer crystals have substantially higher order and layer alignment than their amorphous analogues. This chain order gives them higher optical absorption and improved effective charge transport.[13,43,45,46] However, the emergence of high-performing polymers such as PBDB-T and its derivatives, seems to refute the old paradigms. This is because polymers that are apparently disorder and lack of long-range crystalline order by DSC[47] or X-ray techniques,[48,49] perform similar to crystalline materials.[50,51] Noriega et al.[14] suggested that although highly disorder in the π-stacking, their ability to form aggregates allows locally efficient intermolecular charge transport providing effective pathways

for charge transport. While some works have tried to address the complex microstructure of these polymers rendering overwhelming properties[31,52,53] nowadays no one has attempt to fulfil it.

1.3.2. Acceptor materials

Acceptor materials have been strongly defined by the evolution from fullerenes to non-fullerene small molecule acceptors (SMAs). Through novel synthesis and design methodologies of organic semiconductors, chemists have made a major breakthrough introducing small molecules (SMs) as electron accepting materials. These acceptors have extended the photon absorption from the visible to the near-infrared, which facilitates the charge generation capacity for organic blend films.

1.3.2.1. Fullerenes

Fullerene-based electron acceptors have been widely used in OPV applications. Though derivatives of the well-known [6,6]-phenyl-C61-butyric acid methyl ester (PCBM) and the higher order $PC_{70}BM$ have been the most used materiales for BHJ, a number of other promising fullerene derivatives have also been reported.[25,54] The bulky-shape offers them a three-dimensional electron transport property and the capability of forming favourable nanoscale morphology (similar to the exciton diffusion length) with the donor polymer. Their limited solubility and strong tendency to aggregate is overcome by the introduction of functional groups (**Figure 1.4**). Moreover, fullerenes have a high electron affinity for charge separation and high electron mobility (7.8×10^{-2} $cm^2\cdot Vs$ for [60]PCBM)[55] for efficient charge transport.[56] Importantly, the P3HT:PCBM mixture was key to the advancement of the field, as it helped in learning to control certain characteristics (such as composition, most suitable solvents, post-processing treatments, etc.) necessary for optimal morphology of the active layer.[57]

The main reason for the switch to SMA is the lack of absorption in the visible region of the solar spectrum. Fullerenes possess the maximum absorbance in UV region between 200 and

400 nm.[58] Chemical modification of their backbone is limited, resulting in low structural flexibility and difficulty in tuning the electronic/optical properties.[59] For example, it has been shown that some device parameters such as open-circuit voltage V_{OC}, are dependent on the energy difference between HOMO of the donor and the LUMO of the acceptor.[60] This leads to an increase in synthetic complexity, and also makes the fullerenes less likely to achieve light harvesting complementary to that of the polymer. Regarding stability, fullerenes have shown to undergo detrimental aggregation under thermal stress and they have high sensitivity to light and air in both pristine and blend film.[60]

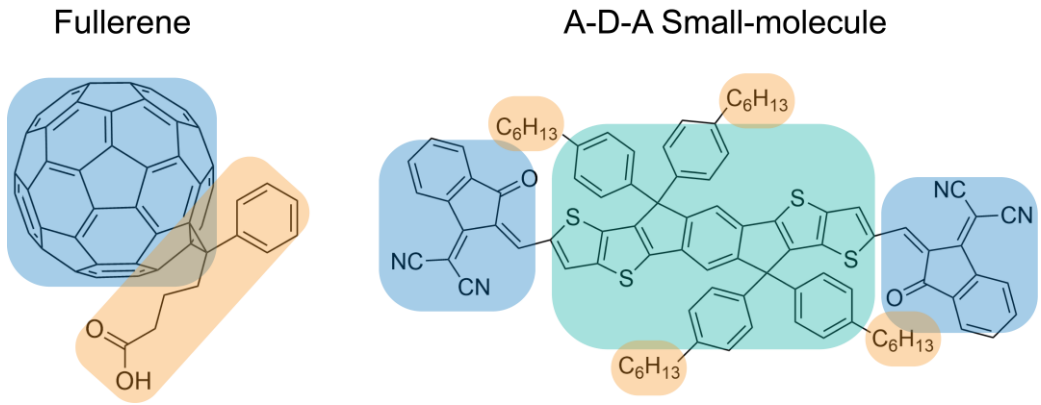

Figure 1.4 Chemical structural template of a fullerene design including the acceptor bulky core (blue) and the soluble group (yellow); and the A-D-A type push−pull NFAs including the donor core (green) linked to two electron-withdrawing moieties (blue) and soluble alkyl side-chains (yellow).

In polymer:fullerene BHJ the polymer (donor) is the responsible of light absorption due to the low absorptivity of the fullerenes. Small-molecule acceptors contain strong dye-based chromophores that could make them an even stronger light absorber than polymers. This means that in a polymer:SMA systems both materials could be photoexcited and tranfer electrons from the donor to the acceptor or holes from the acceptor to the donor.[61] Consequently, through precise design of donors and small molecule acceptors, complementary absorption spectra could be achieved and thus, extend the coverage of the solar spectrum and maximized the photocurrent.

1.3.2.2. Non-fullerene acceptors

The potential of these small molecules is underpinned by their excellent synthetic flexibility. NFA can be specifically design to overcome the poor optical properties of fullerenes and to work with certain polymers. In fact, NFAs exhibit strong absorption in regions of the visible and NIR spectrum. By tailoring their optical properties and energetic levels, they can easily match the electron accepting and transport properties of fullerene acceptors. In general, their molecular structure is based on a conjugated backbone with π-conjugated functional groups (such as cyano groups) that confer them strong electron-accepting abilities and easy electron delocalization into the backbone.[62] Compared to the three-dimensional structures of fullerenes, their 2D planar conjugated structures exhibit anisotropic crystalline structures and charge transport. This may complicate the formation of effective electron-extraction pathways.[63] It is therefore essential to find a donor:acceptor pair that guarantees an optimal molecular orientation, favouring their π–π interactions.[62]

SMAs for OPV can be generally categorized in diimide-based NFAs and acceptors based on acceptor–donor–acceptor (A–D–A)-type fused ring electron acceptors (FREAs). Although fused aromatic diimides were considered as promising candidates for OSCs,[64] the difficulties to find a balance between solubility and effective π–π interactions has hampered their application.[62] Using the same strategy as for push-pull copolymers, A-D-A small molecules, have delivered the highest PCE to date.[2] FREAs consist in a planar electron rich donor central core consisting on fused rings substituted with aryl or alkyl side chains projecting out of the plane and electron deficient acceptor units on their sides (**Figure 1.4**).[59] The leading molecule was synthesized in 2015 by Zhang et al.[35] under the acronym ITIC. This molecule is formed by a indacenodithieno[3,2-b]thiophene (IDTT) core with dicyanovinylindanone (DCI) units as electron-withdrawing units and four out-of-plane 4-hexylphenyl side chains that improve its solubility and prevent excessive aggregation. The side chains in ITIC projecting out of the plane suppresses the formation of 1D π-stacks. By contrast, intermolecular π-π interactions occur between the acceptor end-groups forming a robust 3D network.[65] Because ITIC is a model NFA

and can be easily tune by the incorporation or substitution of several groups, many works focusing on structural modifications of ITIC have been published recently. The structural modifications affect the energy levels and absorption regions of NFAs as well as the molecular ordering and film morphology of the corresponding active layers. For example, by the introduction of an electron-rich group like methyl into the end-capping units (ITIC-M),[66] by the incorporation of electron-deficient atoms such as fluorine (ITIC-2F)[32] or chlorine (ITIC-2Cl)[67] or by the substitution of the phenyl units by thienyl groups (ITIC-Th).[68] These structural changes resulted in modified LUMO levels through changes in molecular interactions, leading to an overall improvement in PCE from 11% to 14%.[69] Moreover, it was shown that only by engineering the side-chain isomerism of the alkyl-phenyl substituents of the ITIC, a higher crystallinity and a preference face-on orientation could be achieved. This minor modification resulted in an increased the electron-mobility, and enhanced PCE.[70] Therefore, the abovementioned works prove that chemical modifications may lead to dramatically different molecular ordering behaviours and play a critical role in tuning morphological properties in the blend. Thus, an in-depth understanding of such microstructural variations is a must for device optimization.

Several modifications of the ITIC moiety has resulted in the development of the so-called Y-series acceptors.[71] Thus, the PCEs for NFA-based solar cells have exceeded the 18% threshold in lab devices, now far beyond the best fullerene systems. [2,72]

1.4. Bulk heterojunction polymer solar cells

Silicon-based photovoltaic solar cells are by far the most widely used solar cell technology.[73] The p-n junction silicon solar cell provides efficient absorption of photons (>1.1 eV) in the visible and near-infrared region of the electromagnetic spectrum and delocalisation/dissociation of photogenerated excitons[74,75] The first breakthrough in organic photovoltaics happened in the 1980s, when Tang[76] introduced the importance of generating an interface region within an n-type and a p-type semiconductor using planar or bilayer heterojunction (PHJ) device geometry (see **Figure 1.5**).[77] This geometry contributed to maximised photosensitivity by overlapping the

absorption spectra of the two materials, thus enhancing the photogeneration of charges at the interface to diffuse into the bulk of the films. However, the structure of the bilayer limited charge generation to the 10-20 nm thick donor-acceptor interface, leading to loss of absorbed photons beyond the interface and resulting in low quantum efficiencies.[78,79]

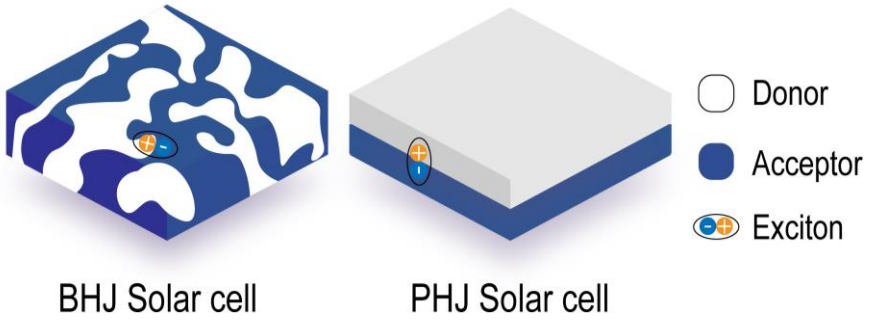

Figure 1.5 Schematics of bulk heterojunction and planar heterojunction.

Subsequently, Heeger and his collaborators emerged as pioneers in the field. First, they unveiled the use of the polymer:fullerene blend for ultrafast charge transfer (occurring in 300 fs) approaching unity in quantum efficiency, and providing a very effective way to overcome charge recombination.[80–83] And then introducing the concept of bulk heterojunction structure (BHJ).[11] Interestingly, in the same year Friend and co-workers reported the advantages of using phase-separated polymer photodiodes to effectively dissociate excitons in the polymer:polymer interpenetrating network.[84] The main advantage of these BHJs was the large D-A intimately intermixed interfacial area distributed in the whole volume of the layer within a distance less than the exciton diffusion length from the absorbing site (see **Figure 1.5**).[27,79] Bulk heterojunction is characterised by a bicontinuous interpenetrating network of polymer donor and acceptor[84] that neatly solves the problem of exciton dissociation and charge transport. Since then, although there has been a transition from fullerenes to small-molecule acceptors, the BHJ has been established as the preferred choice for organic solar cell architecture.

To build this BHJ architecture both donor and acceptor materials are normally simultaneously solution-cast in a common solvent.[85,86] Therefore, the phase structure of the donor-acceptor components defines the resulting BHJ morphology. Currently, the most efficient BHJs

develop a multi-scale morphology composed of amorphous donor (semiconducting polymer)-acceptor (small molecule) phases, coexisting with acceptor-rich domains and donor-rich domains, if semi-crystalline polymers are used. For efficient operation, the arising morphology must provide a sufficient interface for the dissociation of the photogenerated excitons, which can be accomplished by an adequate amount of donor-acceptor mixture, and on the other hand, it must generate percolation pathways for electrons and holes to accumulate at the electrodes. Optimising BHJ morphology requires extensive control of many different parameters, from the design of optimal molecular structures to the treatment of specific processing conditions, such as casting solvent and additives,[87,88] the control of film casting conditions and possible post-deposition treatments. The rapid increase in efficiency is linked to the availability of a wide range of new organic materials. These materials have been reported to give rise to a wide variety of microstructures requiring further understanding of the effect of different processing protocols. In addition, it is essential to understand the thermodynamic and kinetic factors that underpin the long-term morphological stability of the film.[89]

1.4.1. Importance of morphology control

Since the discovery of the BHJ architecture, many works have assess the importance of a fine control over the morphology as the device performance parameters seem to be extremely sensible to the nanomorphology induced by the spontaneous phase separation of the D:A blends.[90–94] For this reason, improving the understanding of the interplay between desirable microstructural features and optoelectronic processes is crucial to design strategies for processing such a diverse range of materials into efficient cells.

1.4.1.1. Processing and post-processing variables

For obtaining a fine multi-length scale morphology, the synergistic effect of casting solvent, additive inclusion, molecular structure and temperature-dependent aggregation has to be

considered (**Figure 1.6**). These variables are expected to improve the structural order of at least one of the components and the phase separation between donor and acceptor, leading to a more favourable nanomorphology.[95]

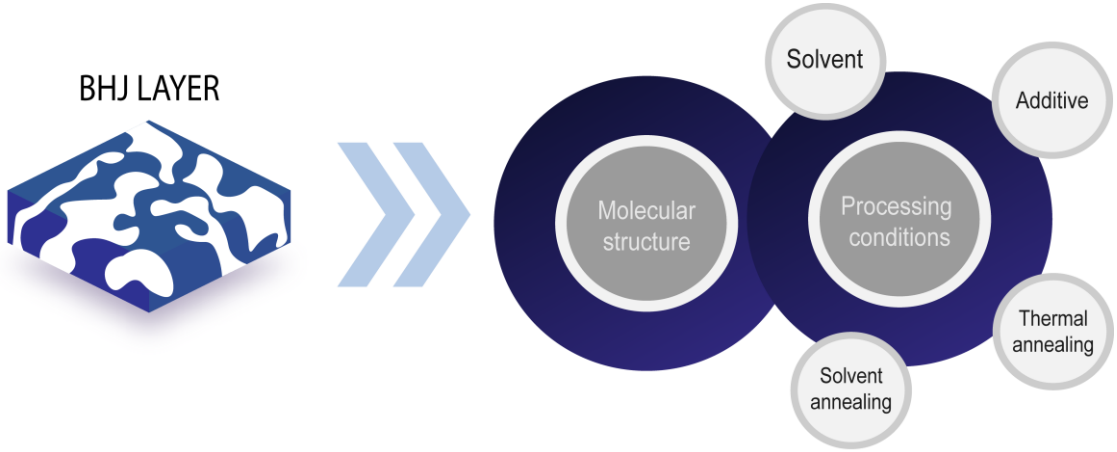

Figure 1.6 Factors that affect the bulk heterojunction morphology.

To date, record OPV yields are achieved by solution-casting from harzarous halogenated solvents i.e. chlorobenzene (CB), orto-dichlorobenzene (o-DCB) and chloroform (CF), which are harmful for human health and the environment. For this reason, halogen-free solvents, such as o-xylene (o-Xy), 1,2,4-trimethylbenzene (1,2,4-TMB), toluene (Tol) and tetrahydrofuran (THF), have emerged as a new processing strategy offering comparable device outputs.[85,96–98] The relevance of the selection of the solvent lies mainly in its solubility, but also in its boiling point and wettability, among others. Consequently, halogen-free solvents generally have a lower solubility due to their different chemical structures.[99] Differences or lack of solubility may induce excessive phase separation, because donors or acceptors will tend to produce large aggregates during the solution process. This handicap is usually overcome by fine molecular control[100,101] and designing new molecules with longer, soluble branched side chains.[102–105]

Regarding solvent additives, Bazan and co-workers revealed that the addition of a small amount of alkanethiols in the initial blend formulation solution could positively modify the final BHJ morphology and thus, device operation.[87] Since then, the best high-performing OPVs have been obtained adding the proper amount of additive (~2−6 v/v %) being the most popular

additives include 1,8-diiodooctane (DIO),[67,96,106] 1-chloronaphthalene (CLN)[68,72,107] and 1,8-octanedithiol (ODT)[59], among others. The criterion for a good choice of additive requires that it selectively dissolves one of the components and has a higher boiling point than the primary solvent.[88] A novel approach in OPVs based on non-fullerene acceptors is to add a small amount of fullerene derivative, i.e. use fullerene as an additive, to increase the photostability of the device.[108] In general, additives selectively dissolved small molecules and fullerenes acceptors.[109] The addition has a pronounced effect in provoking structural changes across multiple-length scales. For example, at molecular scale, increasing crystallite population and degree of crystallinity, together with more texture orientation.[110–112] But also, on larger length scales either improving phase separation or suppressing oversized phase segregation, leading to purer and optimized domains beneficial to exciton dissociation (domain size) and charge transport (pure domains).[109,112,113] However, it is necessary to optimise the right amount to achieve high purity variation and highly ordered packing at the smallest length scales, avoiding the exaggerated enlargement of crystalline domains which can strongly affect their connectivity through the layer thickness.[114] Interestingly, non-fullerene donor:acceptor mixtures, in general, show a lower solvent additive demand than fullerene-based OPVs.[115]

Another approach for morphology matching is based on post-treatment processes such as thermal annealing or controlled solvent evaporation among others.[116] Both treatments provide an external driving force for the re-arrangement of donor and acceptor domains improving the crystallinity and average purity composition in the blend. [111]

1.4.1.2. Thermodynamic and kinetic effect

In general, bulk heterojunction morphologies develop, at least, a complex three-phase system comprising donor- and acceptor-rich domains coexisting with an amorphous intermixed donor-acceptor region. For efficient operation, an optimal trade-off between the intermixed donor:acceptor regions (in most cases amorphous) and aggregation within the pure donor and/or acceptor phases must be accomplished. These phase morphology depends on the miscibility of

the two components and the processing routes used for the deposition.[90] Thus, the composition of the intermixed domains is highly dependent on thermodynamic molecular interactions and kinetic factors governing the casting processes.[59,117]

The miscibility of the components of a binary system is determined by the Flory-Huggins parameter dictated by the Gibbs free energy of mixing. Positive values of the Flory-Huggins parameter, χ, lead to incompatibility, while negative values favour mixing. Therefore, by estimating the interaction parameter as a function of composition, one can determine the critical value of χ that separates the range of perfect mixing, i.e. compatibility across all compositions, from the range with a miscibility gap. The phase separation between two components can be described by phase diagrams through binodal and spinodal lines (**Figure 1.7**). In a binary system, the binodal line delimits the single-phase and two-phase regions in a phase diagram and is therefore the local thermodynamic equilibrium stoichiometry or, in other words, the maximum purity achievable in amorphous mixed domains.[8]

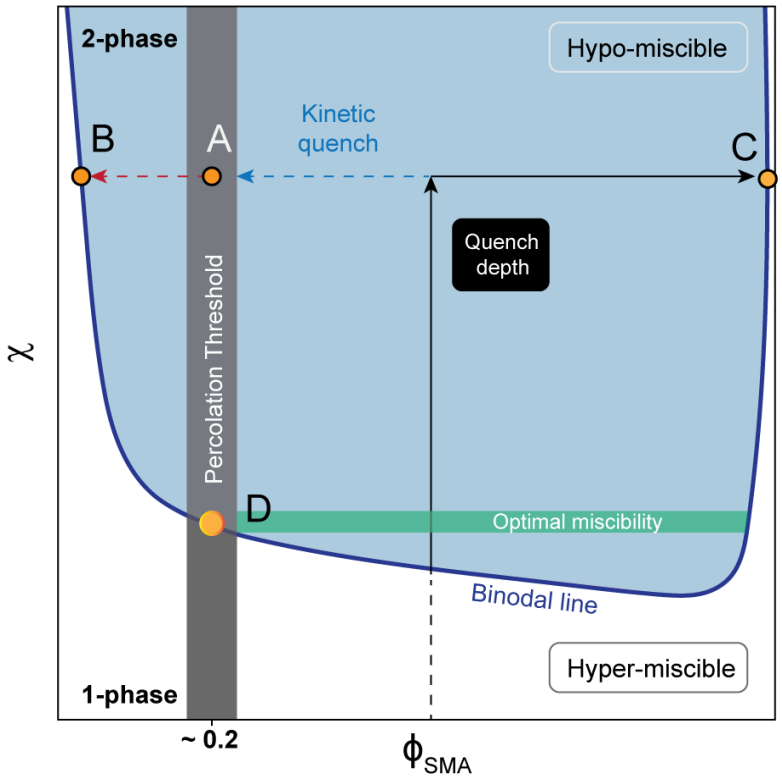

Figure 1.7 Asymmetric model Flory-Huggings parameter–composition phase diagram with binodal line separating one-phase and two-phase regions and with different scenarios represented. This scheme is adapted from reference [47].

In BHJ systems, it is widely agreed that a relatively high χ is needed to develop strong phase separation between the components; however, too high values could lead to an over-purification of the intermixed domains negatively affecting the properties of the device.[89,117] If two materials are too miscible, the volume fraction of the amorphous mixed phases will be too large and therefore the lack of pure donor and acceptor domains will hinder proper charge transport (hyper-miscible region in **Figure 1.7**). It is therefore necessary to find two components with lower miscibility; however, overly immiscible systems will eventually result in the formation of large aggregates of pure donors and acceptors, also damaging the device function (C in hypo-miscible region in **Figure 1.7**).[118,119] To ensure a fine phase separated morphology in the system, the morphology is initially quenched. The initial quench depth i.e. depth that describes how deep a system is located inside the two-phase region of the phase diagram in the initial composition, [119] will be strongly determined by kinetic drivers during morphology formation.[89] This initially quenched morphology is driven to a lower purity state compared to its equilibrium state during the deposition period (quench depth in **Figure 1.7**). This quenching normally restricts the crystallisation of SMA or fullerene acceptor.[120] At this stage, the morphology which is out-of-equilibrium, may evolve towards its equilibrium state over the device operation.[121] For this reason, to avoid detrimental phase separation in hypo-miscible systems, the morphology evolution must be kinetically quenched to obtain a composition of the amorphous mixed phases close to the percolation threshold, i.e. a critical volume fraction where this interpenetrating network first appears corresponding to the lower limit of electron transport,[119,122] in coexistence with pure donor-acceptor region (0.1-0.2 fullerene composition[44,123] and 0.2-0.3 NFA composition[119]) (A, **Figure 1.7**). However, in such case (B, **Figure 1.7**), where the percolation threshold is far from the miscibility gap, i.e. the binodal, if kinetically possible, the system will undergo morphological instabilities due to thermodynamic relaxation of the mixed domains or crystallisation of the NFA, leading to excess purification. Thus, the optimal morphology will be the one whose phase diagram has the percolation threshold close to the binodal line as it is expected to have greater stability over time (D, **Figure 1.7**) or one whose morphology can be vitrified preventing detrimental phase separation through crystallization.[124]

Through several noteworthy contributions, Ade and co-workers have built a framework based on the binodal determination of the systems and parameterised with the Flory Huggins interaction parameter, to track the purity of mixed domains in donor:NFA systems as a function of various thermodynamic and kinetic factors, offering high accuracy in relating morphological characteristics to device function. On the basis of early studies, it is accepted that the optimal interaction parameter is one that is high enough to lead to strong phase separation with a mixed phase composition close to the percolation threshold leading to the best efficiencies. [89] Since then, they developed the first phase diagram based on the polymer:non-fullerene acceptor blend and revealed, for systems differing only in polymer molecular weight, the importance of controlling kinetic factors during casting. Early polymer aggregation, i.e. liquid-solid transition, caused by higher molecular weights, resulted in smaller pure domains and vitrified mixed domains far from the binodal composition (in the system studied), but close to the percolation threshold..[119] By exploiting the temperature dependence of the Flory–Huggins parameter versus the composition of amorphous mixed phases, they discover the importance of controlling the physical properties of the individual components. Thus, systems consisting of acceptors with high glass transition temperature (T_g) and low ductility polymers can kinetically stabilise thermodynamically metastable phases against crystallisation and demixing by lowering diffusion coefficients.[48,120,124] In addition, they recently shown that highly hypo-miscible systems reveal lower interdiffusion making demixing and depletion through crystallisation kinetically unfavourable and, therefore, opening a new route for long-term stability.[47,125] They claim that the key lies in a molecular level understanding focusing on the physical properties of the constituent materials (higher T_gs reduce diffusivity), and the application of processing and post-processing protocols based on fine control of the phase diagram for each system to ensure morphological stability. It is noteworthy that in these novel studies, while thermodynamic and kinetic factors concerning SMA have been explored, little attention is paid to the mechanical and thermal properties of the polymers due to the difficulties encountered in measurement.[47]

1.5. Device performance and relation with morphology

Briefly, current production in a BHJ OPV unfolds through photon absorption and exciton (electron-hole pair closely bound by Coulombic attraction) formation, followed by diffusion towards the donor-acceptor interface where it either dissociates or returns back to the ground state realising energy. Dissociated charges then diffuse through the donor and acceptor domains to accumulate at the electrodes (**Figure 1.8**).[126,127] The solar cell performance is mostly parametrized by three values namely short-circuit current (J_{SC}), open-circuit voltage (V_{OC}) and fill-factor FF which deliver the efficiency value (PCE). The PCE is the parameter that defines the overall performance of the device and it is defined by the ratio between the output power (P_{out}) and the incident light (P_{in}):

$$PCE = {P_{out}}/{P_{in}} = {V_{oc} \cdot J_{sc} \cdot FF}/{P_{in}} \quad \textbf{(Equation 1.1)}$$

These values will be strongly affected by the molecular design of the donors and acceptors (see section 1.2), including the optical bandgap, absorption spectra and energy level alignment of the photovoltaic materials; the nanomorphology of the active layer (see section 1.4), including phase purity, phase size and crystallinity; and finally, the device architectures and operating mechanisms.

In general, it is accepted that some donor-acceptor mixed phase is needed for proper exciton dissociation rendering optimal short-circuit current .[89] At the same time, pure domains are necessary for proper charge transport and are therefore effective in reducing recombination energy losses, resulting in increased FF.[128,129] Thus, the high purity of mixed domains facilitate the charge separation; however, an over-purification may affect the percolation pathways for the electrons.[95] Beyond these, the short exciton diffusion length compels to the development domain sizes between 10-20 nm, although diffusion lengths up to 45 nm have been found in some NFAs.[130] These considerations imply the requirement of achieving a compromise between the fraction of pure and intermixed phases in order to achieve optimum performance achieved at the percolation threshold.[47]

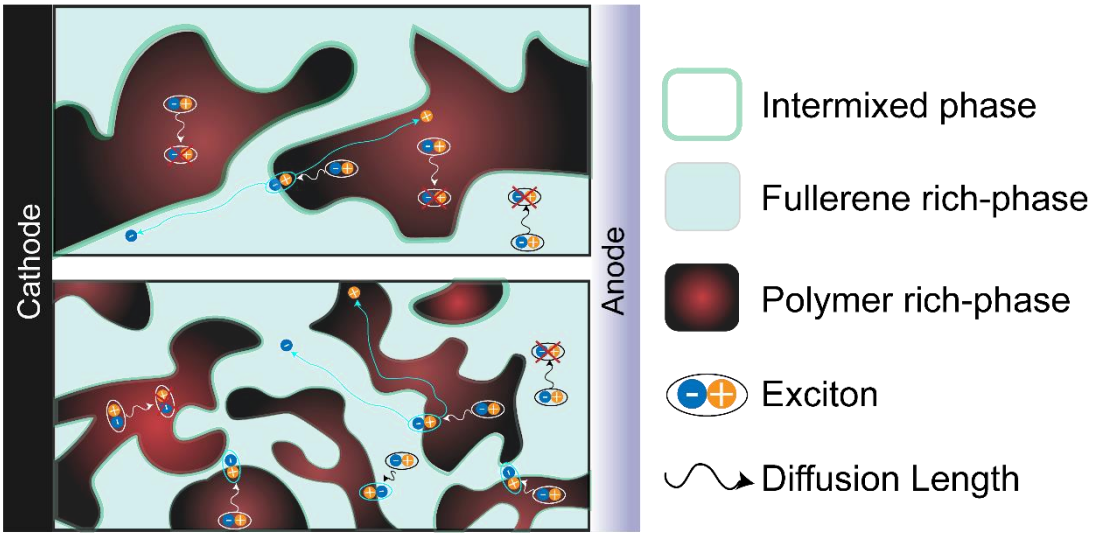

Figure 1.8 BHJ morphology and photocurrent generation in two different donor-acceptor morphologies.

Unfortunately, due to the weak non-covalent interaction between donor and acceptor materials and the disordered nature of the organic materials used in BHJ solar cells, predicting the precise morphology of the output is more complicated compared to their inorganic crystalline counterparts. Moreover, this optimal morphology may evolve over time due to various external factors, such as prolonged exposure to light and temperature (i.e. under realistic operation), resulting in photodegradation of the NFA[131,132] and polymers,[133] and/or diffusion of the NFA into the polymer matrix, leading to detrimental aggregates, demixing of the donor-acceptor phases and vertical segregation throughout the films.[48] Furthermore, all these parameters have shown to be directly related with the molecular structure.[131,134] All this translates into an accumulation of defect and traps for the charges rendering the undesired burn-in (i.e. standard terminology for an early state degradation).[121,133] It is therefore necessary to find a balance between molecular design, performance, stability as well as commercialisation.

2

In this part you will find all the information related to the materials used throughout the thesis. Moreover, you will familiarise with the different processing protocols employed for sample preparation and the techniques that helped me develop my methodology.

2. Materials and methods

2.1. Materials

The polymers, fullerenes, small-molecules and others materials used during this thesis are presented in **Table 2.1**.

Table 2.1 Materials used to develop this thesis.

Name	**M_w (kg·mol^{-1})**	**Provider**
regioregular poly(3-hexylthiophene) (RR-P3HT)	135	Merck
regiorandom poly(3-hexylthiophene) (RRa-P3HT)	-	Merck
poly(3-dodecylthiophene) (P3DDT)	~60	Merck
poly[(2,6-(4,8-bis(5-(2-ethylhexyl)thiophen-2-yl)-benzo[1,2-b:4,5-b']dithiophene))-alt-(5,5-(1',3'-di-2-thienyl-5',7'-bis(2-ethylhexyl)benzo[1',2'-c:4',5'-c']dithiophene-4,8-dione)] (PBDB-T)	70.5	Ossila Ltd.
poly[(2,6-(4,8-bis(5-(2-ethylhexyl-3-fluoro)thiophen-2-yl)-benzo[1,2-b:4,5-b']dithiophene))-alt-(5,5-(1',3'-di-2-thienyl-5',7'-bis(2-ethylhexyl)benzo[1',2'-c:4',5'-c']dithiophene-4,8-dione)] (PBDB-T-2F)	>50	Ossila Ltd.
poly[(2,6-(4,8-bis(5-(2-ethylhexyl-3-chloro)thiophen-2-yl)-benzo[1,2-b:4,5-b']dithiophene))-alt-(5,5-(1',3'-di-2-thienyl-5',7'-bis(2-ethylhexyl)benzo[1',2'-c:4',5'-c']dithiophene-4,8-dione)] (PBDB-T-2Cl)	77.3	Ossila Ltd.
poly[(2,6-(4,8-bis(5-(2-ethylhexyl-3-fluoro)thiophen-2-yl)-benzo[1,2-b:4,5-b']dithiophene))-alt-5,5'-(5,8-bis(4-(2-butyloctyl)thiophen-2-yl)dithieno[3',2':3,4;2",3":5,6]benzo[1,2-c][1,2,5]thiadiazole)] (D18)	95	1-Materials
poly(benzodithiophene-alt-dithienyl difluorobenzotriazole) (PBnDT-FTAZ)	~60	-
poly [[4,8-bis[(2-ethylhexyl)oxy]benzo[1,2-b:4,5-b']dithiophene-2,6-diyl][3-fluoro-2-[(2-ethylhexyl)carbonyl]thieno[3,4-b]thiophenediyl]] (PTB7)	78.8	Ossila Ltd.
indacenodithiophene-co-benzothiadiazole (IDT-BT)	321.6	-

poly[bis(4-phenyl)(2,4,6-trimethylphenyl)amine (PTAA)	-	-
poly(ε-caprolactona) (PCL)	-	Merck
poly(vinylidene fluoride) (PVDF)	~60	Polyscience Inc.
poly(ethylene oxide) (PEO)	1000	Merck
mono-adduct of the *o*-xylenyl C_{60} (OXCMA)	-	-
bis-adduct of the *o*-xylenyl C_{60} (OXCBA)	-	-
[6,6]-Phenyl-C61-butyric acid methyl ester (PC[60]BM)	0.91	Solenne
3,9-bis(2-methylene-(3-(1,1-dicyanomethylene)-indanone))-5,5,11,11-tetrakis(4-hexylphenyl)-dithieno[2,3-d:2',3'-d']-s-indaceno[1,2-b:5,6-b']dithiophene (ITIC)	1.42	Ossila Ltd.
3,9-bis(2-methylene-((3-(1,1-dicyanomethylene)-6/7-methyl)-indanone))-5,5,11,11-tetrakis(4-hexylphenyl)-dithieno[2,3-d:2',3'-d']-s-indaceno[1,2-b:5,6-b']dithiophene (ITIC-M)	1.45	Ossila Ltd.
3,9-bis(2-methylene-(3-(1,1-dicyanomethylene)-indanone))-5,5,11,11-tetrakis(5-hexylthienyl)-dithieno[2,3-d:2',3'-d']-s-indaceno[1,2-b:5,6-b']dithiophene (ITIC-Th)	1.45	Ossila Ltd.
3,9-bis(2-methylene-((3-(1,1-dicyanomethylene)-6,7-difluoro)-indanone))-5,5,11,11-tetrakis(4-hexylphenyl)-dithieno[2,3-d:2',3'-d']-s-indaceno[1,2-b:5,6-b']dithiophene (ITIC-2F)	1.49	Ossila Ltd.
poly(3,4-ethylenedioxythiophene) polystyrene sulfonate (PEDOT:PSS) ink dispersion	-	Clevios™
Zinc oxide (ZnO) nanoparticle dispersion	-	Avantama Inc.
Molybdenum oxide (MoO_3)	-	-
silver (Ag) pellets	-	Merck
D-(+)-glucose	-	Merck

As solvents, chlorobenzene (CB), orto-dichlorobenzene (o-DCB), chloroform ($CHCl_3$), dichloromethane (CH_2Cl_2), orto-xylene (o-Xy), and diiodoctane (DIO) were purchased from Merck and used as received. To clean the substrates, analytic grade acetone, 2-propanol, ethanol, sodium hydroxide 10 vol%, Hellmanex solution diluted at 10% in water and toluene were acquired from Merck and Labbox and used as received.

2.2. Sample preparation

The polymer and small molecule films, as well as active layers were deposited by spin coating (2000 rpm, 60 s) from 10-20 $mg \cdot mL^{-1}$ solutions. Prior to depositions, the solutions were stirred during minimum 2 hours to overnight at 35 ºC for samples dissolved in chloroform and dichloromethane, and 80 ºC for the remaining solvents (CB, o-DCB, o-Xy).

2.2.1. Film casting

Along the thesis three different casting techniques were used to produce thin film materials: spin-coating (1), drop-casting (2) and blade-coating (3). The vast majority of the samples analyzed in this work were deposited by spin-coating. On the other hand, the performance of the solar devices detailed in Chapter 6, was studied on blade-coated samples. Finally, the drop-casting method was used when thick films (i.e. thicknesses > 1 μm) were required

(1) Spin-coating: A certain volume of a solution is pipetted onto a pre-cleaned substrate placed on the spin-coater rotating plate. Then, just after deposition, the spin-coater program is started, which contains spinning parameters, i.e. spinning rate and time (e.g. typical parameters used are 2000 rpm and 60s were employed). Finally, the film is allowed to dry under ambient conditions before any thermal protocol is applied. In this thesis, a spin-coater supplied by Ossila Ltd. was used.

(2) Drop-casting: A small volume of solution (20μL) is placed with a micropipette on a pre-washed substrate and leave it air-dry at ambient conditions. Often, for FLASH DSC or DSC measurements, solution is dropped onto a glass slide and then scratch off the material once the solvent has fully evaporated.

(3) Blade-coating: Active layer solutions are blade coated onto the ITO substrates in atmospheric conditions using an automatic blade coater Zehntner ZAA 2300 with an aluminum applicator Zehntner ZUA 2000, at a constant speed or varying the speed across the length of the glass to obtain a thickness gradient.

The following substrates were used to support organic thin films: n(arsenic)-doped silicon (100) polished on both sides from Neyco, glass slides from Merck and indium tin oxide (ITO) substrates purchased from Ossila Ltd. Prior to casting, the glass and silicon substrates were cleaned by consecutive sonication baths in acetone and then in isopropanol. Afterwards, the substrates were dried with air and placed in an ozone cleaner (Ossila Ltd.) for 15 minutes. On the other hand, the ITO substrates were cleaned by consecutive sonication baths in acetone, soap (Hellmanex), isopropanol and 10% sodium hydroxide (5 to 10 minutes each), with a distilled water rinse after each step.

2.2.1.1. Thin film preparation on top of UFS Chip calorimeter

Generally, organic solar cells are solution-processed and manufactured as thin films. Given the large surface area of the interface relative to the volume of the material, the thermal properties can significantly deviate from those of the corresponding bulk system. One of the main advantages of ultrafast calorymetry (FSC) lies in the applicability to measure thin films. Film preparation is performed on the backside of the chip as shown in **Figure 2.1**[135–137]

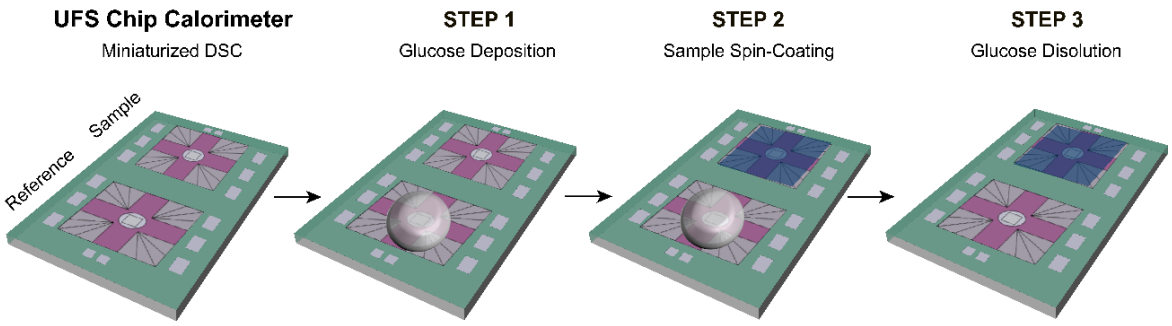

Figure 2.1 Sample deposition method onto the chip calorimeter.

The casting protocol consist in the following steps: First, the reference sensor is covered with glucose. Once the glucose droplet partialy solidifies/gelates, it becomes insoluble in halogenated solvents, and the organic semiconductor solution can be safely spin coated on the other chip, i.e. the on the sample chip. Finally, glucose is removed from the reference by

dissolving it in water.[135] This procedure rises the possibility of fabricating thin film on top chip calorimeters and gain insigths into thermal properties of device-relevant samples rather than bulk.

2.3. Characterization methods

In this section we present the characterisation techniques used to study the structural features of different materials and their relationship with device performance. Our methodology to unravel the microstructure and morphology of high-performance donor polymers and small molecules used in organic solar cells is mainly based on the rational combination of three techniques: Fast Scanning Calorimetry (FSC), Temperature-resolved Polarised Light Optical Microscopy and Spectroscopy (PLOM-S) and, ex-situ and in-situ Grazing Incidence Wide Angle X-ray Scattering (GIWAXS) at synchrotron facilities (**Figure 2.2**). In addition, atomic force microscopy (AFM) and Grazing Incidence Small Angle X-ray Scattering (GISAXS) with synchrotron radiation have been used to perform a comprehensive analysis of the morphology of the thin films. On the other hand, to evaluate the optoelectronic properties of the active layer and pure materials and the performance of the device, measurements have been performed with different spectroscopic techniques (absorption, photoluminescence, Raman, transient-absorption, and ultraviolet-photo-electron spectroscopies) and current-voltage measurements in solar cell devices (OPV) and charge mobility measurements in organic field effect transistors (OFET)

Figure 2.2 Methodology used for microstructural study.

2.3.1. Fast Scanning Calorimetry (FSC)

Fast Scanning Calorimetry has proved to be a key tool in this project, as it has turned out to be able to trace thermal processes and microstructural features undetectable by other conventional techniques. Using this technique, it is possible to heat and cool materials at a rate of one thousand Kelvin per second. As a consequence, sample masses are drastically reduced from a few mg by standard DSC to tens of ng by FSC, thus reducing early degradation. FSC measurements were carried out using a Mettler Toledo Flash DSC 1 fast scanning calorimeter based on a power compensation twin-type chip, equipped with an intracooler allowing temperature control between -90 and 450 °C, and with nitrogen purge (75 $mL \cdot min^{-1}$ N_2 gas flow). MultiSTAR UFS1 (24 × 24 × 0.6 mm^3) MEMS chip sensors were conditioned and corrected according the specifications prior to use. The thin film samples were cast on the backside of the chip sensor, while the bulk samples were placed on the frontside of the chip sensor.

The properties of the amorphous and crystalline regions of the materials and the blends, as well as the mechanism involved during annealing, were identified using different thermal protocols, modifying the isothermal temperatures and times, as well as the annealing sequences and heating and cooling rates. The detected thermal processes can be endothermic or exothermic depending on whether they absorb thermal energy or release it (in the thesis, endothermic processes are represented upwards). The glass transition temperature (T_g), a transition related to the amorphous domains of the material, is detected as a step-like increase in the heat-flow-temperature diagram. In general, crystalline domains will lead to melting and sometimes crystallisation transitions. Melting processes are detected as an endothermic peak in the heat flow, meaning that the system requires heat to progress towards higher temperatures. Crystallisation, on the other hand, is an exothermic process that is usually detected above the glass transition temperature. In this phase, chains with sufficient mobility can reorganise into ordered periodic crystals.

Often, due to the low energy of the transitions, there may be no sign of a stepwise increase in the FSC trace that can be linked to the glass transition temperature despite being a completely amorphous sample.

2.3.1.1. Annealing protocols in FSC

A particularly useful type of experiment in FSC are isothermal "annealing" experiments. In general, throughout this thesis we have employed three different isothermal step protocols that helped us to disentangle the different thermal events occurring in our pure materials and mixtures. Thus, by taking advantage of the possibilities of using FSC, such as the proposal by Cangialosi et al.[135] to perform the so-called isochronous ageing/annealing experiments to evaluate the T_g of thin films, we were able to unravel the thermal behaviour of these new high-performance materials that remain elusive due to the low sensitivity of previously used techniques.

In a first attempt, we detect the presence and nature of thermal events occurring in the material just after deposition and optimise the boundary temperatures, heating and cooling rates that allow an excellent compromise to obtain high signal intensities, resulting in low thermal lag and avoiding thermal degradation of the samples as well as secondary crystallisation.[138] Subsequently, different isothermal step protocols (1) isochronous ageing/annealing and (2) isothermal annealing were judiciously applied.

(1) ISOCHRONOUS AGEING/ANNEALING: The thermal protocol employed for the isochronous aging/annealing experiments is shown in **Figure 2.3**. It was first employed by Cangialosi et al.[135] to identify the T_g of thin films by FSC. Samples are first brought to a high temperature, T_H, much higher than the T_g, where the miscibility of the components of the blend lies into the one-phase region (above melting temperature) or the pure material is in the melt state. Films are then quenched from T_H to a certain temperature, T_a, at a given cooling rate (β) and held there for a certain time scale (t_a). If T_a is below the T_g of the glassy domains formed during cooling at β cooling rate, physical aging will occur in those glassy domains (this phenomenon will be

described in detail below). Then, films are cooled down to a temperature (T_L) much lower than the expected T_g and subsequently reheated to T_H. This heating scan will show the effect of the aging step if any. This heating step is plotted in green in **Figure 2.3**. As a reference, we employ the calorimetric signal of the unaged material, i.e., the calorimetric heating signal of samples that are cooled down from T_H to T_L and then heated back to T_H without any isothermal step. This reference heating step is plotted in blue in **Figure 2.3**.

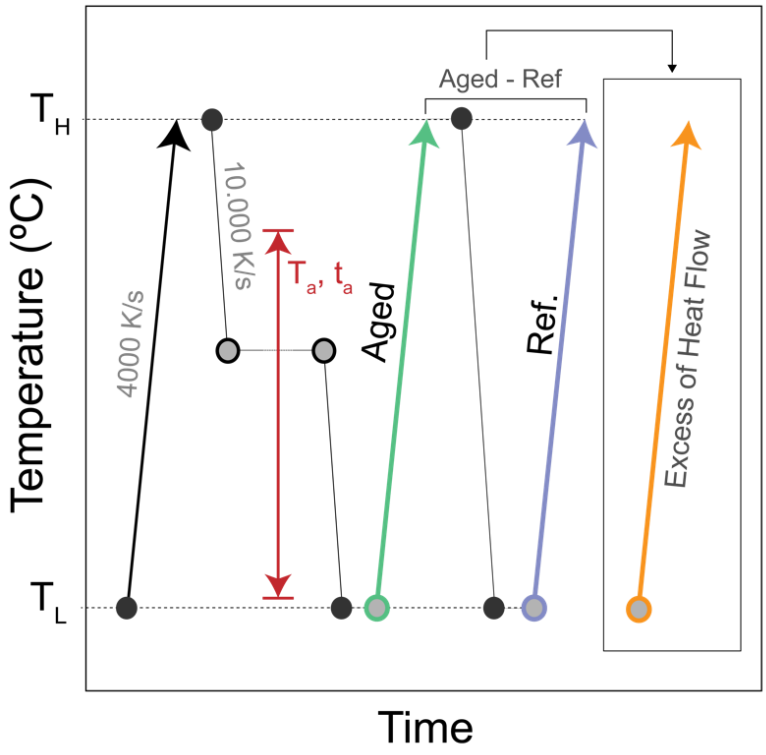

Figure 2.3 Isochronous (constant annealing time) and isothermal (constant temperature) annealing thermal protocol.

Cangialosi´s method to identify the T_g of thin films by FSC is supported by the fundamental definition of the T_g,[135] that is, the temperature defining the intersection between a supercooled melt in (metastable) equilibrium and the out-of-equilibrium glass[139]. From this definition, a system in the glassy state, which is far from thermodynamic equilibrium, will spontaneously evolve towards a more equilibrated state by reducing its enthalpy level (this evolution is depicted in Case 1 of **Figure 2.4**).[135] In calorimetry, this physical aging process can

be detected in a subsequent heating scan as an endothermic overshoot (peak) at temperatures closet to T_g (**Figure 2.4**b, green line). Conversely, a system that is above its T_g, i.e. in the melt state, will exhibit no physical ageing as it is already in (metastable) equilibrium (**Figure 2.4**a: Case 2). Therefore, the T_g is defined as the temperature below which a system can physically age, giving rise to an enthalpy relaxation peak detectable by calorimetry.[140,141] We note that this definition provides the temperature of the upper onset of the glass transition on cooling, which is why it is denoted as $T_{g,onset}$ throughout the different chapters.

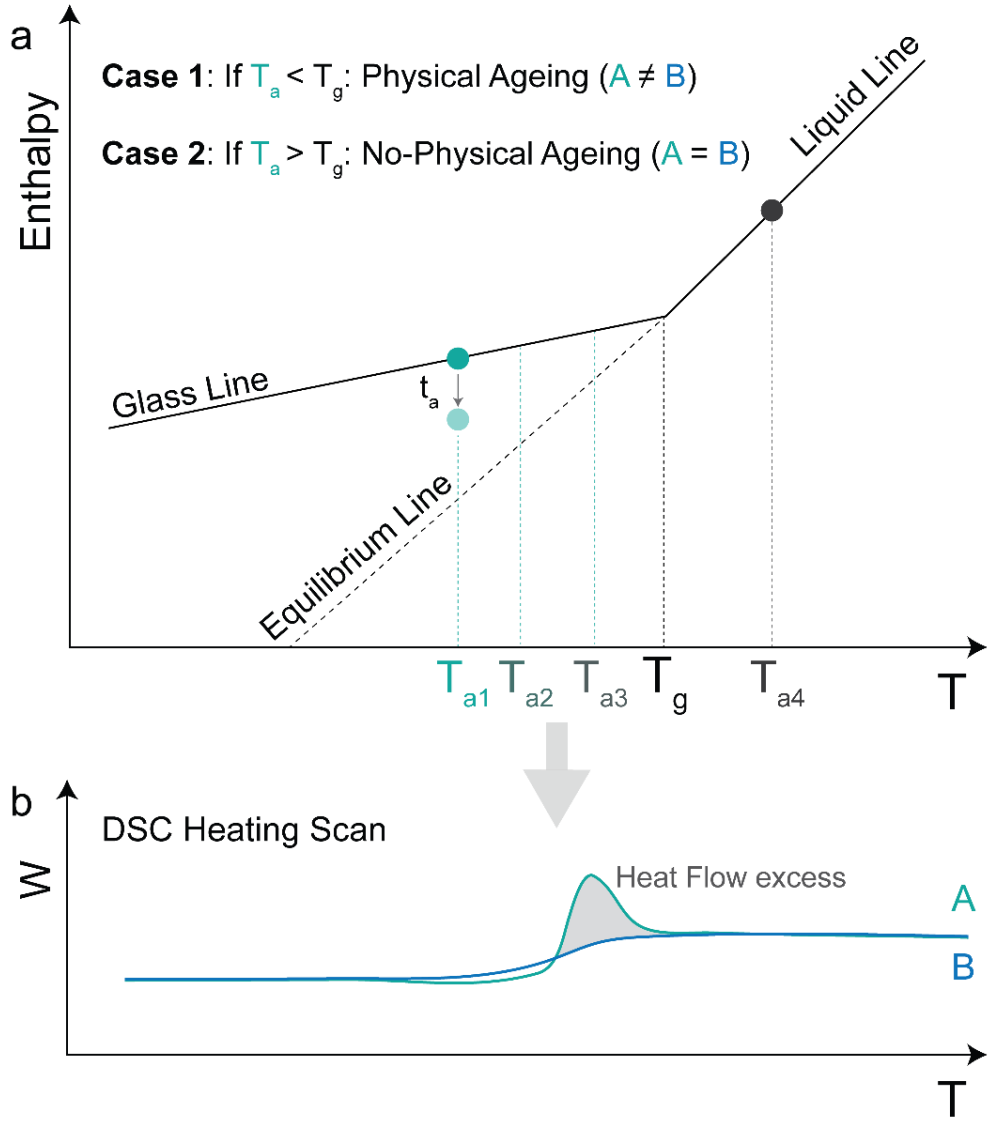

Figure 2.4 Schematic representation of the temperature dependence of the enthalpy for a typical glass former cooled down at a given cooling rate β. The fate of the enthalpy in case the glass former is aged below (case 1) and above (case 2) the $T_{g,onset}$ is shown. Panel below, shows the example of the effect of annealing below and above the $T_{g,onset}$.

(2) ISOTHERMAL ANNEALING: the thermal protocol used is depicted in **Figure 2.3**. In this case, after bringing the sample to a high temperature, T_H, the sample is quenched to the isothermal temperature, T_a, to further be aged at that temperature for different t_a. The kinetics of formation of the isothermally developed thermal process can therefore be followed by monitoring the total integrated ΔW across the temperature range of the endothermic peak. Thus obtained ΔH values can be plotted vs t_a and in order to describe the evolution of the enthalpic relaxations, fitted to a Kohlrausch-Williams-Watts law:

$$\Delta H = a - (a - b) \cdot \exp\left(-t/\tau\right)^{\beta} \quad \textbf{(Equation 2.1)}$$

where ΔH_{max} the maximum enthalpy value measured in the experiments, k is a constant associated with the overall crystallization rate and β, which is often referred to as the Avrami exponent, provides insights into the nucleation and the crystal growth.

2.3.2. Microscopy techniques

2.3.2.1. Polarized Light Optical Microscopy and Spectroscopy (PLOM-S)

The thermally induced phase transitions, annealing treatments, crystallization kinetics, etc of samples were evaluated by polarized optical microscopy and spectroscopy (PLOM-S).[142] temperature-resolved optical and spectroscopically experiments allowed the lab-scale study of different processed that after helped us to benefit from the time at the synchrotron.

Samples were directly deposited by drop casting or spin coating on a glass substrate from a 20 mg·mL^{-1} solution at 2000 rpm. The glass slide was placed within a hot stage (Linkam Scientific Instruments Ltd.), which was positioned between the polarizer and the orthogonally oriented analyzer of a bright-field optical microscope (Zeiss Axio Scope A1) equipped with a 10X objective and a tungsten-halogen bulb. At the end of the light path a portable UV-vis spectrometer and a camera was placed in order to acquire optical images and spectra (in visible wavelength region) simultaneously during heating scans at 10 °C·min^{-1} (if needed).

The thermally induced phase transitions are probed as follows. The transmitted intensity at each temperature that the UV-vis spectrometer receives is integrated between the suitable wavelength ranges (400 to 720 nm) to obtain the value of the total intensity of visible light transmitted through the materials. Since light photons reach the spectrometer solely because structurally ordered material domains (e.g. crystalline domains) are birefringent, the normalized integral value of the transmitted light intensity is directly correlated with the normalized amount of structurally ordered fraction that is present at each temperature. By analogy with a differential scanning calorimetry (DSC) experiment, we can also plot [d(I)/dT] vs T, which relates to how much birefringent material is phase transforming upon heating at 10 °C·min^{-1} and, thus, is somehow analogous to the heat flow signal of a DSC experiment.

2.3.2.2. Atomic Force Microscopy (AFM)

AFM images were obtained using a scanning probe microscope (Dimension ICON, Bruker) under ambient conditions. Tapping mode was employed in air using an integrated tip/cantilever (125 μm in length with ca. 300 kHz resonant frequency). Scan rates range from 0.7 to 1.2 Hz·s^{-1}. Measurements were performed with 512 scan lines and target amplitude around 0.9 V. The amplitude setpoint for all investigated samples was ~300 mV. Different regions of the samples were scanned to ensure that the morphology of the investigated materials was the representative one. In the AFM, phase images, the brighter regions correspond to areas of the sample with higher modulus (hard domains) and darker regions correspond to softer areas. Samples were spun cast from 20 mg·mL^{-1} solution at 2000 rpm during 60s. The thermal treatments were performed in a Linkam hot stage under N_2 atmosphere. Samples were annealed for 10 minutes at selected temperature and quenched at 50ºC·min^{-1} to room temperature.

Quantitative information about the paracrystallite size was obtained from power spectral density (PSD) analysis applied on the AFM phase-contrast images using the NanoScope Analyses 1.9 software.

2.3.3. X-ray techniques with synchrotron radiation

2.3.3.1. Wide-angle and small angle X-ray scattering (WAXS and SAXS)

Along this thesis all the experiments involving X-ray have been carried out in a synchrotron facility. Grazing Incidence Wide-Angle X-ray Scattering (GIWAXS) measurements were performed at the BL11 NCD-SWEET beamline at ALBA Synchrotron Radiation Facility (Spain). The incident X-ray beam energy was set to 12.4 eV using a channel cut Si (1 1 1) monochromator. The angle of incidence αi was set between 0.1-0.15° to ensure surface sensitivity. The scattering patterns were recorded using a Rayonix® LX255-HS area detector, which consists of a pixel array of 1920 × 5760 pixels (H × V) with a pixel size of 44 × 44 μm^2. Data are expressed as a function of the scattering vector (q), which was calibrated using Cr_2O_3 as standard sample, obtaining a sample to detector distance between 145.6 and 200.93 mm depending on the beamtime. The geometry is represented in **Figure 2.5**.

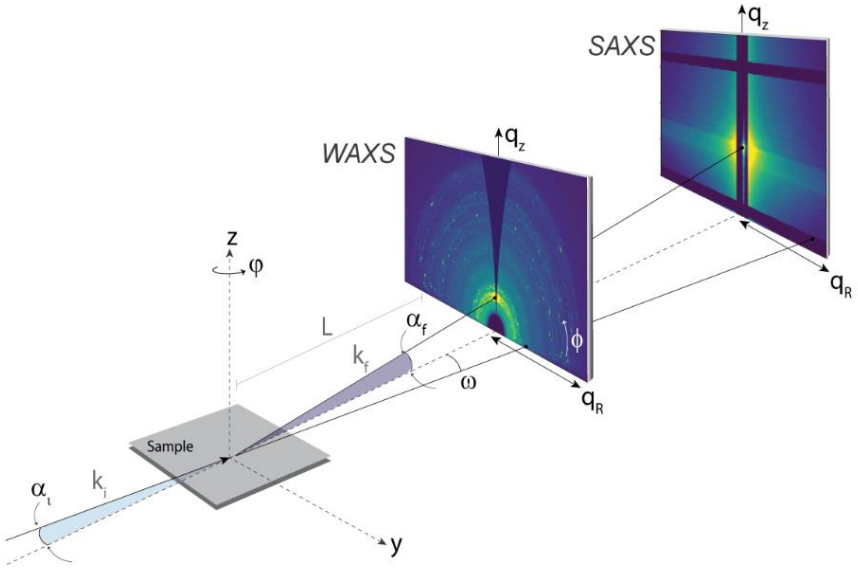

Figure 2.5 Grazing incidence wide-angle and small-angle X-ray scattering geometry.

Temperature-resolved in situ X-ray experiments were performed using a Linkam® THMS 600 stage adapted for grazing incidence experiments. The heating rate used was 10 °C·min^{-1} and the temperature difference between frames was 4 °C. Sample alignment was

automatically performed each 50 °C. Exposure times for in situ and ex situ experiments were 1 and 5 s, respectively. All the measurements were performed under N_2 atmosphere to minimize the damage of the films.

2D GIWAXS patterns were corrected as a function of the components of the scattering vector, *q*, which is defined as the difference between the incoming and scattered wave vectors.[143] Samples for GIWAXS were prepared by spin casting 20 mg·mL^{-1} solutions on Si wafers at a spin rate of 2000 rpm. For thick film samples, the same solutions were directly drop casted. The thermal treatments were performed in a Linkam® hot stage under N_2 atmosphere. Edges of the samples were removed to eliminate edge effects in the GIWAXS experiment. To perform the analysis of the diffraction patterns, the 2D patterns were integrated, corrected with respect to the reference and the 1D profiles were extracted. The different integrations carried out throughout this thesis are represented in **Figure 2.6**.

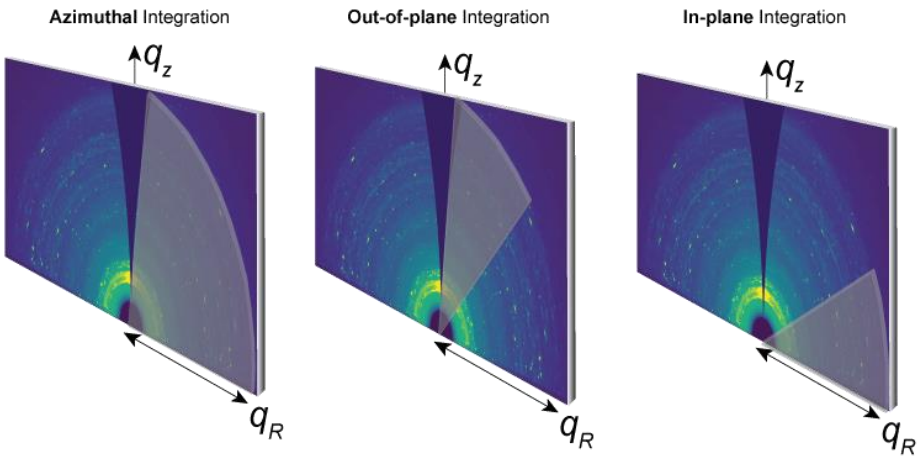

Figure 2.6 1D integrations performed in 2D GIWAXS patterns.

Grazing Incidence Small-Angle X-ray Scattering (GISAXS) experiments were conducted at NCD-SWEET beamline of ALBA synchrotron (Spain) (**Figure 2.5**). A monochromatic X-ray beam with an energy of 12.4 keV was shone on the samples with an incidence angle of 0.12° and 0.15°. The exposure time for room temperature measurements was 1 s and the sample to detector distance was 2.54 m. The 2D patterns were recorded with a Pilatus3 S 1 M detector, which consists of a pixel array 1043 × 981 (V × H) pixels of 172 × 172 μm^2. Horizontal line q_y cut

profiles were done at the Yoneda peak. For GISAXS experiments samples were spin cast on Si wafers. The thermal treatments were performed in a *Linkam* hot stage under N_2 atmosphere. Edges of the samples were removed to eliminate edge effects in the GISAXS scattering pattern.

X-ray techniques have proven to be succefull in uncovering a broad range of microstructural and morphological features,[144] and the extraction of several parameters allowed us to further describe the organic semiconductors presented in this thesis. A stated above, data are expressed as a function of the scattering vector (q). The scattering vector is expressed as

$$q = \left(\frac{4\pi}{\lambda}\right) \cdot \sin\theta \qquad \textbf{(Equation 2.2)}$$

where θ is the scattering angle and λ is the X-ray wavelength. The diffraction angle θ is related to the spacing between planes given by the Bragg condition. Thus, we can extract the distance spacing between periodic planes in a crystals lattice with

$$\lambda = 2d \sin\theta \qquad \textbf{(Equation 2.3)}$$

The shape and distribution of the diffraction peaks in the reciprocal space will help us to describe the texture and orientation of the diffracting crystallites.[144] Thus, we can determine the preferred configuration of the crystallites based on the orientation of the different planes as observed in i.e. edge-on, where chain lay perpendicular to the substrate, or face-on where backbones lay parallel to the substrate (**Figure 2.7**).

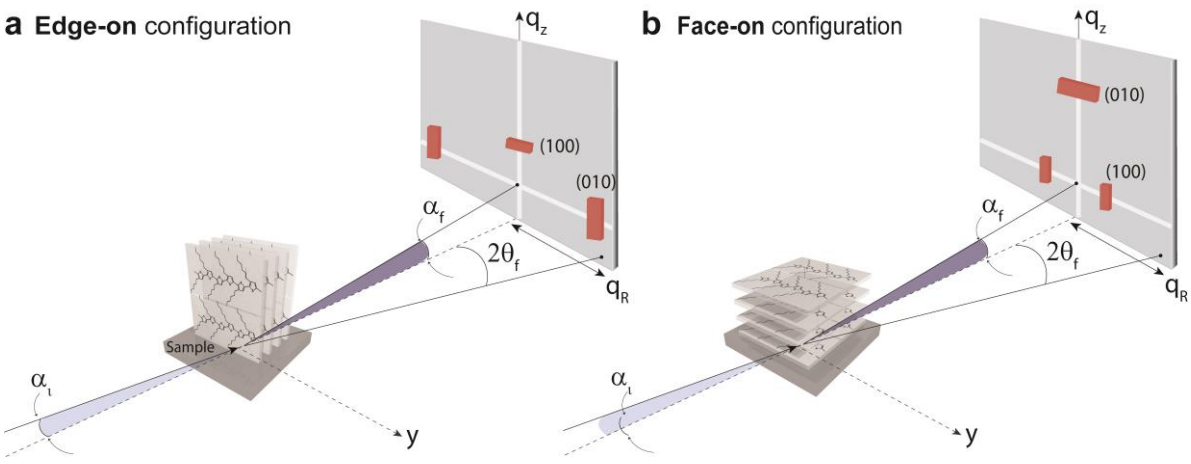

Figure 2.7 Crystallite/Paracrystallite configuration to the substrate: (a) edge-on and (b) face-on.

Moreover, based on the isotropicity or definition of the reflection (i.e. amorphous materials will show broad scattering intensity while highly crystalline materials will depict intensity spots) in the diffraction pattern we can infer the texture of the film and therefore, the perfection of the crystals will be determine by the width of the scattering peak. From the width we can calculate the coherence length by applying the Scherrer equation:

$$L_c = {}^{2\pi K}/_{\Delta q} \qquad \textbf{(Equation 2.4)}$$

where K is the shape factor (~0.9-1)[145] and Δq is full width half maximum of the peak. However, while a diffraction profile from a finite-size-dominated sample has peaks of equal breadth for this progression, it is found that many organic semiconductors possess a cumulative disorder within the film,[144145] which is visible in the successive broadening of the higher-order peaks. That is, when there is cumulative disorder, the lattice "forgets" its origin (initial location) after a certain distance. This is different from non-cumulative disorder, where the lattice average is maintained regardless of the distance between lattice sites; cumulative disorder is often referred to as paracrystalline disorder or lattice disorder.[144] This cumulative disorder can be calculated by the paracrystalline parameters, g.

$$g = \sqrt{{}^{\Delta q}/_{2\pi q_0}} \qquad \textbf{(Equation 2.5)}$$

where q_0 is the peak center position and Δq is full width half maximum of the peak.[14] Thus, the g-parameter scale based on a-SiO_2 reference classifies the semiconducting polymer thin films between crystalline with minimum lattice disorder (g<1%) and amorphous (g~10-20%) showing high amount of paracrystalline disorder[14].

2.3.4. Spectroscopic techniques

UV–vis spectra were recorded with a Shimadzu UV-2550 spectrometer with a film adapter and for thickness normalization a mechanical profilometer P16+ (KLA Tencor) was used. ***Photoluminescence spectra*** were recorded on a LS55 Perkin-Elmer Fluorescence spectrometer

on the same samples analyzed by UV–vis. ***Raman and photoluminescence spectra*** were also acquired with a WITEC Alpha 300 RA confocal microscope, coupled with am Olympus objective with 10x magnification at the wavelengths of 488 and 633 nm. ***Ultraviolet photoelectron spectroscopy*** (UPS) was performed on a Kratos Axis Ultra XPS/UPS System using helium arc source with incident photon energy of 21.2 eV, a scan step size of 0.05 eV, and a dwell time of 200 ms from 25 to −5 eV. ***External quantum efficiency*** (EQE) was measured with a home-made system (developed by Mr. Martí Gibert) that uses a Supercontinuum light source (LLTF contrast, Fianium) coupled to a monochromator filter and normalised by the light power as measured by a silicon diode. EQEs were recorded from 400 nm to 900 nm excitation wavelength by focusing the 50 μm diameter laser spot. This set-up was also controlled with LABVIEW- based software. ***Transient absorption measurements*** were carried out by using an ultrafast laser system (Pharos Model PH1-20-0200-02-10, Light Conversion) generating 1030 nm pulses at 100 kHz repetition rate and ~220 fs pulse duration, 10 W of the output is sent into a commercial optical parametric amplifier (Orpheus, Light Conversion) to generate pump source covering a spectral range of 360-2600 nm. Probe source is generated by a Sapphire crystal which is focused with 2W of the laser output, to obtain a single filament white light continuum with spectral range 480-1100 nm. ***Pump-probe experiments*** were performed in a transient absorption commercial set-up (Light Conversion Hera), the detection consists of a multichannel detector (200-1100 nm spectral sensitivity range, 256 pixels) along with an imaging spectrograph (Shamrock193i, Andor Technology).

2.3.5. Device characterization

2.3.5.1. OPV

The organic solar cells devices were prepared in the inverted architecture. As semi-transparent electrode a pre-patterned ITO coated glass (25x75 mm) with 24 pixels, 12 in each side of the sample leading to 24 devices with an 8 mm2 a provided from Ossila Ltd. are used. After a sequential cleaning of the ITO-coated substrates. The electron transport layer (ETL) ZnO

nanoparticles dispersion (N-10, N-20X, Avantama) in isopropanol (IPA) is then blade-coated (ZUA 2300, Zehntner) and annealed at 100ºC during 10 minutes for solvent evaporation. After that the devices are introduced into the glove box and the active layer y blade coated. Taking advantage of the substrates, we performed high-throughput combinatorial approach to vary thickness decelerating the blade from 99 mm/s to 1 mm/s during solution spreading across the substrate length (7.5 cm). These is the moment to perform any temperature annealing treatment. Finally, the hole transporting layer (HTL) MoO_3 and the silver are thermally evaporated. Note that after each blade coating the material remaining on top the pixel must be carefully remove.

The OPV devices were developed during my stage in Dr. Mariano Campoy-Quiles lab (NANOPTO Group) at the ICMAB Institute.

2.3.5.1.1. J-V characterization

The current-voltage characteristics (IV) of the OPV devices were extracted by using a Keithley 2400 Sourcemeter and an Arduino based multiplexer and switcher. All the electronic components were automatically controlled with a LABVIEW software tool (designed by Mr. Martí Gibert). This allows the fast measurement of 24 devices in less than 6 minutes. As an illumination source, a solar simulator (XES-100S, SAN-EI Electric) under AM 1.5G (Air Mass 1.5 Global) and 100 $mW \cdot cm^{-2}$ illumination was employed. This solar simulator is AAA class, which ensures a homogenous illumination in a 10 cm x 10 cm area, needed for the accurate evaluation of the gradient-based OPV devices. The solar simulator was calibrated with a certified silicon solar cell (Oriel, Newport).

To judge the performance of an OPV device we extracted several parameters from the J-V curve as depicted in **Figure 2.8**. The open circuit voltage (V_{OC}) is the value of the maximum voltage of the solar cell that occurs when the current is 0. The short-circuit current (J_{SC}) is the current across the solar cell when the voltage equals 0. The fill factor (FF) gives a value of the ratio between the hypothetical maximum power and the one obtained for the solar device. As depicted in **Figure 2.8**, the combination of these values divided by the incident power gives the

power conversion efficiency (PCE) of the solar cell device. For standard characterisation, Pin matches the incident spectral irradiance of sunlight at Earth namely Air Mass1.5 Global spectrum (AM 1.5G), with an average power density of 1000 W/m^2.

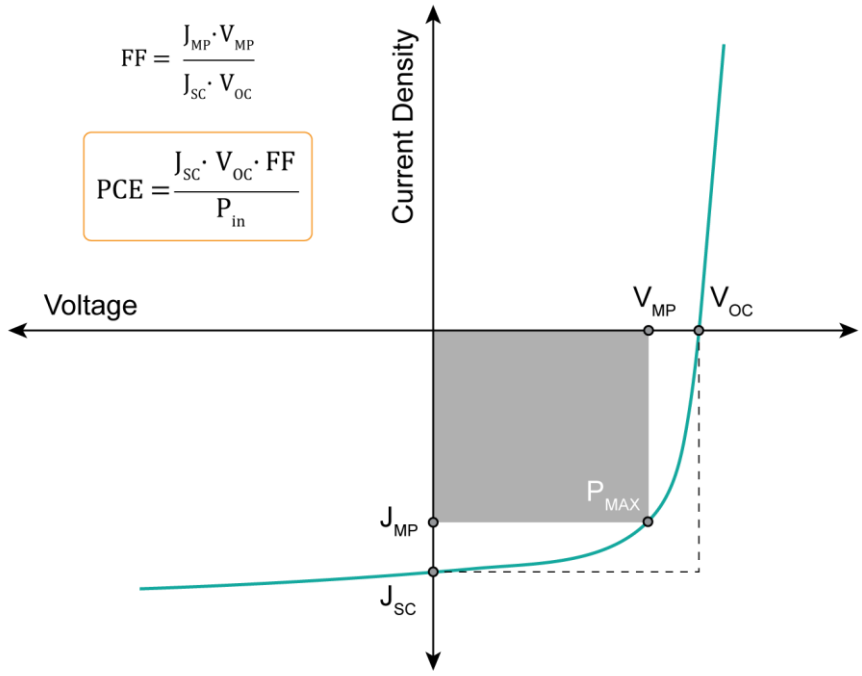

Figure 2.8 Example J-V curve highlighting key OPV parameters.

2.3.5.2. OFET

In this thesis, in collaboration with the Group of Thomas Anthopoulos from KAUST, Mario Caironi from Istituto Italiano di Tecnologia and Luis Hueso from Nanogune, we fabricated-type and n-type organic filed-effect transistors (OFETs) measuments were developed.

The p-type (conduct holes) field-effect transistors in a bottom-gate bottom-contact geometry were fabricated by spin coating the different polymers onto Si/SiO_2 (150 nm) substrates with pre-patterned pairs of Ti/Au (5 nm/ 36 nm) electrodes. The n++ Si substrate was used as gate electrode, the SiO_2 (150nm) as gate dielectric and the Ti/Au contacts as source (S) and drain (D). The prepatterned pairs of electrodes with interdigitated geometry were fabricated using conventional lithographic techniques. Channel length (L) and widths (W) varied in the range L ~ 5-50 μm and W ~ 5000-10000 μm.

The individual chips were cleaned with acetone and later with isopropanol. Before spin coating the polymers the chip were introduced in the ozone cleaner (supplied by Ossila Ltd.) for 1h. Samples were spin cast from 10 mg·mL^{-1} solution at 2000 rpm during 60s. The thermal treatments were performed in a Linkam hot stage under N_2 atmosphere. Samples were annealed for 10 minutes at selected temperature and quenched at 50 °C·min^{-1} to room temperature.

The electrical characteristics of the transistors were measured using a Keithley 4200-SCS semiconductor analyzer connected to a variable temperature Lakeshore probe station. The measurements were carried out with the samples in high vacuum, and the samples were left 12 hours in vacuum prior to the measurements, to minimize the effect of oxygen doping. To extract the field-effect mobility, the transfer curves were analyzed using standard field-effect transistor equations for the saturation regime:

$$I_{DS} = {}^{W}/_{2L} \cdot \mu C \cdot (V_{GS} - V_{Th})^2 \qquad \textbf{(Equation 2.6)}$$

where I_{DS} is the drains source current, μ is the mobility, C is the capacitance per unit area, V_{GS} is the gate-source voltage and V_{Th} is the threshold voltage. In each chip, more than 10 devices were tested to extract the average mobility, and the error is given by the standard deviation.

To prepare the n-type (conduct electrons) OFETs standard top-gate bottom-contact configuration was used. Gold source/drain contacts were thermally evaporated on a borofloat glass after cleaning via ultrasonication in acetone and isopropanol and a subsequent O_2 plasma exposition at 100 W for 5 min. Solutions of the organic semiconductor were dissolved in chlorobenzene (10 mg·mL^{-1}), stirred at 80 °C for 2 h and then spin-coated in a nitrogen- filled glovebox at 2000 rpm for 60 s. A Cytop layer (≈550–600 nm) was spin-coated on top of the semiconductor film at 4000 rpm, 400 rpm·s^{-1} for 90 s, and then an annealing at 90 °C was performed for 1 h. Al gate contact was finally thermally evaporated through a shadow mask. The devices were then tested in glovebox using a Keysight B2912A Precision Source/Measure Unit without exposing them to ambient conditions

2

Get ready! This section is divided into 4 chapters containing the most relevant scientific findings of my work. The results follow a pyramidal scheme. This way, you can plan the reading as if you were preparing a professional cocktail. First you will get to know in depth the ingredients, then we will mix them, and finally, we will taste it.

The experimental section follows a PYRAMIDAL SCHEME, where each part plays a critical role in unfolding the hierarquical architecture. We focus on controlling the microstructure of the individual components (donor (D) and acceptor (A)) to learn how to manipulate their phase transformations and solid-state order. Thus, we were able to tailor and manipulate the final morhology (D:A) and delineate its impact on the function of the solar cell device.

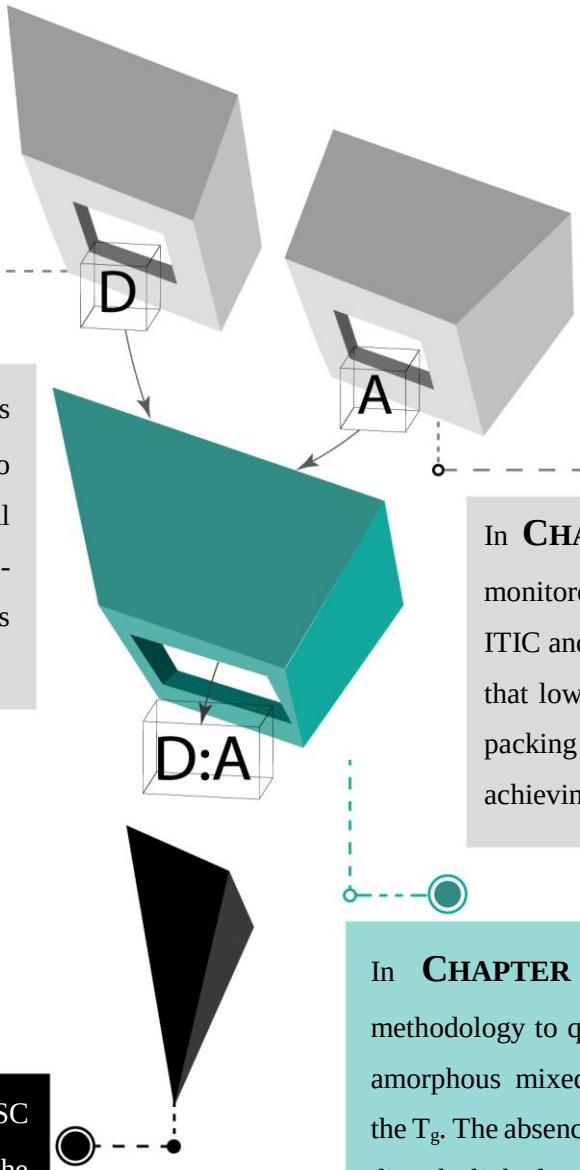

CHAPTER 3 PBDB-T and its congeners have driven us to establish a new microstructural model called "semi-paracrystallinity" that explains their outstanding performance.

In **CHAPTER 4** we uncovered and monitored the rich polymorphism of ITIC and its derivatives, thus revealing that low temperature crystalline phase packing can be an important feature in achieving high efficiencies.

In **CHAPTER 5** we have developed a methodology to quantify the composition of the amorphous mixed domains through measuring the T_g. The absence of a T_g in the donor polymers, directly linked to their complex microstructure, prevented us from applying the methodology to the PBDB-T:ITIC system and, therefore, we employ a system based on the well-known conjugated polymer P3HT.

In **CHAPTER 6** we prepared OSC devices and found that the performance is more sensitive to the acceptor crystals than to an enhancement of the paracrystallinity of the polymer.

3. Solid-state microstructure of high-performing donor polymers and its impact on electronic and optoelectronic properties

3.1. Summary

Due to the fast progress in materials engineering for various organic electronic technologies, precise determination of the solid-state microstructure of semiconducting polymers and its relation to device-function has become of paramount importance. In this chapter, we study the molecular organization of some of the best performing donor polymers for organic solar cells, namely PBDB-T-2F (aka PM6), PBDB-T-2Cl (aka PM7) and PBDB-T. Previous analysis of the microstructure of these polymers resulted in conundrums in which X-ray scattering and optical microscopy yielded seemingly contradicting results. In order to solve this apparent paradox, we introduce a new structural model for polymers: the semi-paracrystalline model. The semi-paracrystalline organization is based on the presence of dense arrangement of very small paracrystallites (i.e., highly defective ordered domains) coexisting with more disordered sites. Our work outlines that fast-scanning calorimetry is a key experimental technique to identify semi-paracrystallinity. Moreover, we establish that semi-paracrystalline solid-state microstructure may be a common morphological feature among other high-performing polymers for OPV, donor:acceptor blends included. Our data reveals that field effect charge carrier mobility is linked to the interconnection of paracrystallites, the degree of paracrystallinity, the statistical lattice disorder, and the paracrystallite orientation, while the optical absorption characteristics turn out to be rather tolerant to structural changes. Hence, we anticipate our results to be critical in advancing more refined structure-function models for OSCs.

3.2. Introduction

Over the past few years, solution processed polymer/small molecule blends are receiving great attention due to their potential as active layers in organic solar cells.[1,42,146–148] The key headway in surpassing the efficiencies achieved by fullerene-based OPVs was the fine combination of donor: acceptor materials and the intermolecular arrangement in BHJ active layers.[59,149–151] Although the acceptor has been steadily swapped by better performing novel small molecules,[35,71] donor materials have been championed by PBDB-T-based conjugated polymers.[31,148,152,153] The ability of semiconducting polymers to transport charges has proven to be closely connected with their solid-state microstructure[14,144,154,155] and, more specifically, with the presence of ordered molecular structures, such as crystalline domains, their characteristics (i.e. size, orientation, intrinsic disorder, etc.) and the interconnection between them, e.g. via tie-chains.[14]

From the solid-state microstructure standpoint, (non-liquid-crystalline) polymeric materials have been typically classified as either amorphous (glassy) or partially crystalline (i.e. semicrystalline).[8] In general, an amorphous polymer material consist of polymer chains adopting disordered coil-like conformations resulting from the enormous number of possible rotational isomeric states of chains. In partially crystalline polymers, traditional models, e.g. the "fringed micelle model"[156] or the spherulitic model,[157] assume that amorphous regions coexist with crystalline regions in which chain segments with relatively extended conformations are stacked in lamellar crystallites.[8,158] Thus, these structural models for semicrystalline materials allow for a simple parametrization of the overall degree of structural order in terms of the degree of crystallinity, i.e. the fraction of crystalline regions to the total volume/mass of the sample. Interestingly, the analysis of solution-spun lyotropic polymers, such as aramid fibers,[159,160] revealed, moreover, a different solid-state order – somehow between that of crystalline and amorphous materials – described by the so-called paracrystalline model[28,161] In the paracrystalline model introduced by Hosemann,[161] the non-ordered regions appear as defect sites of the paracrystalline lattice and, therefore, no experimental evidence whatsoever of the existence of discrete amorphous regions is observed (i.e. no T_g). Contrarily to semicrystalline materials, the

overall degree of structural order in paracrystalline materials is not given by the volume fraction occupied by molecularly ordered and disordered regions, but by the quality of the paracrystalline lattice, i.e. the cumulative lattice disorder as captured in the paracrystallinity distortion parameter, g.

The characteristics of the semicrystalline microstructure (e.g. semi-crystalline morphology and structure parameters) can be inferred from the combination of diffraction techniques (e.g. X-ray diffraction),[14,144,145] microscopies (optical, electronic and force microscopies[49,155] and methods probing the melting of crystals, the most common being differential scanning calorimetry (DSC)[49] or measuring the viscoelastic properties (DMA).[8,52] Thus, the identification and quantification of structural order in semi-crystalline polymeric materials has been traditionally realized analyzing e.g. the Bragg peaks of the X-ray diffraction patterns, measuring the birefringence under a cross-polarized optical microscope (POM), and/or quantifying the enthalpy change during the melting of crystals by DSC. Obviously, amorphous polymer materials do not feature any of the aforementioned signals.

Progress in materials engineering for organic electronics has led to the development of semiconducting polymers with solid-state microstructures ranging from completely amorphous, e.g. PTAA[14] to some with moderate-to-high degrees of structural ordering, e.g. P3HT and PBTTT.[14,162] The degree of order in these highly-order semiconducting polymers can be readily characterized by, e.g., DSC and X-ray methods[163,164] like in commodity semicrystalline polymers. However, the analysis of the quality of the molecular packing in semiconducting polymers revealed that even the most ordered materials feature a fairly disordered π-stacking (e.g. g-parameters of 7.3% were measured for PBTTT).[145] Hence, it was proposed that ordered structural elements in many semi-conducting polymer films exhibit greater similarity with paracrystals than with regular crystals.[14] But unlike typical paracrystalline materials, such as aramide fibers, semiconducting polymer thin films tend to contain also significant fractions of structurally disordered regions. Hence, the g-parameter seems not sufficient to characterize the overall degree of structural order of these materials, as it is solely related to paracrystalline units. Indeed, this

practice may have led to conundrums and misinterpretations in the past. For example, based on the *g*-parameter value, Poly[[4,8-bis[5-(2-ethylhexyl)-2-thienyl]benzo[1,2-b:4,5-b′]dithiophene-2,6-diyl]-2,5-thiophenediyl[5,7-bis(2-ethylhexyl)-4,8-dioxo-4H,8H-benzo[1,2-c:4,5-c′]dithiophene-1,3-diyl]] (PBDB-T), and its fluorinated (PBDB-T-2F or PM6) and chlorinated (PBDB-T-2Cl or PM7) congeners (**Figure 3.1**) have been classified as structurally amorphous.[49] Moreover, the absence of optical birefringence and measurable melting signals in DSC[49] supported this conclusion. As a result, most advanced morphology-function models for OPV materials systems have been established on the premise that these polymers are structurally disordered.[165,166] However, distinctive aggregate-like structures are clearly revealed when these materials are inspected by electron or probe microscopies, reflecting some sort of ordered molecular packing.[28,33,167] These seemingly contradictory results suggest that (i) *g*-parameter –on its own– is not adequately reflecting the overall structural order in these polymer materials, therefore (ii) the actual degree of structural order –and, hence, the overall solid-state microstructure – of many of the best-performing semiconducting polymers for OPV remains still unknown.

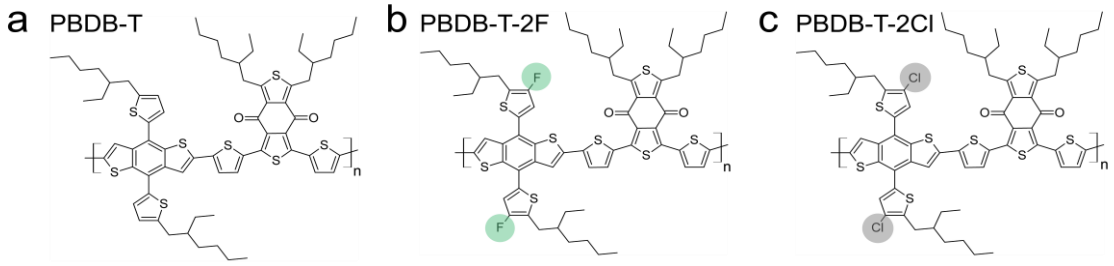

Figure 3.1 Chemical structures of (a) PBDB-T, (b) PBDB-T-2F (PM6) and (c) PBDB-T-2Cl (PM7).

The electronic and optoelectronic properties of semiconducting polymers are profoundly affected by the presence of crystals and their characteristics (i.e. size, orientation, defects, etc.)[14] as well as the tie-chains between crystals and amorphous regions. For example, the molecular packing of crystalline regions, through the better average overlap of π-orbitals, tend to exhibit better charge transport properties than disordered amorphous regions. However, it is accepted that a certain amount of amorphous polymer is needed for a suitable development of intermixed

domains, where charges are preferentially generate[168,169]–although too much intermixing promotes unfavourable charge recombination effects[170] and lack of percolation can create islands that trap charges.[169,171] As a consequence, having a realistic picture of the solid-state microstructure of semiconducting polymer materials is pivotal for establishing successful models for the operation of electronic devices such as organic solar cells (OSCs).

In this chapter, we address this apparent paradox and, in order resolve it, we introduce some new concepts: the semi-paracrystalline model and the degree of paracrystallinity. Analogously to the degree of semicrystallinity in semicrystalline materials, the semi-paracrystalline model establishes that paracrystalline domains and more disordered, i.e. amorphous, domains coexist. Moreover, the degree of paracrystallinity features the mass/volume fraction of paracrystalline regions in semi-paracrystalline materials, without considering (in a first approximation) how ordered the molecular packing within paracrystalline units is. Hence, the characterization of the overall structural order in semi-conducting polymers for OPV would rely in two parameters: the *g*-parameter, which accounts for the lattice disorder within paracrystals, and the degree of paracrystallinity, which measures the mass/volume fraction of ordered material. (The likely existing connection between both parameters needs to be investigated in future studies). In addition to introducing the concept, we show that the degree of paracrystallinity of device-relevant thin films can be readily obtained by fast scanning calorimetry (FSC). Hence, we demonstrate that PM6, PM7 and PBDB-T polymer films, which seem amorphous based on the *g*-parameter criteria, are in fact notably ordered, with degrees of paracrystallinity exceeding 50 % for PM7, i.e. similar to some of the most ordered semiconducting polymers like P3HT.[163]

We outline that the combination of this information with the characterization of nanomorphology and paracrystalline lattice distortion (*g*-parameter) provides complete information about the solid-state microstructure of high performing OPV materials for the first time. We thus establish that the moderate-to-high degree of paracrystallinity in PM6, PM7 and PBDB-T is underpinned by a highly dense arrangement of very small and very disordered paracrystallites. Having elucidated the semi-paracrystalline microstructure of polymer films, we

investigate the interplay between the long-range charge transport and the structural features, to finally state the field-effect charge mobility is very sensitive to the presence of small paracrystallites interconnecting primary paracrystals.

3.3. Results and Discussion

3.3.1. Analysis of the pristine microstructure

First, we focused on verifying the structural observations previously found in the literature by testing PBDB-T based semiconducting polymer thin films (**Figure 3.1**) using GIWAXS, PLOM and DSC. For this purpose, PBDB-T and PBDB-T-2Cl were spun cast from 20 $mg.mL^{-1}$ chlorobenzene solution and PBDB-T-2F from chloroform solution on a silicon (for GIWAXS measurements) or glass substrate (for PLOM analysis) following literature reports.[33,34,72] In full accordance with previous reports,[49] when typical methods to assess the solid-state microstructure of polymeric materials are employed, results seem to suggest the absence of crystals in PBDBT, PBDBT-2F and PBDBT-2Cl spin cast thin films, thereby implying their amorphous nature.

Figure 3.2 shows the pristine pattern and integrated profiles after spun cast from solution. 2D-GIWAXS patterns of the three polymeric materials reveal some weak and local short-range order diffraction peaks. The qualitative comparison of one-dimensional scattering profiles (**Figure 3.2**) obtained by out-of-plane and in-plane integrations reveal anisotropic films oriented in the out-of-plane direction with broad diffraction peaks from the π-stacked planes [i.e. the (010)] and the lamellar packing of aromatic backbones and aliphatic side chains [i.e. the (100)], indicating the absence of long-range crystalline order. The π-stacking reflection is related to a single distance of 0.37 nm located on the out-of-plane, suggesting principally a face-on arrangement. Although the differences are minor, GIWAXS patterns of the halogenated derivatives feature novel weak diffraction peaks in the in-plane. The reflections were indexed following previous reports.[172] Moreover, the out-of-plane oriented (010) reflexion revealed limited packing distance of 3 molecules and paracrystalline values of the π-stack between 15-

20% estimated by the peak shape analysis (**Table 3.1**). Comparing with a typical π-stack of conjugated polymers (such as 9% for regioregular P3HT)[14] together with above shown results, could easily infer a structure closer to amorphous than crystalline.

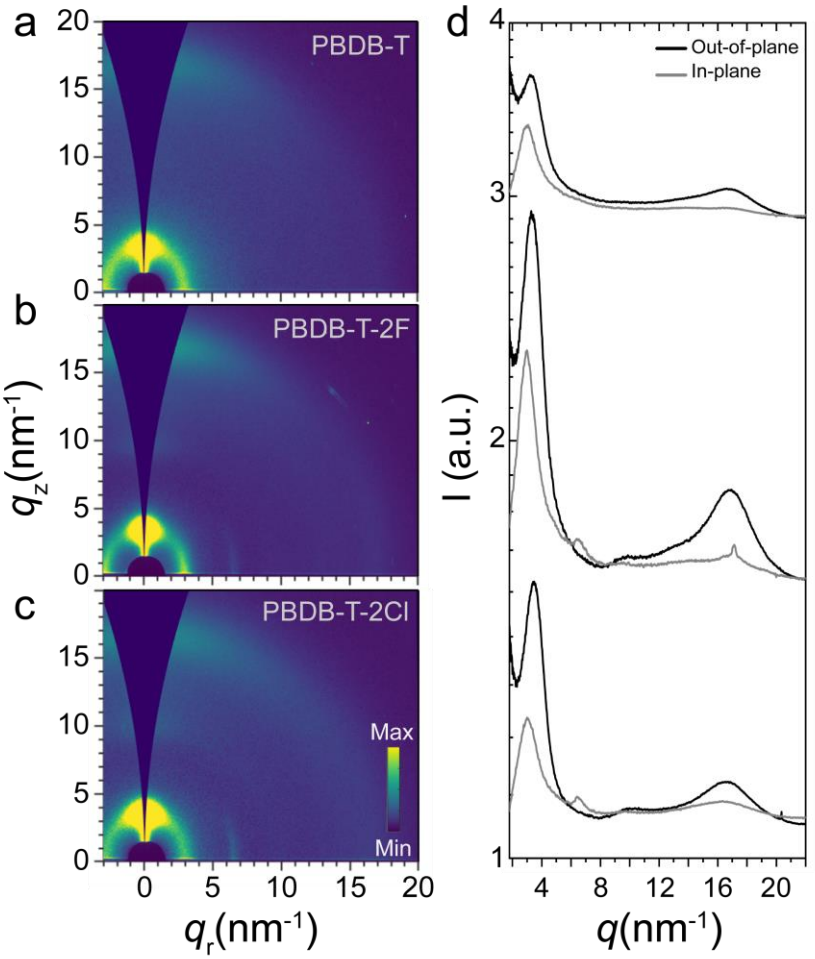

Figure 3.2 2D-GIWAXS pattern for spin-cast (a) PBDB-T, (b) PBDB-T-2F and (c) PBDB-T-2Cl. (d) Out-of-plane and in-plane profiles.

Table 3.1 Peak position and crystalline coherence length (CCL) values of the GIWAXS reflections

Polymer	Lamellar (100)			(200)			π-π stacking		
	q (nm^{-1})	*CCL* (nm)	*g* (%)	*q* (nm^{-1})	*CCL* (nm)	*g* (%)	*q* (nm^{-1})	*CCL* (nm)	*g* (%)
PBDB-T	3.4	5.8	22.6	/	/	/	17.0	2.2	16.5
PM6	3.4	5.3	23.5	6.6	11.2	11.7	16.8	1.6	19.1
PM7	3.5	5.4	23.0	6.4	11.6	11.6	17.0	2.2	16.5

Figure 3.3 Polarized optical microscopy (PLOM) images of spin cast polymer films (from a 20 mg·mL^{-1} chlorobenzene solution) (a) PBDB-T, (b) PBDB-T-2F and (c) PBDB-T-2Cl. The width of the micrographs corresponds to 100 µm.

The pristine thin film surface morphology was examined with PLOM to identify the presence of polymer crystals. Distinctively, the films were non-birefringent under polarized optical microscope suggesting the absence of anisotropic crystals at least in the length scale that PLOM can probe (**Figure 3.3**). For further clarifications, DSC thermograms of the bulk polymers were obtained. All the DSC traces showed degradation approximately above 300 ºC and no reliable evidence of endothermic peaks that could be ascribed to a crystal melting processes (**Figure 3.4**). Therefore, based on the above result and in agreement with previous reports, the semiconducting polymer investigated in this chapter display non-crystalline in nature when examined by DSC, PLOM and X-ray methods.

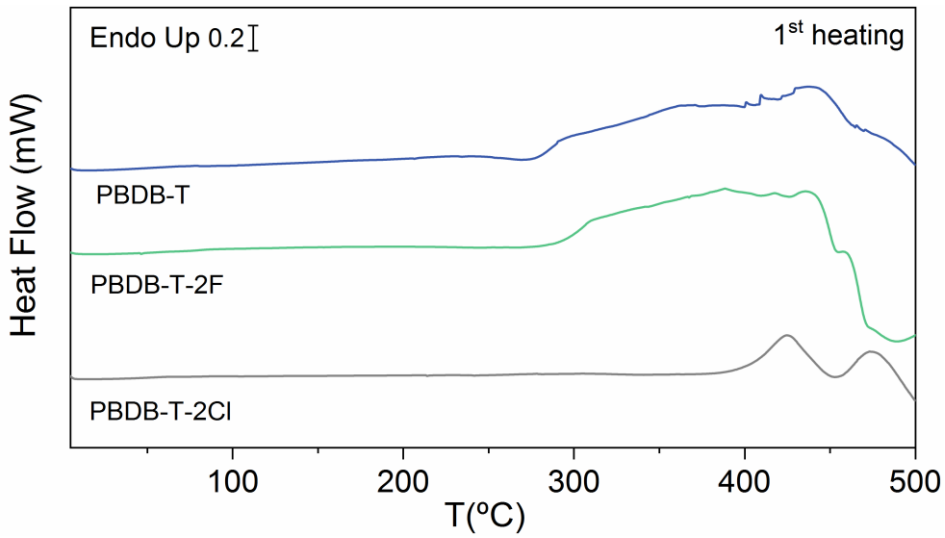

Figure 3.4 Differential scanning calorimetry thermograms collected during a heating ramp from 0 ºC up to 500 °C at 20 °C·min^{-1} (a) PBDB-T, and (b) PBDB-T-2F and (c) PBDB-T-2Cl.

3.3.2. Evidence of order domains

To gain further insight into the microstructure of these polymers, spin-cast films are characterised by fast scanning calorimetry (FSC). We spun cast polymer films on top of the calorimetric chip sensors to analyse films rather than bulk samples (see section 2.2.1.1). **Figure 3.5** shows the first and second heating thermograms and the first cooling scan for PBDB-T, PBDB-T-2F and PBDB-T2Cl polymer films. First heating thermograms of the pristine films reveal clear endothermic signals at ~400 °C (shadowed in blue) (panel labelled as "1st heating" in **Figure 3.5**). Indeed, temperature-resolved *in-situ* GIWAXS experiments shown in (Appendix **Figure A-1**) demonstrate that (100) diffraction peaks disappear at the temperatures where the endothermic peaks are observed by FSC. Hence, because we detect clear, intense melting processes by calorimetry, these polymer films ought to present certain order. It should be noted that compared to regular DSC, FSC allows for the application of much faster scanning rates (scanning rates of 4000 °C·s^{-1} were applied in our experiments), which on the one hand, prevents thermal degradation of compounds at high temperatures as demonstrated by the overlapping of the thermograms after successive heating scans up to melting temperature (**Figure A-2**), thereby enabling the detection of melting processes, and, on the other hand, allows the measurements of spin cast films that can be safely correlated with GIWAXS data.

The subsequent FSC cooling sweeps for the three polymer films (panel labelled as "cooling" in **Figure 3.5**), show exothermic peaks at ~370 °C due to the formation of crystals/aggregates upon cooling. Interestingly, the order aggregates are also formed from the polymer melt and at extremely high cooling rates (-4000 °C·s^{-1}), as it can be observed in the exotherm of the cooling scan and the melting endotherm of the second heating thermogram (panel labelled as "2nd heating" in **Figure 3.5**). Interestingly, the structural characteristics of the aggregates/crystals developed by cooling the film from the melt seems to be quite like those of spun cast films, because 1st and 2nd heating scans exhibited endothermic processes alike in enthalpy and position. (we note that crystallization of polymers is most frequently suppressed at

similar cooling rates even for highly crystalline polymers like poly(ethylene oxide) (Appendix **Figure A-3**).

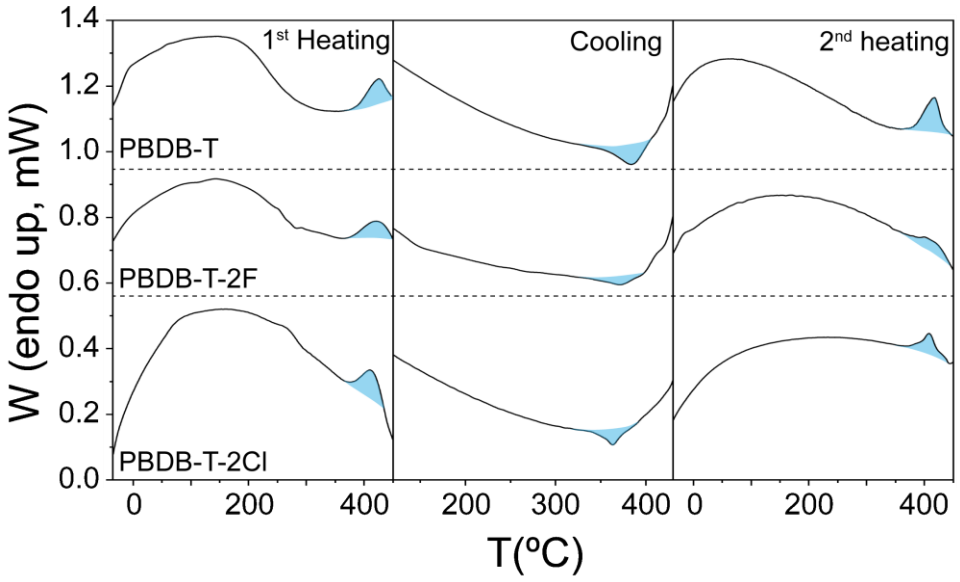

Figure 3.5 Representative fast scanning calorimetry (FSC) thermograms (raw data) for PBDB-T, PBDB-T-2F and PBDB-T-2Cl: 1st heating, cooling and 2nd heating scans are shown from left to right. Scanning rate was 4000 °C·s^{-1} in all experiments.

3.3.3. Analysis of thermal transitions

The heating and cooling thermograms of pristine thin films are characterised by a strong endothermic and exothermic processes, respectively, and, in addition, by the absence of a glass transition temperature. To gain insight into the different physical transitions and further describe the microstructure of such polymers, we conducted isothermal annealing experiments using FSC following the approach by Cangialosi et al.[135136] (see Section 2.3.1.1). Films were first heated up to 450 ºC and then quenched from the isotropic melt state to the aging temperature, T_a, using a cooling rate of -10000 ºC·s^{-1} and held there for 2 hours (t_a). After that, samples were cooled down to - 90 ºC and subsequently heated to 450 ºC (at 4000 ºC·s^{-1}). Thermal protocol is depicted in **Figure 3.6**a.

Figure 3.6b shows the plot of the isothermal annealing scans against the reference curves of PBDB-T films cast from a 20 mg·mL^{-1} chlorobenzene (see Appendix **Figure A-4** for PM6 and

PM7 experiments). On the one hand, it should be noted that a long-term isothermal annealing is necessary to observe the endothermic peaks. On the other hand, we can assure that no decomposition of the material is observed after several heating thermograms, as can be deduced from the perfect overlapping of the ageing and reference curves and in the shape of the melting peak. The three polymers present a similar behaviour as can be confirmed from **Figure 3.6**b and **Figure A-4**. We can also appreciate that the maximum temperature achieved by the equipment (i.e. 450ºC) is not high enough to perfectly resolve the melting peak of PBDB-T-2F.

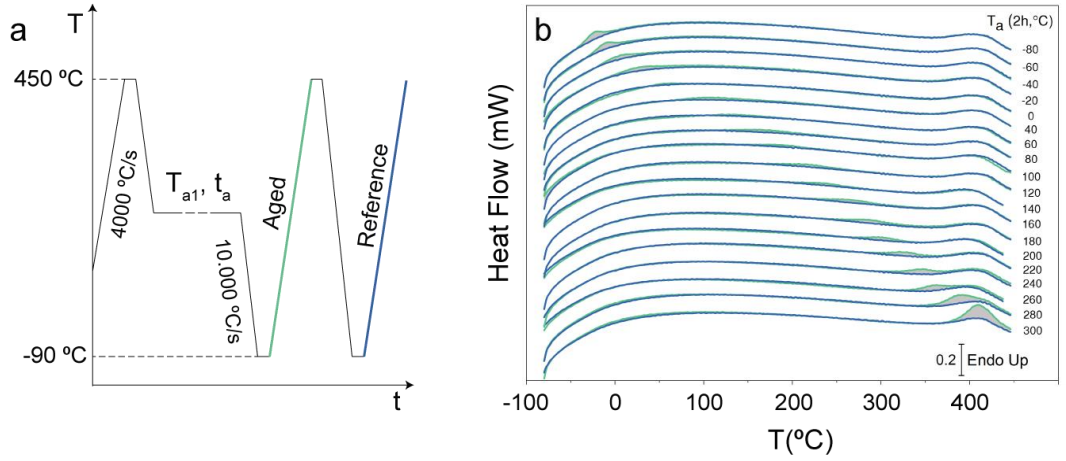

Figure 3.6 Isochronous annealing protocol (a). Annealing experiments conducted by FSC. Green curves correspond to the heating traces (at 4000 ºC·s^{-1}) after ageing samples for 2 h at the temperatures indicated on the right-hand side of each curve. Cooling and heating rates were 4000 ºC·s^{-1}.

To observe the trend of the excess heat flow, both scans (aged and reference) were subtracted and the endothermic overshoot distributions were followed. **Figure 3.7** shows the excess of flow rate scans for the semiconducting polymers PBDB-T, PM6 and PM7 obtained after the aging protocol at indicated temperatures. As displayed in **Figure 3.7d-f**, we can basically detect two distributions (shaded in light and dark grey in **Figure 3.7d**): a first overshoot were the heat flow decreases from -80 ºC to 0 ºC and a second peak that overlaps with the low temperature overshoot and steadily increases until it overlaps with the melting process. We associate the low-T process with the physical ageing of a glass consisting of aliphatic side chains.[52,136,173,174]

Furthermore, we argue that the second process must be related with the melting of order regions (i.e. nanometer sized aggregates/crystals) formed during the aging process until they merge with the melting of the rearranged aggregates during cooling. We rule out that the overshoot is generated by the physical ageing of the disordered amorphous phase, as the increase of the enthalpy of the peak as increasing the T_a should be followed by a decrease until its total disappearance when T_a equals T_g. Contrarily, in our case, the enthalpy never drops as increasing the T_a.

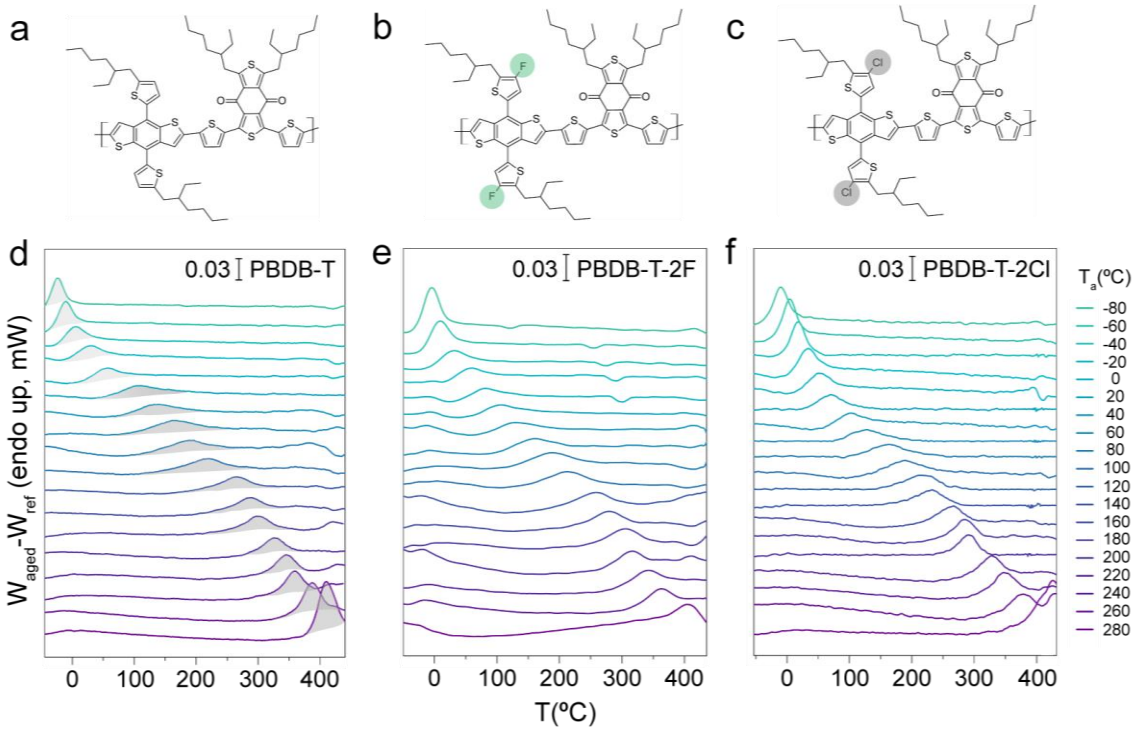

Figure 3.7 Chemical structures of (a) PBDB-T, (b) PBDB-T-2F and (c) PBDB-T-2Cl. Excess heat flow rate, meaning the difference between the heat flow rate of samples annealed at the indicated temperatures and that of the reference, which was not aged, as a function of temperature of (d) PBDB-T, and (e) PBDB-T-2F and (f) PBDB-T-2Cl annealed during 2h. The depicted thermograms belong to the thin film polymer samples.

3.3.4. Morphology analysis

To unveil how these polymers are arranged in the films, we investigated the morphology of the thin films in the length-scale of a few tens of nm by grazing incidence small angle X-ray scattering

(GISAXS) and atomic force microscopy (AFM). The GISAXS were analyzed by extracting horizontal cuts nearly at the Yoneda peak. The intensity profiles, in function of q_y, are compared and fitted using the Unified model by Beaucage.[175] GISAXS profiles of the three polymers shown in (**Figure 3.8**), yield intense scattering patterns due to a high electronic contrast at ranges between 10-100 nm. Since the patterns come from one single material, we associate this intensity to the density difference between small ordered clusters and more disordered regions. However, the horizontal cuts from **Figure 3.8**c do not display any clear peak or shoulder, suggesting a high polydispersity of sizes and lack of correlation between the order regions. Moreover, the Unified model by Beaucage allowed us to extract an average radius of gyration of these structures being 23 nm for PBDB-T and PM7 and 29 nm for PM6.

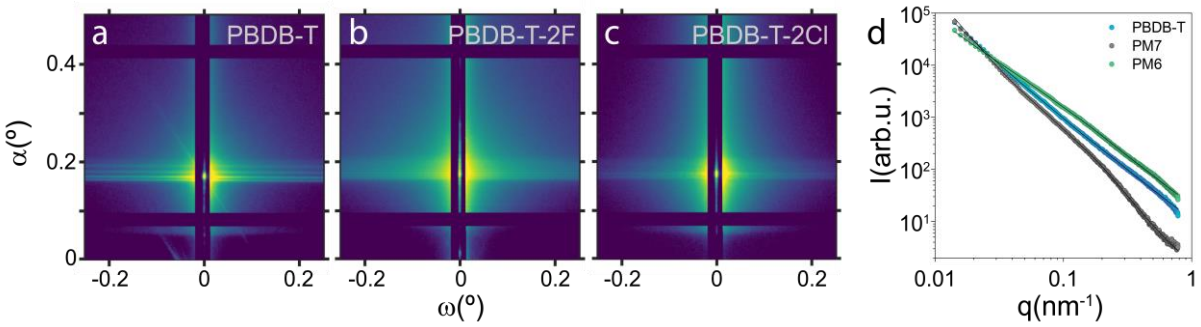

Figure 3.8 GISAXS patterns of PBDB-T, PM7 and PM6 at a grazing angle of 0.12°, and (right) the horizontal cuts at Yoneda Peak, together with their corresponding fitted curves.

For further morphological clarification, AFM images of the three films were obtained. **Figure 3.9** shows the phase-contrast images of the spun cast pristine films. The images (**Figure 3.9**a-c) suggest a multiphasic nanomorphology that is compatible with the coexistence of small order regions separated by more disordered regions. The power spectral density (PSD) analysis was extracted from the AFM images (**Figure 3.9**d-e), indicating that the solid-state microstructure in these polymers has an average characteristic size of 35-45 nm, which is most likely related to the spacing between aggregates/crystallites.

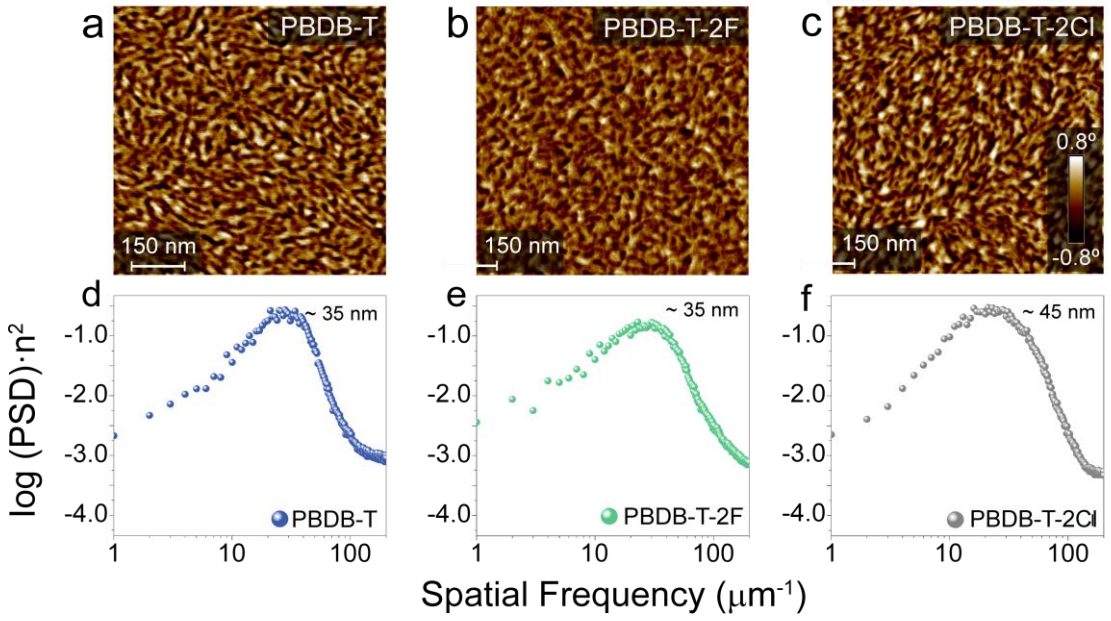

Figure 3.9 (a-c) AFM phase-contrast images and for PBDB-T, PBDB-T-2F and PBDB-T-2Cl, respectively, and corresponding power spectral density (PSD) curves (d-f).

3.3.5. Introducing semi-paracrystalline microstructural model

Consequently, based on the different physical properties measured in the pristine thin film, we proceed to argue to which microstructure this family of polymers corresponds. Depending on the types of transition that the polymers undergo, which in turn depend on the contribution of the different macro-conformations of the chain, the polymers can be classified as depicted in **Figure 3.10** (table from Van Krevelen's book).

Let us discuss the experimental facts so far:

- Our data suggest that the studied polymer films cannot be semi-crystalline as (i) they displayed almost featureless X-ray patterns and distortion lattice parameters (*g*) with values between 22 and 24 %, i.e. well-beyond those typically found for semicrystalline materials (which typically exhibit *g*-parameters between 0 and 12 %).[176] (ii) PLOM analysis revealed that films are non-birefringent. (iii) DSC did not show any reliable crystal melting process.

Figure 3.10 Classification of polymers on the basis of morphology (reproduced from Van Krevelen[177])

- Remarkably, FSC thermograms depicted clear intense melting processes and a strong tendency to order upon impressively high scanning rates.

- Our morphological results (iv) clearly showed that these polymers are based on a dense arrangement of exceedingly small "hard" domains (of ~30 nm) which pack closely together as determined by GISAXS and PSD analysis.

- Moreover, our data seems incompatible with such solid-state microstructure being a solidified liquid-crystal, as has been suggested. A solidified liquid crystal would become mechanically softer at temperatures much lower than that of the order-disorder transition, i.e., at the T_g, which does not occur in the films. In fact, we do not observe experimental evidence of a glass transition process in our films. Moreover, the appearance of weak annealing-induced peaks is more compatible with a solid-state order than with a liquid-crystalline-like order.

Hence, we argue that these polymer films ought to be-at least- paracrystalline (see **Figure 3.10**).

Intriguingly, we found that both melting and formation of paracrystals occurred at extremely high temperatures. In general, any thermodynamic phase transition, paracrystal melting, and formation must fulfil that $T \cdot \Delta S = \Delta H$ during the transition. On one hand, in this sort of system, ΔS is expected to have a reduced value because the structural order of the paracrystalline arrangement is rather low and, therefore, paracrystallites are expected to have large entropy values; and due to the moderate-to-large persistent lengths (about 7 nm) of these polymers which would induce to a low entropy of the melt. On the other hand, ΔH seems to be large, which would partially explain why we observe such strikingly high experimental melting enthalpies in FSC scans. Therefore, being ΔS small and ΔH large, the transition temperature T must be irretrievably high in order $T \cdot \Delta S = \Delta H$ to fulfil.

As a complement and confirmation of the above experiments, as well as to introduce a parameter to provide insights into the amount of order material, we estimated the degree of paracrystallinity, which, analogously to the degree of crystallinity in semicrystalline materials, would account for the mass/volume fraction of paracrystalline domains in the material. Because the enthalpy change during the melting of spin cast paracrystals can be measured from the FSC 1st heating scan, we can estimate the apparent degree of paracrystallinity of the films by normalizing the measured enthalpy to that of the 100% paracrystalline material, ΔH_m^∞. Lacking a ΔH_m^∞ value for the polymers studied, the ΔH_m^∞ value reported for P3HT was used, instead.[164] The degree of crystallinity can be deduce from:

$$DoPC = {}^{\Delta H_m}/_{\Delta H_m^\infty} \cdot 100\% \approx {}^{\Delta H_m}/_{\Delta H_m^\infty (P3HT)} \cdot 100\% \qquad \textbf{(Equation 3.1)}$$

where the volume of investigated samples could be calculated as the chip area (0.25 mm^2) was known and the film thickness was measured by atomic force microscopy (115 ± 5 nm (PBDB-T); 236 ± 1 nm (PBDB-T-2F); and 130 ± 5 nm (PBDB-T-2Cl)). The volume value was then transformed into mass value employing the density value for P3HT (1.1 $g \cdot cm^{-3}$). The heat-flow rate signal directly obtained from FSC experiments was transformed into heat capacity (c_p) values with the calculated mass and the heating rate ($2.34 \pm 0.17\ mW \cdot ℃$ (PBDB-T); $3.47\ mW \cdot$

℃ (PBDB-T-2F); and 3.77 $\pm$ 1.7 $mW \cdot$ ℃ (PBDB-T-2Cl).). The integral for the melting peak in the c_p vs T curve divided by the enthalpy for the 100% crystalline material (ΔH_m^{∞}) accounts for the fraction of paracrystals in the samples. The ΔH_m^{∞} for P3HT has been considered here $\Delta H_m^{\infty}(P3HT)$ is 49$\pm$ 2 J.g^{-1}.[164]

The degree of paracrystallinity thus obtained amount to ~38% for PBDB-T, ~27% PBDB-T-2F and ~54% PBDB-T-2Cl which, despite of the uncertainty of the methodology, suggests that the PBDB-T family of polymers exhibit a remarkable molecular order, indeed, similar to that of P3HT films.[163,164] (note: the value for PBDB-T-2F is most probably underestimated as the maximum temperature covered in the experiment, i.e. 450 °C, is not high enough to resolve completely the endothermic peak and moreover).

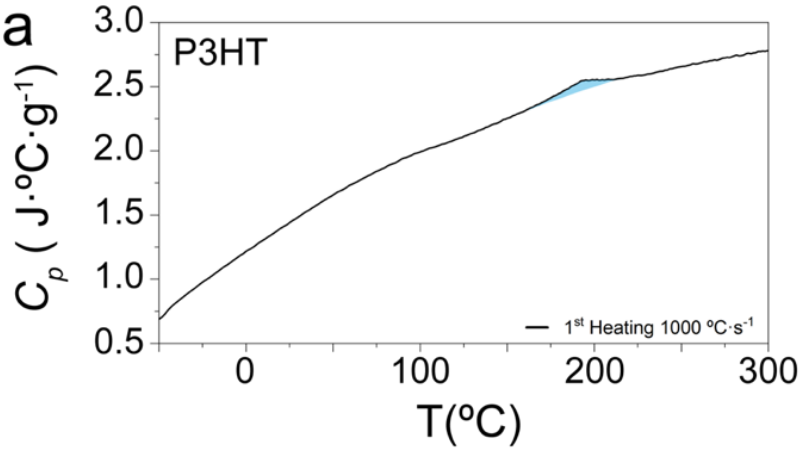

Figure 3.11 (a) First heating fast scanning calorimetry (FSC) thermogram (raw data) for P3HT calibrated to thickness.

To probe the reliability of our calculations we applied the same procedure to a thin film of regioregular P3HT (**Figure 3.11**). We calculated the enthalpy of melting of a P3HT pristine spin cast film, and we estimated the degree of order normalizing the measured enthalpy to that of the 100% paracrystalline P3HT. The degree of paracrystallinity thus obtained for a regioregular P3HT film yielded 12% proving that PBDB-T and congeners depict a higher degree of order that

a P3HT film even if the exhibit apparently disorder structures by X-ray comparing with P3HT, thus, supporting our hypothesis.

As stated above, estimated values for the degree of paracrystallinity imply the existence of significant fractions of disordered material together with the paracrystals. However, FSC experiments did not reveal any thermal transition related to these disorder phase i.e. a T_g (see section 3.3.3). We attribute the absence of a thermal transition to the fact that the highly viscous disordered domains are constrained between the dense arrangements of small paracrystallites. The glass transition temperature involves a movement of the chain segments towards dense packing, producing an additional free volume in their neighborhood. In this case, the high density of paracrystals together with the enlarge viscosity of the disorder regions restricts the movement of the chains.[8,31] Hence, unlike previously reported paracrystalline materials like aramide fibers, which do not include discrete amorphous regions and thus the degree of structural disorder can be parametrized solely by the *g*-parameter, the degree of disorder in the polymers analyzed here must have two contributions: (i) a first contribution associated with the distortion of the paracrystalline lattice (like the one in aramide fibers) and (ii) a further contribution associated with a non-paracrystalline, disordered domains. In other words, the microstructure of these semiconducting polymers is not adequately represented by the paracrystalline model, which must be adjusted to include non-paracrystalline regions. Hence, in order to describe the microstructure of these polymer materials we introduce the parameter of degree of paracrystallinity and the semi-paracrystalline model (**Figure 3.12** and **Figure 3.13**). This microstructure was already implicit in Salleo' paper[14]; however, no one attempted to described it as such.

Hence, we propose the semi-paracrystalline model that relies on the presence of a very dense arrangement of small paracrystallites that coexist with a non-paracrystalline region. Within these paracrystallites, molecular packing lacks of long-range order, or much order at all along both the lamellar direction and the π-stacking direction, as evidenced by GIWAXS. A schematic depicting this solid-state microstructure is shown in **Figure 3.12**. As a result, our data suggests thus, that GIWAXS and calorimetry disagree when traditional definitions and *g*-parameter

boundary benchmarks are used. We can argue that the *g*-parameter scale based on a-SiO_2 reference may not be appropriate to classify semiconducting polymer thin films, and that a higher *g*-value than a 12 % needs to be established as the correct boundary benchmark for amorphous polymer semiconductors.

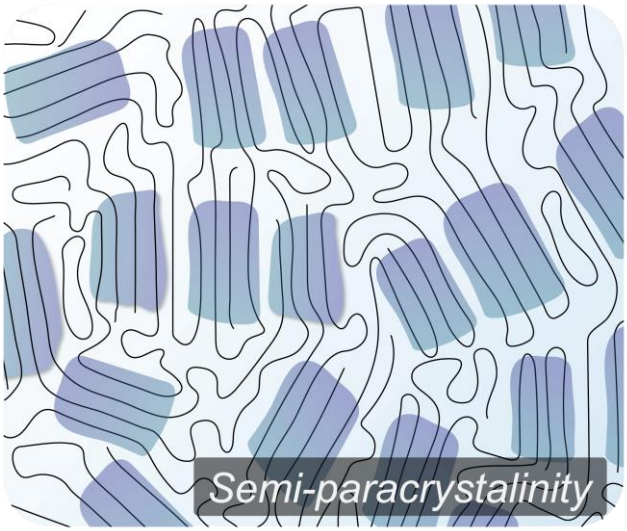

Figure 3.12 Schematic of the semi-paracrystalline solid-state microstructure found in PBDB-T, PM6 and PM7 polymers.

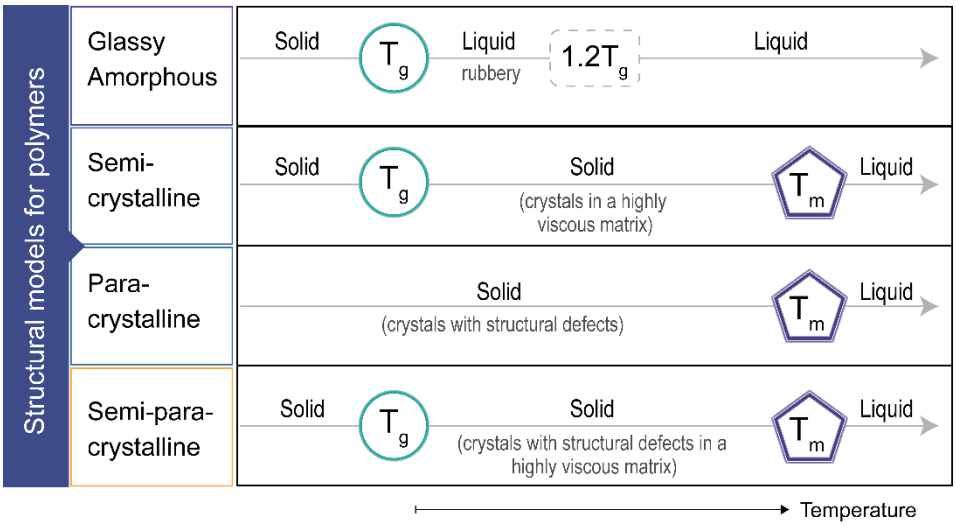

Figure 3.13 Updated classification of polymers on the basis of morphology (reproduced from Van Krevelen[177])

3.3.6. Extension to other high-performing polymers

Having shown that melting of paracrystals can be detected by FSC in seemly amorphous materials, we explore the extension of our framework to other semicrystalline polymers with efficient photoconversion capability or high-field effect mobility that, based primarily on X-ray diffraction data, have been so far considered poorly-ordered or amorphous. To extend our premises we select the following polymers: the current champion in OPV power conversion efficiency D18 (**Figure 3.14**a),[42,178] a fluorobenzotriazole-based polymer PBnDT-FTAZ (**Figure 3.14**b),[101] the polythieno[3,4-b]-thiophene-co-benzodithiophene PTB7 (**Figure 3.14**c)[179] and, the indacenodithiophene–benzothiadiazole IDT-BT (**Figure 3.14**d).[180] For the sake of comparison, a well-known amorphous semi-conducting polymer, poly[bis(4-phenyl)(2,4,6-trimethylphenyl)amine (PTAA) has been analyzed by FSC and the commodity semi-crystalline polymers poly(ε-caprolactona) (PCL) and poly(vinylidene fluoride) (PVDF), and the semiconducting polymer poly(3-hexylthiophene) (P3HT) have been analyzed by GIWAXS (**Figure A-5**).

We first investigated this polymer films by means of GIWAXS. On one hand, the D18 pattern (**Figure 3.15**a) reveal multiple scattering peaks including higher backbone (00l) and lamellar orders (l00) parallel and perpendicular to the substrate, respectively. The π-stacking peaks along the out-of-plane and in-plane direction revealed the presence of both molecular orientation preferentially in face-on in full agreement with previous reports.[178] However, Ade et al. reported the absence of melting peaks measured by DSC at least below decomposition temperature. [178] On the other hand, the patterns of the pristine films revealed partially disordered films for PBnDT-FTAZ, PTB7 and IDT-BT (**Figure 3.15**a) like PBDB-T and its derivatives. D18, PTB7, PBnDT-FTAZ and IDT-BT films exhibited comparatively larger g-values and lower CCL values than common semi-crystalline polymers (data included in **Table 3.2**).While GIWAXS patterns revealed amorphous or low-order patterns (unless D18)[178], FSC results provided compelling evidence that the four polymer thin films present a clear endothermic peak at high temperatures probably related to the melting of paracrystals being the enthalpic overshoot from

D18 highly energetic as expected from the GIWAXS pattern revealed the presence of the glass transition temperature related to the non-paracrystalline regions. Contrarily, amorphous polymers like PTAA, did not show any endothermic peaks (**Figure 3.15**b). Hence, we speculate that the solid-state microstructure described in this paper might be a common feature among thin films of many high-performing rigid polymers employed for OSCs. Although, the detailed interplay between thermal and diffraction characterization has to be more explored and understood. Notwithstanding, we can identify some common experimental signatures of the semi-paracrystalline organization: (i) unlike semicrystalline materials, semi-paracrystalline materials seem to exhibit *g*-parameters comparable to those of amorphous materials (frequently > 15) and CCL values in the range of 1-3 nm (see **Table 3.2**); but (ii) in contrast to amorphous materials they exhibit order-disorder transitions visible by calorimetry.

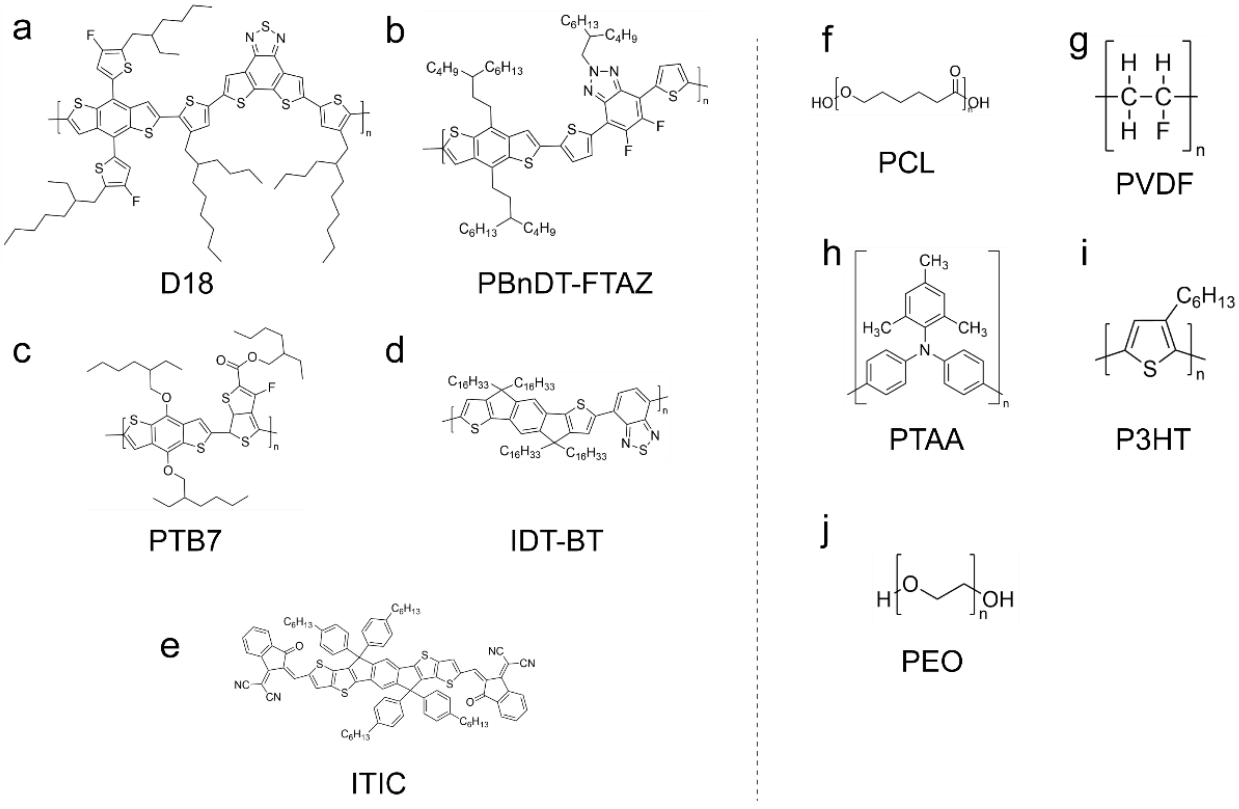

Figure 3.14 Molecular structures of (a) D18, (b) PBnDT-FTAZ, (c) PTB7, (d) IDT-BT, (e) ITIC, (f) PCL, (g) PVDF, (h) PTAA, (i) P3HT.

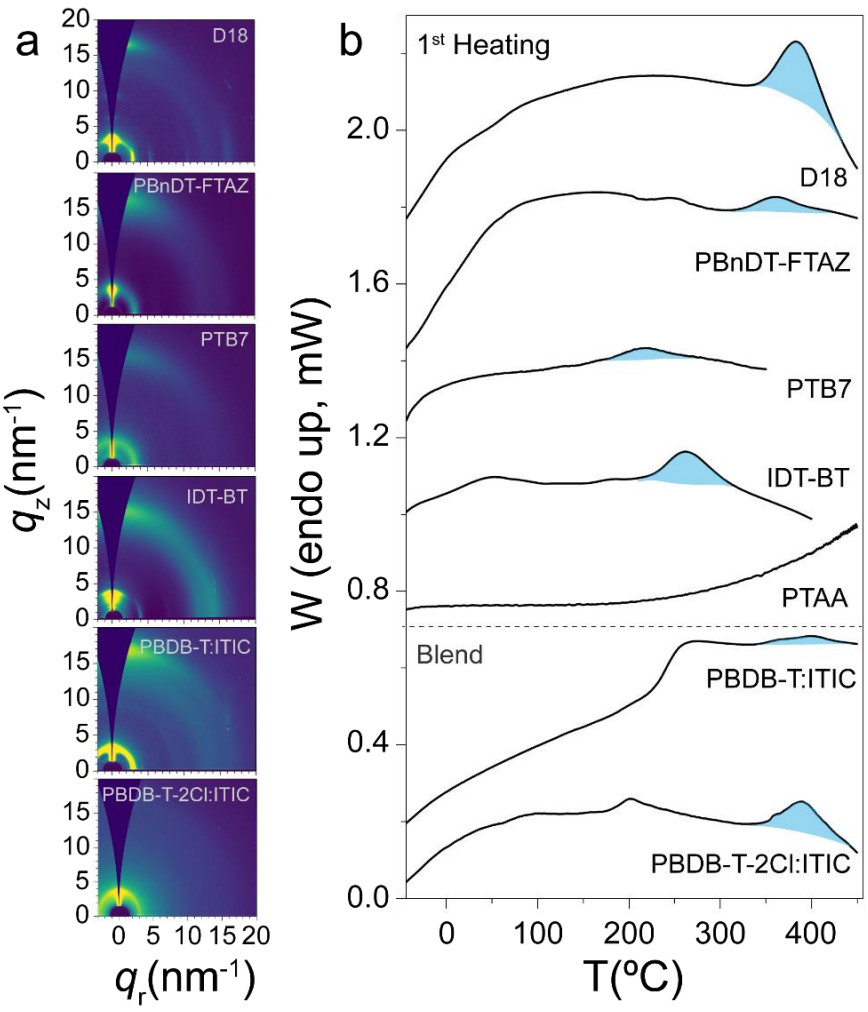

Figure 3.15 GIWAXS patterns (a) and FSC heating traces (b) for a variety of polymers (D18, PBnDT-FTAZ, PTB7, IDT-BT, PTAA) and photovoltaic blends (PBDB-T:ITIC and PBDB-T-2Cl:ITIC).

To elucidate whether this semi-paracrystalline microstructure presented in the pristine polymer is retained in the donor:acceptor blend, we endeavoured to explore a donor:acceptor blends like those employed in OSC devices. To do so, we investigated a PBDB-T:ITIC (1:1) binary blend produced using similar processing conditions as those employed in efficient device preparation (i.e. spin casting a chlorobenzene solution containing 0.5% 1,8-diiodooctane, DIO, followed by a thermal annealing at 160 °C) and a PBDB-T-2Cl:ITIC bland cast from chlorobenzene.[34] Like neat polymer films, photovoltaic blends seem to be amorphous when they are characterized by GIWAXS (**Figure 3.15**a). From FSC data (as shown in **Figure 3.15**b) we

could observe the endothermic peak at about 260 °C is attributed to overlapped calorimetric signals from ITIC domains[49] and an endothermic feature showing up at about 400 °C (shadowed in blue in **Figure 3.15**b) reflecting the melting of PBDB-T paracrystals. Accordingly, we could confirm that paracrystalline order is also presented in donor domains of binary blends.

Table 3.2 Peak parameters for a variety of polymers.* Correspond to (110) plane of PCL and # (021) plane from α-phase of PVDF.

	Microst.	Lamellar (100)			π-π peak		
		q, nm^{-1}	*CCL (nm)*	*g (%)*	*q*, nm^{-1}	*CCL (nm)*	*g (%)*
Polymer	D18	3.2	12.9	15.4	16.8	3.2	13.6
	PBnDT-FTAZ	3.4	4.9	24.1	16.6	1.5	20.1
	PTB7	--	--	--	16.8	1.7	18.6
	IDT-BT	3.8	12.1	14.8	14.9	1.5	21.0
	P3HT	2.8	10.2	18.6	16.8	7.0	9.3
	PCL	-	-	-	15.5*	161.1	4.4
	PVDF	-	-	-	19.0#	33.2	1.8
Blend	PBDB-T:ITIC	3.3	5.9	22.6	16.8	1.4	20.6
	PBDB-T-2Cl:ITIC	3.9	9.0	16.9	16.3	3.3	13.6

3.3.7. Evolution of the microstructure with temperature

To uncover microstructural variations in the semi-paracrystalline microstructure in the thin film as a function of temperature, GIWAXS, FSC and AFM measurements were conducted. At this point, we recall the aging/annealing experiments carried out (see section 3.3.3) by FSC in which we observed different regimes. For clarity, the microstructure generated after annealing

treatments at temperatures within each regime are named as A-, B- and C- microstructures: (i) The ambient temperature regime in which no noticeable changes in the material are observed when aging/annealing treatment are applied (denominated hereafter as *A*-microstructure). (ii) A second regime (at intermediate temperatures i.e. ~160 ºC) in which we observe a process related to the melting of the order regions formed during the annealing process (called hereafter *B*-microstructure) and (iii) a third high temperature regime in which an large increase in the enthalpy of the melting peak is observed (so-called *C*-microstructure).

3.3.7.1. GIWAXS: Effect of temperature on the paracrystalline distortion parameter

We followed the variations in the disorder lattice parameter, *g*, estimated for the different main reflexions (100), (010) and (002). To do so, thin films of the three polymers spun cast from a 20 $mg \cdot mL^{-1}$ chlorobenzene (PBDB-T and PM7) or chloroform solution (PM6) were annealed at selected temperatures during 10 minutes and measured at room temperature by means of GIWAXS. All the measured temperatures are included in **Figure A-6**, **Figure A-7** and **Figure A-8**, and selected GIWAXS patterns are depicted in **Figure 3.16**a-c.

We estimated the lattice disorder parameter, *g*, for each sample and we plot the values versus annealing temperature to examine the trend. The estimation of the lattice disorder parameter, *g*, obtained GIWAXS patterns of the three polymers revealed a minor reduction of *g* for the (100) and (010) planes in *B*-microstructures comparing with the pristine *A*-microstructure (summarized in **Table 3.3**) [we note that the (010) planes are expected to be connected with the overlap of π-orbitals and thereby linked to preferential electronic pathways]. On the other hand, *C*-microstructures featured, however, substantial structural changes compared to *A*- and *B*-microstructures. The estimated *g*-values reflected a rapid reduction of the lattice disorder when films are annealed at high temperature. It is worth noting that the *g*-values for the (002) planes are fairly insensitive to the temperature in the temperature range analyzed.

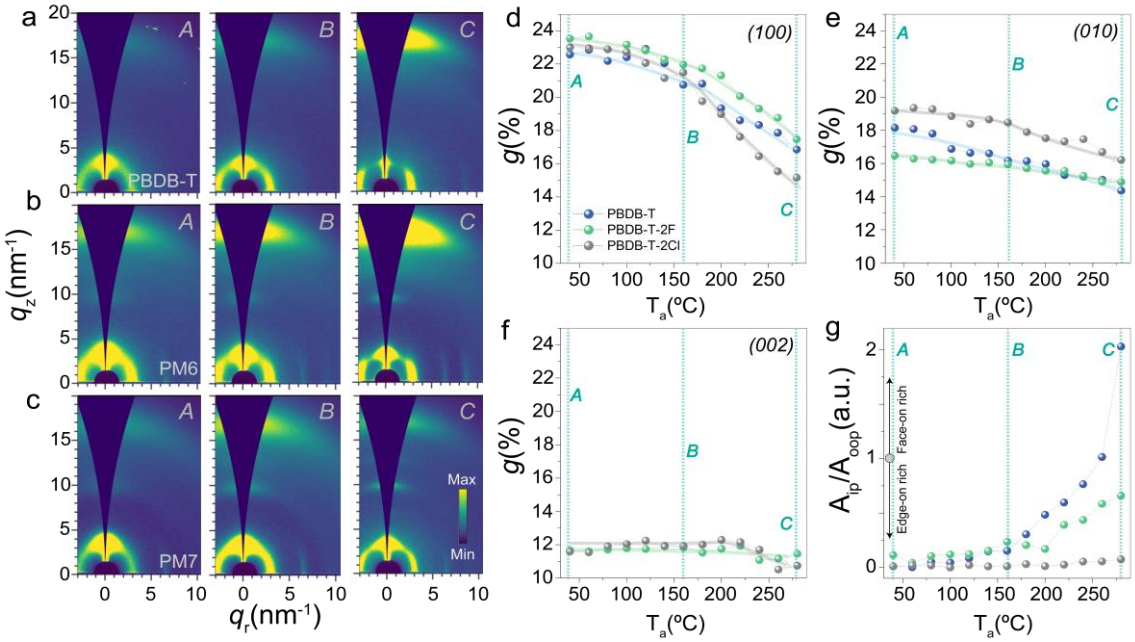

Figure 3.16 Ex situ 2D-GIWAXS pattern of (a) PBDB-T A-, B- and C-microstructures; (b) PBDB-T-2F A-, B- and C-microstructures; and (c) PBDB-T-2Cl A-, B- and C-microstructures. Paracrystalline distortion parameter, *g*, for the (d) (100) planes, (e) (010) planes and (f) (00l) planes as a function of the annealing temperature, T_a. (*g*) Ratio between the (100) diffraction maxima along the out-of-plane and in-plane directions (A_{ip}/A_{oop}), for the different polymers as a function of T_a.

Table 3.3 Peak position and crystalline coherence length (CCL) values of the GIWAXS reflections.

Polymer	Microstruc.	Lamellar (100)			(200)			π-π stacking		
		q, *nm*$^{-1}$	*CCL* *(nm)*	*g* *(%)*	*q*, *nm*$^{-1}$	*CCL* *(nm)*	*g* *(%)*	*q*, *nm*$^{-1}$	*CCL* *(nm)*	*g* *(%)*
PBDB-T	A	3.4	5.8	22.6	/	/	/	17.0	2.2	16.5
	B	3.2	7.1	20.7	/	/	/	17.1	2.3	15.9
	C	3.2	11	16.9	/	/	/	17.1	2.6	14.9
PM6	A	3.4	5.3	23.5	6.6	11.2	11.7	16.8	1.6	19.1
	B	3.2	6.4	22.0	6.5	11.0	11.8	16.8	1.7	18.5
	C	3.2	10	17.5	6.5	11.6	11.5	17.0	2.2	16.2
PM7	A	3.5	5.4	23.0	6.4	11.6	11.6	17.0	2.2	16.5
	B	3.3	6.5	21.5	6.5	10.9	11.9	17.1	2.3	15.9
	C	3.4	13	15.1	6.5	13.3	10.7	17.1	2.6	14.9

Moreover, we observed some progressive change in orientation in the lamellar planes as a result of the thermal annealing, and, therefore, we developed a texture analysis depicted in **Figure 3.16**g. We plotted A_{ip}/A_{oop} which refers to the ratio between the (100) diffraction maxima along the out-of-plane and the in-plane directions, against annealing temperature. Our results highlight that PBDB-T paracrystals suffer from a progressive change of orientation as the T_a increases, yielding face-on oriented crystallites at the higher T_as analyzed, i.e. those leading to *C*-microstructures. Face-on oriented paracrystals have their (010) planes parallel to the substrate, which is the opposite direction to the current flow in OFETs, and, thus, it may hinder the in-plane charge transport.[181]

3.3.7.2. AFM: morphological analysis

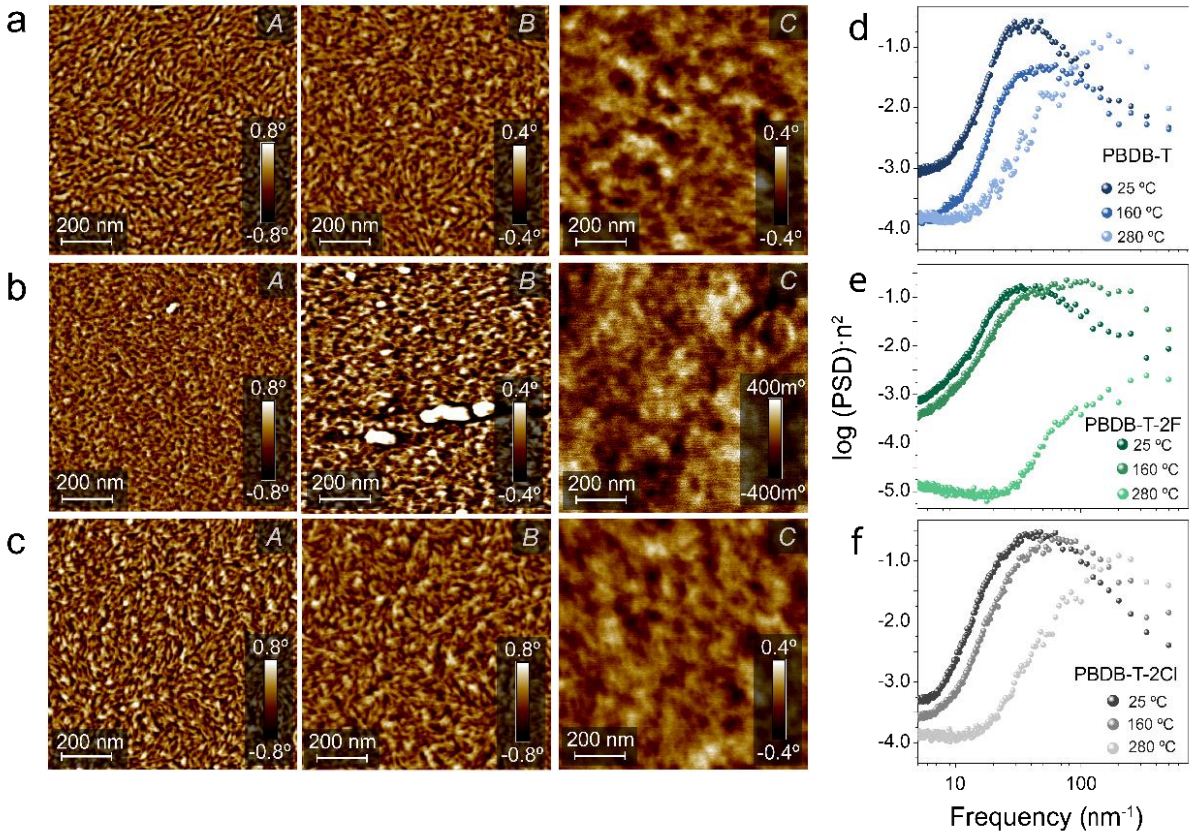

Figure 3.17 Atomic force microscopy phase images for (a) PBDB-T *A*-, *B*- and *C*-microstructures, (b) PBDB-T-2F *A*-, *B*- and *C*-microstructures and (c) PBDB-T-2Cl *A*-, *B*- and *C*-microstructures. (d-f) Power spectral density (PSD) curves of AFM phase contrast images.

Thin films were then investigated by AFM to observe the effect of temperature on the film morphology. We selected room temperature, 160ºC and 280ºC as the temperatures to obtain selectively the different microstructures and we used the same films to ensure a fair comparison. **Figure 3.17** shows the phase-contrast images. The general nanomorphology of *A*- and *B*-microstructures is pretty similar when inspected by AFM (**Figure 3.17**a-c). We detected a minor increase of the characteristic length-scale of the microstructure as suggested by the PSD analysis (**Figure 3.17**d-e). Conversely, C-microstructure depicted a significant enlargement of the domains, which reach >100 nm, as probed by PSD analysis. This enlargement of the domains coincides with an increase of the degree of paracrystallinity, the enlargement in the enthalpy of melting of preexisting paracrystal and the decrease of the *g*-values for the (100) and (010) planes as estimated from GIWAXS measurements.

3.3.7.3. Thermotropic behaviour of the semi-paracrystalline microstructure

Based on our framework and having verified our findings, we present the scheme in **Figure 3.18** illustrating the thermotropic behaviour of the semi-paracrystalline microstructure. Thus, the pristine microstructure, *A*, consist of very dense arrangement of small paracrystallites which lack of molecular packing with long-range order. Upon annealing at an intermediate temperature (i.e. 160ºC), secondary (para)crystallization and recrystallization processes in the polymer form new small-paracrystallites, leading to microstructure *B*. We based our hypothesis in the fact that no changes are observed in the melting peaks of preexisting paracrystals and the emergence of an additional weak endothermic peaks between 200 and 300 °C that we associate with the melting of new paracrystallites grown during the annealing (**Figure 3.5**). Moreover, the new paracrystallites must be even smaller and/or more defective than the preexisting ones because they exhibit melting temperatures that are more than 100 °C lower and a minor reduction of *g* for the (100) and (010) planes were obtained. We deem that the new paracrystallites may grow within non-ordered regions between preexisting paracrystals, thereby improving their interconnection pathways. Lastly, a further annealing at higher temperatures (i.e. 280 ºC) shows large enthalpy

changes in the melting of the preexisting paracrystal, thus larger degrees of paracrystallinities. This statement is in full agreement with (i) a reduction of the lattice distortion; (ii) the larger enthalpy changes obtained during paracrystals melting by FSC; (iii) the increased degree of paracrystallinity calculated for a thin film annealed at 280 ºC yielded 47 % for PBDB-T and 62 % for PM7 (the value for PM6 cannot be safe extracted from our calorimetric data); and (iv) the size of paracrystals extracted from AFM and PSD analysis. In this manner, we assume that the final *C*-microstructure represented in **Figure 3.18** is composed of larger paracrystals with melting temperatures resembling preexisting paracrystals.

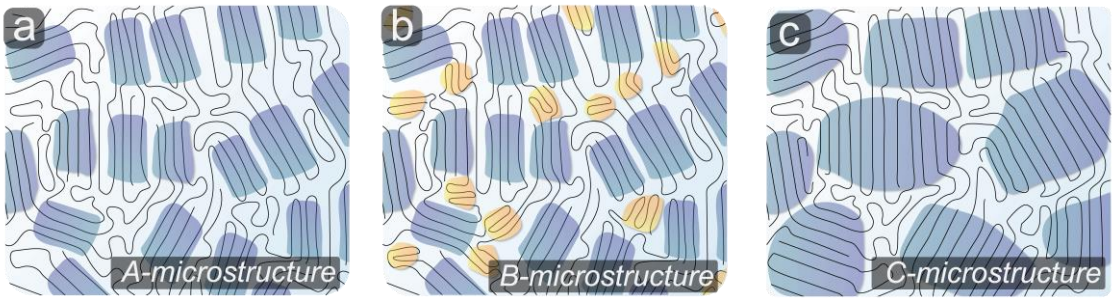

Figure 3.18 Schematics depicting the semi-paracrystalline microstructure of as-cast films (and films annealed at 25 ºC, denoted as *A*-microstructure) (a) and films annealed at 160 ºC (b, denoted as *B*-microstructure) and 280 ºC (c, denoted as *C*-microstructure).

3.3.8. Interplay between microstructure and electronic properties

Having decoded the microstructure of spin-cast PBDB-T, PBDB-T-2F and PBDB-T-2Cl films, we set on to investigate the interplay between the characteristic aspects of the semi-paracrystalline microstructure and the optoelectronic properties and charge transport.

To analyze the effect of molecular arrangements in the optoelectronic properties, thin films were annealed every 20 ºC from room temperature to 280 ºC and measured by UV-Vis spectroscopy (see **Figure 3.19**). In general, we found that the vibronic structure is less distinctive for PBDB-T (**Figure 3.19**a) than for PBDB-T-2F and PBDB-T-2Cl (**Figure 3.19**b-c). Moreover, the ratio between the intensities of the bands corresponding to the transition to the lowest vibronic level (i.e. the 0-0 transition at ~610 nm) and the transition to the next vibronic level (i.e. the 0-1

transition at ~570 nm), is greater for PBDB-T-2F and PBDB-T-2Cl than for PBDB-T. **Figure 3.19**d shows the $A_{0\text{-}0}/A_{0\text{-}1}$ ratio as a function of annealing temperature. These ratio can be used to parameterize the intrachain optoelectronic coupling of neighboring chromophores.[182] A higher $A_{0\text{-}0}/A_{0\text{-}1}$ value is usually interpreted as a higher abundance of chain segments with planarized conformations. Therefore, our UV-vis results suggest that PBDB-T-2F and PBDB-T-2Cl exhibit, on average, a higher fraction of chain segments with planarized conformations than PBDB-T. In any case, while temperature revealed strong effects on solid-state microstructure, it seems to have a little impact on molecular conformation and short-range molecular arrangement. We observed a slightly positive trend of the $A_{0\text{-}0}/A_{0\text{-}1}$ ratio for PBDB-T with temperature, whereas PBDB-T-2Cl and PBDB-T-2F seems rather insensitive to T_a.

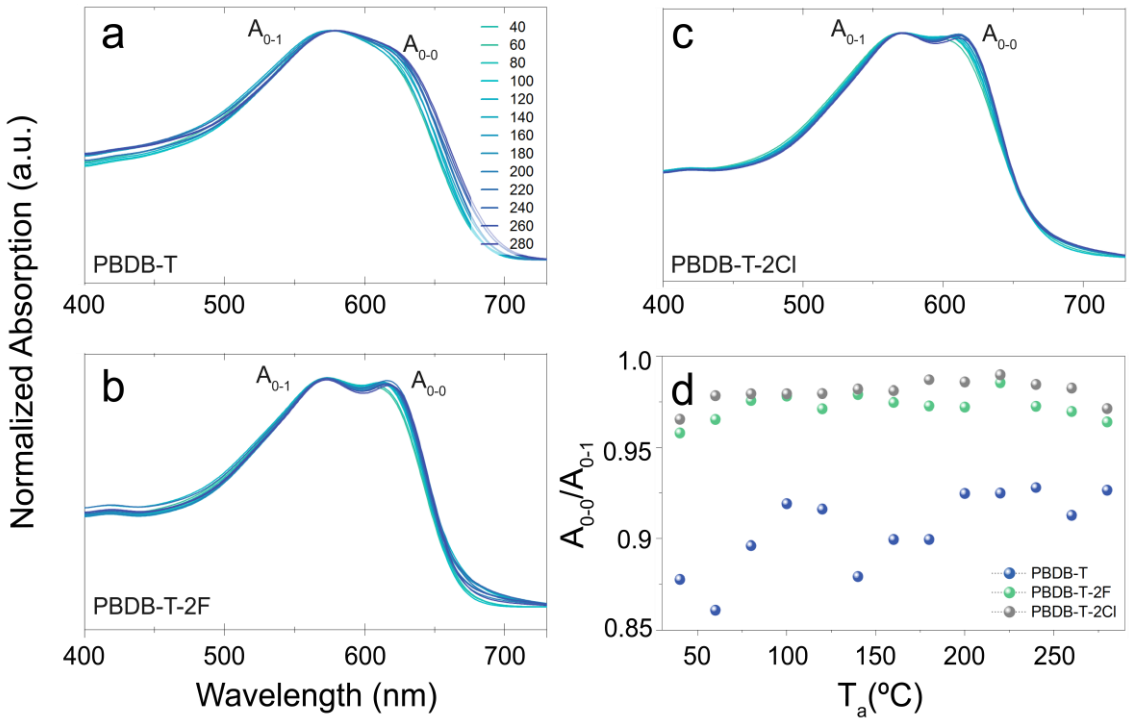

Figure 3.19 UV-vis absorption spectra for (a) PBDB-T, (b) PBDB-T-2F and (c) PBDB-T-2Cl films annealed at different temperatures. (d) Ratio between the intensities of the bands corresponding to the 0-0 transition (at ~610 nm) and the 0-1 transition (~570 nm).

To probe a quantitative microstructure-function relation, organic field-effect transistors (OFETs) were fabricated with semi-paracrystalline films exhibiting microstructural modifications

resulting from thermally annealing the films at different temperatures (T_as). The selected T_as were 25 °C, 160 °C and 280 °C and the resulting solid-state microstructures, referred to as *A*-, *B*-, and *C*-microstructures, respectively. **Figure 3.20**a shows the representative transfer characteristics for the PBDB-T, PBDB-T-2F and PBDB-T-2Cl transistors, respectively. **Figure 3.20**b-e shows the mobility values of the three microstructures as a function of some parameters related to the semi-paracrystalline microstructure. The higher μ-values for *B*-microstructures compared to *A*-microstructures in all polymers results from a more efficient long-range charge transport due to the presence of small paracrystals between primary paracrystals (in *B*-microstructure, see **Figure 3.18** and **Figure 3.20**b), which enhances the interconnection pathways of the structural network that sustain the charge transport. This idea is in line with the charge transport model by Noriega, Rivnay and Salleo,[14] and furthermore highlights that long tie-chains are not the only possible mechanism of interconnection of ordered regions, which can occur also through small paracrystallites.

Furthermore, we found that the large increase of the degree of paracrystallinity (**Figure 3.20**c) coincides with a significant enlargement of the paracrystals, as deduced from the increase of the CCL-value of lamellar packing, (100), from 5-7 to 10-13 (**Table 3.3**). Intriguingly, the g-values for the (100) and (010) planes are significantly lower in C-microstructures (see **Table 3.3** and **Figure 3.20**d), reflecting a reduction of the lattice disorder of paracrystalline domains. Therefore, the increase of the degree of paracrystallinity, the larger paracrystals and the reduction of lattice distortion can explain the larger μ-values of C-microstructures in PBDB-T-2F and PBDB-T-2Cl compared to B-microstructures.

However, while a 2.5-to-4-fold increase in μ is found for transistors exhibiting B-microstructure compared to those with A-microstructure, the comparison between transistors having B- and C-microstructures shows uneven results: maximum μ-values are recorded for PBDB-T-2F and PBDB-T-2Cl transistors with C-microstructures, but in the case of PBDB-T transistors, the optimized μ-values are found for the B-microstructure. Interestingly, our texture,

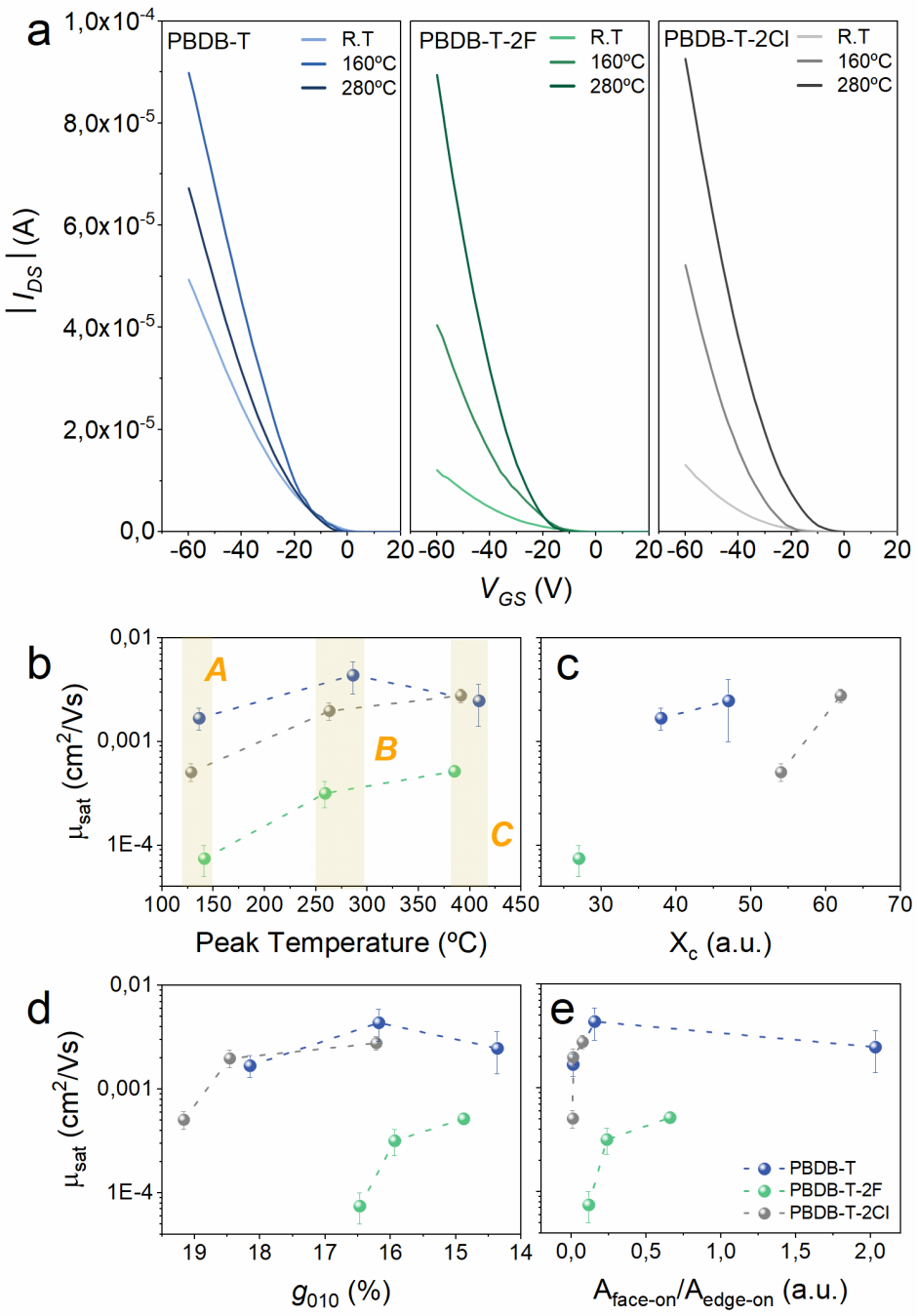

Figure 3.20 Representative transfer characteristics for (a) PBDB-T, PBDB-T-2F and PBDB-T-2Cl field-effect transistors annealed at 25 ºC, 160 ºC and 280 ºC. All transfer characteristics were measured in transistors with width W = 10000 and length L = 40. (b) Field-effect mobility, μ, for the different polymer samples plotted vs the endothermic peak temperature (for A-microstructures, the broad endothermic signal appearing between 100 and 200 ºC is considered, while for B-and C-microstructures the endothermic peak derived from the isothermal annealing step is considered). μ vs degree of paracrystallinity of films (c); μ vs lattice distortion parameter of the π-π stack, g_{010}, (d); and μ vs the ratio between the area of the (100) diffraction maxima along the out-of-plane and the in-plane directions, A_{ip}/Aoop (e)

analysis in **Figure 3.20**e highlighted that PBDB-T paracrystals suffer from a progressive change of orientation as the T_a increases, yielding face-on oriented crystallites at the higher T_as analyzed i.e. those leading to C-microstructures. Face-on oriented paracrystals have their (010) planes parallel to the substrate, which may hinder the in-plane charge transport, resulting in the low mobility observed for the PBDB-T *C*-microstructure.

3.4. Conclusions

In this chapter, we shed light on the long-standing debate about structural order in high-performing semiconducting polymers. So far, the characterization of the amount of structural order in these materials resulted in conundrums, in which scattering and microscopy methods led to seemingly contradicting conclusions. Thus, based on most-standardized X-ray analysis these materials have been assumed to be amorphous and thus have been considered in most advanced morphology-function and stability prediction models for OSCs.[47,89] Employing fast scanning calorimetry, we discover and demonstrate, however, that they can be in fact notably ordered. The misinterpretation originates from employing the *g*-parameter as the only criteria to assess structural order of semiconducting polymers. These materials often exhibit *g*-parameter values that are similar to those of amorphous a-SiO_2, which can lead to mistakenly interpret that these materials are amorphous. Though paracrystalline lattices in these materials are indeed largely distorted (hence the large *g*-parameter values), we find a surprisingly small fraction of total polymeric material that is actually disordered. Thus, we conclude that the precise assessment of structural order in semiconducting polymers requires information about -at least- two parameters: the *g*-parameter, which accounts for the paracrystalline lattice distortion, and the degree of paracrystallinity (introduced here for the first time), which measures the mass/volume fraction of paracrystalline material from the analysis of order-disorder peaks in FSC scans. The relationship between both parameters needs to be analyzed in future studies.

We demonstrate that the remarkably high degree of structural order in these semi-paracrystalline polymers is underpinned by a dense arrangement of very small and disordered

paracrystallites that coexist with more disordered regions. The disordered fractions of semi-paracrystalline materials are reasonably expected to exhibit a glass transition process. This too needs to be researched and our work opens up an avenue of quantitative and much more complete understanding of complex materials that semi-conducting polymers represent. Partially in line with the charge transport model of semicrystalline polymers by Noriega, Rivnay and Salleo,[14] the field-effect charge mobility of semi-paracrystalline polymer materials is very sensitive to the interconnection of paracrystal units through further small paracrystallites. The reduction of the paracrystalline lattice disorder, the degree of paracrystallinity and the paracrystallite's orientation are also proven to impact charge transport.

Because the semi-paracrystalline microstructure is likely to be a common feature among many polymers having semi-rigid backbones and some amphiphilicity, including some kinds of biomacromolecules, we believe that our results can have direct implications not only in the organic electronics arena, where e.g. device operation models must now include the degree of paracrystallinity, but also in other now seemingly unconnected fields.

4. Processing–structure–function relationships of non-fullerene acceptors based on indacenodithienothiophene

4.1. Summary

Despite of the impressive efficiency values of organic solar cells based on polymers and non-fullerene acceptors (NFA), little is known about how the structure of the NFA impacts the solar cell operation. Hence, many of the reported materials and devices may not have demonstrated their full potential yet, because device processing is too often optimized using a trial-and-error approach rather than knowledge-based strategies pursuing optimal microstructures. The design of rational processing protocols requires first a deep study of the solid-state microstructure. In this chapter, introducing a comprehensive structural analysis of their crystalline and glassy phases of NFAs, we show that the indacenodithienothiophene family of NFAs, namely ITIC, ITIC-M, ITIC-2F and ITIC-Th, exhibit a rich polymorphism. We demonstrate that all the studied NFAs arrange into a low-temperature metastable phase that is readily promoted via solution processing and leads to the highest device efficiencies. Interestingly, our data reveal that the low-temperature forms feature a continuous network that favours charge transport despite having little order along the π-π stacking direction. Interestingly, the electron mobility of the metastable phase I is comparable to that in the highly ordered high-temperature polymorphs. Since the optical absorption of the structurally more disordered low-temperature phase can surpass that of the more ordered polymorphs, we outline that such a packing structure may be an important feature for reaching highest device efficiency, thus, providing guidelines for future materials design and crystal engineering activities.

This work was published in *Advanced Functional Materials* (DOI: 10.1002/adfm.202103784)[183] and the work related to ITICs glassy phase was partially published in *ACS Applied Materials and Interfaces* (DOI: 10.1021/acsami.9b04554).[49]

4.2. Introduction

The remarkable increase in the power conversion efficiency (PCE) of organic solar cells (OSCs) has been achieved through significant research efforts in the chemical tailoring of non-fullerene acceptors.[62,63] The major breakthrough in the field was achieved with the indacenodithienothiophene-based acceptor ITIC. Originally synthesized by Zhan et al. in 2015,[35] ITIC is an A-D-A structured molecule with indacenodithieno[3,2-b]thiophene (IT) as central donor unit and 2-(3-oxo-2,3-dihydroinden-1-ylidene)malononitrile (IC) as acceptor end groups (see **Figure 4.1**a). While it delivered an initially modest power conversion efficiency (PCE), ulterior optimization of the device processing[34] and/or incorporation of various chemical functionalities such as methylation, fluorination (ITIC-2F,[32] **Figure 4.1**b, ITIC-M,[172] **Figure 4.1**c) or substitution of phenyl units by thiophene units (ITIC-Th,[68] **Figure 4.1**d), have resulted in the improvement of the PCE over 14%.[33] The discovery of A-D-A' type non-fullerene acceptors and the improvement achieved in terms of performance compared to fullerene-based acceptor devices, prompt the field to further development of novel NFA acceptors.[184] The emergence of the Y-type acceptor[185] so-called Y6 which currently have reached record PCE of ~18%.[42,72]

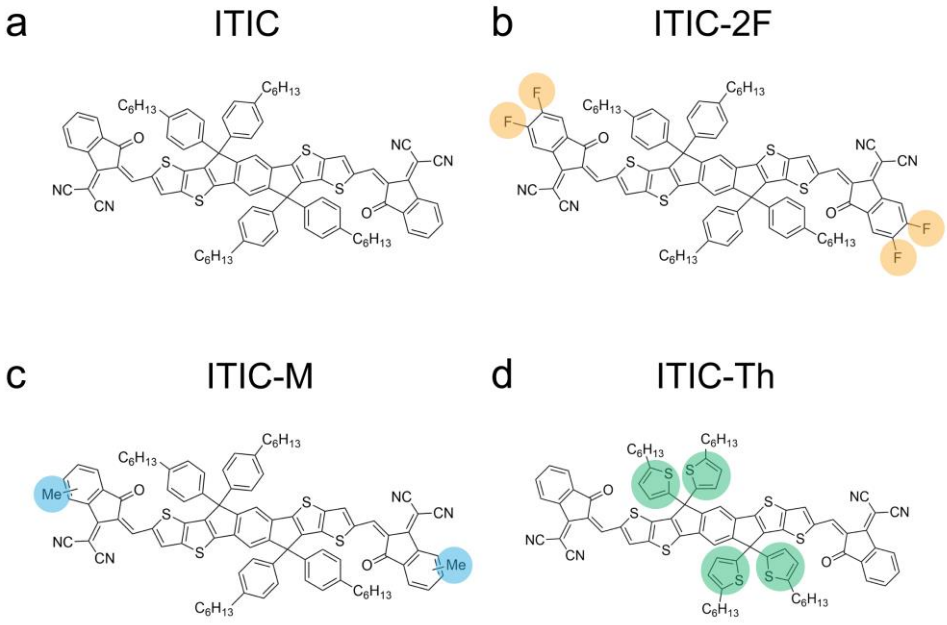

Figure 4.1 (a-d) Chemical structures of ITIC, ITIC-2F, ITIC-M and ITIC-Th, respectively.

Due to the dominance of fullerene acceptors in the field of organic solar cells over decades,[186,187] much of the current understanding of processes that originate morphological instabilities and more specifically, the effect of crystallization in its photovoltaic performance its partially unknown. Moreover, giving the clear difference in the molecular structure of both acceptors, the data of fullerene devices cannot be extrapolated.[188–190] Several studies have addressed the relationship between the blend morphology and the performance in NFA OSCs,[166,191,192] however, little attention has been paid so far to microstructural features of the NFAs. Indeed, NFAs including ITIC-derivatives, often develop crystalline domains when they are solution-processes (e.g. by spin coating, wire-bar coating, etc.)[49,193–195] and, importantly, can crystallize in various polymorphs; i.e. in different crystal forms. Consequently, the solid-state microstructure and phase morphology of polymer:NFA BHJs often includes a crystalline acceptor phase. However, the identification and structure-property relationship of the different crystalline phases that NFAs may present, remains mainly unnoticed by the field. Few studies have addressed the often-rich phase behaviour of these promising acceptor materials. Hence, the impact of the different crystalline forms on the electronic properties still remains unclearly understood. Consequently, significant differences in the efficiency and thermal and morphological stability of polymer:NFA blends, lead the field to rely on "Edisonian" protocols for optimization in device fabrication.

The occurrence of polymorphism is common phenomenon observed for many small-molecule pharmaceutical compounds such as paracetamol and ibuprofen,[196,197] and some organic semiconductors such as TES-ADT[198] and TIPS-pentacene.[199] Polymorphs are different crystalline forms of the same chemical composition but with a different arrangements or lattice structure i.e. different unit cell dimensions and packing.[200] The basic concept of polymorphism was originally rationalized in terms of the empirical Ostwald´s rule of stages,[201] which states that in the crystallization of polymorphic systems, the most thermodynamically stable form is the last to appear; whereas the polymorph initially formed is less thermodynamically stable but its formation requires to overcome a lower energy barrier. In the case of crystallization from solutions, this can

be, for example, due to a favourable solvent-polymorph interfacial free energy.[202] Dominant interactions between organic semiconducting molecules, including the ITIC derivatives studied here, are in general weak, e.g., van der Waals, π–π interactions, hydrogen bonds, and/or electrostatic interactions, which, in addition, are frequently nonspecific. This results in the general tendency of organic semiconductors to adopt multiple packing modifications upon solidification.[202] For crystalizable NFAs, the crystallization into different forms can impact into a wide range of physical and chemical properties and, thus, the identification of the different polymorphs and a deep phase behaviour understanding is required for the design of future materials. Moreover molecular polymorphism may also affect device performance via different mechanism: for example, different polymorphs can exhibit different optoelectronic properties because of different overlap between π-orbitals.[203–205] Moreover, crystal habits might differ between polymorphs, affecting the overall microstructure and leading to different BHJ phase morphologies.

The few literature reports addressing structural aspects of ITIC-based NFAs agree that ITIC tend to exhibit a low degree of crystallinity –thus, large amounts of disordered glassy phase– when it is spin coated from typical solvents such as chlorobenzene (CB), *orto*-dichlorobenzene (o-DCB),[35,68] chloroform (CF),[35] *orto*-xylene (o-Xy),[98,206] dichloromethane (DCM), etc.[49,70,194,195,207–210]. The inclusion of new chemical moieties to the ITIC building block seems to increase crystallinity and PCE values, as it is the case for ITIC-M[172,211] and ITIC-Th[195,212] (the chemical structures of these compounds are shown in **Figure 4.1**). Recent reports have nonetheless suggested that the degree of crystallinity may have a complex effect on the PCE: a slight increase of crystallinity induced by thermally annealed ITIC below the glass transition temperature, T_g ($T_{g,ITIC}$~ 180 °C [49]), by solvent annealing[194] or by using the right amount of solvent additives[213] seems to be beneficial for PCE and stability[192]; whereas the larger crystallinity resulting from thermal annealing ITIC above the T_g seems to be detrimental.[49] To rationalize the above results, Yu et al.[49] and Ciammaruchi et al.[214] have suggested that ITIC is able to crystallize into different polymorphs; i.e., a low temperature polymorph that develops via diffusion limited

crystallization at temperatures below T_g and a high-temperature polymorph that develops by regular cold crystallization at temperatures above the T_g. Besides that, Mai et al. have recently proposed that the enhancement of the device performance in BHJs using a mixture of ITIC and ITIC-Th results from the development of a large-cell crystalline structure having improved order along the molecular backbone direction.[195] Although relevant, it is not sufficient to gain a complete understanding of the structural behavior of indacenodithienothiophene-based NFAs.

In this chapter, we identify, characterize and gain understanding of the crystalline forms of indacenodithienothiophene-based NFAs, namely ITIC, ITIC-2F, ITIC-M and ITIC-Th and their glassy phases. We show that the low-temperature metastable polymorph, which seem to be a common feature among highest performing OSCs, including ITIC derivatives[195] and the benchmark Y6,[215] may play a key role in charge transport in high performing OSCs. To achieve so, we have used an experimental approach based on fast scanning calorimetry (FSC), grazing incidence X-ray scattering (GIWAXS) and polarized optical microscopy-spectroscopy (POM-S), with which we can study in detail both crystalline and glassy phases of spin cast thin films. To establish a link to optoelectronic properties, we measure the identified polymorphs by spectroscopic techniques and charge transport properties in field-effect transistors. Importantly, our data reveal that high charge transport and stronger light absorption are obtained from metastable polymorph I, characterized by continuous 1D-chain or multidimensional mesh-like aromatic structures and seemingly poor structural order along the π–π stacking direction. Concurrently with correlating the solid-state microstructure to the optoelectronic properties, we explore the impact of relevant processing variables i.e. the temperature –connected to postprocessing thermal treatments–, the solvent and the employment of co-solvent additives relative to the microstructure. Our data disclose that certain processing conditions yield a rich polymorphism in some of the NFAs. We anticipate that a precise identification and understanding of processing-structure-function relationship will allow the prediction of implications in the long-term stability of the devices.

4.3. Results

4.3.1. Polymorphs identification and characterization

The polymorphic phases in indacenodithienothiophene-based NFAs are investigated in 90 to 110-nm-thick films processed by spin coating 20 mg·mL^{-1} solutions at 2000 rpm, which are standard processing conditions in OSC device manufacturing [32,34] Phase I polymorphs are obtained from a CB/DIO solution while higher-temperature polymorphs are cast from CB solution (see Appendix B for Raman for trapped solvent (**Figure B-1**) and TGA for degradation (**Figure B-2**). We find that all indacenodithienothiophene-based NFAs exhibit polymorphism: Three different polymorphs are found in case of ITIC, denoted as phase I, phase II and phase III, while ITIC-M, ITIC-2F and ITIC-Th exhibit two polymorphs, namely phase I and phase II. Phase I polymorphs develop during casting under specific processing conditions (discussed in detail in Section 4.3.3) while phase II polymorphs (and phase III in ITIC) are obtained upon thermal treatment (not for ITIC-Th). For example, ITIC phase III develops at temperatures above 270 °C from phase I and at 220 °C from amorphous ITIC (**Figure 4.2**m). ITIC phase II polymorph is obtained by heating phase I at intermediate temperatures between phase I and phase III (**Figure 4.2**i). Lastly, Phase II polymorphs develop during heating ITIC-M, ITIC-2F and ITIC-Th films at respectively, 220 °C, 220 °C and 170 °C (ITIC-2F **Figure 4.2**j; ITIC-M **Figure 4.2**k; ITIC-Th **Figure 4.2**l). Such a rich polymorphism in NFAs with differences in the terminal acceptor groups, may be the consequence of different molecular interactions. Hence, the differences in the physicochemical characteristics of terminal groups (e.g., electronegativity, volume), resulting from the different chemical functionality, might alter the intermolecular packing and, eventually, the development of a diverse polymorph set. The Grazing incidence wide angle X-ay scattering (GIWAXS) patterns of the polymorphs found are presented in **Figure 4.2**, and the peak parameters are summarized in **Table 4.1**.

Ex-situ GIWAXS measurements of the different polymorphs found were carried out in order to study differences in packing. The GIWAXS patterns for Phase I forms (ITIC **Figure 4.2**a; ITIC-2F **Figure 4.2**b; ITIC-M **Figure 4.2**c; ITIC-Th **Figure 4.2**d) are characterized by a number

of intense diffraction maxima in the low-*q* region and rather diffuse peaks in the high-*q* region. Polymorphs II (for ITIC-M, ITIC-2F and ITIC-Th) and polymorph III (for ITIC) exhibit, in general, a higher amount of well-defined diffraction peaks compared to phase I forms, which highlights that phase II (for ITIC-M, ITIC-2F and ITIC-Th) and Phase III (for ITIC) lattices possess more symmetry elements and, likely, larger ordered domains than their phase I counterparts. **Figure 4.2** gathers all the unveiled polymorphs and **Table 4.1** the peak parameters of the indexed patterns. The crystalline coherence length of each reflexion was estimated with Scherrer equation.[144] A more precise development of how these polymorphs packed and procedure to identify them is explained in the following sections.

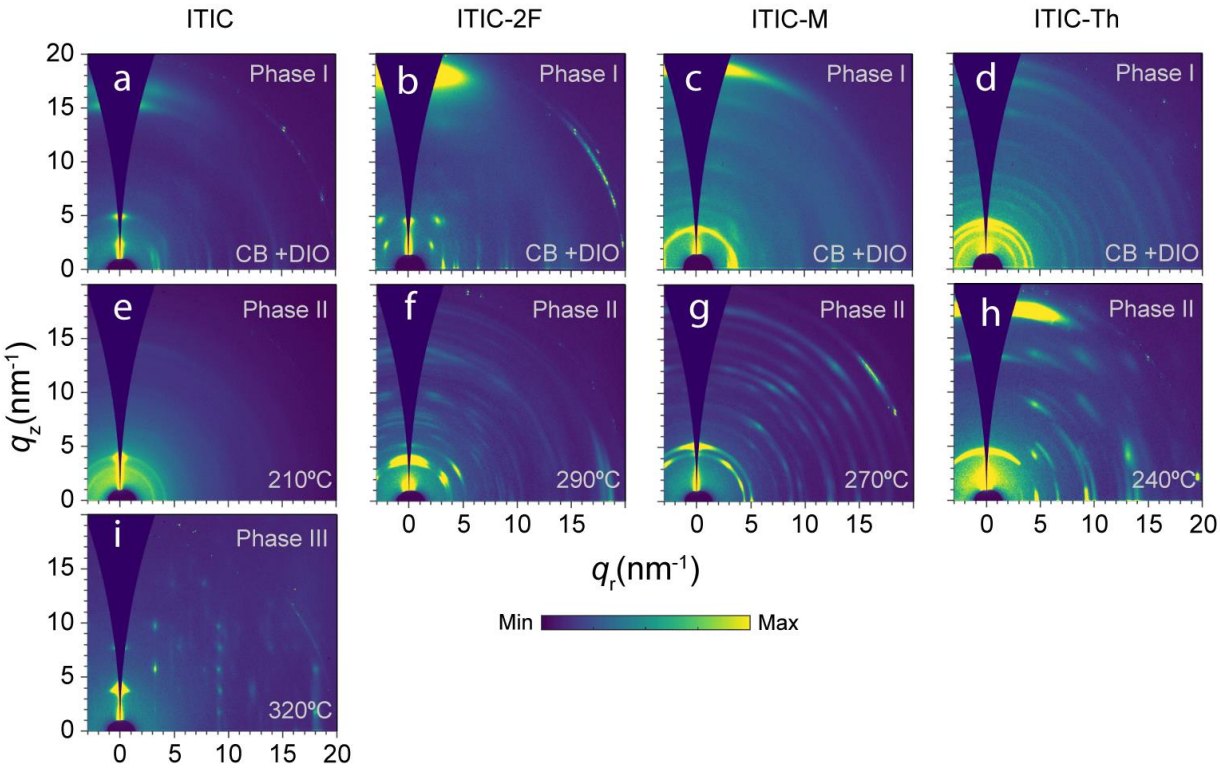

Figure 4.2 (a-i) 2D GIWAXS patterns for ITIC phase I (a), phase II (e) and phase III (i); ITIC-2F crystallized in phase I (b) and phase II (f); ITIC-M crystallized in phase I (c) and phase II (g); and ITIC-Th crystallized in phase I (d) and phase II (h). All phase I forms are produced by casting chlorobenzene (CB) solutions containing small amounts of DIO (0.5-1 %). Phases II and phase III are obtained by annealing the thin films at the temperatures indicated in each panel and cast from CB.

Table 4.1 Peak position and crystalline coherence length (CCL) values of the GIWAXS reflections for identified ITIC-X polymorphs.

NFA	Polymorphs	periodic aromatic-aliphatic packing		π-π peak	
		q(nm^{-1})	*CCL (nm)*	*q(nm^{-1})*	*CCL (nm)*
ITIC	Phase I	3.2	23.2		
		3.6	23.8	15.5	4.0
		4.7	14.7	17.1	5.1
		5.1	11.3		
	Phase II	3.2	24.0	/	/
		4.1	18.1		
	Phase III	4.1	11.7	18.1	5.9
ITIC-2F	Phase I	2.5	64.9	18.1	3.5
		3.2	29.7		
		4.2	24.4		
		4.6	16.1		
	Phase II	3.7	37.2	18.5	16.7
		4.1	23.4		
ITIC-M	Phase I	3.0	36.5	18.6	5.8
		3.8	15.5		
	Phase II	4.4	23.4	18.0	6.6
		5.3	15.7		
ITIC-Th	Phase I	2.8	20.2	17.3	7.2
		3.8	18.8		
		4.4	18.2		
	Phase II	4.7	16.1	17.9	7.4

4.3.1.1. ITIC

To identify the different polymorphs of ITIC, a 20 mg·mL^{-1} solution in CB was first spun cast on top of a silicon substrate. To assure a fair comparison, the same film was in-situ annealed at depicted temperatures (**Figure 4.3**), then cooled down to room temperature and finally measured. Patterns of the film annealed at different temperatures are exhibited together with the out-of-plane and in-plane integrated profiles (**Figure 4.3**).

PHASE I (**Figure 4.2**a and **Figure 4.3**a): In agreement with Mai et al.,[195] we interpreted this pattern as follows: For ITIC as spun on SiO_2, a broad diffraction maxima at scattering vector (q) equal to 3.2 nm^{-1} (d-spacing = 1.90 nm) originates from the backbone periodicity along the in-plane direction. We also found some multiple diffraction peaks in the low-q region. Among them, a sharper peak at q = 5.1 nm^{-1} (d-spacing = 1.21 nm). The broad maxima around q ~ 17 nm^{-1} (d-spacing ~ 0.36 nm) can be indexed as the lamellar peak and the π-π stacking peak, respectively. Moreover, we find that Phase I is favoured if a small amount of 1,8-diiodooctane (DIO), an additive frequently used during processing of OSCs, is added to the casting solution (**Figure 4.2**a) The diffuse scattering from π-π planes indicates largely disordered molecular packing along this direction. However, all the reflections are localized in relatively narrow range of azimuthal angles, denoting a preferred molecular orientation in crystals and disordered glassy regions.

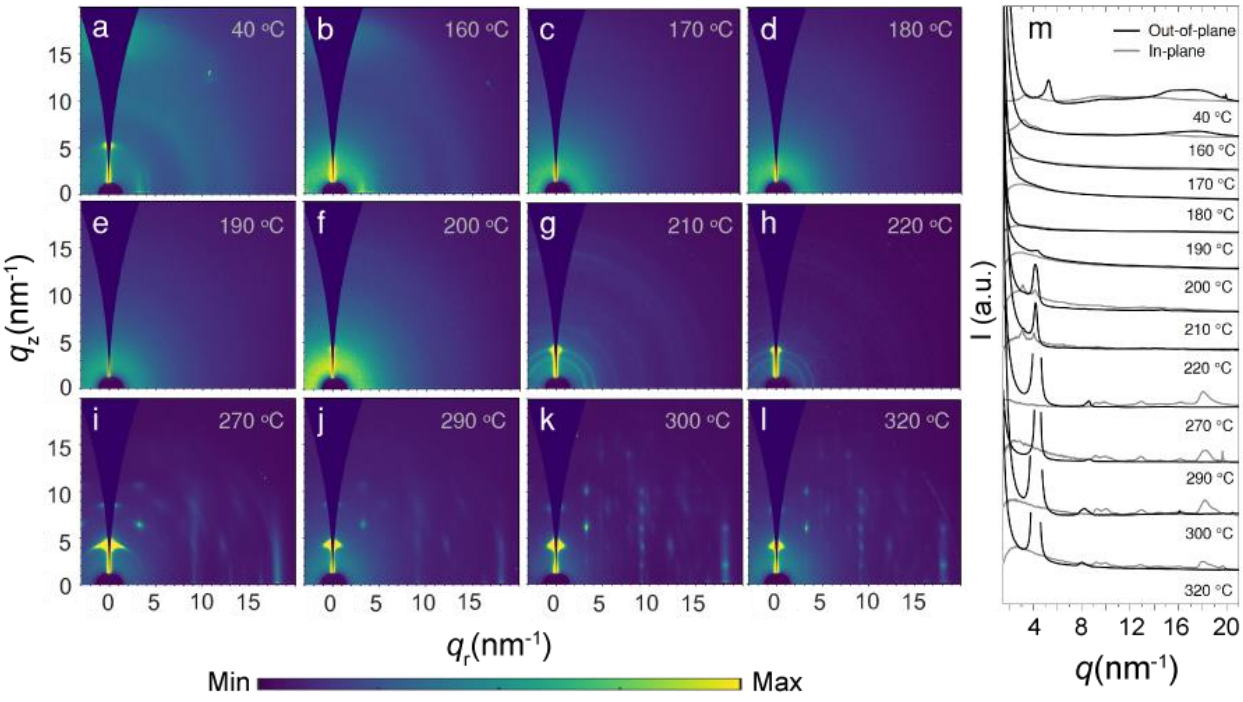

Figure 4.3 2D GIWAXS patterns after *ex situ* annealing the ITIC samples at specified temperature during 5 min, followed by a rapid cooling to ambient temperature at 50 ºC·min^{-1}. Annealing temperatures: (a) 40 °C, (b) 160 °C, (c) 170 °C, (d) 180 °C, (e) 190 °C, (f) 200 °C, (g) 210 °C, (h) 220 °C, (i) 270 °C, (j) 290 °C, (k) 300 °C and (l) 320 °C. (m) Out-of-plane and in-plane scattering profiles.

PHASE II (**Figure 4.2**e and **Figure 4.3**g): Phase II is characterized by two main diffraction maxima at q = 3.2 nm^{-1} and q = 4.1 nm^{-1} in addition to weak ring-like isotropic signals at larger q-values.

PHASE III (**Figure 4.3**l): Compared to phase I and phase II, the patterns for the phase III exhibit a higher number of well-defined scattering features. The main reflection at q~ 4.1 nm^{-1} should be originated from the lamellar packing along the out-of-plane direction, while the reflection at q = 18.1 nm^{-1} can be indexed as the edge-on π-π stacking with a distance of 0.34 nm, thus slightly tighter than in the low-temperature phase I. The scattering peaks of phase III are also significantly narrower than those of the phase reflecting larger CCL values and mixed indexed peaks appear. Interestingly, because there is a remarkably good agreement between the peak positions of phase III with the lattice reported by Aldrich et al.,[216] we can hypothesize that this is a triclinic brick-wall structure in which ITIC backbones are separated by their alkyl substituents. Interestingly, we observe that already at 270 ºC the formation of Phase III is observed; however, higher order reflexion and narrower diffraction peaks are observed at higher annealing temperatures. We would like to mention that we also tried to grow single crystals from CB to characterize the lattice in phase I and phase II with no success.

4.3.1.2. ITIC-2F

For ITIC-2F polymorph identification, ITIC-2F was spun cast into a silicon substrate from a CB solution (Note that phase I is only obtained from CB/DIO solution (see Section 4.3.3)). Again, same film was annealed at depicted temperatures and measured at room temperature (**Figure 4.4**).

PHASE I (**Figure 4.4**a): Phase I pattern shows well-defined reflections. In addition to the lamellar peak at q = 4.6 nm^{-1} (d-spacing = 1.36 nm) and a diffuse π-π stacking peak at q~ 18 nm^{-1} (d-spacing ~ 0.35 nm), this pattern shows further reflections at q= 3.2 nm^{-1} (d-spacing = 1.96 nm) along the in-plane and at circa 45° from the equator that might be related to the backbone periodicity. Similar to ITIC, Phase I from ITIC-2F depicts multiple diffraction peaks in the low-

q region. Interestingly, Aldrich et al. reported a single-crystal structure for ITIC-2F that included both face-to-face and edge-to-face molecular packing,[216] which might agree with the double orientation of molecular backbones found for both crystalline forms.

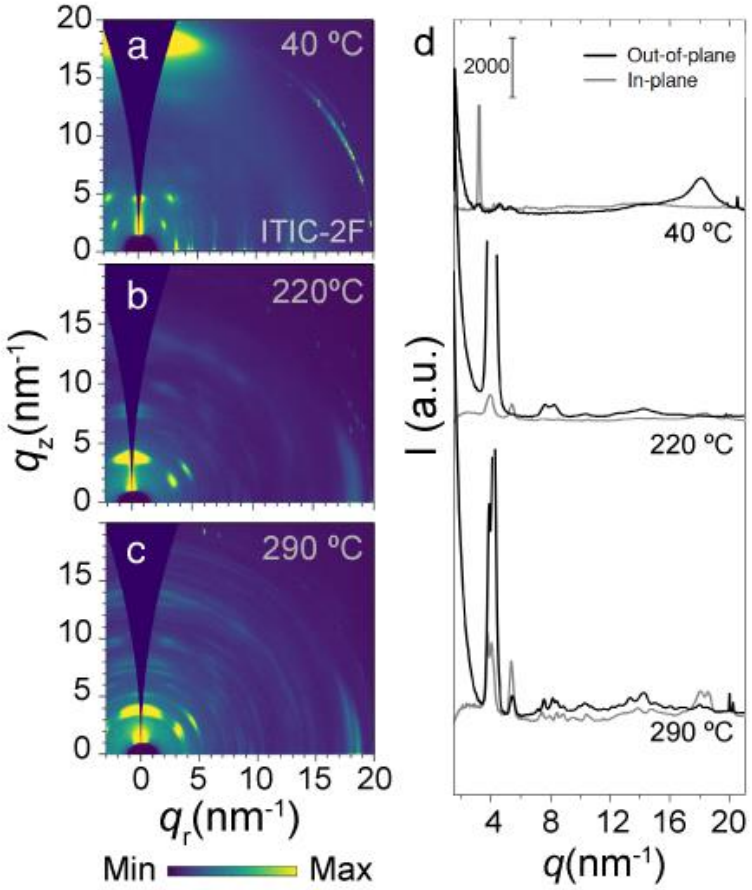

Figure 4.4 2D GIWAXS patterns after *ex situ* annealing the sample at specified temperature during 10 min, followed by a rapid cooling to ambient temperature at 50 ºC·min^{-1}. ITIC-2F: (a) cast from CB/ DIO and annealed at 40 °C, (b) cast from CB and annealed at 220 °C and (c) cast from CB and annealed at 290 °C (d) Out-of-plane and in-plane scattering profiles

PHASE II (**Figure 4.4**c): The intense peak at q = 4.1 nm^{-1} (d-spacing = 1.53 nm) along the out-of-plane direction and at approximately 45° from the equator is related here to the lamellar packing. The reflection at q = 18.5 nm^{-1} (d-spacing = 0.35 nm) along the in-plane direction is ascribed to the π-π stacked planes. On annealing, the peaks intensify and mixed index peaks appear. Interestingly, the lamellar peak in the ITIC-2F crystal appears at lower *q*-values than

those of ITIC and ITIC-M (see the **Table 4.1**), suggesting that the crystal lattice is significantly expanded in the former. With increasing annealing temperature, we did not observe the development of a third polymorph. Simply, we observe a peak narrowing and the appearance of new reflections due to a higher crystallinity.

4.3.1.3. ITIC-M

ITIC-M was spun cast into a silicon substrate from a CB solution (Note that phase I is only obtained from CB/DIO solution (see Section 4.3.3)). Again, same film was annealed at depicted temperatures and measured at room temperature (**Figure 4.5**).

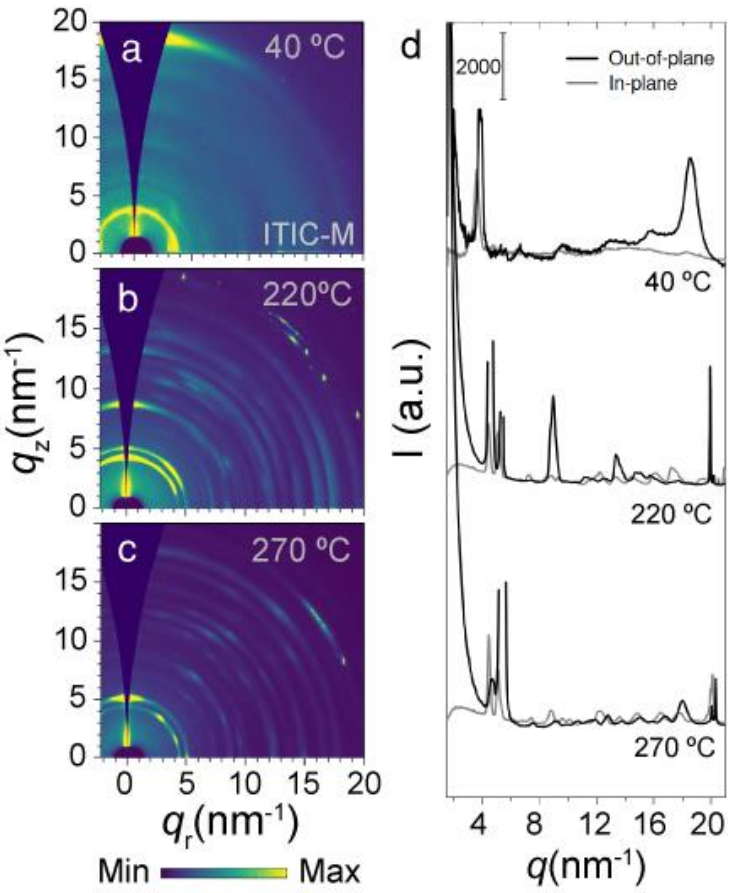

Figure 4.5 2D GIWAXS patterns after *ex situ* annealing the sample at specified temperature during 10 min, followed by a rapid cooling to ambient temperature at 50 ºC·min^{-1}. ITIC-M: (a) cast from CB/ DIO and annealed at 40 °C, (b) cast from CB and annealed at 220 °C and (c) cast from CB and annealed at 270 °C (d) Out-of-plane and in-plane scattering profiles

PHASE I (**Figure 4.5**a): Interestingly, the position of the main peak q = 3.8 nm^{-1} (d-spacing = 1.69 nm) –most probably associated with the lamellar packing— does not match with that of the high-temperature crystalline form, indicating that casting from CB/DIO results in the formation of either a low-crystalline metastable form in ITIC-M similarly to phase I in ITIC or a rather well-ordered mesophase. Moreover, the diffraction maxima at scattering vector (q) equal to 3.0 nm^{-1} (d-spacing = 2.1 nm) originates from the backbone periodicity along the in-plane direction, while maxima around q~ 18.6 nm^{-1} (d-spacing ~0.34 nm) can be indexed as the π-π stacking peak.

PHASE II (**Figure 4.5**c): Well-defined reflections appeared at 240 °C [at q = 4.4 nm^{-1} (d-spacing = 1.40 nm) and q = 5.3 nm^{-1} (d-spacing = 1.19 nm)] confirming that ITIC-M cold crystallizes at that temperature. Several mixed index peaks off the q_z and $q_{x,y}$ axes appear as well. The texture increases with temperature, until reaching uniaxial crystal orientation in which the lamellar planes lay parallel to the substrate (peak positions are summarized in **Table 4.1**).

4.3.1.4. ITIC-Th

The procedure to identify the different ITIC-Th polymorphs was the same as presented above for the other ITIC derivatives (see Section 4.3.3). It is important to emphasize that ITIC-Th seems to differ from the other NFAs possibly because the different chemical moiety is in the central building block and not in the terminal groups as for ITIC-2F and ITIC-M. See section 4.3.5 for a more detailed description.

PHASE I (**Figure 4.6**): The GIWAXS pattern for the spun-cast ITIC-Th film allowed also to resolve the reflections associated to the lamellar order at q= 4.4 nm^{-1} (d-spacing = 1.43 nm) and a diffuse π-π stacking maximum at ca. q = 17.3 nm^{-1} (d-spacing = 0.35 nm) of the low temperature crystal form. Unlike the low-temperature Phase I of ITIC, ITIC-M, and ITIC-2F, the GIWAXS patterns for ITIC-Th Phase I do not exhibit an intense and broad π–π peak. This observation agrees with the packing motif reported for β-ITIC-Th single crystals.[195]

PHASE II (**Figure 4.6**b): The pattern is indexed as follows: the intense peak at q= 4.7 nm^{-1} (d-spacing = 1.34 nm) is associated with the lamellar packing and the reflection at q = 17.9 nm^{-1} (d-spacing = 0.35 nm) corresponds to the scattering from the π-π stack. On annealing, the (*h*00) peaks sharpen and intensify, and mixed index peaks appear. Contrarily to the other ITIC derivatives analysed above, the π-π stacking peak of ITIC-Th appeared in the out-of-plane direction, which denote a noticeable fraction of face-on crystals and likely related to the reported α-ITIC-Th lattice.[217]

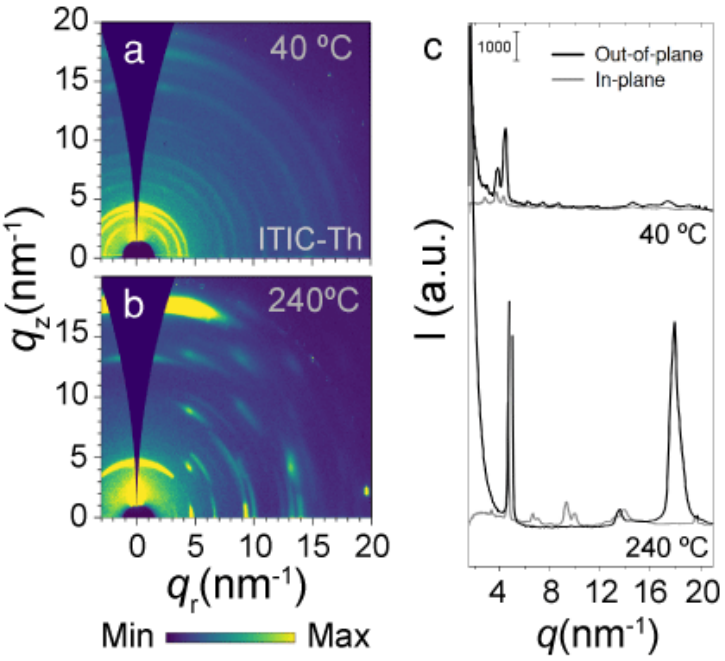

Figure 4.6 2D GIWAXS patterns after *ex situ* annealing the sample at specified temperature during 10 min, followed by a rapid cooling to ambient temperature at 50 ºC·min^{-1}. ITIC-Th: (a) cast from CB/ DIO and annealed at 40 °C, and (b) cast from CB and annealed at 240 °C. (c) Out-of-plane and in-plane scattering profiles

4.3.2. Phase I Polymorphs

The GIWAXS patterns found for the phase I polymorphs show comparable patterns characterised by multiple diffractions in the low-q region (**Figure 4.2**a-d). These large d-spacing symmetry planes suggest that ITIC based NFAs Phase I pack into a 1D-chain or multidimensional mesh-like structures, as those proposed previously for NFA single crystals.[195,215,217–222] Interestingly,

these packing motifs are expected to exhibit a high magnitude of electron transfer integral and therefore efficient charge transfer between molecules. These mesh-like structures feature continuous aromatic packing that are separated by aliphatic chains[215,217,218,220,221,223], which agrees with the presence of multiple diffraction peaks in the low-q region.[221] Moreover, we further support these observation with the π–π stacking diffraction that, interestingly, is oriented along the same direction (i.e., the out-of-plane direction) as the main aromatic–aliphatic periodicity peaks (at least for low-temperature phases in ITIC, ITIC-M, and ITIC-2F). Having aliphatic groups in ITIC-based NFAs pendant from the central building blocks, terminal acceptor groups are free to π–π stack with further terminal groups promoting continuous aromatic structures that result in 1D- or multidimensional structures.

4.3.3. Screening the effect of casting solvent and additive (processing-structure relationship)

The microstructure of ITIC films spin cast from CB –i.e. conditions that are typically employed in OSC fabrication– comprises phase I crystals, which are proven to be metastable. This suggests that the processing stage plays a major role in the structure development of ITIC. As such, in order to gain further knowledge about the origin of phase I, we went on to investigate whether phase I is related to the solvent used. Solvent induced polymorphism is a well-known phenomenon in organic compounds –including some organic semiconductors like TES-ADT[198] and TIPS-pentacene[199] —and has been rationalized with the existing connection between the energy barrier for the nucleation of crystals and the solvent-polymorph interfacial free energy.[202]

2D GIWAXS patterns for the spun-cast ITIC films from some typical solvents employed in OSC device processing [32–34,172] o-Xy,[206] CF[35] and DCM are shown in **Figure 4.7**. To assure a fair and simple comparison, the films were fabricated using equal concentration (20 mg·mL^{-1} solution) and spinning rate (2000 rpm). As it can be observed in the scattering profiles, films processed from CB and *o*-DCB exhibit the diffraction peak at q = 5.2 nm^{-1} characteristic of phase

I crystals. Moreover, the broad peak located at q ~17 nm^{-1} can be indexed as π-π planes oriented in the same out-plane direction. The scattering profiles of samples processed from *o*-Xy, CF and DCM revealed fairly amorphous films, probably because the higher vapor pressure of these solvents (at least those of CF and DCM) induced fast solvent evaporation and ITIC vitrified before crystallization.

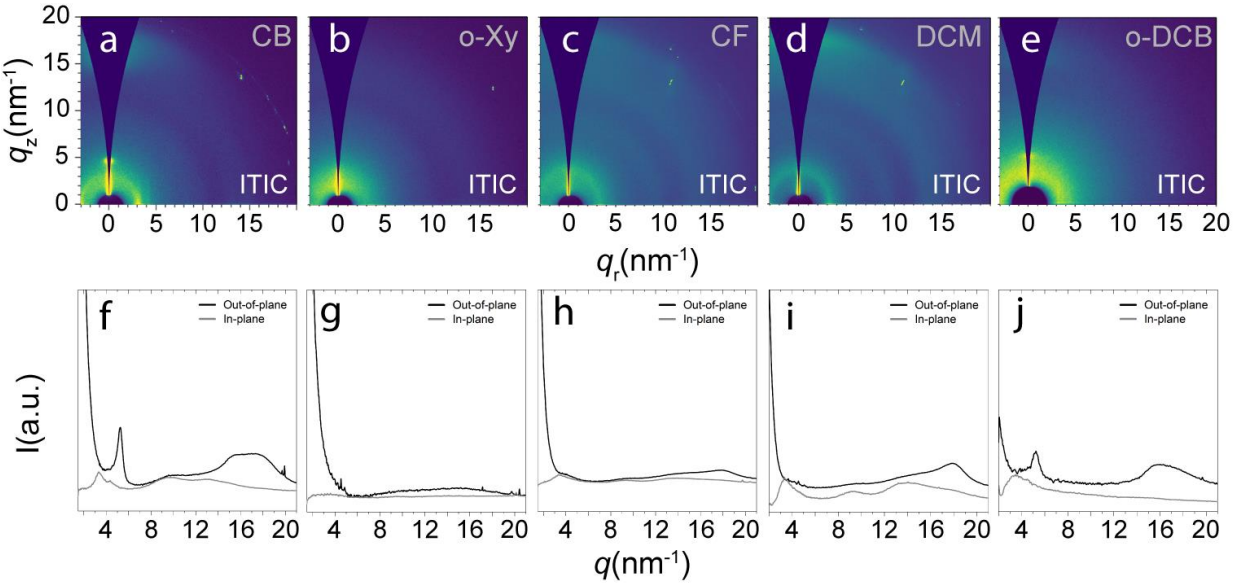

Figure 4.7 2D GIWAXS patterns of ITIC cast from specified solvent: (a) CB, (b) o-Xy, (c) CF and (d) DCM. Out-of-plane and in-plane scattering profiles of ITIC cast from (e) CB, (f) o-Xy, (g) CF and (h) DCM.

Having characterized the microstructure of as-cast ITIC film, we tried to gain further structural information of ITIC thin films by monitoring the evolution of the microstructure with temperature. In-situ temperature dependent GIWAXS experiments of ITIC spun cast from each solvent, provides valuable information to understand the effect of casting solvent plus the post-processing thermal treatments that are frequently applied in NFA-based OSC.[66,70] **Figure 4.8** gathers the 2D GIWAXS patterns azimuthal integrations recorded during a heating process at 10 °C·min^{-1} of the same films analyzed by ex-situ GIWAXS experiments. As displayed in **Figure 4.8** contour plots, a low-crystalline phase I polymorph or an amorphous film is achieved when ITIC is cast on top of the silicon wafer (as previously observed in **Figure 4.7**). Our results show

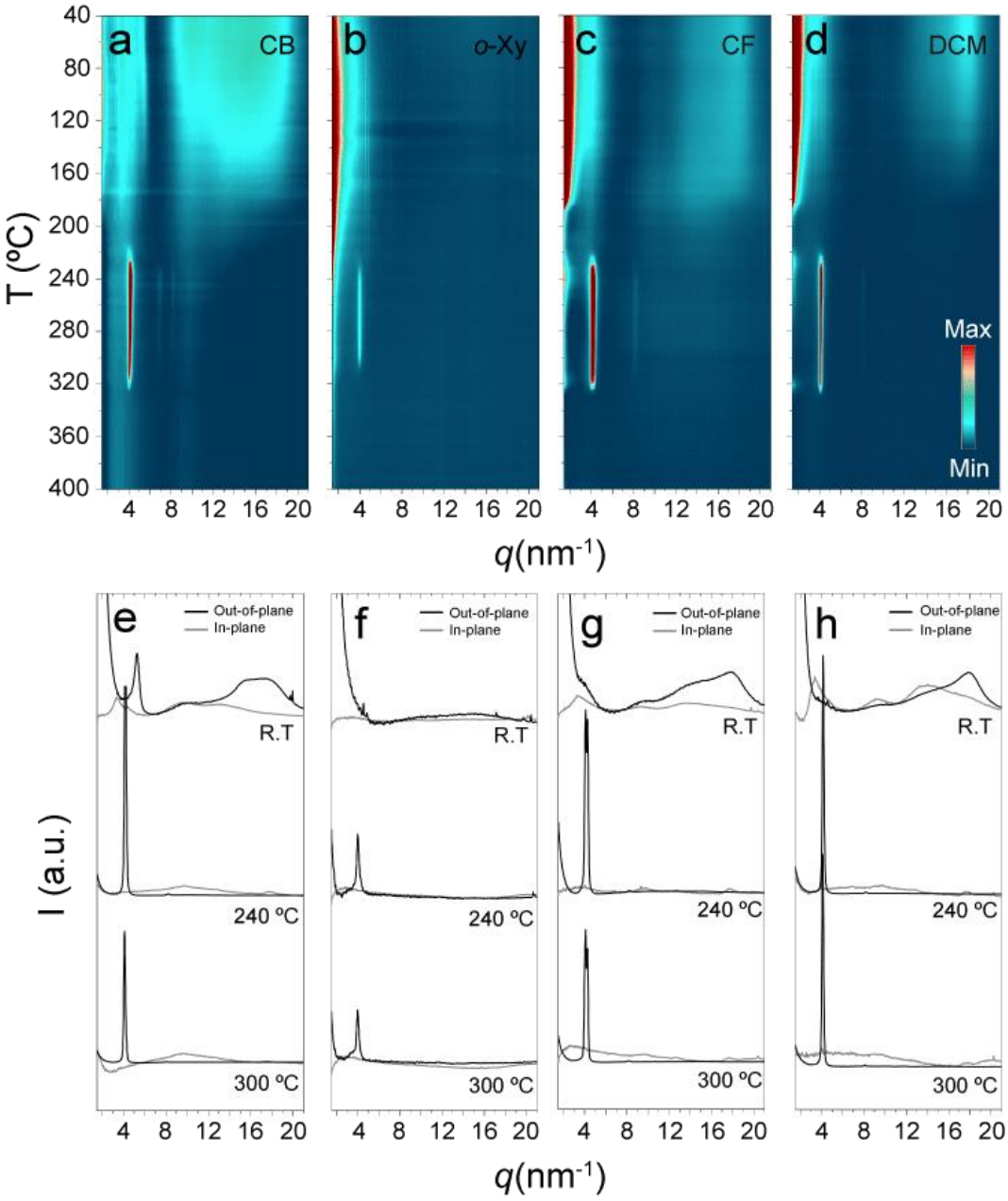

Figure 4.8 (a-d) Contour plots for the cake-integrations of the 2D-GIWAXS patterns along the out-of-plane direction (cake width was 5°) for ITIC films spin cast from (a) CB, (b) o-Xy, (c) CF and (d) DCM collected during a heating ramp from 40 °C to 400 °C at 10 °C·min^{-1}. (e-h) Out-of-plane (black line) and in-plane (grey line) scattering profiles at relevant temperatures for ITIC spin cast from (e) CB, (f) o-Xy, (g) CF and (h) DCM.

a phase I that remains stable until it reaches approximately 150°C. Above a certain temperature, a progressive decrease of reflexion intensities and diffused scattering is observed, until the development of phase III polymorph accompanied by the appearance of new reflexions (**Table**

4.2). These results are consistent with a glass transition process taking place in that temperature range (see Section 4.3.4).[49] It is worth noting, that no phase II is developed in ITIC during heating and ITIC is directly transitioned into Phase III. Subsequently, we state that phase III is a common high-temperature phase in all examined samples. The GIWAXS peak positions and CCL values for the spun cast samples at relevant temperatures are summarized in **Table 4.2**.

Table 4.2 Peak parameters of the identified polymorphs: Peak position and crystalline coherence length (CCL) values of the GIWAXS peaks for ITIC films spin cast from different solvents

Polymorphs	Solvents	Lamellar peaks		Backbone peak		π-π peak	
		q(nm^{-1})	*CCL (nm)*	*q*(nm^{-1})	*CCL(nm)*	*q*(nm^{-1})	*CCL(nm)*
Phase I	CB	5.2	10.7	3.3	9.4	18	4.0
	o-Xy	/	/	/	/	/	/
	CF	/	/	3.5	4.6	/	/
	DCM	/	/	3.2	4.1	18.7	2.8
Phase III	CB	4.1	11.7	3.1	24.0	18.1	5.9
	o-Xy	4.1	28.7	/	/	/	/
	CF	4.1	15.3	/	/	/	/
	DCM	4.1	35.3	/	/	/	/

To shed further light on the effect of processing solvents on the microstructure of ITIC, the impact of adding small amounts (0.25 %, 0.5 % and 1%) of the high-boiling-point co-solvent 1,8-diiodooctane (DIO) in the CB solution[32–34,68] was explored. Shown in **Figure 4.9** are the 2D GIWAXS patterns of spin cast ITIC films thus prepared (20 $mg \cdot mL^{-1}$ solution) and the corresponding scattering profiles, respectively. Overall, the addition of DIO enhances the fraction of phase I crystals in the films (**Figure 4.9**), especially when 1% DIO is added, which is in line with previous reports.[115,213] To correlate the effect of processing the film from a solution containing small amount of a high-boiling-point co-solvent, films spin cast from *o*-Xy/DIO were examine (**Figure 4.10**). The use of these non-halogenated solvent has gain attention because it is considered more environmentally friendly and has proven its worth in the development of OPV

technology.[98] Likewise, the pattern and scattering profiles confirmed that films with DIO resulted in larger and coarser crystalline domains.

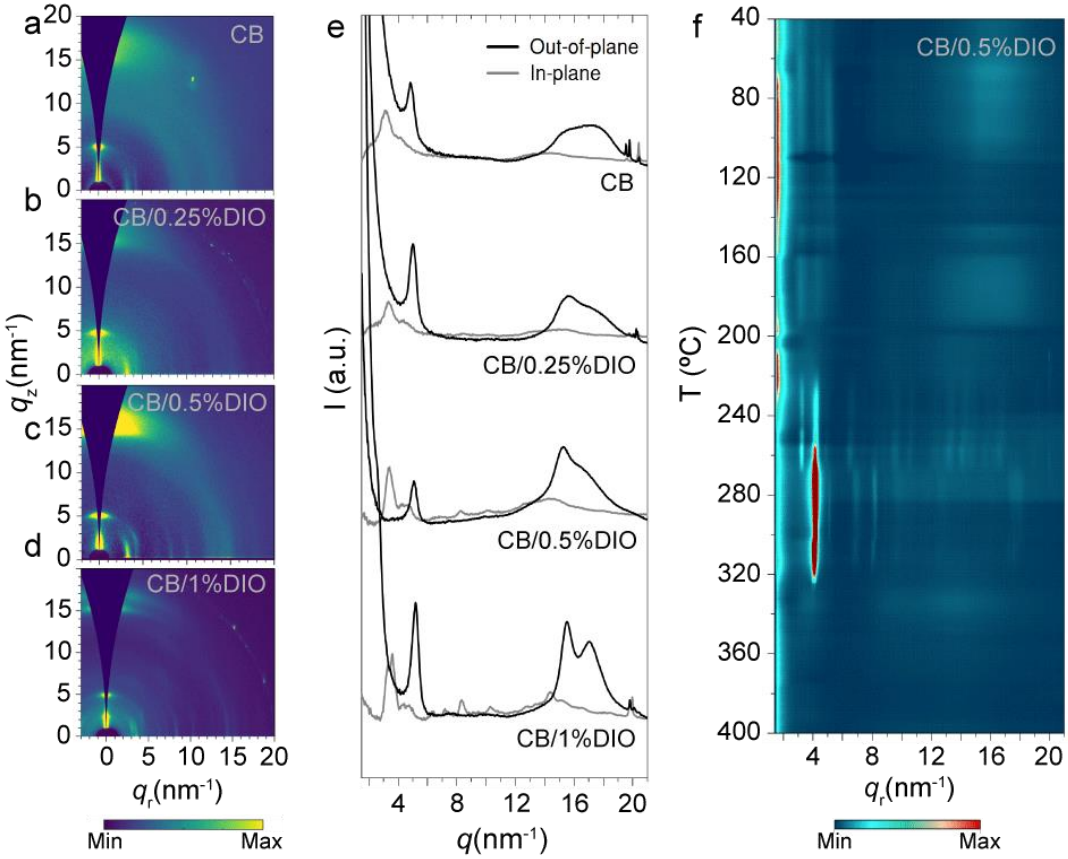

Figure 4.9 (a-d) Ex situ, room temperature 2D GIWAXS patterns for ITIC spin coated from CB solutions containing (a) 0 %, (b) 0.25 %, (c) 0.5 % and (d) 1 % of the high-boiling point co-solvent 1,8-diiodooctane (DIO). (e) Out-of-plane (black line) and in-plane (grey line) scattering profiles extracted from the patterns.(f) Contour plots for the cake-integrations of the 2D-GIWAXS patterns along the out-of-plane direction (cake width was 5°) for ITIC films spin cast from CB with 0.5% DIO.

Additionally, the thermotropic behaviour by in-situ temperature-dependent GIWAXS experiments of ITIC films cast from both CB and *o*-Xy solvents in presence of 1% DIO (see **Figure 4.9**f and **Figure 4.10**f) were carried. Analogously, the phase I polymorph was identified immediately after casting the solution over the silicon. Upon heating, this phase I remains stable until approximately 160 °C, at which point the reflections become diffuse and gradually lose their intensity. Hereby, we observe that phase II develops above 200 °C to later transform into phase

III, indicating that the formation of phase II crystals is conditioned by the previous presence of phase I crystals. Indeed, when ITIC is processed from conditions not leading to the development of a well-ordered phase I (e.g., no DIO is used), Phase II is absent and ITIC is directly transitioned into Phase III during heating as observed in **Figure 4.8**. The GIWAXS peak positions and CCL values for the spin cast samples in presence of DIO at relevant temperatures are summarized in **Table 4.3**. Thus, we have probed that the presence of a crystalline phase I is crucial for the formation of phase II, while phase III is formed from either ordered or more disordered phases.

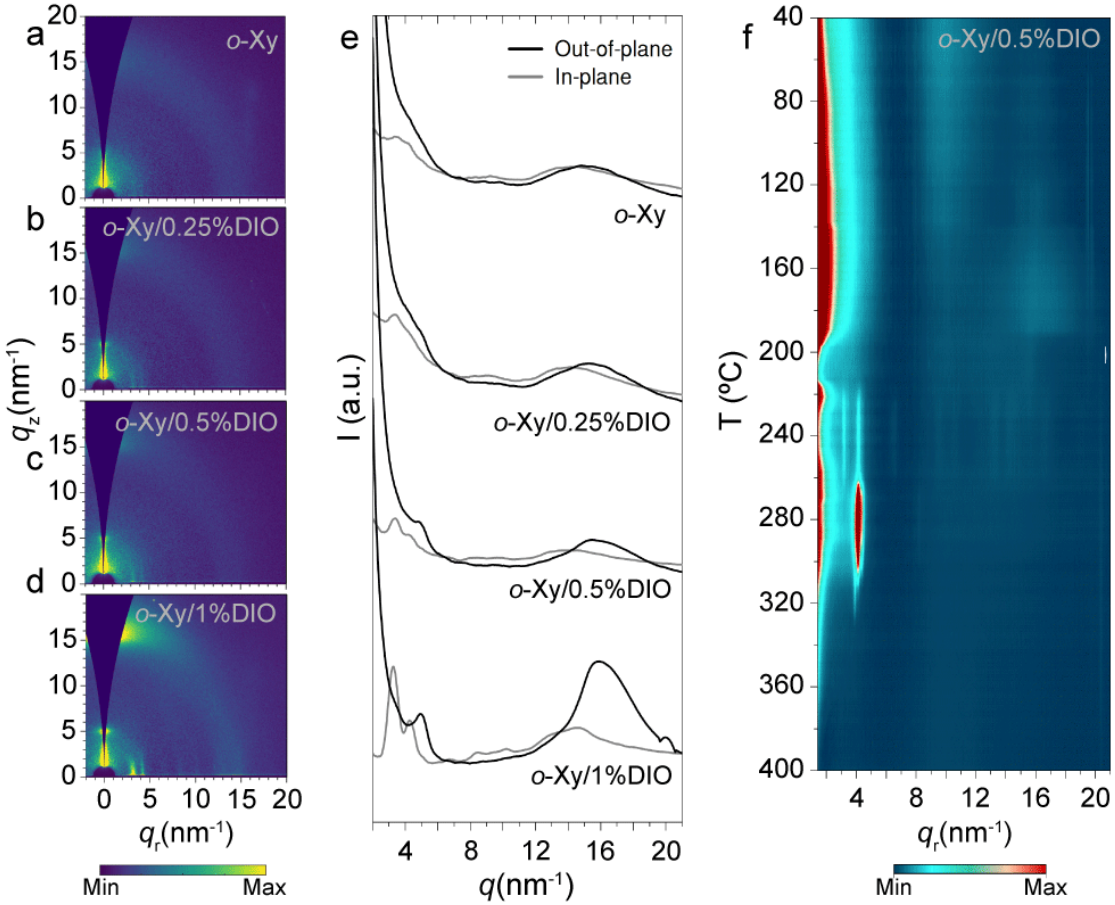

Figure 4.10 (a-d) Ex situ, room temperature 2D GIWAXS patterns for ITIC spin coated from o-Xy solutions containing (a) 0 %, (b) 0.25 %, (c) 0.5 % and (d) 1 % of the high-boiling point co-solvent 1,8-diiodooctane (DIO). (e) Out-of-plane (black line) and in-plane (grey line) scattering profiles extracted from the patterns.(f) Contour plots for the integrations of the 2D-GIWAXS patterns along the out-of-plane direction for ITIC films spin cast from CB with 0.5% DIO.

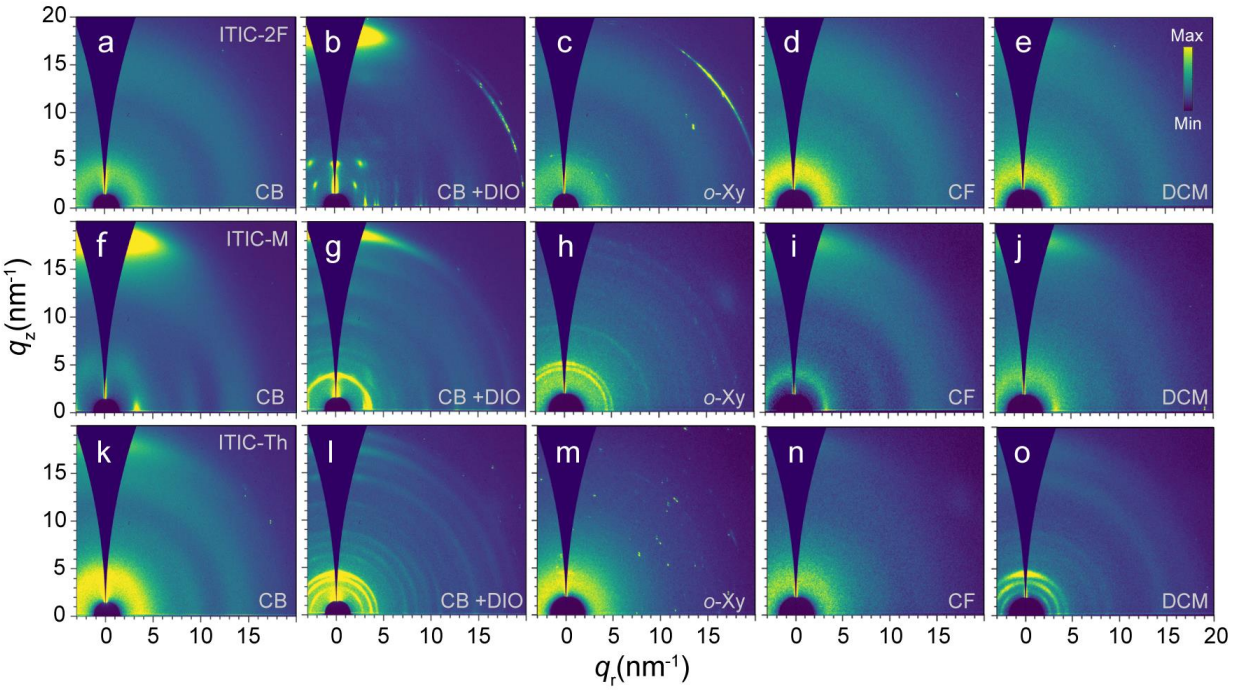

Figure 4.11 2D GIWAXS patterns of ITIC derivatives cast from specified solvent: ITIC-2F cast from (a) CB, (b) CB + DIO, (c) o-Xy, (d) CF and (e) DCM. ITIC-M cast from (f) CB, (g) CB + DIO, (h) o-Xy, (i) CF and (j) DCM. ITIC-Th cast from (k) CB, (l) CB + DIO, (m) o-Xy, (n) CF and (o) DCM.

Table 4.3 Peak parameters of the identified polymorphs: Peak position and crystalline coherence length (CCL) values of the GIWAXS peaks for ITIC films spin cast from chlorobenzene and o-xylene with 1,8-diiodoctane, DIO.

Polym.	Solvents	Lamellar peaks		Backbone peak		π-π peak	
		q(nm^{-1})	*CCL* (nm)	*q*(nm^{-1})	*CCL* (nm)	*q*(nm^{-1})	*CCL* (nm)
Phase I	CB/DIO	5.2	10.7	3.2	26.1	17.1	5.1
	o-Xy/DIO	5.1	7.4	3.2	8.8	16.0	1.7
Phase II	CB/DIO	4.2	16.8	3.2	30.1	/	/
	o-Xy/DIO	4.1	23.6	3.1	25.9	/	/
Phase III	CB/DIO	4.1	28.8	/	/	17.6	18.6
	o-Xy/DIO	4.1	30.4	/	/	/	/

To generalize the effect of the processing solvent with the metastable phase I development in the indacenodithienothiophene-based NFAs, we checked by GIWAXS scattering the effect of different casting solvents within the phase I of the different derivatives. Contrary to ITIC, the three derivatives give rise to largely amorphous films in the presence of chlorobenzene. Moreover, 2D GIWAXS pattern from **Figure 4.11** demonstrate that the molecular order substantially increases when the film is processed in presence of DIO, consistent with the effect observed for ITIC. ITIC-2F and ITIC-M films spun cast from o-Xy, CF and DCM depicted rather amorphous patterns. Interestingly, ITIC-Th showed neat reflections when is spun cast from DCM. Spin coating ITIC-Th in o-Xy, and CF resulted, on the contrary, in amorphous films.

Altogether, we have identify and characterize by means of ex-situ and in-situ GIWAXS the rich polymorphism of a set of non-fullerene acceptor based on indacenodithienothiophene. However, films have demonstrate to present large amount of disorder glassy phase that needs to be understood.

4.3.4. Glassy phases

The microstructure of spun cast ITIC comprises large amount of disordered glassy phase, which must also be characterized in order to have a full picture of the microstructure of the material. To achieve so, we probed the thermal behavior of the glassy phase via the analysis of the enthalpy recovery by fast scanning calorimetry (FSC). The methodology employed,[136] is described in Chapter 2 Section 2.3.1.1. Briefly, we followed the enthalpic recovery attributed to the glassy state along different temperatures to determine the onset glass transition temperature e.g. the $T_{g,onset}$. Interestingly, the approach developed by Cangialosi et al.[135,136] allowed us to measure thin films processed and spun cast as the films measured by GIWAXS.

Shown in **Figure 4.12**a are the heat flow rate (W) heating scans (conducted at 4000 °C·s^{-1}) for ITIC thin films deposited by spin coating (2000 rpm from 20 mg·mL^{-1} CB solution) onto the FSC chip sensors. Blue and green lines correspond to the W for non-aged films and films aged

for 1h at the indicated ageing temperatures, T_a, respectively. Endothermic overshoots due to the enthalpy recovery are clearly visible after ITIC was aged at temperatures between 90 and 180 °C, which highlights that at least a fraction of ITIC is in the glassy state in that temperature range. The plot of the amount of relaxed enthalpy (ΔH) vs T_a (lower panel in **Figure 4.12**b) shows that the relaxed enthalpy equals to zero when samples are aged at temperatures above 184 °C, indicating that 184 °C corresponds to the first temperatures at which ITIC starts to vitrify upon cooling at 4000 °C·s^{-1} (i.e. the $T_{g,on}$).

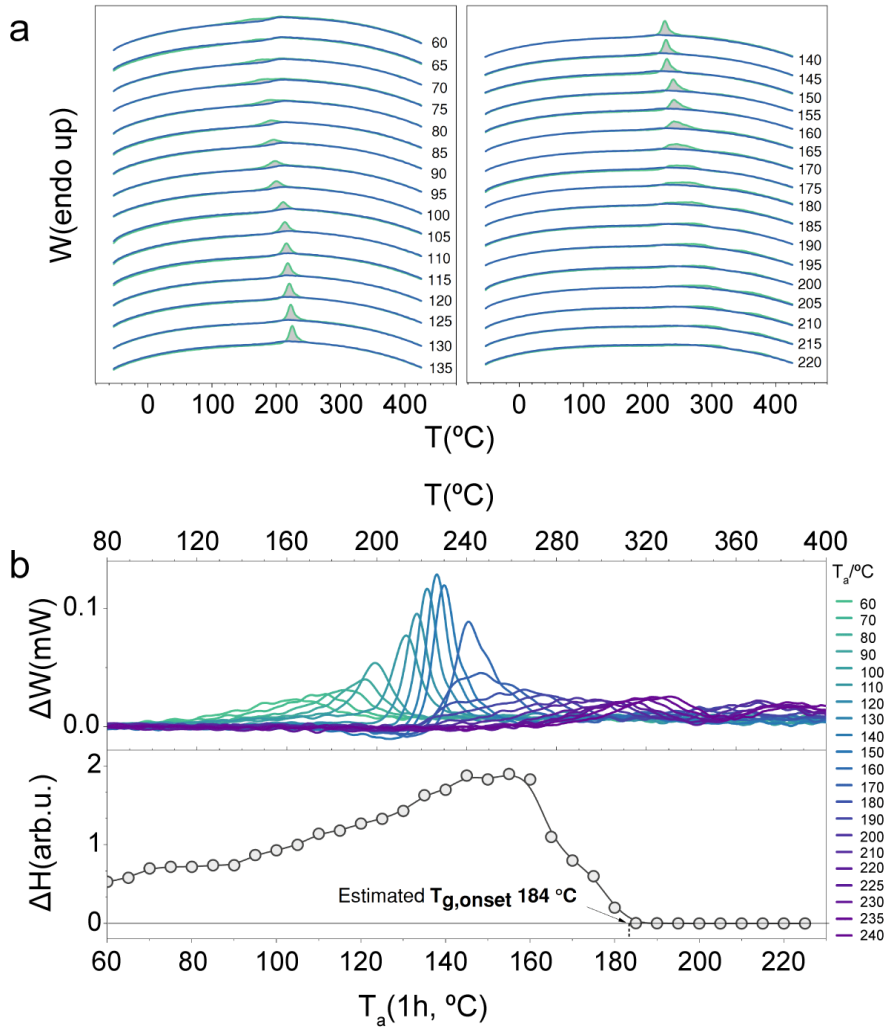

Figure 4.12 (a) FSC heat flow rate (W) scans (at 4000 °C·s^{-1}) for ITIC thin films. Blue and green lines correspond to the calorimetric signals for non-aged ITIC and ITIC aged for 1h at the indicated temperatures, respectively. (b) Upper panel: excess of heat flow rate (ΔW, i.e. the difference between the W of the samples aged for 1h and the W of the reference) due to the enthalpy recovery plotted against the scanned temperature for each ageing temperature, T_a.

We recall that our data shown above evidenced that the metastable phase I transformed into phase II at temperatures below 200 °C, hence the same temperature region where the glass transition of ITIC is detected. Thus, in order to validate that the endothermic peak found in our FSC analysis is due to the aging of the ITIC glass, we monitored the time evolution of the overshoot at a temperature below the $T_{g,on}$, e.g. T_a = 120 °C. This was achieved conducting isothermal relaxation experiments (see section 2.3.1.1). The upper panel of **Figure 4.13**a shows how ageing ITIC at 120 °C results in the progressive increase of the enthalpy recovery peak as increasing the ageing time, t_a. Because the integration of this peak should provide an enthalpy value that is proportional to the advance of the physical process that is occurring in the material (enthalpy recovery, crystallization, etc.), one can fit the data to a Kohlrausch-Williams-Watts (KWW) law[224] (equation 4.1) and calculate the exponent β, which will inform about the nature of such physical process:

$$\Delta H = a - (a - b) \cdot exp(-t/\tau) \cdot \beta \qquad \textbf{(Equation 4.1)}$$

The value of the β exponent was in this case 0.30, which is a typical value for the glassy dynamics involved in the aging of glasses[225] and moreover incompatible with the Avrami-like kinetics expected for crystallizations, for which $\beta > 0.5$ could be expected. This would confirm that the endothermic peaks above analysed are indeed associated with the aging of the ITIC glassy phase. We note in addition that the value of the $T_{g,onset}$ found in these experiments agrees well with the step-like jump of the W observed in the reference heating scan.

Oddly, ageing ITIC at temperatures below 90 °C results in the appearance of a different endothermic signal in the W scans **Figure 4.13**b), whose associated enthalpy scales with t_a according to the KWW law with a stretching exponent $\beta = 0.34$, thus again compatible with glassy dynamics. As a result, we interpret this signal as originated by a second mechanism of equilibrium recovery of the glass below the T_g. Indeed, this partial equilibration of the glass occurs in the timescale of days at 20 °C, which may affect the morphological stability of bulk heterojunctions.

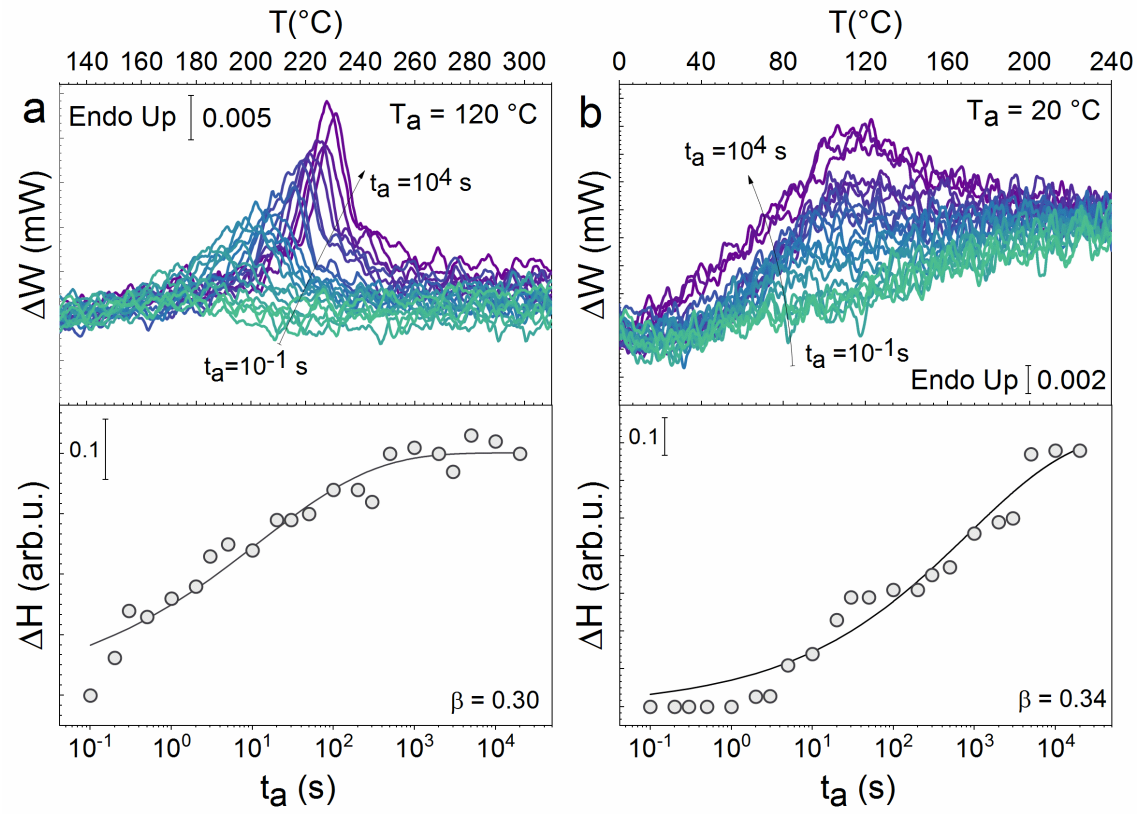

Figure 4.13 The amount of enthalpy change (ΔH) *vs* Ta. Upper panels correspond to ΔW after aging the sample for different ageing periods (t_a, from 10^{-1} to 10^4 s) at 120 °C (a) and, 20 °C (b). Lower panels show the amount of ΔH as a function of ta at each isothermal temperature. Grey lines are fits to KWW functions.

Likewise, in-situ temperature-dependent GIWAXS analysis conducted during heating ITIC (**Figure 4.14**a) showed that phase II polymorph appears when glass transition temperature detected by FSC and DSC (**Figure 4.14**b) is surpassed. This is compatible with a classical cold crystallization process in which a supercooled liquid evolves to a thermodynamic state of lower free energy via crystallization. Based on these results, we were able to estimate the T_g and melting temperature values of the different ITIC derivatives. In full agreement with the DSC data (ITIC-2F, **Figure 4.14**d; ITIC-M, **Figure 4.14**f; ITIC-Th, **Figure 4.14**h), well defined reflexions appeared when the T_g was surpassed. Interestingly, ITIC-Th showed a step-like increase at around 130 °C depicting the lowest T_g among the studied ITIC derivatives. This was accompanied by the

appearance of sharp diffraction peaks in the temperature-resolved GIWAXS. The data regarding the values of thermal transitions collected from the different techniques are included in **Table 4.4**.

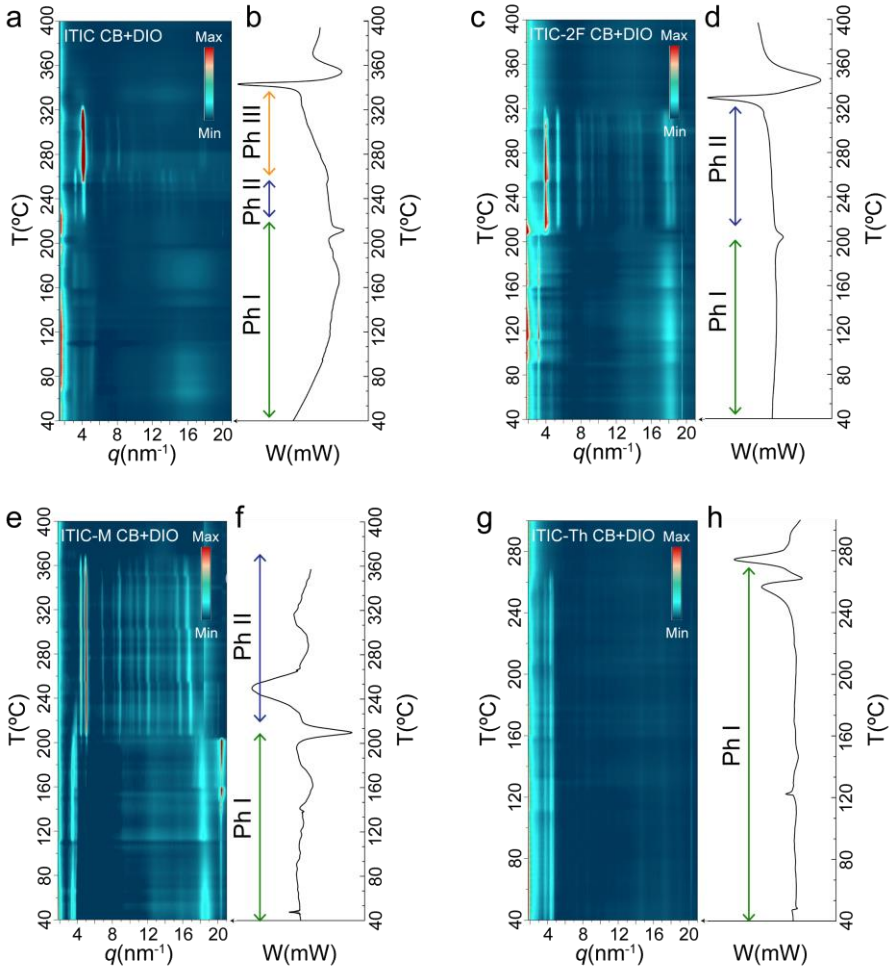

Figure 4.14 Azimuthal integrations of the 2D GIWAXS patterns recorded for (a) ITIC, (c) ITIC-2F, (e) ITIC-M and (g) ITIC-Th spin cast films (with 0.5% DIO) plotted against temperature and *q* while heating the samples at 10 °C·min^{-1}. DSC 1st heating scans for drop cast films: (b) ITIC, (d) ITIC-2F, (f) ITIC-M and (h) ITIC-Th.

Table 4.4 Summary of experimentally measured backbone T_g with DSC, $T_{g,onset}$ measured with FSC and Tm measured with DSC.

	ITIC	ITIC-2F	ITIC-M	ITIC-Th
T_g (°C) DSC	177	165	174	125
$T_{g,onset}$ (°C) FSC	184	195	-	-
T_m (°C)	342	328	>350	275

4.3.5. What makes ITIC-Th distinct?

As previously highlighted, ITIC-Th compared to ITIC-2F and ITIC-M NFAs, has the different chemical moiety in the central building block and not as terminal group. Consequently, its molecular packing and thermotropic behaviour seems to differ from the other NFAs: (i) as eluded before, 2D-GIWAXS pattern of Phase I does not exhibit an intense and broad π–π peak (**Figure 4.2**d) and, the π-π stacking peak of ITIC-Th Phase II appeared in the out-of-plane direction, which denote a noticeable fraction of face-on crystals (**Figure 4.2**h). (ii) Phase II polymorph is only developed from amorphous ITIC-Th film both during heating and after annealing (see **Figure 4.15**a-b and **Figure 4.15**e). (iii) Interestingly, we found that Phase I polymorph is the thermodynamically stable form of ITIC-Th. This conjecture is supported by our in-situ GIWAXS observations that Phase II does not appear during heating Phase I (**Figure 4.14**g) and neither after annealing the film at 240 ºC during 10 minutes (**Figure 4.15**c-d).

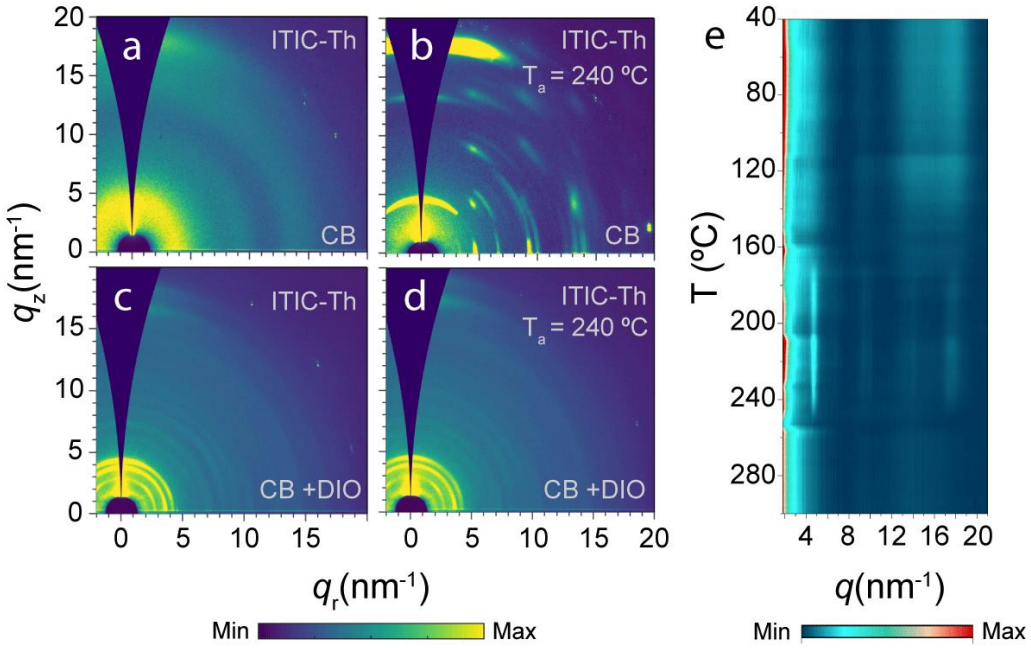

Figure 4.15 Ex situ, room temperature 2D GIWAXS patterns for a) ITIC-Th cast from CB, b) ITIC-Th cast from CB and annealed at 240 ºC, c) ITIC-Th spin coated from CB/DIO solutions and d) ITIC-Th spin coated from CB/DIO solutions and annealed at 240 ºC. Azimuthal integrations of the 2D GIWAXS patterns recorded for e) ITIC-Th cast from chlorobenzene plotted against temperature and q while heating the samples at 10 ºC·min^{-1} . The formation of Phase II from the molten ITIC-Th is detected.

4.3.6. Phase behaviour correlation analysis

To further elucidate the complex thermotropic behaviour and to establish a proper structure-function relation, we discuss, using an energy diagram depicted in **Figure 4.16**, the phase behaviour of indacenodithienothiophene-based NFA. From now on, the discussion will focus on ITIC, as it has the richest polymorphism and it is the core from which the other SMAs have been derived. We argue that phase I polymorphs are thermodynamically metastable whereas high temperature phase II and phase III are thermodynamically stable-phases. We base our hypothesis that phase I forms are metastable (unless ITIC-Th Phase I) on two main arguments: (i) the transitions between phase I and the high-temperature phases (phase II and phase III) are not reversible. We deduce this from the data given in, e.g., **Figure 4.2**, which displays the GIWAXS patterns of phases II and III acquired from samples that were first thermally annealed (for 5 min) at the temperatures indicated and then cooled to 25 °C at 50 °C·min^{-1} proving that after annealing phase I cannot be recovered. (ii) The DSC data (**Figure 4.16**c and **Figure 4.14**) shows that the transitions from phase I to phase II polymorph is exothermic in all cases, characteristic of a monotropic transition, i.e., a transition from a metastable phase to a stable phase. Therefore, the as-cast phase I does not correspond to the phase having the lowest free energy content in the temperature range and pressure.

In the case of ITIC, the polymorphic transition between phase II and phase III seems to be enantiotropic because the transition is endothermic (**Figure 4.16**c), meaning that phase II and phase III are both thermodynamically stable in their respective temperature ranges. To confirm reversible transitions between both polymorphs DSC experiments cycling between these two temperatures were performed (see Appendix **Figure B-3** and **Figure B-4**). Doubtless, cooling scans displayed an exothermic transitions related to the polymorphic transition from phase III to phase II. Subsequent heating scans showed the endothermic overshoot related to the crossover between the temperatures of the thermodynamic equilibrium of the phases. Thus, we argue that the transition between phase II and III polymorphs is enantiotropic because it is a reversible transition that occurs when cooling phase III. Nevertheless, phase III would correspond to the

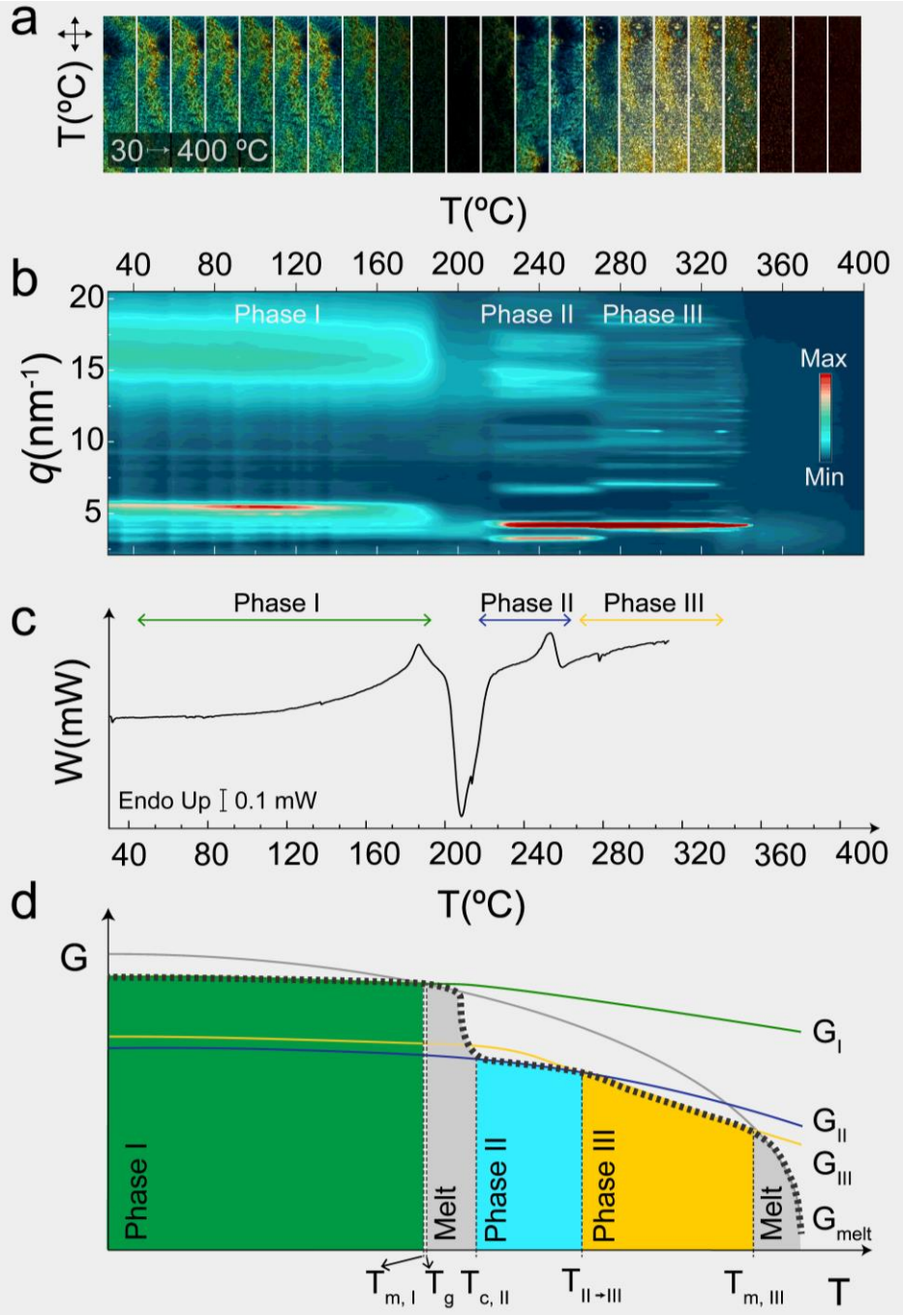

Figure 4.16 (a) Polarized optical microscopy (POM) images (b) Contour plot of the azimuthal integrations 2D GIWAXS patterns. Both experiments were acquired from room temperature up to 400 °C at 10 °C·min^{-1} and recorded for a drop cast ITIC film (20 mg·mL^{-1} in CB) (c) DSC 1st heating scan acquired during a heating ramp from -50 °C to 320 °C at 20 °C·min^{-1}. (d) Schematic free energy (G) versus temperature (T) diagram for ITIC crystalline phases. The green, blue, yellow and grey solid lines correspond to the free energy for the phase I, the phase II, the phase II and the ITIC melt (G_m), respectively. The dashed red line describes the evolution of G for a 100 % crystalline ITIC during heating. $T_{I\rightarrow II}$, $T_{II\rightarrow III}$, and $T_{m,III}$ represent the phase transition temperatures from phase I to phase II, from phase II to phase III and from phase III to ITIC melt, respectively.

thermodynamically preferred crystalline phase in ITIC because, first it is the last form to evolve prior to the solid-melt transition, and second it develops independently of the processing conditions applied (**Figure 4.8**).

Supporting above mentioned results, PLOM micrographs collected upon heating the sample at 10 °C·min^{-1}, evidenced that ITIC goes through alternating steps where birefringence is lost and recovered during the heating scan (**Figure 4.16**). This image line clearly evidences that the as-cast partially-ordered material progressively losses the birefringence as increasing the temperature from 100 to 210 °C. At 220 °C birefringence starts recovering again, which is accompanied by the appearance of new reflexions recorded by in-situ GIWAXS (**Figure 4.16**b) suggesting that a new crystal form is developed at those temperatures in full agreement with Yu's work.[49] At 280 °C a further increase of birefringence accompanied by a change of colour is detected. Lastly, birefringence decreases to zero at approximately 350 °C. By analogy with typical differential scanning calorimetry (DSC) experiments and in-situ temperature-dependent GIWAXS, POM data evidences two phase transitions as heating ITIC where molecular order is lost and another two transitions in which molecular order is enhanced during sample heating.

Hence, the thermotropic behavior of ITIC can be understood employing the free energy (G) diagram shown in **Figure 4.16**d. In it, the crystalline phase with the lowest value of G at a certain temperature is the thermodynamically stable form at that temperature. Hence, the temperatures at which two G-lines intersect correspond to thermodynamic phase transition temperatures, as it is the case for the melting of phase III at the temperature $T_{m,III}$. However, as mentioned above, phase I would not be the thermodynamically stable phase in their temperature regions, hence, their G-value should be higher than that of phase III in those regions. As mentioned above, the Ostwald´s rule of stages[201] states that in the crystallization of polymorphic systems, the most thermodynamically stable form is the last to appear; whereas the polymorph initially formed is less thermodynamically stable but its formation requires to overcome a lower energy barrier. Being phase I monotropic phase, phase II and phase III could be in principle achieved by heating phases I at specific temperature, however, the transformation rate is expected

to be faster at higher temperatures. Moreover, although the heating of phase I would eventually lead to the phase III, phase II is first developed when heating phase I, which suggests that phase II corresponds to another partial minimum in the G landscape of ITIC in s certain range of temperatures.

4.3.7. Interplay between phase behaviour and electronic properties

To link the effect of different crystal polymorphs with the device function, we first focused on the charge transport properties of the different polymorphs, hypothesizing that different molecular packing may affect the latter. For this purpose, we fabricated field-effect transistors (OFETs), using a top-gate bottom-contact device architecture, as shown in **Figure 4.17**a. Despite mobility in OFETs is typically different from the one of bulk films because current flows solely within the few nanometres at the interface with the dielectric, it is a useful parameter to assess the impact of microstructural variations on transport properties. Representative transfer characteristics for ITIC phase III, both in the linear (V_d =10V) and saturation (V_d =60V) regimes, from which the mobility values were extracted, are shown in **Figure 4.17**b (see Appendix B for additional devices **(Figure B-5**)). The device exhibited a good ideality in terms of linearity of drain current (I_d) as a function of gate voltage (V_g), at a given drain voltage (V_d; source voltage V_s is set to 0 V), and a reliability factor in saturation, r_{sat}, of 30%, where the main source of non-ideality is related to a consistent shift of the threshold voltage (V_T) towards positive voltage, reaching 32 V probably associated to a non-negligible contact resistance. The result that stands out is that all phase I polymorphs in the four derivatives investigated exhibit comparable saturation field-effect mobilities (μ_{sat}) to the high-temperature polymorph, despite the inherent disorder along the π-π stacking planes found in phase I polymorphs (**Figure 4.17**a), which may be expected to limit charge transport. More precisely, Phase II and Phase III ITIC devices show a slight enhancement of the mobility compared to phase I devices, but the opposite trend is observed for ITIC-M, ITIC-2F and ITIC-Th, for which higher saturation mobility values are measured for phase I than for phase II (see Appendix B for additional devices (**Figure B-6**)). Mobility values are summarized in **Table 4.5**

We note that best phase III devices were fabricated applying an annealing temperature of 270 °C, which differs from the optimal annealing temperature for phase III development according to GIWAXS (i.e. 300 °C). In fact, annealing at temperatures above 270 °C resulted in extremely poor devices despite the high crystallinity of the materials (see Appendix B **Figure B-7**).

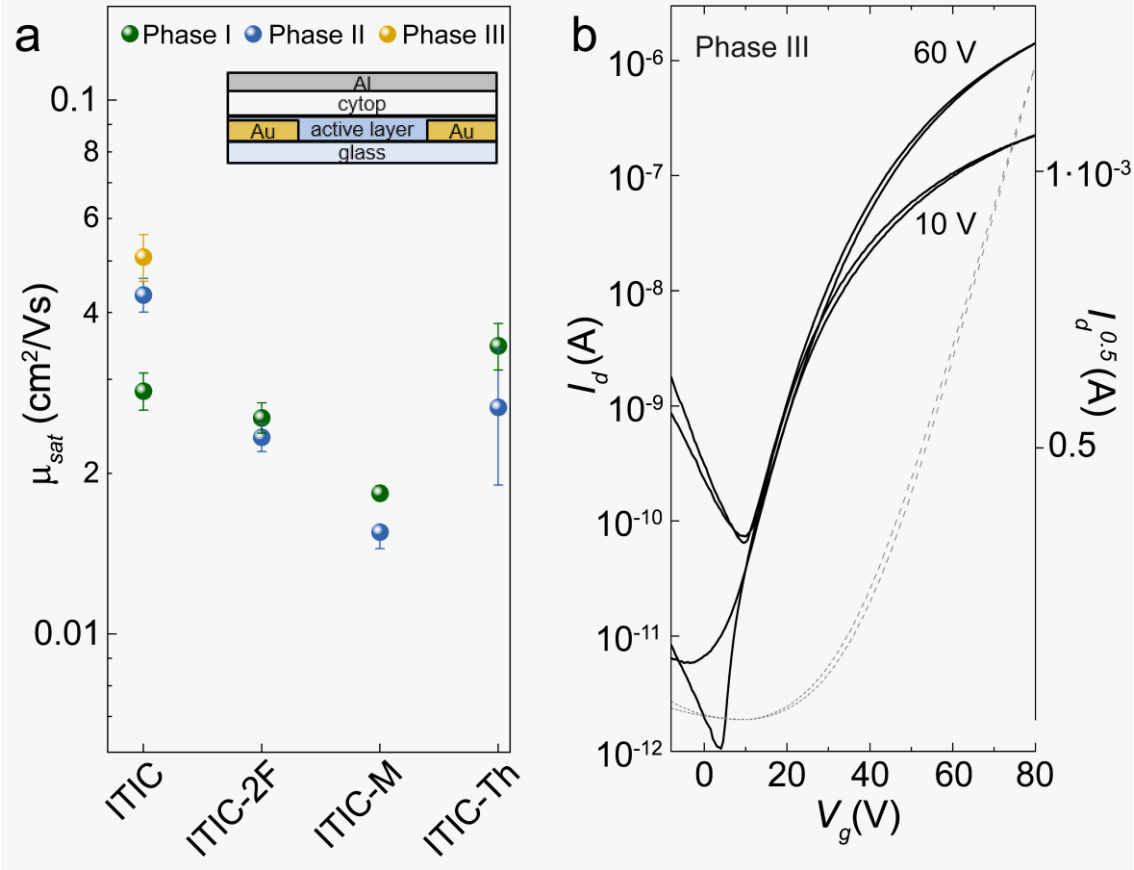

Figure 4.17 (a) Saturation field-effect mobility, μ_{sat}, values measured for the different ITIC polymorphs. The inset shows a schematic of the OFET device architecture used. (b) Representative transfer characteristic of ITIC phase III (annealed at 270 °C for 5 min) in the linear (V_d = 10 V) and saturation (V_d = 60 V) regimes. Dashed line corresponds to the square root of the current in saturation regime is shown.

To gain insights why polymorph I phases generally seem to lead to the highest-performing devices, absorption and photoluminescence spectra of each polymorphs normalized to thickness were studied. Intriguingly, strong difference in the optical absorption and emission of the NFA films crystallized in phase I, phase II and phase III were found in UV-Vis absorption

and photoluminescence spectroscopy (PL) measurements (**Figure 4.18**). UV-vis absorption and PL measurements for each NFA were performed at room temperature on a single sample

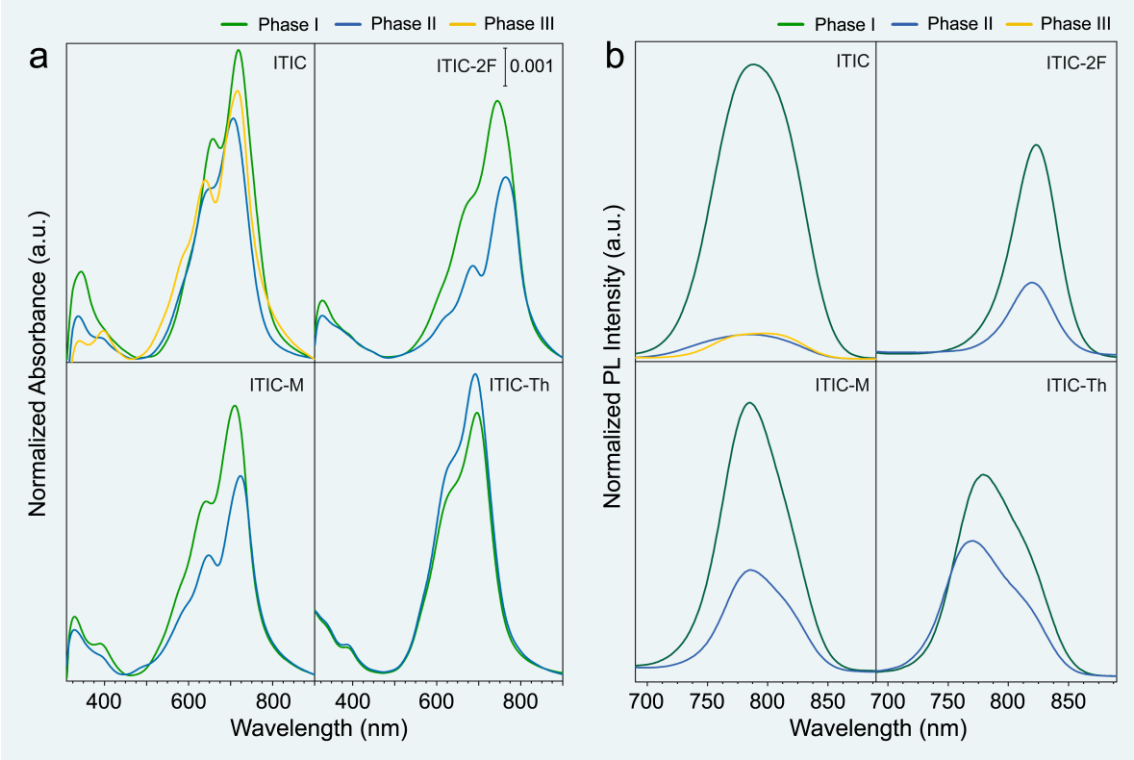

Figure 4.18 (a) Room temperature UV-Vis absorption spectra for phase I (green lines), phase II (blue lines) and phase III (yellow lines) for ITIC, ITIC-2F, ITIC-M and ITIC-Th. (b) PL spectra for ITIC, ITIC-2F, ITIC-M and ITIC-Th films in the phase I, phase II and ITIC phase III. All the samples were measured under the same excitation wavelength (633 nm). The films are normalized to thickness

crystallized into phase I and phase II (and Phase III in the ITIC case) and normalized to thickness, so that absorbed intensities for the different polymorphs are comparable. Our data clearly shows that the light absorption (and emission) is significantly stronger in phase I polymorphs than the high-temperature polymorphs, i.e. phase II in ITIC-2F and ITIC-M and phase II and III in ITIC. This is interpreted to result from an increased J-aggregate coupling in continuous aromatic structures found in Phase I forms, which could be the reason why phase I polymorphs outperform the other forms (phase II and III) in photovoltaic devices. It should be note that for ITIC-Th the absorption of phase II is slightly higher to phase I, however, phase I showed significantly higher

intensity when measured by photoluminescence spectroscopy. A further analysis of the absorption spectra reveals, moreover, that the absorption maxima (λ_{max}) of the high-temperature polymorphs (phase II and III) appears, in general, to be slightly red-shifted compared to that of phase I polymorphs. This results in lower optical bandgaps (E_g) for the former phases (data are summarized in **Table 4.5**). The phase II of ITIC is the exception (solid blue line in Figure 3c) as it exhibits λ_{max} and the absorption onset blue-shifted, resulting in a larger optical band-gap (E_g).

Table 4.5 Optoelectronic parameters for the different microstructures identified in ITIC, ITIC-M, ITIC-2F and ITIC-Th.

	ITIC			ITIC-2F		ITIC-M		ITIC-Th	
	Ph I	Ph II	Ph III	Ph I	Ph II	Ph I	Ph II	Ph I	Ph II
μ_{sat} (cm^2/Vs)	0.028	0.043	0.05	0.025	0.023	0.018	0.016	0.034	0.027
E_g (eV)	1.49	1.53	1.49	1.48	1.40	1.57	1.55	1.55	1.54
λ_{max} (nm)	712	705	716	726	732	743	777	695	700
Thick. (nm)	81.9	68.2	60.9	55.9	57.8	52.7	70.1	64.6	56.3

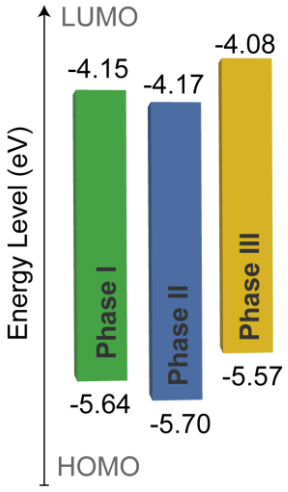

Figure 4.19 Energetic levels for the ITIC polymorphs calculated from UPS and UV–vis data

The energetic levels of the ITIC polymorphs were assessed in more detail using ultraviolet photoelectron spectroscopy (UPS) (details are included in the Appendix B **Figure B-8**). As shown in the inset of the upper panel in **Figure 4.19**, the HOMO level of phase I is at 5.64 eV, that of phase II is at 5.70 and the one for phase III is at 5.57 eV. The LUMO levels, on the other hand, are at 4.15, 4.17, and 4.08 eV for phase I, phase II and phase III, respectively. Therefore, in principle, while differences exist, all polymorphs in ITIC exhibit relatively good energy level alignments relative to the donor polymers from the benzodithiophene-benzodithiophenedione-based donor copolymer family, such as PBDB-T.[34]

4.4. Conclusions

In conclusion, we have rationalized the structural behaviour of high-performing indacenodithienothiophene-based NFAs with different functionalities. Our structural investigation encompassed the study of both crystalline phases and disordered glassy phases, which was achieved thanks to the rational combination of mainly FSC and GIWAXS. From our results we conclude the following:

- Our findings indicate that indacenodithienothiophene based NFAs present a reach polymorphism with at least two crystalline phases: a metastable phase I characterized by an ordered structure with a multidimensional mesh-like continuous aromatic structures and poor along the π-π stacking planes; and a highly ordered thermodynamically stable high-temperature phase (or phases, in the case of ITIC phases). Interestingly, packing motifs as found for polymorphs I (continuous aromatic structures, poor π-π stacking) seem to be a common feature among highest performing OSCs, including ITIC derivatives[195] and the benchmark Y6.[215] This packing may be the consequence of a chemical structure with aliphatic chains pendant form the central molecular building blocks while having the terminal acceptor groups free to π-π stack into a continuous network.

- Processing variables of OSCs such as processing solvent, thermal treatments and the use-of co-solvent additives have proven to be key in the development of phase I polymorphs. Furthermore, in the case of ITIC, its formation resulted to be critical in the transition to phase II. Engagingly, ITIC Phase I is developed from chlorinated aromatic solvents while the three derivatives require a co-solvent to develop Phase I.

- Diversely, ITIC-Th having a different chemical moiety in the central building block and not as terminal group, turned out to develop a different thermotropic behaviour and molecular packing than its counterparts. Thus, ITIC-Th's Phase I polymorph is a thermodynamically stable polymorphs as it is Phase II.

- ITIC and its congeners are also characterized by a large amount of disordered phase independent of the solvent used for processing. This tendency to vitrify is reflected in their high T_g values, which ranges between 160 and 200 °C for the different derivatives. Indeed, high T_gs seems to be a common feature among high-performing acceptor molecules for OPV, such as $PC_{70}BM$, Y_6, etc. as the formation of percolated nanoscale domains would require the rapid quenching of the morphology right after the liquid-liquid phase separation occurs. In addition to the glass transition, we found a second partial equilibration process of the ITIC glass that progresses in the timescale of few days at 20 °C. For a structural viewpoint, this equilibration results in the densification of the glassy domains and thus may affect the stability of devices.

- Moreover, phase I polymorphs exhibit a stronger light absorption comparing to their high-temperature counterparts, and outperform comparable charge transport properties as measured in field-effect transistors. Anyhow, it is interesting to highlight that indacenodithienothiophene-based NFAs exhibit, in general, rather similar μ_{sat} values and optical properties regardless of the different degrees of crystallinity and crystal structures. This tolerance to structural modifications confers them a large flexibility for device processing, which can be a major advantage as the processing conditions can be focused on other aspects of the active layer, e.g. a suitable morphology, with little impact on the optoelectronic properties of acceptor domains.

This framework will provide crystal engineering and materials design guidelines and will encourage searching for similar structural-function relation studies for other higher performing NFAs, such as Y6, N3, etc. Most significantly, demonstrates that the understanding of phase I polymorph is critical in order to establish meaningful structure-function relationships in OSCs and obtain insights, for instance, into structural degradation mechanisms of NFA-based devices.

5. Determining the absolute composition of amorphous mixed phases in bulk heterojunctions of organic photovoltaics

5.1. Summary

It is well-known that non-crystalline, i.e. amorphous, fractions of π-conjugated polymer donors and molecular acceptors are partially miscible, which often results in the creation of amorphous intermixed domains in organic solar cells. It is also well-known that such intermixed amorphous domains actively participate in the photophysical and transport properties of devices. Hence, molecular donor:acceptor intermixing must be precisely controlled and optimized to reach high device-performances. However, prior to this work, no experimental methodology existed that allowed to quantify the amount of intermixing, i.e. the composition, of these mixed phases in actual devices, which has clearly hindered the establishment of direct links between the morphology and device function. In this chapter, we present a novel methodology based on ultrafast calorimetry that allows for the first time to determine the absolute composition of mixed domains in bulk heterojunction (BHJ) of device-relevant thin films. On one hand, by quantifying the composition of our systems of reference, we unravel that the most efficient charge generation is obtained with a relatively small fraction (<15 wt%) of an acceptor in the intermixed amorphous phase. On the other hand, we learned that a considerable amount of acceptor in the intermixed phase (~55 wt%) is needed to upheld charge transport. In general, our work outlines that fast scanning calorimetry is a powerful tool for establishing a complete compositional characterization of organic bulk heterojunctions. Hence, it will be critical in advancing quantitative morphology-function models that allow for the rational design of these devices, and in delivering insights in, e.g., solar cell degradation mechanisms via phase separation, especially for more complex high-performing systems such as nonfullerene acceptor:polymer bulk heterojunctions.

This work was published in *Advanced Materials* (10.1002/adma.202005241).[137]

5.2. Introduction

Bulk heterojunction (BHJ), the most efficient organic photovoltaic layer to date, is composed of a blend between a semiconducting donor and an semiconducting acceptor material[226] in an attempt to achieve charge separation after photo-excitation.[227] Since the introduction of the bulk heterojunction,[86] the field of OSC has progressed exponentially reaching ~18% efficiency and offering environmentally friendly processing for single-junction devices.[42,172,228–230] Efficient BHJs are easily obtained via scalable printing and coating techniques. However, solution processing often leads to rather complex phase morphologies with various scenarios.[231,232] The morphology of polymer:fullerene or non-fullerene blends is characterized by donor-rich domains, if semicrystalline polymers are used; acceptor-rich domains, and a third amorphous phase where both components are molecularly intermixed (see **Figure 5.1**).[179,233–236] The degree of intermixing in this amorphous phases relies on the molecular interplay between the donor and acceptor components[166,237] and contribute to determining the performance of the OSCs with either positive or adverse effects.[168,238–240]

The miscellaneous impact of the amorphous donor:acceptor intermixed phase on various optoelectronic processes is well-known. For instance, charge generation is positively enhanced [168,170,241] and, thus, short circuit current; whereas charge recombination emerges as a collateral-effect with a certain degree of intermixing, negatively affecting charge transport/extraction and therefore lowering fill factor (FF).[93,95,166,242] However, a direct correlation has not yet been established[176] and a quantitative picture of how much intermixing is required is missing. The experimental characterization of the composition of mixed phases has turned out to be challenging, among other reasons, because advanced experimental techniques providing quantitative compositional information with 10-nm-scale resolution are required. For example, energy filtered TEM[243,244] and scanning transmission X-ray microscopy (together with NEXAFS spectroscopy)[166,168,245] have attempted to this end; but resonant soft X-ray scattering (R-SoXS) and near-edge X-ray absorption fine structure spectroscopy[166,168,234,245,246] have emerged as the preferred choice to asses mixed amorphous phases. Via the analysis of the total scattering

intensity, R-SoXS allows estimating the average relative purity of domains as compared to a reference sample.[247,248] However, despite being established techniques, do not provide absolute values of domain composition in device-relevant films but rather estimate an average purity as compared to the macroscopic size reference sample.[249] Concurrently, the identification of a methodology and a parameter that directly correlates morphology is required to complement the more "Edisonian" approaches of materials design and device optimization.

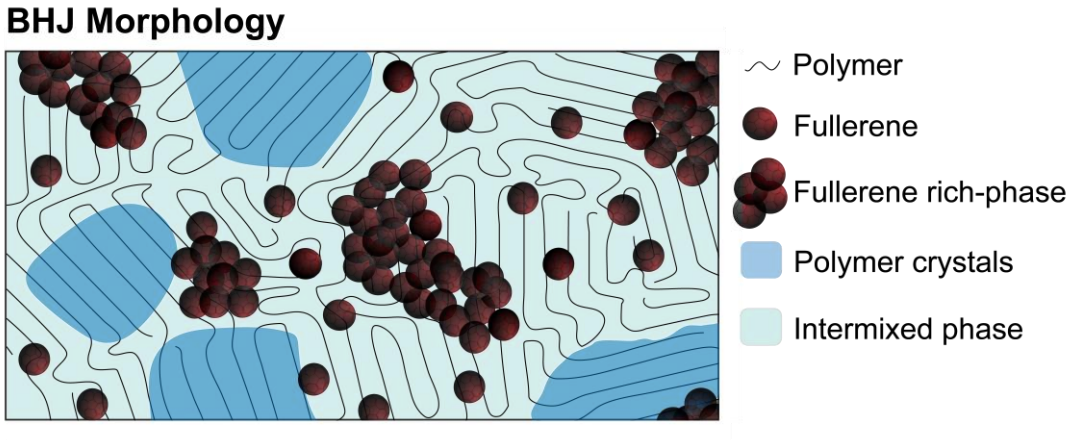

Figure 5.1 Schematic of an exemplary multi-phase morphology in a polymer:fullerene organic solar cell. Such a blend may comprise, among other things, a crystalline polymer phase, fullerene-rich domains and amorphous intermixed regions.

In this chapter, we envisage this issue from a polymer physics fundamental standpoint.[250] The miscibility of a blend is complex and may lead to several possible scenarios. The two rather limiting situations where (i) an immiscible system due to chemical incompatibility between components yields a morphology consisting of two phases based on each of the pure compounds or (ii) a miscible binary system, rendering a homogenous mixed phase. However, the current perception of miscibility also includes systems with compositional nanoheterojunctions where the degree of the intermixing depends on the intermolecular interactions of both components and, thus, can be associated with the Flory–Huggins interaction parameter χ, [8,166] and the glass transition temperature (T_g) is the parameter for the evaluation and quantification of the degree of miscibility.[250] The determination of the mixing is based on the measurement of the glass transition

signal of the blend which is typically located in-between the glass-temperatures of the pure components and consistent with the composition of the blend as proposed by Gordon and Taylor[251], however, there are genuine difficulties in measuring the T_g of these semiconducting donor:acceptor blends. Furthermore, the T_g values for organic blends in actual devices are mostly unknown , and entail additional difficulty since techniques employed for the determination of the T_g such as dynamical mechanical analysis (DMA) or differential scanning calorimetry (DSC), require large quantities of bulk samples.[252]

Here, we demonstrate on model systems based on blends of high molecular weight semicrystalline polymer poly(3-hexylthiophene) (P3HT),[253] and two fullerene derivatives having different miscibility with P3HT, namely the mono and the bis-adducts of the o-xylenyl C60 (denoted as OXCMA and OXCBA, respectively)[254][250] (**Figure 5.2**), that fast scanning calorimetry (FSC) allows for the direct determination of the absolute composition of the intermixed domains in BHJ OSCs. We not only develop a methodology to accurately determine the composition of the intermixed phases but are also introducing fast scanning calorimetry as the key tool to identify and measure structural order in semiconducting polymers. The novelty and effectiveness of fast scanning calorimetry (FSC) is based on the fact that (i) multiple glass transition temperature signals can be detected at a level of heterogeneity characterized by a domain size within the rage of 15-20 nm; (ii) device-relevant thin films can be measure by using the approach developed by Cangialosi et al.[135]; and (iii) the high cooling and heating rates (> 4000 $^{o}C \cdot s^{-1}$) allow to measure highly vitrified reference blends (iv) avoiding thermal degradation. Thus, Chapter 5 gathers the detail description and validation of a novel approach for the quantitative determination of the composition of amorphous intermixed phases in OSC which is based on the following steps: (i) we first determine the glass transition temperature of the ideal mixed systems as a function of composition, by quenching the polymer:fullerene material system at extremely high cooling rates. (ii) We then build a glass transition versus polymer concentration master curve on the grounds that the glass transition of mixed domains is coherently affected by the relative amount of donor

and acceptor molecules in the phase. (iii) We determine the T_g of the intermixed phase of the device-relevant sample to finally establish a direct link between morphology and device function.

5.3. Results and Discussion

5.3.1. Model systems

To determine the absolute composition of the intermixed domains in BHJ OSC blends, we use as a model system blends of the semicrystalline poly(3-hexylthiophene) (P3HT, M_w = 135 kg/mol, $Đ$ = 1.6, regioregularity: 99.9 %)[253] and two different fullerene derivatives, *i.e.* the mono- and the bis-adducts of the *o*-xylenyl C_{60}, denoted as OXCMA and OXCBA, respectively[254,255] (**Figure 5.2**). Thin films were spin cast at 1000 rpm from a 20 mg·mL^{-1} *orto*-dichlorobenzene solution.

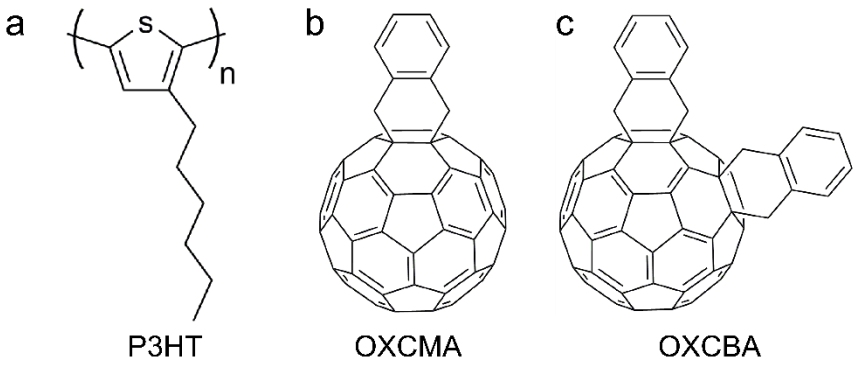

Figure 5.2 Chemical structures of the model materials used in this work: poly(3-hexylthiophene-2,5-diyl) (P3HT) (a), o-xylenyl C60 mono-adduct (OXCMA) (b) and bis-adduct (OXCBA) (c).

The rationale for the choice of P3HT:OXCMA and P3HT:OXCBA binary systems is as follows. On one hand, regioregular P3HT has proven to give rise to a multi-phase morphology upon mixing with fullerene derivatives in solution,[246] leading to the formation of vitrified intermixed domains. To confirm the vitrification of the blend, P3HT:OXCMA and P3HT:OXCBA blends were evaluated by means of GIWAXS ex-situ experiments. As displayed in **Figure 5.3**, grazing-incidence wide-angle X-ray scattering (GIWAXS) data reveal well-defined

scattering features for neat polymer film. P3HT film exhibits the characteristic meridional reflexions (h00) of the crystalline phase o plus a diffuse (010) attributed to π-π stacking indicating that the lamella are in "edge-on" orientation.[256] Interestingly, the addition of the fullerene acceptor causes the reduction of (100) diffraction intensity and the vanishing of higher order of the (100) reflection, indicating a lower degree of crystallinity in the blend (Note that this effect is stronger for OXCBA where the (100) is not even discernible). In view of these results, we confirm that vitrified thin films are obtained for both P3HT:OXCMA and P3HT:OXCBA binaries.

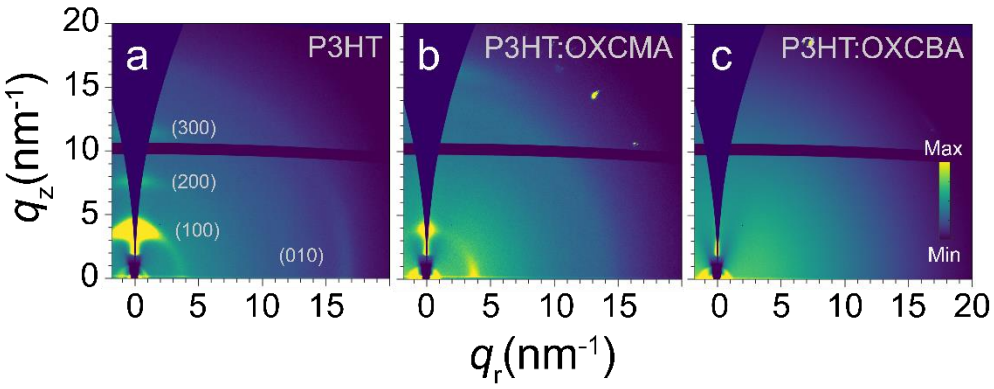

Figure 5.3 (a) GIWAXS patterns for as-cast films of neat P3HT, and P3HT:OXCMA (50:50) and P3HT:OXCBA (50:50) blend films, indicating the vitrifying effect blending has on P3HT. (b) Out-of-plane and in-plane profiles.

For further structural clarifications, differential scanning calorimetry (DSC) was employed. DSC samples were prepared dissolving the appropriate weight ratio of P3HT to OXCMA or OXCBA in chlorobenzene, to a total concentration of 20 mg·mL^{-1}. The blends were then drop cast on to glass slides, which were dried for 3 days in a vacuum oven to remove residual solvent. These films were then peeled off from the glass slides for analysis. **Figure 5.4**a-b shows the first heating thermograms of drop cast binaries using different compositions recorded at 20 ^{o}C·min^{-1} (Note that endothermic is upwards). All the thermograms of the binary blends showed the characteristic melting peak at ~240 ^{o}C. Interestingly, upon the addition of the fullerene adducts a drastic reduction of the melting enthalpies is observed. (**Figure 5.4**a-b). This effect is characteristic of significantly reduced molecular order, highlighting the severe effect blending

can have on the solid-state structure of semicrystalline polymers. In addition, the melting point reduction turned out to be more distinct for blends containing OXCBA (**Figure 5.4**c-d), indicating a larger miscibility between OXCBA and P3HT compared to OXCMA in complete agreement with our GIWAXS observations. Anyway, a significant decrease of the enthalpy of fusion is noted for both blends, which indicates that intermixing leads to partial vitrification – i.e., blending reduces the degree of order in P3HT.

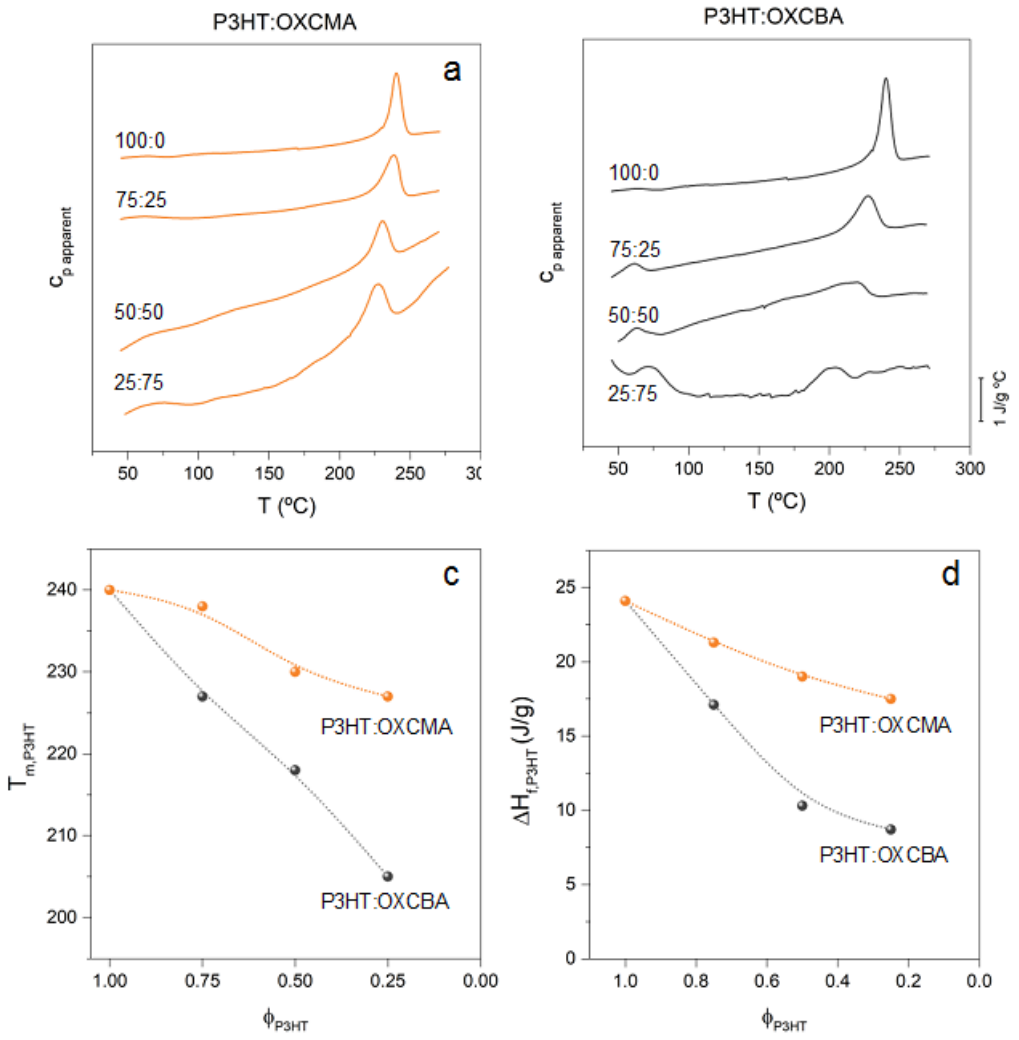

Figure 5.4 DSC heating thermograms of P3HT:OXCMA (a) and P3HT:OXCBA blends (b) of different composition ratios. (c) P3HT melting temperature, $T_{m,P3HT}$, as a function of the composition ratio for P3HT:OXCBA and P3HT:OXCMA blends. (d) Enthalpy of fusion, $\Delta H_{f,P3HT}$ as a function of the composition for P3HT:OXCBA and P3HT:OXCMA blends.

5.3.2. Methodology to quantify the composition of amorphous intermixed phases in organic solar cells

Having proved the consistency of the selection of the model systems and the simplifications deemed, we proceeded with the application of our novel methodology. The use of fast scanning calorimetry to quantify the composition of amorphous phase P3HT:OXCMA and P3HT:OXCBA binaries proceeds as follow:

5.3.2.1. STEP 1: Determination of the glass transition temperature of the donor: acceptor intermixed phases as a function of temperature

Since the T_g of the donor:acceptor blends depends on blend composition, a T_g *vs* composition "calibration" master curve needs to be established. In order to determine the T_g of fully vitrified blends of different compositions, we employ the thermal protocol depicted in **Figure 5.5**a, exploiting the compositional dependence of the glass transition temperature of binary solid solutions.[250] We proved our methodology with the two P3HT:OXCMA and P3HT:OXCBA systems. To construct our T_g vs composition "calibration curve", we prepared 10 $mg \cdot mL^{-1}$ chloroform solution having different compositions ratios, namely 100:0, 75:25, 50:50, 25:75 and 0:100, which after two hours stirring at 40 ºC, were spun cast on the backside of the chip calorimeter at 2000 rpm resulting in films of 80 to 100 nm thickness. Following the procedure established by Cangialosi *et al*.[136,257] we measured the T_g^{blend} of highly amorphous model systems (see section 2.2.1.1 and 2.3.1.1). We selected a T_H of 300 ºC for neat P3HT samples, i.e. a temperature above the melting temperature of P3HT; while for the blends a T_H of 360 ºC was used, which is above the melting temperatures of P3HT, OXCBA, and OXCMA (**Figure 5.4**) without inducing degradation. Films were then quenched from T_H to the aging temperature, T_a, using a cooling rate of -4000 $ºC \cdot s^{-1}$ and held there for 30 minutes (t_a). Samples were then quenched to - 70 ºC (T_L) and subsequently heated to T_H (4000 $ºC \cdot s^{-1}$). When T_a was, lower than the $T_{g,onset}$ aging occurred and an endothermic overshoot was recorded in the aged scans (see **Figure 5.5**).

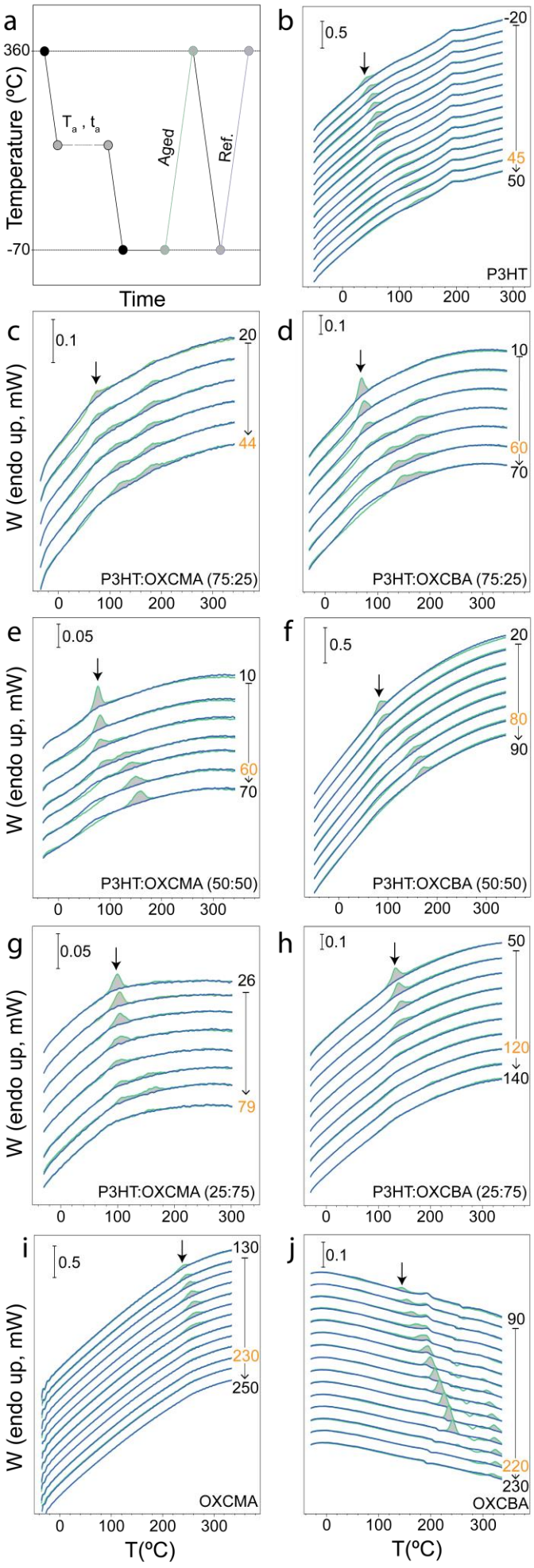

Figure 5.5 (a) Thermal history applied to determine the $T_{g,onset}$ of P3HT:OXCMA and P3HT:OXCBA blends. (b-j) Heat flow rate (W) heating curves for aged samples (green lines) and reference samples (blue lines) for neat P3HT (b), and P3HT:OXCMA blends with the following compositions: 75:25 (c), 50:50 (e) and 25:75 (g); neat OXCMA (0:100) (i), P3HT:OXCBA blends with the following compositions: 75:25 (d), 50:50 (f) and 25:75 (h), and neat OXCBA (j). The ageing temperature, Ta, applied in the experiments are indicated on the right-hand side of the curves. In orange are shown the Ta values after which no overshoots in the glass transition region are recorded.

In the latter scans since no aging step was used, no physical aging occurred and, in turn, no endothermic overshoot was observed in the glass transition region. Analysing different aging temperatures above and below the $T_{g,onset}$, we found a lower limit for T_a where no physical aging occurred and no enthalpic overshoot .was recorded in the glass transition region (these T_as are highlighted in orange in **Figure 5.5**b-j)

The $T_{g,onset}$ values of the blends were extracted from **Figure 5.5**. The onset glass transition values thus determined were 41 ± 3 ºC, 225 ± 5 ºC and 215 ± 5 ºC for neat P3HT, OXMA and OXCBA, respectively; 44 ± 5 °C (75:25 weight ratio), 55± 5 °C (50:50) and 75 ± 5 °C (25:75) for P3HT:OXCMA blends; and 55 ± 5 ºC, 75 ± 5 ºC, and 115 ± 5 ºC for the 75:25, 50:50, and 25:75 P3HT:OXCBA blends. These results allowed us to establish T_g-composition master curves from which the composition of amorphous phases in partly crystalline structures can be extracted once their T_g is known.

Once the $T_{g,onset}$ of the different blends were determined, the obtained values were plot versus the composition. Assuming ideal mixing, binary blends exhibit one single glass transition, occurring at a temperature intermediate between the glass transition temperatures of the two neat components. Thereby, the glass transition temperature of the blend, T_g^{blend}, can be estimated using the Gordon–Taylor equation:[98]

$$T_g^{blend} = \frac{x_A \cdot T_{g,A}^0 + k \cdot x_B \cdot T_{g,B}^0}{x_A + k \cdot x_B} = \frac{x_A \cdot T_{g,A}^0 + k \cdot (1 - x_A) \cdot T_{g,B}^0}{x_A + k \cdot (1 - x_A)} \quad \textbf{(Equation 3.1)}$$

where k is typically considered an empirical constant-; $T_{g,A}^0$ represents the glass transition temperature of neat component A (with a T_g that is lower than the one of B; *i.e.* A is the low-T_g component), x_A is its weight fraction in the fully vitrified, ideally mixed blend; while $T_{g,B}^0$ is the glass transition temperature of neat B (the high-T component) and x_B is the corresponding weight fraction of B in the system.

Figure 5.6 shows that the experimental $T_{g,onset}$ data of both binaries can be remarkably fitted with the Gordon-Taylor equation (Equation 3.1), suggesting that mixed phases strongly

resemble miscible blends. These master curves can now be used to identify the composition of the amorphous phase of any P3HT:OXCMA and P3HT:OXCBA device-relevant blends, independent of the fraction of the amorphous intermixed phase that is present in the system, as already alluded to above.

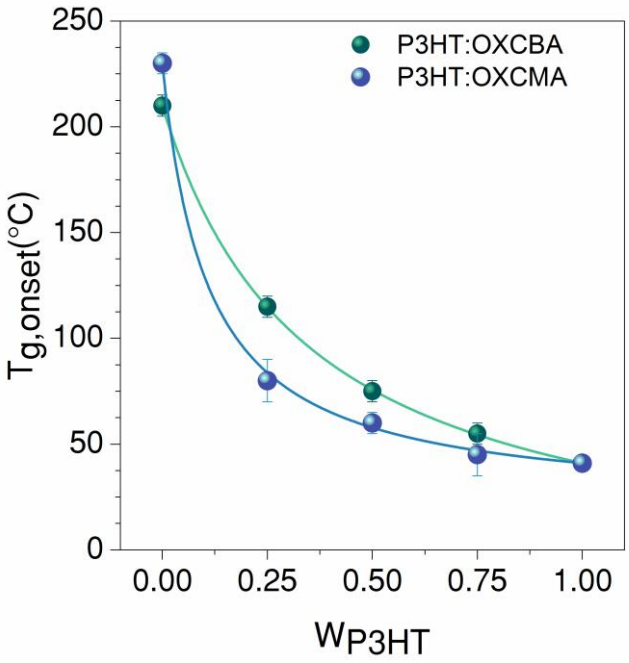

Figure 5.6 T_g^{blend}-vs-composition (T_g^{blend}-w) plot obtained for binaries of P3HT:OXCBA (green circles) and P3HT:OXCMA (blue circles) that were fully vitrified via cooling with -4000 ºC·s^{-1}. Solid lines are fits to the Gordon-Taylor model.

5.3.2.2. STEP 2: Determination of the glass transition temperature of the intermixed phase of a "real solar cell"

The second step of our methodology is based on the determination the $T_{g,onset}$ of a device-relevant OSC. For this end, although a real replica of an OSC device cannot be placed on top of a FSC chip, we reproduced the morphology of a real OSC device using similar parameters as those employed for efficient device fabrication. Thus, for thin film fabrication, the reference sensor was first covered with glucose. Once solidified, a poly(3,4-ethylene dioxothiophene):poly(styrene sulfonate) (PEDOT:PSS, Clevios™) thin film was spin cast onto the sensor and baked at 150 ºC for 20 min. PEDOT:PSS is usually employed as hole transport layer and in order to avoid effect

of surface interactions.[258] Prior to blend deposition, glucose was carefully dissolved and, ensure that PEDOT:PSS did not interfere with calorimetric response of the donor:acceptor blends. Once again, the reference was carefully covered with glucose. Subsequently, the P3HT:OXCBA and P3HT:OXCMA (1:1 by weight) were spin cast on top of the PEDOT:PSS from a 20 mg·mL^{-1} *orto*-dichlorobenzene solution at 1000 rpm. The glucose was removed with water avoiding contact with the sample sensor and finally, the active layer was annealed at 150 ºC during 10 minutes.

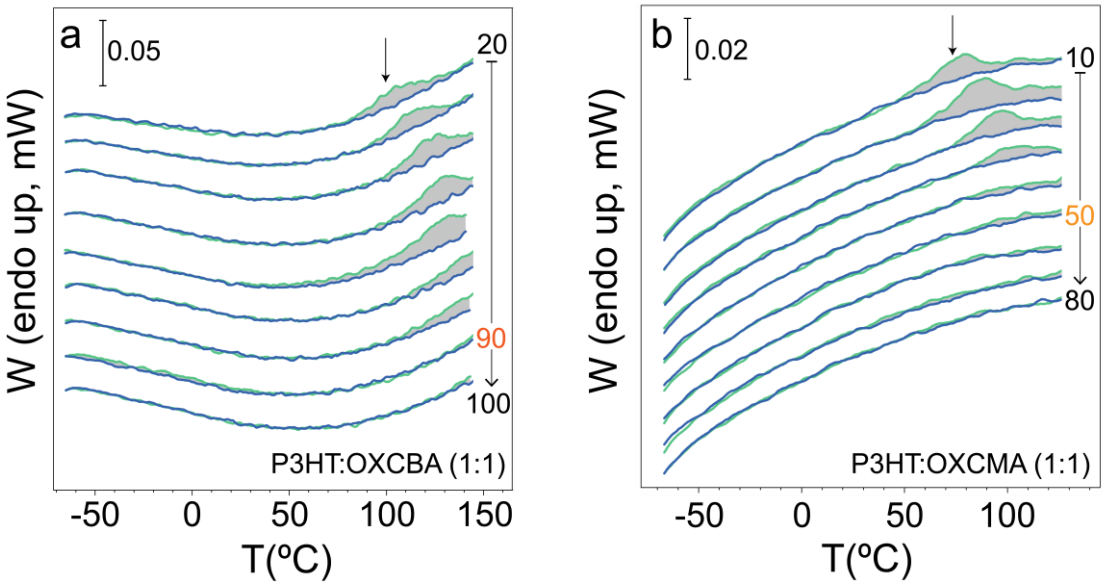

Figure 5.7 FSC heating scans (recorded at 4000 ºC·s^{-1}) for 1:1 P3HT:OXCMA (b) and P3HT:OXCBA blend films, produced as for device fabrication, from which T_g values of 85 ± 5 °C (1:1 P3HT:OXCBA) and 45 ± 5 °C (1:1 P3HT:OXCMA) are determined: green and blue lines correspond to the W signals for the aged and non-aged materials, respectively. Ageing temperature are indicated next to the curves.

Again, we employed the thermal protocol depicted in **Figure 5.5.**In this particular case, in avoidance of modifying the morphology of the blend treated as for device fabrication, the T_H value was adjusted to 150 ºC, which is the maximum temperature used in device fabrication. The endothermic overshoot are shadowed in grey in **Figure 5.7** and the temperature marking the crossover between the metastable glass and the equilibrium state where no aging occurs. These

temperatures are highlighted in orange in **Figure 5.7**a-b. We find the T_g of such P3HT:OXCMA and P3HT:OXCBA blend films to be, respectively, 45 ± 5 °C and 85 ± 5 °C.

5.3.2.3. STEP 3: Quantitative determination of the blend composition

The final step from our approach consists on the determination of the composition of the real devices by plotting the $T_{g,onset}$ values in our calibration curve (**Figure 5.8**). Accordingly, we can deduct from our master curve that $T_{g,onset}$ of 45 ± 5 °C for the 1:1 P3HT:OXCMA blend films corresponds to a system with w_{P3HT} = 0.85 and that $T_{g,onset}$ of 85 ± 5 °C for the 1:1 P3HT:OXCBA blend films corresponds to a system with w_{P3HT} = 0.42. In other words, the composition of the mixed phase of our P3HT:OXCMA replica is highly rich in P3HT having a composition 85:15; while the one of 1:1 P3HT:OXCBA blends is compositionally more equilibrated, having a composition of 42:58, slightly richer in fullerene acceptor.

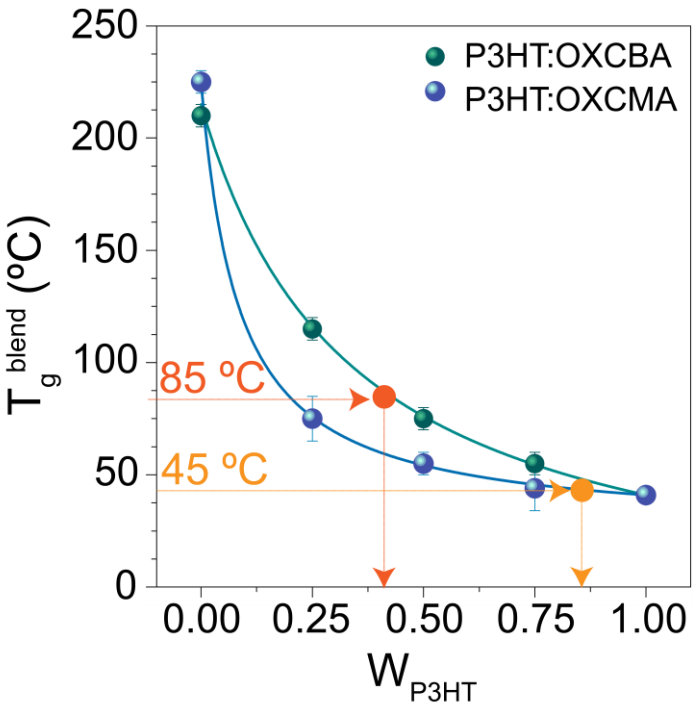

Figure 5.8 T_g^{blend}-vs-composition (T_g^{blend}-w) plot obtained for binaries of P3HT:OXCMA (green circles) and P3HT:OXCBA (blue circles) that were fully vitrified via cooling with -4000 °C·s^{-1}. Solid lines are fits to the Gordon-Taylor model. The dashed lines indicate the T_g measured for

device-like blend films, from which a P3HT weight fraction, w_{P3HT}, in the intermixed domains can be deduced.

5.3.3. Connection with optoelectronic properties of the BHJ

To correlate the effect of different amorphous intermixed phase composition with the device performance, devices were fabricated to measure the effective mobilities, μ_{eff}. To ensure a fair comparison, active layer were prepared using the same conditions as for the active layer measured by FSC. After PEDOT:PSS layer deposition, the substrates were annealed at 150 ºC during 20 minutes. 20 mg·mL^{-1} of P3HT:OXCBA and P3HT:OXCMA blend solutions were prepared with a D:A ratio of 1:1 in dichlorobenzene, spin cast and then annealed. The effective mobilities of the binary P3HT:OXCMA and P3HT: OXCBA blends are depicted in **Figure 5.9**.

Effective mobilities are important to consider in the context of BHJs as they provide values for organic solar cells under realistic operating conditions in contrary to charge mobilities measured using single carrier diodes or field-effect transistors.[259] The analysis requires knowledge of the carrier density, *n*, which can be obtained via voltage and frequency dependent capacitance spectroscopy.[260] The capacitance of the bulk-heterojunction is then corrected for unwanted effects such as the series resistance and parasitic inductance. This corrected capacitance can be converted to the carrier density, *n*, in the BHJ (**Figure 5.9**c). Once *n* is known, the following relationship between the current density, *J*, and carrier density, *n*, yields the effective mobility, μ_{eff},:

$$\mu_{\mathrm{eff}} = \frac{JL}{2qn(V_{\mathrm{bi}} - V_{\mathrm{cor}})}, \qquad \textbf{(Equation 3.2)}$$

where *J* is the current density from the *J-V*-curves (**Figure 5.9**a-b), *L* is the film thickness, *q* is the elementary charge, V_{bi} is the built-in voltage, and V_{cor} is the voltage corrected for the series resistance ($V_{cor} = V_{app} - J \cdot R_{series}$)[153,260–262]

Overall, both binary blends feature significant differences in charge transport characteristics. The P3HT:OXCBA film with an intermixed composition of 42:58 and a higher tendency to vitrified as verified by GIWAXS (**Figure 5.3**) displayed in the dark six times higher

effective mobilities, μ_{eff} , at relevant operating condition (**Figure 5.9**d) comparing with the P3HT:OXCMA blend having a composition 85:15 (**Figure 5.9**a).

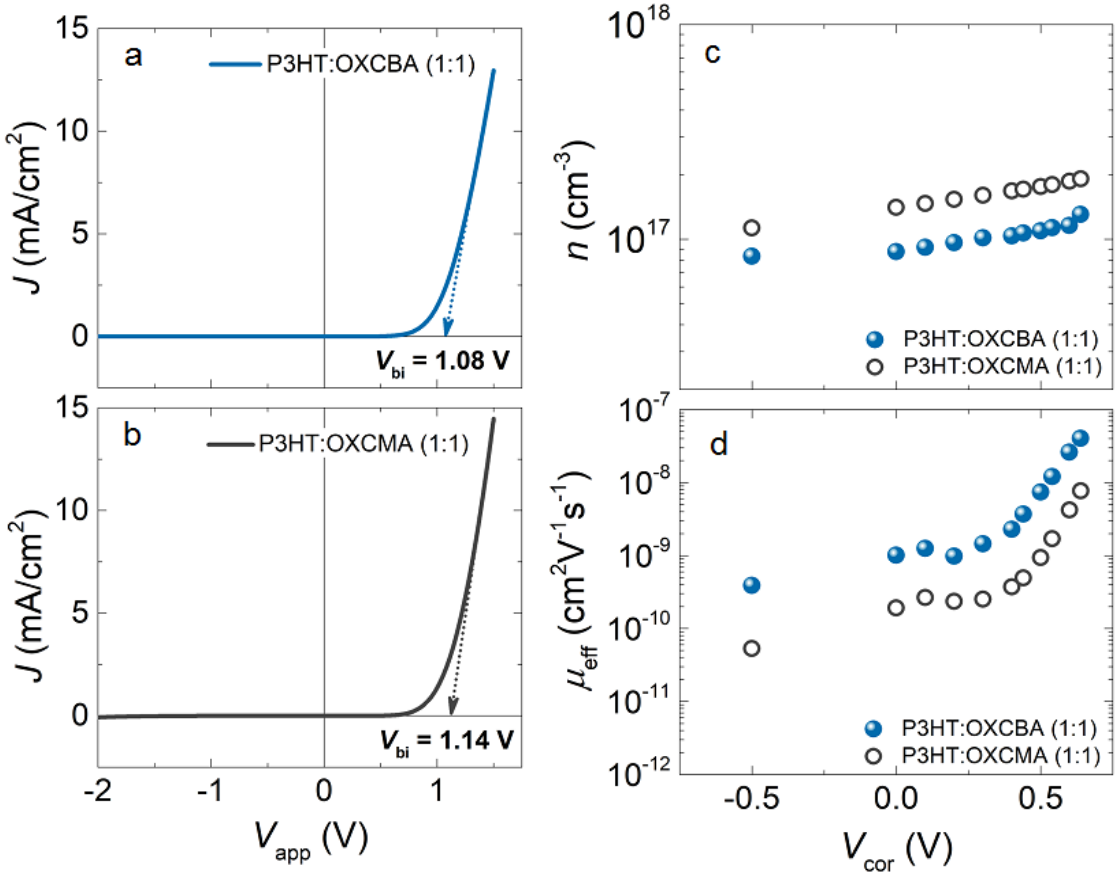

Figure 5.9 (a, b) *J-V*-characteristics of the two studied devices in the dark; the built-in voltage was also determined. (c) Charge carrier density *n* calculated via capacitance spectroscopy. (d) Effective mobility μ_{eff} of P3HT:OXCMA and P3HT:OXCBA (1:1 by weight) blends.

For further device comparisons, transient absorption spectroscopy was further used to characterize the charge generation. As displayed in **Figure 5.10**, both blends exhibit very similar tendencies to generate charges and depict an equivalent photophysical response. This can be inferred from the spectral region spanning from 2-2.5 eV which represents the ground state bleach with broad and structured spectral signatures corresponding to the absorption bands previously reported for this type of donor:acceptor systems.[153,261,262]. The transient absorption data furthermore showed that in both blends, the photogenerated species are long lived, in the order of nanoseconds, as the same spectral signatures prevail over this temporal scale This timescale is

consistent with the lifetime of excitons and polaron pairs.[263] Finally, note that in **Figure 5.10**, the spectra of both systems are very similar also in the region below 2 eV, where a broad photoinduced absorption is present. Around 1.7 eV there is an overlap between a photoinduced absorption and the stimulated emission band, such that the opposite sign signals lead to almost zero intensity in this spectral region. Previous reports have attributed this photoinduced absorption signal to polaronic absorption in P3HT-based blends, which is consistent with the observed long-lived bleach recovery.[263] (Note that the samples were again prepared respecting the same processing protocol)

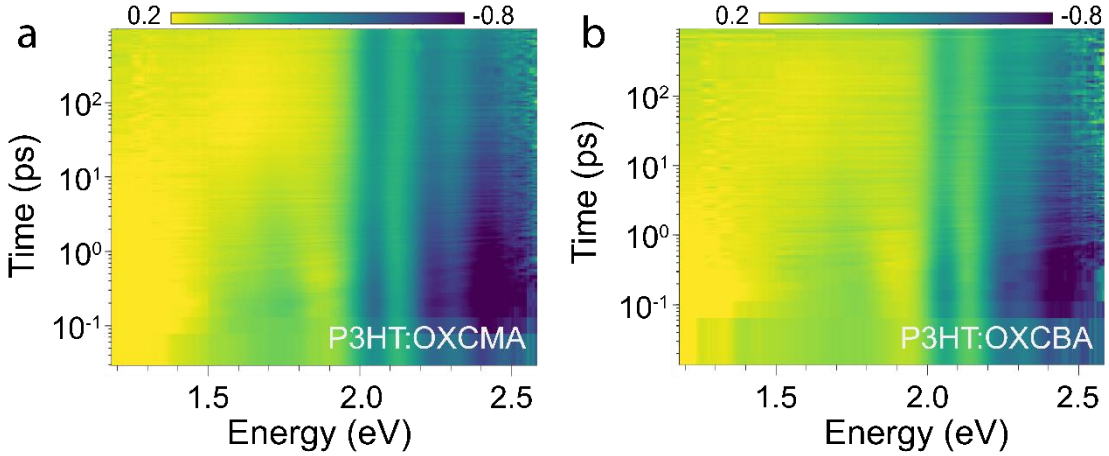

Figure 5.10 Two-dimensional transient absorption maps obtained by pumping at 2.76 eV for (a) P3HT:OXCMA and (b) P3HT:OXCBA (1:1) blends.

Since morphology composition seems to dominate charge transport and charge generation behavior, grazing incidence small-angle X-ray scattering (GISAXS) was further used to characterize the phase morphology of the P3HT:OXCMA and P3HT:OXCBA 50:50 binary blends. In GISAXS, as displayed in **Figure 5.11**, Yoneda peak intensities for both blends are plotted versus the in plane scattering vector, q_y, where $q_y = 2 \cdot \pi \cdot \lambda^{-1} \cdot sin(\theta) \cdot cos(\alpha)$ (λ is the wavelength of the X-rays used; θ and α are the in plane and out of plane scattering angles), and the fitted using the Unified model by Beaucage.[175] As readily observed in **Figure 5.11**c, intensity profiles with a shoulder centered at 0.2 nm^{-1} and the same decay rate in the higher q_y

region are achieved for both blends. Importantly, P3HT:OXCMA blend, which by our approach revealed a composition of 85:15 meaning a higher content of polymer in the mixed phase, depicted higher intensity leading to two possible scenarios: (1) the film either contains a larger amount of phase-separated domains or (2) a "purer" intermixed phase. Thus, in agreement with the compositional result obtained from our approach, both possibilities imply stronger phase separation in the P3HT:OXCMA bulk heterojunction compared to the P3HT:OXCBA blend. (Note that the samples were again prepared respecting the same processing protocol)

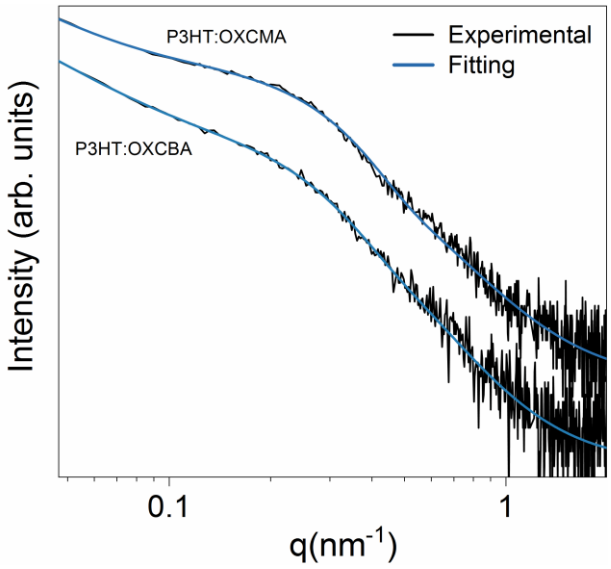

Figure 5.11 GISAXS patterns of (a) P3HT:OXCMA and (b) P3HT:OXCBA. (c) Horizontal cuts of the GISAXS patterns at qz corresponding to the Yoneda peak. Profiles were vertically shifted for the sake of comparison.

5.3.4. Validation of the methodology

Having demonstrate the effectiveness of our approach, quantitatively measure the amorphous intermixed phases of two model systems and proved its impact on device-function, we explored the validity of our approach. To prove our approach, we selected the binary system composed of regiorrandom P3HT (RRa-P3HT) and PC[60]BM whose compositions have been already reported in the literature.[234,264] The main reason for this choice is that, since RRa-P3HT is amorphous and, thus, the complexity of the morphology is reduced compared to a semi-crystalline

donor. Such morphology is characterized by acceptor-rich domains and an amorphous polymer mixed phase where both components are molecularly intermixed.

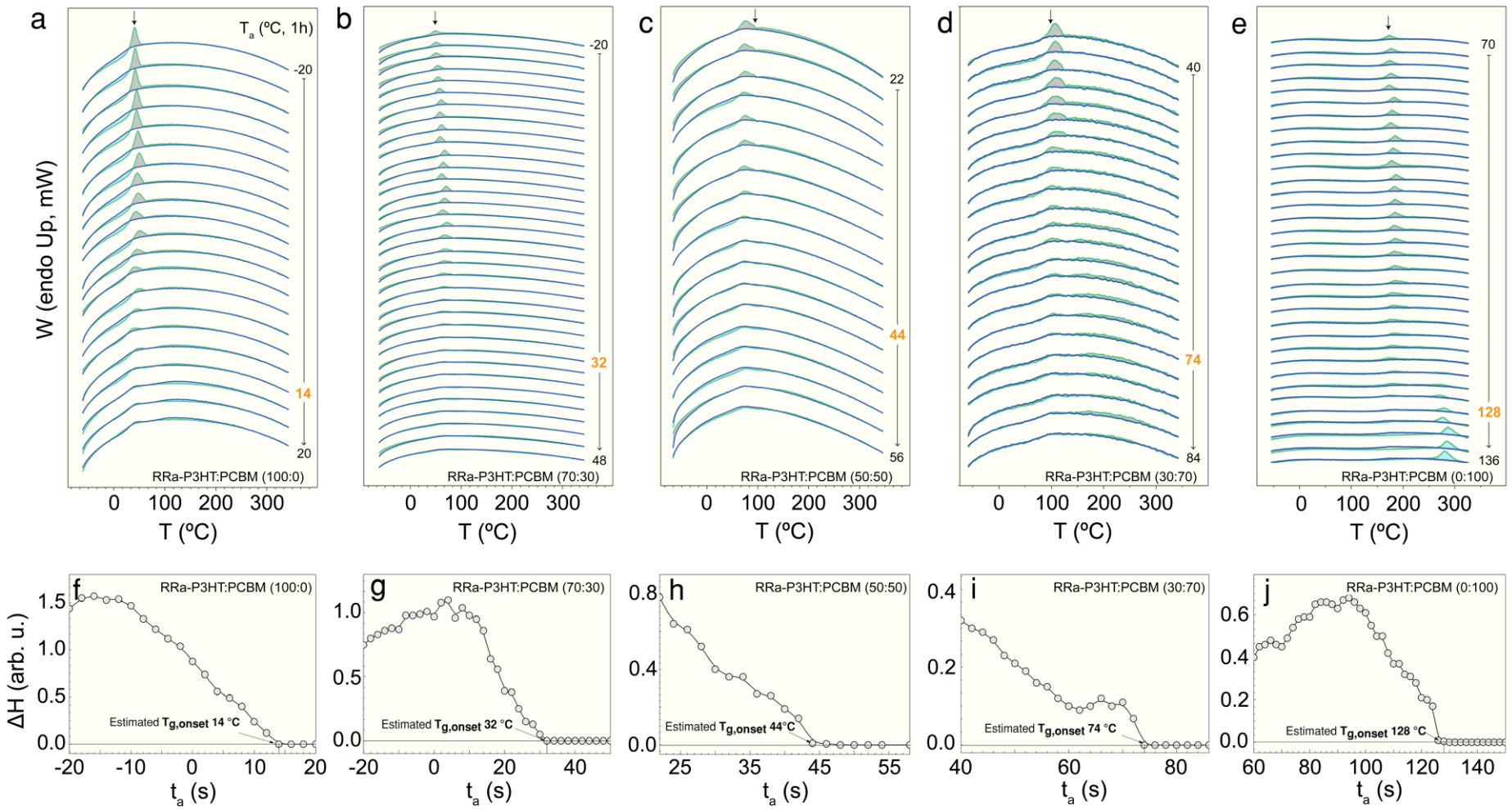

Figure 5.12 Upper panels: FSC heating scans recorded at 4000 °C·s^{-1} for pure RRa-P3HT (a), RRa-P3HT:PC[60]BM blends with compositions 70:30 (b), 50:50 (c) and 30:70 (d), and pure PC[60]BM (e) after cooling the samples from 350 °C to the annealing temperature Ta for 30 min (green curves) or to -70 °C at -4000 °C·s^{-1}. The Ta applied in each experiment is indicated on the right-hand side of each curve. Lower panels: Relaxed enthalpy as a function of aging temperature after aging for 1h. The dashed lines represent a linear extrapolation of the high frequency flanks of the distributions of relaxed enthalpies.

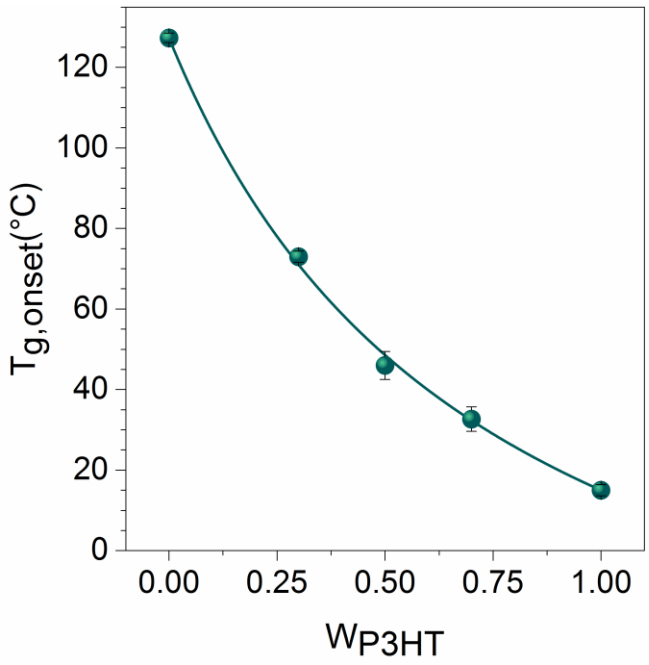

Figure 5.13 T_g^{blend}-vs-composition (T_g^{blend}-w) plot obtained for binaries of RRa-P3HT:PC[60]BM (green circles) that were fully vitrified via cooling with -4000 °C·s^{-1}. Solid line is fits to the Gordon-Taylor model.

To determine the amorphous intermixed composition of the RRa-P3HT:PC[60]BM blend, we applied the three steps of our approach. We first determined the $T_{g,onset}$ values of the vitrified pure materials and blends with different compositions. To do so, we prepared 10 mg·mL^{-1} chlorobenzene[234] solution having different compositions ratios, namely 100:0, 70:30, 50:50,30:70 and 0:100, which were spun cast on the backside of the chip calorimeter at 2000 rpm. Applying the approach established by Cangialosi et al.[135,136,265] we measured the T_g^{blend} of highly amorphous systems. In this case, we selected a T_H of 350 ºC and - 70 ºC for T_L. For a higher resolution, films were then quenched from T_H to the aging temperature, T_a, using a cooling rate of -4000 ºC·s^{-1} and held there for 1 hour (t_a). Heating temperature scans were recorded at 4000 ºC·s^{-1}. The $T_{g,onset}$ values of the blends were extracted from **Figure 5.12**. The onset glass transition values thus determined were 14 ± 2 ºC and 128 ± 2 ºC for neat RRa-P3HT and PC[60]BM, respectively; 32 ± 2 °C (70:30 weight ratio), 44 ± 2 ºC (50:50) and 74 ± 2 °C (30:70) for the blends. We successfully developed the $T_{g,onset}$ versus composition master curve of RRa-

P3HT:PC[60]BM binaries and the perfect fitting to the Gordon-Taylor equation (Equation 3.1), suggests that the model system resembles a miscible blends (**Figure 5.13**).

The second step consists on the measurement of the $T_{g,onset}$ a device-relevant OSC. Herein, we have prepared a replica of the films prepared Ade's[234] and Gomez's papers[264] on top of the FSC chip. Ade's group reported that the concentration of RRa-P3HT in the intermixed phase of 1:1 blend annealed at 180 ºC for 18 h was 74 ± 2 wt.% [78 ± 2 % (V/V)];[234] and Gomez's group found that the concentration of RRa-P3HT in the 1:1 blend annealed 190 ºC for 30 min amounted to 53 wt.% [58 % (V/V)].[264]

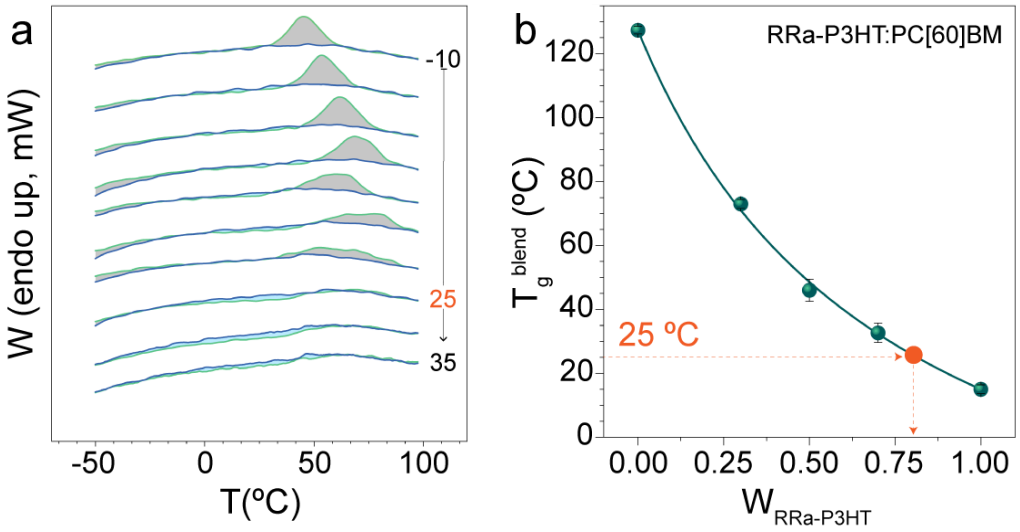

Figure 5. 14 (a) FSC heating scans recorded at 4000 ºC·s^{-1} for RRa-P3HT:PC[60]BM 1:1 blends. Green curves, refer to the samples aged at T_a for 30 min while the blue traces refer to the unaged samples. The T_a applied in each experiment is indicated on the right-hand side of each curve. Prior to this measurements the samples were annealed at 180 ºC for 18 h.[234] (b) $T_{g,onset}$ vs $w_{RRa-P3HT}$ for the RRa-P3HT:PC[60]BM blend (green circles) employed for testing our methodology. Solid grey line is the fit to the Gordon-Taylor model. The arrow corresponds to the concentration of the intermixed phase of the sample annealed at 180 ºC for 18 h.

To compare our approach with Ade's NEXAFS based obtained blend composition, we annealed the chip at 180 ºC during 18h and we applied the isothermal aging protocol. In order to avoid modifications in the morphology of the thermally treated blend, the T_H value was adjusted to 100 ºC. Our approach delivered a $T_{g,onset}$ of 25 ± 5 °C (**Figure 5. 14**a). By introducing the $T_{g,onset}$

value in the calibration curve, we can deduct that $T_{g,onset}$ of 25 ± 5 °C for the 1:1 RRa-P3HT:PC[60]BM blend annealed at 180 ºC during 18h corresponds to a system with w_{P3HT} = 0.78, in fully agreement with Ade's report.[234]

For further comparisons, we followed the processing protocol developed by Gomez et al.[264] where the film was at 190 ºC during 30 minutes. Following our approach, we obtained $T_{g,onset}$ of 50 ± 5 °C and therefore, a polymer composition of w_{P3HT} = 0.57 for the 1:1 RRa-P3HT:PC[60]BM blend annealed at 190ºC during 30 min, again, in fully agreement with Gomez´s paper. (**Figure 5.15**). These two cases demonstrate the validity and effectiveness of our methodology to determine the absolute composition of the amorphous intermixed phases.

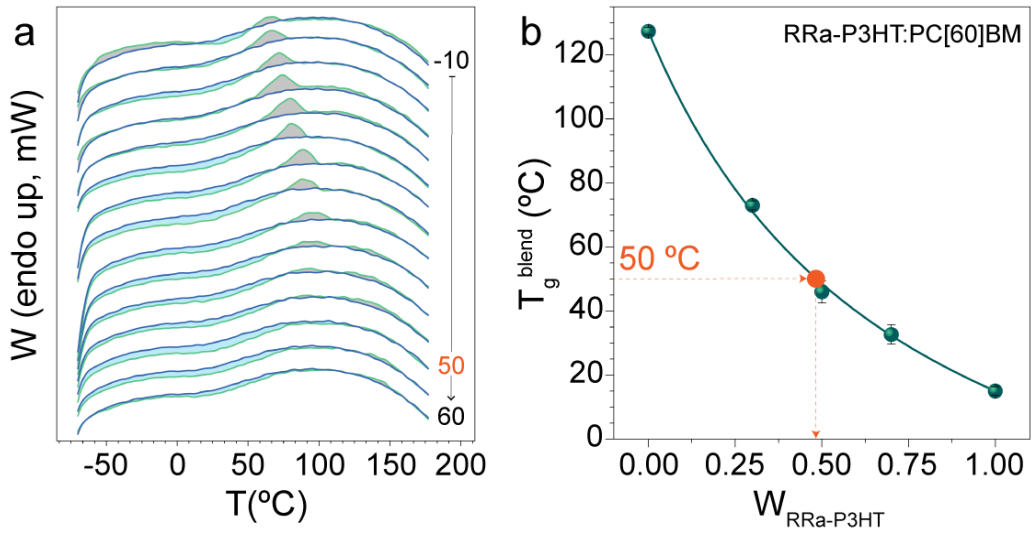

Figure 5.15 (a) FSC heating scans recorded at 4000 °C·s^{-1} for RRa-P3HT:PC[60]BM 1:1 blends. The T_a applied in each experiment is indicated on the right-hand side of each curve. Prior to this measurements the samples were annealed at 190 ºC for 30.[264] (b) $T_{g,onset}$ vs $w_{RRa-P3HT}$ for the RRa-P3HT:PC[60]BM blend.. Solid grey line is the fit to the Gordon-Taylor model. The arrow indicates the concentration of the intermixed phase of the sample annealed.

5.4. Conclusions

To summarize, in this chapter we have developed a novel methodology based on fast scanning calorimetry to quantitatively measure the absolute composition of amorphous intermixed domains in donor:acceptor thin films for solar cells. To do so, different polymer:fullerene binary blend

systems have been studied and we have learned the importance of knowing the composition of these intermixed phases as they have a direct impact on the device's characteristics. In general we have extracted the conclusion included below:

- The model binary systems with regioregular P3HT polymer and OXCMA and OXCBA fullerene adducts display a complex phase nanomorphology with amorphous intermixed domains and relatively-phase pure domains. We found that P3HT:OXCBA blend present a higher miscibility compared to P3HT:OXCMA binaries.

- The Tg of binary blends vitrified from the miscible state can be readily determined by applying the approach developed by Cangialosi et al. .[135] Thus, we used this experimental data to build the "master curves" for each multicomponent system. The experimental data from FSC fitted well with the Gordon-Taylor model, from which we conclude that ultra-fast cooling from the melt with the FSC fully prevents phase separation and formation of crystalline moieties, essentially fully vitrifying the blends.

- We have proved that our methodology to determine the composition of intermixed domains is applicable in samples processed as devices, *e.g.* thin films spin cast on PEDOT:PSS layers. we succeeded in recording the endothermic process attributed to amorphous intermixed domains of solar cell replicas.

- Our results indicate in that P3HT:OXCMA blends prepared as for device fabrication, the P3HT enrichment of the amorphous intermixed (w_{P3HT} = 0.85) phase comes at the expense of a reduced fraction of relatively phase-pure P3HT domains (*i.e.*, crystalline P3HT regions). In contrast, in P3HT:OXCBA binaries, the strong vitrification effect of OXCBA does not allow for any structural development (w_{P3HT} = 0.42). The original composition is essentially 'frozen-in', leading to a thin-film structure composed predominantly of the amorphous intermixed phase, in agreement with the featureless SAXS data that we obtained for P3HT:OXCBA.

- We emphasize the importance of quantifying the absolute composition of these amorphous intermixed phases as they present quantifiable consequences in device performance. Higher effective mobilities are achieved for P3HT:OXCBA 1:1 binary system, which has a higher tendency to vitrify 1:1 P3HT:OXCMA blends, while they present similar capability to generate charges.

- Finally, the close agreement of our compositional data with Ade's and Gomez's reports based on RRa-P3HT:PC[60]BM blend allowed as validating the methodology and, most significantly, heralds in particular fast scanning calorimetry as the key tool to open new opportunities for the fundamental investigation of functional materials systems, such as donor:acceptor blends but also other functional materials systems, such as metal halide perovskites and solution-processable oxides.

- Most importantly, complementing current compositional characterizations of organic solar cells with the quantitative analysis of the amorphous phases will contribute to advancing fundamental morphology-function models for rational device engineering.

6. The impact of donor/acceptor ordering on organic solar cell devices

6.1. Summary

Processing variables, such as solvents and additives, have proven to be an effective tool to modify the microstructure and, thus, the active layer morphology of OPV devices. In previous chapters, we proved that the domain size and packing of non-fullerene acceptor domains can be modulated by an appropriate selection of solvents and additives. For example, we found that DIO enhances the crystallization of phase I polymorph regardless of the solvent used. In this chapter, as a proof-of-concept, we exploit the highly efficient state-of-the-art PBDB-T:ITIC blend, which was extensively investigated throughout the thesis, and delineate the relevant effect of enhanced ordering of the individual components within the overall morphology. First, we explore the effect of casting solvent into the polymer paracrystallinity and show that its solution in o-xylene can result in an enhanced paracrystallinity. Then, we discussed four model scenarios with respect to their microstructure/morphology and quality of mixing. We determine specific device-related parameters and we rationalized the results on the basis of the structure-morphology-function relation. Our results showed a superiorly high power conversion efficiency (up to 9.8%) in the systems that revealed the absence of discrete crystalline acceptor domains, in contrast to the specimens were ITIC crystalline regions were found, which dramatically reduced charge generation attributed to a greater phase separation. Additionally, we found that the active layer morphology is more sensible to acceptor crystallization than polymer paracrystallinity perfectioning. Albeit preliminary, we claim that the concept of polymeric paracrystals and their refinement by suitable processing solvents are a parameter to be taken into account in currently established morphology-function models where this polymer microstructure and temperature-dependent evolution has not been accounted for.

6.2. Introduction

The performance of solution-processed organic solar cells (OPV) is driven by the fine microstructure of the carefully optimised bulk heterojunction morphology, comprising precisely mixed and relatively separated donor/acceptor regions.[120,146] This metastable morphology is one of the limiting factors for the stability of OSC devices and currently one of the biggest challenges for the OPV community.[192] Although morphology can be regulated by rational molecular engineering,[131,266–268] changes in molecular weight[101,171,269] and various approaches before film processing,[270,271] it can also be easily altered by external stress, such as photon illumination,[58,192] chemical environment and heat treatment,[272] resulting in modifications to their optical, electronic and optoelectronic properties.[273]

Deviations from device-optimized morphology have been extensively related to the SMA crystallization resulting in mixed phases depletion[48,274] or demixing through thermodynamic relaxation of the initially quenched composition.[120,121] On the contrary, in view of our recently introduced microstructural model,[275] the influence of the polymer paracrystals, the evolution of this ordering and the direct correlation with the morphological characteristics and function of the device remain totally elusive. This is because advanced morphology-function and stability prediction models for organic solar cell[47,166] as well as function models for OFETs[276] were built on the premise that donor polymer materials such as FTAZ,[120] PBDB-T or PM6 are amorphous.

Notwithstanding, the pre-aggregation behaviour of donor polymers in solution has become of great interest, as some studies found that they play a key role in the morphology of the active layer.[150,277,278] In particular, in polymer:fullerene systems, a good control of their optimal temperature-dependent aggregation behaviour, in combination with the suitable choice of solvents and acceptors, has led to optimised morphologies, reaching efficiencies higher than those of the state-of-the-art systems.[94] It is known that the use of solvent additives together with the primary solvent[106,109,114,115] leads to long-term morphological instability as it increases the diffusion capacity of donor and acceptor molecules, due to the uncontrollable drying processes of the high-boiling additives,[106] and, in general, mainly affects the ordering of the non-fullerene

acceptor [109,115,279] similar to fullerene acceptors.[280] On the other hand, primary solvents can induce donor polymer or SMA aggregation linked to their solubility.[281,282] For example, Xiao et al. recently studied the impact of donor and acceptor pre-aggregation on the morphology of the active layer through the selection of proper processing solvents, and showed that the matching of donor and acceptor pre-aggregation contributed to the efficiency and stability of the PTB7-Th;F8IC system. [271] Hence, considering the full microstructural picture, this previous misinterpretation clamours for an exploration of the influence of individual donor and acceptor aggregation with respect to the overall morphology, thus providing useful guidelines in the development of more complete morphology-function models.

In this work, inspired by the diverse and intricate microstructural features reported earlier in the thesis, we explored how the structural order to PBDB-T and ITIC impact on the solar cell function. For that, we produced organic solar cell devices in which the degree of structural order of the individual components and thus the overall morphology has been selectively adjusted. We managed to tailor individually the degree of structural order of both materials via processing in suitable solvents. More specifically, films were processed from solvent/additive mixtures, i.e. o-xylene/1%diiodoactane, chlorobenzene/1%diiodactane, o-xylene and chloroform, and fabricated with a thickness gradient, thus providing additional information on the optimal thickness and thickness dependent effects. As a key finding, we identified the paracrystalline order enhancement effect induced by o-xylene casting. This enabled the comparative study between the impact of crystalline-acceptor regions or improved paracrystalline domains, as well as systems in which both components present an improved or strongly reduced ordering. We found that the best device characteristics were obtained in the system where the materials were presented in their most disordered state (note that PBDB-T even from chloroform presents a dense arrangement of paracrystals) and present a largely mixed morphology. Meanwhile, systems with higher order of both components resulted in an over-purification of the mixed domains and were detrimental to the device.[120] Intriguingly, solar cells with enhanced paracrystalline polymer domains showed comparable properties to the top performers in addition to being cast from non-halogenated

solvent. Therefore, although additional work must be undertaken, advanced morphology-function and stability prediction models considering polymer paracrystalline microstructure should be developed.

6.3. Results and Discussion

6.3.1. Screening of processing solvents

In this section, we identify the effect of various solvents and the well-known additive DIO in the microstructure of pure PBDB-T and ITIC thin films. For this, we prepare a large number of samples using distinct processing conditions and characterize them by means of Grazing-Incidence Wide-Angle X-ray Scattering (GIWAXS).

In section 4.3.3, we have presented GIWAXS data of ITIC thin films cast with different concentrations of DIO. We draw the conclusion that the addition of a small amount of the additive promotes the strong crystallisation of ITIC phase I polymorph regardless of the solvent used. Furthermore, we selected a variety of solvents of different nature to study the effect of the casting solvent on phase I crystallisation including halogenated, non-halogenated, aromatic and linear solvents. The aforementioned findings showed that low-crystalline phase I is formed when ITIC is cast from chlorobenzene or *orto*-dichlorobenzene, while it remains amorphous or is vitrified when cast from solvents such as chloroform, dichloromethane or orto-xylene.[183]

Consistently, after identifying the processing conditions that promote the crystallization of ITIC, we analyzed the effect of casting solvent into PBDB-T donor polymers paracrystals. To do so, a 20 $mg \cdot mL^{-1}$ solution in chlorobenzene, orto-xylene and chloroform was spun cast on top of a silicon substrate. **Figure 6.1** shows the patterns of pure PBDB-T cast from different solvents. From 2D GIWAXS patterns and 1D profiles, there exist a similar π-π stacking diffraction features concentrated $q =\sim 16.6\ nm^{-1}$ [172,283] while the peak intensity and breadth of the lamellar peak located at $q =\sim 3.3\ nm^{-1}$ varies with processing solvent. The significant enhancement in the

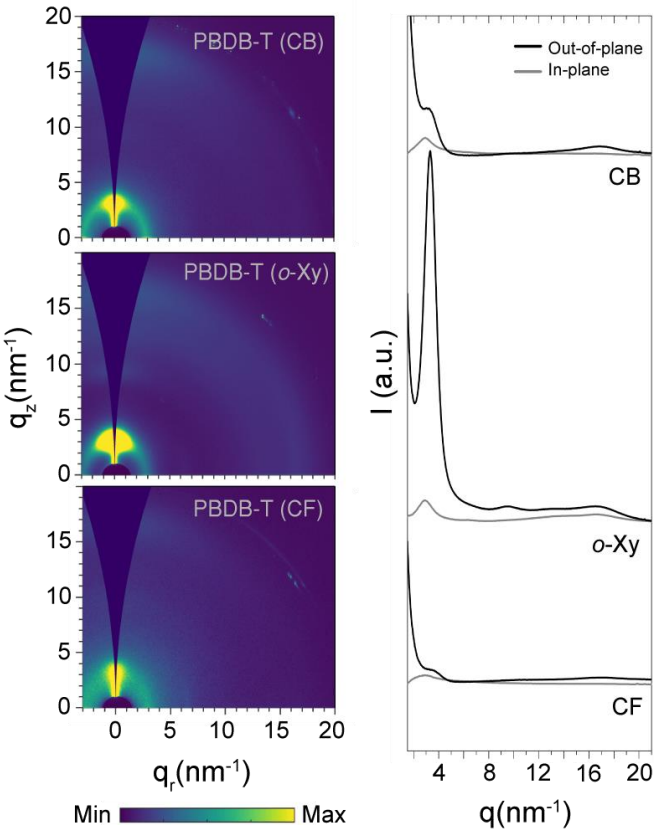

Figure 6.1 2D-GIWAXS patterns of PBDB-T spin-cast from chlorobencene [CB], orto-xylene [o-Xy], and chloroform [CF]. Out-of-plane and in-plane profiles (d).

Table 6.1 Peak position and crystalline coherence length (CCL) values of the GIWAXS reflections for the four different scenarios.

Blend	**Solvent**	Lamellar (100)			π-π peak		
		q, nm^{-1} (d, nm)	CCL	*g* (%)	q, nm^{-1} (d, nm)	CCL	*g* (%)
PBDB-T	**CB**	3.4 (1.84)	5.8	22.8	16.9 (0.37)	1.7	18.7
PBDB-T	**o-Xy**	3.3 (1.90)	7.3	20.3	16.8 (0.37)	1.8	18.2
PBDB-T	**CF**	3.3 (1.90)	6.5	22.1	16.7 (0.38)	1.6	19.0

intensity of the first lamellar order comparing with the π-π stacking peak and the improvement in the resolution of the third lamellar order that emerges as PBDB-T is spun cast from orto-xylene, suggests an improvement in the paracrystalline order. For comparison, the lamellar and π–π

paracrystalline parameter and coherence lengths (L) can be quantified by the full width at half-maximum and the maximum of the (100) and (010) diffraction peak. As summarized in **Table 6.1** while there is no noticeable variation in the π–π coherence length and *g* parameter, the same values for the lamellar order experience a slight decrease by a factor of ~2 when PBDB-T is processed from o-xylene.

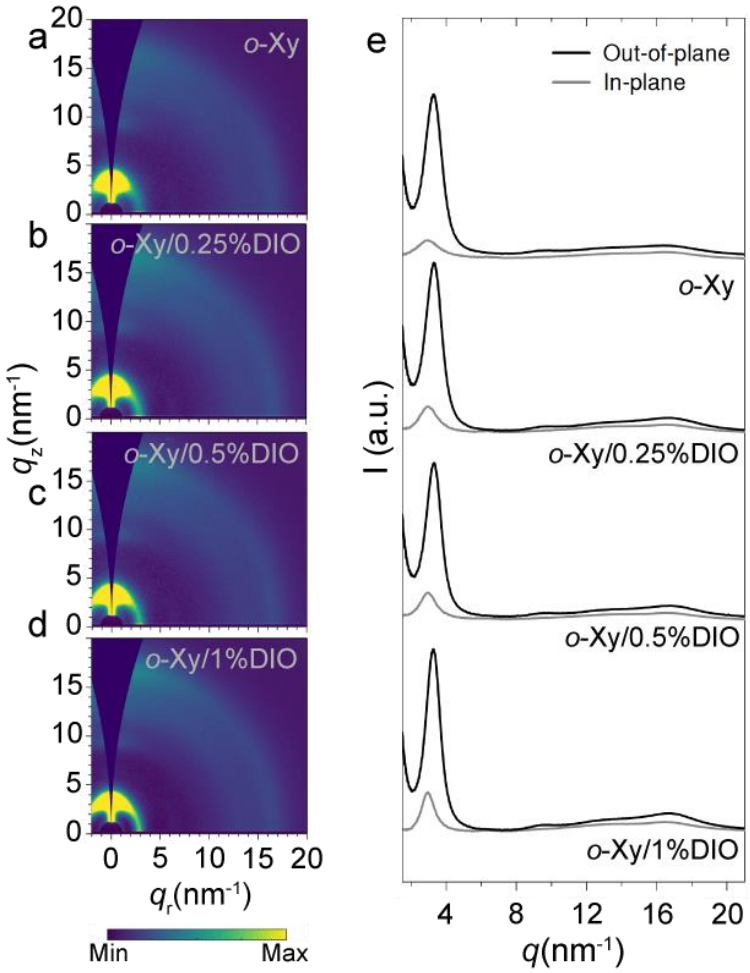

Figure 6.2 2D-GIWAXS patterns of PBDB-T spin-cast from orto-xylene [o-Xy/DIO] (a), orto-xylene and 0.25 v/v% diiodoctane [o-Xy/0.25% DIO] (b), orto-xylene and 0.5 v/v% diiodoctane [o-Xy/0.5% DIO] (c) and orto-xylene and 1 v/v% diiodoctane [o-Xy/1% DIO] (d). Out-of-plane and in-plane profiles (e)

.

On the other hand, **Figure 6.2** illustrates the analysis of PBDB-T thin films measured by GIWAXS to evaluate the effect of DIO addition on the microstructure. In this case, our data revealed that while DIO has a pronounced effect on ITIC crystallisation, the microstructure of

PBDB-T did not show a significant alteration upon addition of the additive. This can be deduced from the comparison between the pure polymer film (**Figure 6.2**a) and the films containing DIO (**Figure 6.2**b-d), where both out-of-plane and in-plane profiles depict only a slight narrowing of the lamellar peaks as the additive concentration rises.

6.3.2. Selective microstructure modification of the active layer components

Here we present the detailed microstructural analysis of the four systems studied in this chapter. For this purpouse, we employ four characterization techniques: (1) GIWAXS, which gives information about molecular ordering in the binary blends and will be the key tool in identifying the four different scenarios. (2) Photoluminescence spectroscopy, which provides information about the quality of blending and (3) GISAXS which was employed for morphological analysis.

Thus, with a rational combination of solvent and additives, we spun cast 50:50 PBDB-T:ITIC solution dissolved in (1) orto-xylene and diiodoctane 99:1 volume ratio, (2) chlorobenzene and diiodoctane 99:1 volume ratio, (3) o-xylene and (4) chloroform. PBDB-T:ITIC 50:50 mass ratio was used as it is reported to be the optimize ratio in literature[34,284] Although donor-acceptor mixing in BHJ usually results in a reduction of the crystallinity of the donor and acceptor phases and makes indexing and visualisation of the scattering pattern challenging, we find that in this case the results show compelling evidence for our findings and assertions. Although it was addressed for these system[106] that 1% DIO resulted in devices with poorer properties due to larger crystal domain sizes, we selected thus for morphology and microstructure comparisons.

6.3.2.1. GIWAXS: identifying the four scenarios

By comparing side-by side the scattering patterns of the binary blend of PBDB-T:ITIC spun cast from carefully selected solvent mixtures, we could clearly confirm the presence of four different scenarios. The corresponding patterns and intensity 1D profiles along the out-of-plane and in-plane direction are depicted in **Figure 6.3**.

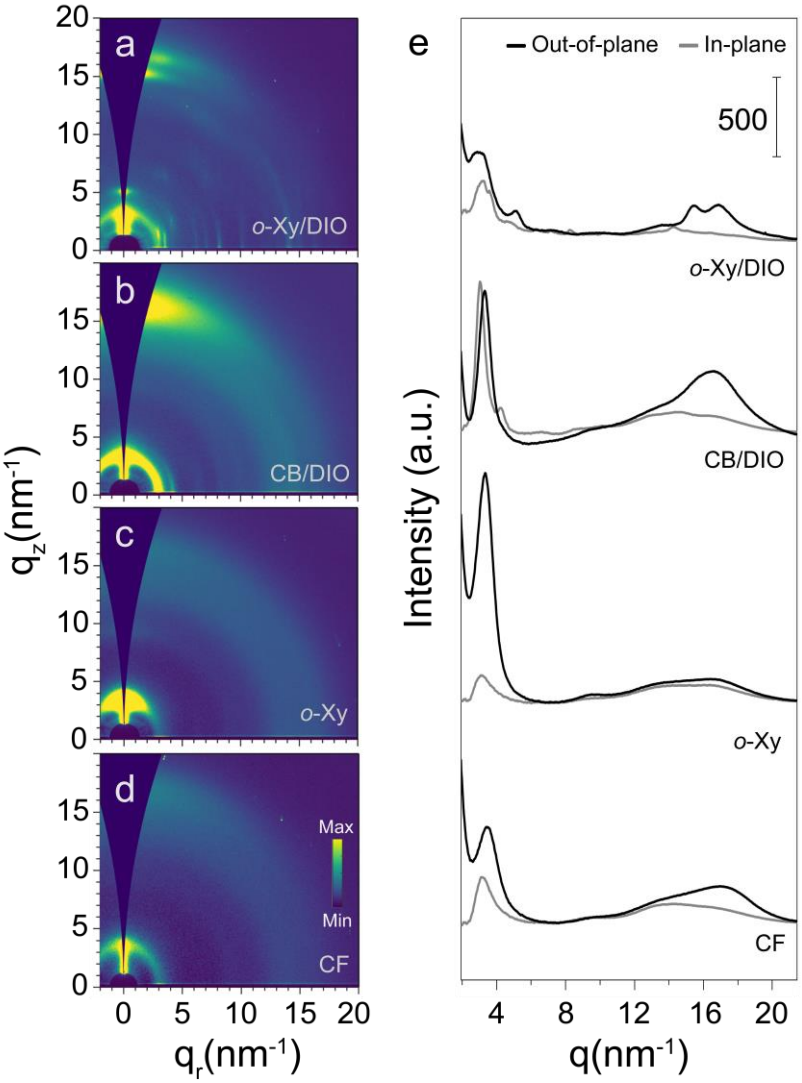

Figure 6.3 2D-GIWAXS patterns of PBDB-T:ITIC 50:50 blend spin-cast from orto-xylene and 1 v/v% diiodoctane [o-Xy/DIO] (a), chlorobencene and 1 v/v% DIO [CB/DIO] (b), orto-xylene [o-Xy] (c) and chloroform [CF] (d). Out-of-plane and in-plane profiles (e).

- (1) HIGHLY ORDERED DONOR AND ACCEPTOR (**Figure 6.3**a): The first system is obtained after casting the mixture from a solution in orto-xylene and diiodoctane. Our GIWAXS results show that the film has multiple diffraction peaks in the low-q region attributed to ITIC with the characteristic sharp lamellar peak at q = 5.1 nm^{-1}. In addition, the pattern shows the diffuse scattering of the π-π planes of ITIC (see section 4.3.1.1). As expected, we have a strong acceptor crystallinity due to the addition of the additive which screens the π-π stacking peak of PBDB-T. Our GIWAXS data, nonetheless, more than demonstrated the effect of o-Xy on the

microstructure of the polymer. As for the polymer scattering signals, we detect a strong lamellar peak related to the polymer preferentially oriented in the out-of-plane direction.

- (2) POORLY ORDERED DONOR AND HIGHLY ORDERED ACCEPTOR (**Figure 6.3**b): The second case obtained by casting the mixture from a chlorobenzene/diiodoctane solution shows the characteristic multiple scattering peak reflections of crystalline ITIC, confirming that the DIO allows selective ordering of the non-fullerene acceptor in the mixture (see section 4.3.1.1). Furthermore, the pattern shows similar PBDB-T packing to that found in the pure PBDB-T film deposited from chlorobenzene (**Figure 6.1**), meaning that the packing is preserved in the mixture.

- (3) HIGHLY ORDERED DONOR AND POORLY ORDERED ACCEPTOR (**Figure 6.3**c): The third scenario is achieved after spun-casting the PBDB-T:ITIC blend from orto-xylene. The GIWAXS pattern shows a much improved lamellar order compared to the π-π stacking reflection in the polymer, similar to that observed in the pure materials depicted in **Figure 6.1**. Nevertheless, no signs of ITIC-related scattering peaks are observed, suggesting that ITIC is either in its amorphous state or that the crystallinity has significantly decreased after blending.

- (4) POORLY ORDERED DONOR AND ACCEPTOR (**Figure 6.3**d): The fourth and final system is obtained from chloroform in which both the polymer and the small molecule are in their most disordered or glassy state. This is mirrored in the diffraction pattern as no reflections related to the crystalline phase of ITIC are observed and the reflections corresponding to the polymer are the same as those observed in the pattern of the pure material cast from chloroform.

Thus, **Figure 6.4** emphasises that by employing specific processing conditions we can selectively fine-tune the order of the individual components in the blend and thereby study the effect of the microstructure on the solar cell device.[271] A complete schematic of the systems developed for this study is illustrated in **Figure 6.4**.

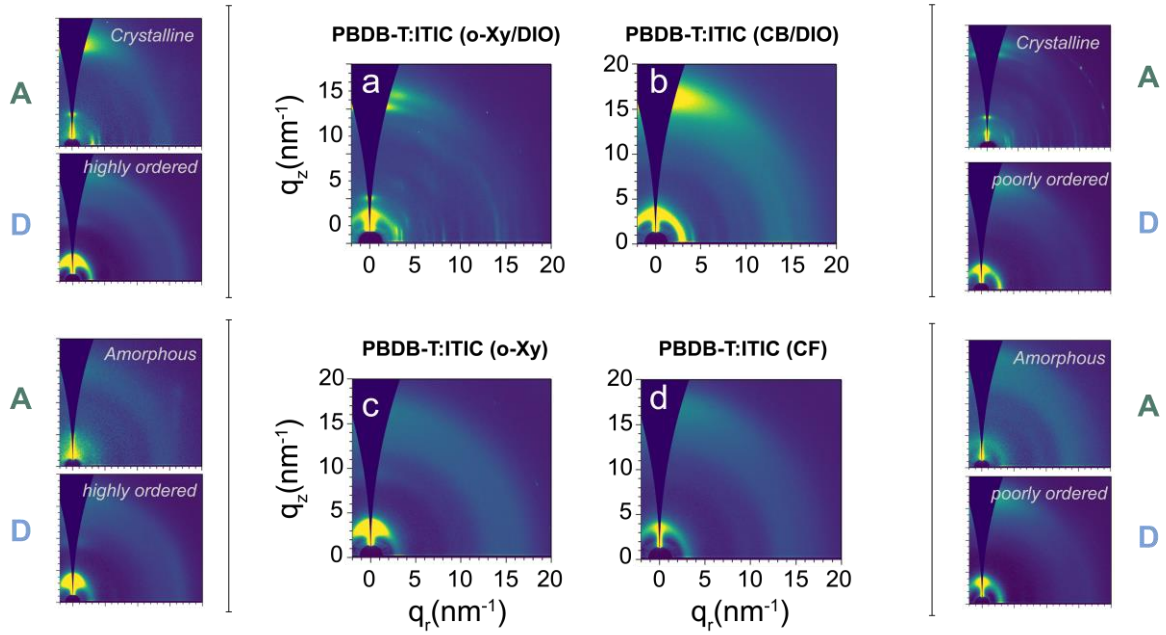

Figure 6.4 Summary of the four different systems in which the microstructure of each of the components has been selectively tuned to obtain the depicted four scenarios: (a) o-Xy/DIO, (b) CB/DIO, (c) o-Xy and (d) CF. Inset patterns correspond to the reference materials cast from the respective solvents.

6.3.2.2. PHOTOLUMINISCENCE: molecular interaction and mixing

Having characterised and rationalised the processing conditions leading to each of the different scenarios, we focused on assessing the quality of the blend with respect to changes in the microstructure. PL measurements were performed on the same thin films measured by GIWAXS and information was extracted based on how the positions and strength of the optical transitions are affected by molecular interaction and mixing. **Figure 6.5** presents the photoluminescence spectra for the PBDB-T:ITIC blends solution cast from o-Xy/DIO, CB/DIO, o-Xy and CF and the corresponding pristine materials cast from the same solvents. All the spectra were obtained exciting the samples with a monochromatic 633 nm laser and normalized to thickness.

The PL emission from the ITIC thin film shows a major emission peak and a faint shoulder. Interestingly, the position of the main PL emission peak for crystalline ITIC is red-shifted by 18 nm compared to vitrified ITIC (754 nm vs. 772 nm). Conversely, PBDB-T films

exhibited much weaker PL emission as compared with ITIC. After mixing, all systems show a strong decrease in PL intensity. The PL quenching has a direct correlation with the effectiveness of exciton dissociation at the donor-acceptor interface.[285] A stronger PL quenching intensity may be related to a more effective exciton separation at the donor-acceptor interface, as the electron, before re-emitting, finds a new path for electron decay towards the acceptor enhancing photoinduced charge transfer.[78] Binary blends obtained from o-Xy and CF, where the ITIC is vitrified, appeared more quenched compared to binaries where the ITIC is highly crystalline which may be attributed to a higher degree of intermixing of the donor polymer and acceptor.[286]

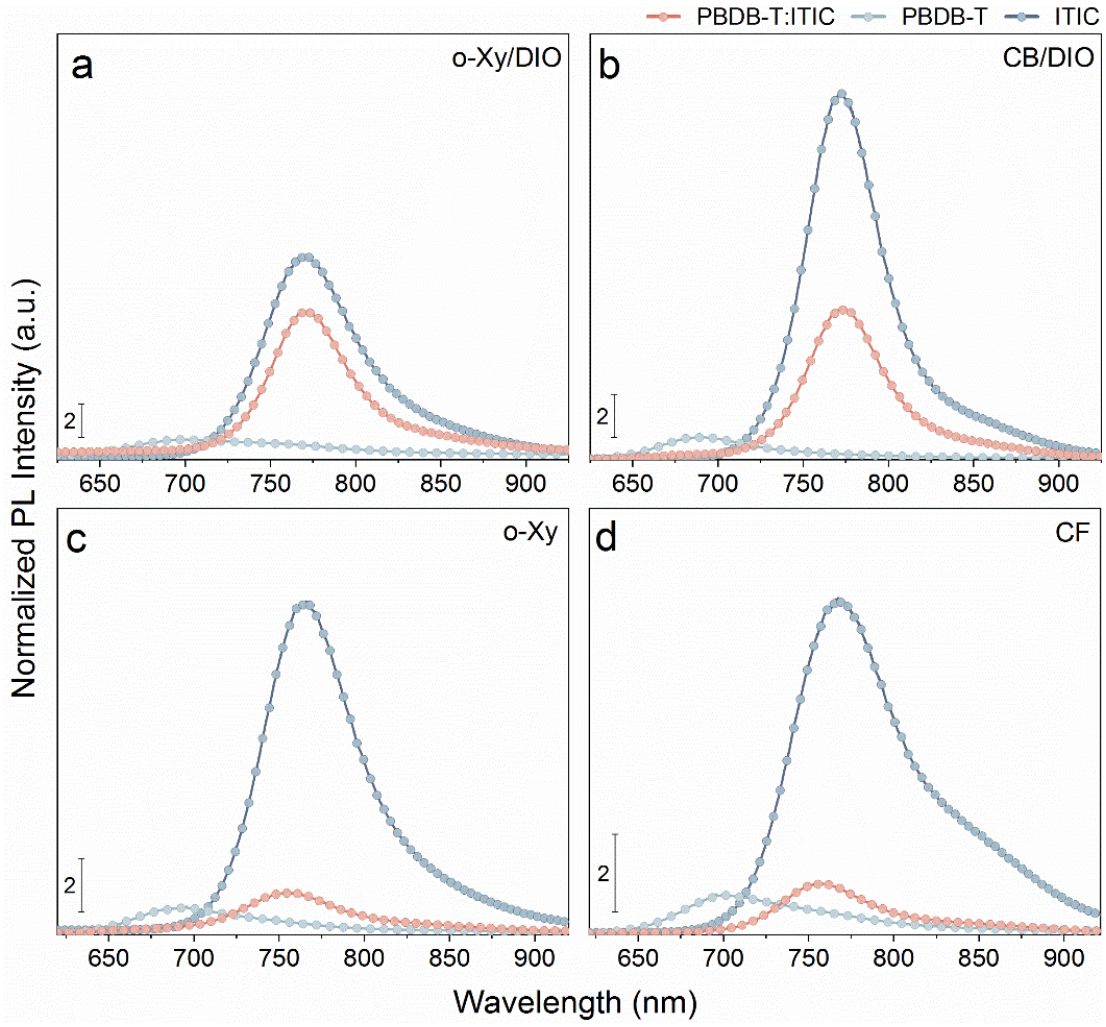

Figure 6.5 Thickness normalized Photoluminescence spectra of PBDB-T:ITIC 50:50 blend and reference materials, PBDB-T and ITIC spin-cast from orto-xylene and 1 v/v% diiodoctane [o-Xy/DIO] (a), chlorobencene and 1 v/v% DIO [CB/DIO] (b), orto-xylene [o-Xy] (c) and chloroform [CF] (d).

This rather low quenching found in the DIO-containing systems may be related to higher phase separation due to higher ITIC crystallisation[48,214,285,287] Additionally, although PL quenching was proven to be dependent on acceptor crystallisation, enhancement of polymer paracrystallinity did not affect the overall BHJ. Hence, the analysis of PL spectra has indeed contributed to highlight the difference between the microstructural scenarios involving the same material blend and composition.

6.3.2.3. GISAXS: morphological characterization

In this section, the morphology at the nanoscale is examined by GISAXS and the effect of selectively tuning the mixture components at the morphological level is visualised. GISAXS measurements were performed on the same thin films measured by GIWAXS and PL to obtain information on the lateral and normal ordering on a surface or inside the thin film. The scattering signals are extracted in the Yoneda region through horizontal cuts, as this is the critical angle at which the scattering signal is strongly enhanced. The horizontal cuts of each system are plotted in **Figure 6.6**.

The greater intensity of the scattering is caused by a higher electron density contrast, i.e. a higher microphase separation of the ITIC crystalline domains, the PBDB-T paracrystals and the mixed amorphous phases. Thereby we confirm that the use of different solvents and additives leads to the modification of the morphology.[288] Generally conceived, all systems show profiles dominated by scattering decay. Interestingly, the system in which both components are in the higher order state (i.e. deposited from o-Xy/DIO) shows the strongest scattering intensity, while the system in which both components are more disordered or vitrified (i.e. spun-cast from CF) feature the weakest scattering intensity. Therefore, we propose as a general concept that the increase of the microstructural order enhances the microphase separation causing the rise of the scattering contrast by domain purification due to aggregation and enlargement of the domains of the pure materials. [106,288] This would agree with a weaker PL quenching found for the films containing DIO.

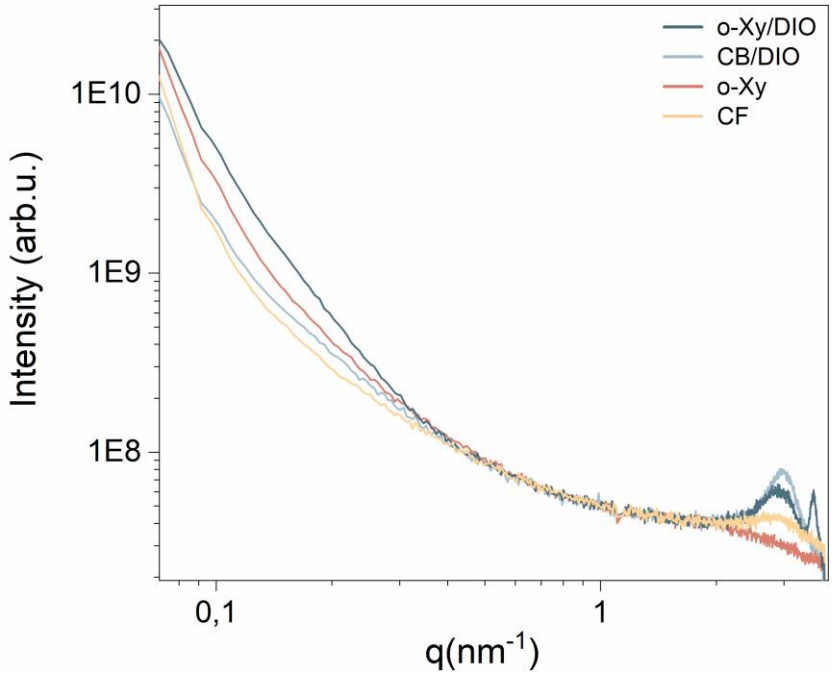

Figure 6.6 GISAXS horizontal cuts of PBDB-T:ITIC 50:50 blend spin-cast from orto-xylene and 1 v/v% diiodoctane [o-Xy/DIO], chlorobencene and 1 v/v% DIO [CB/DIO], orto-xylene [o-Xy] and chloroform [CF].

6.3.3. Interplay between microstructure and device performance

To comprehend the influence of microstructure and morphology on device performance, solar cells were prepared based on the binary blends cast from carefully selected solvents and additive mixtures (see section 6.3.2.1). For this purpouse, solar cells with thickness-gradient blade coated in inverted geometry ITO/ZnO/active layer/MoO_3/Ag have been fabricated (see section 2.3.5.1). To ensure that the studied thin film microstructures are retained in blade coated solar cells devices, GIWAXS measurements of the blade coated films were tested on a glass slide, and the results (see Appendix C **Figure C-1**) gave convincing evidence for the presence of the four different scenarios. For comparison purposes, the thicknesses of these samples were obtained by mechanical profilometry at equidistant points along the active layer. Device parameters and UV-Vis were measured on the non-encapsulated samples, while EQE and current versus light intensity experiments were developed on the encapsulated samples to avoid photoxidation.

6.3.3.1. Device parameters

Representative current density-voltage (J-V) curves of binary solar cells processed from different solvent/additive mixtures and measured under 1 sun illumination are depicted in **Figure 6.7**a and the corresponding device characteristics (J_{SC}, V_{OC}, FF and PCE) are deduced from the J-V characteristics are summarized in **Table 6.2**. **Figure 6.7** exhibits the best and representative J-V curves of the four different scenarios with optimised thickness (i.e. PBDB-T:ITIC (1:1) solution-processed from o-Xy/DIO, CB/DIO, o-Xy and CF), the UV-Vis and EQE spectra of the corresponding devices and, the J_{SC} versus light intensity measurements.

Overall, devices containing DIO (i.e. large crystalline fraction) exhibit worse device performance than binaries where ITIC is mainly amorphous. Amorphous ITIC yields devices with significantly improved performance, while the increase of the paracrystalline order of the polymer appears not to be detrimental to the performance of the device.[171] More specifically, the film processed from o-Xy/DIO solution, in which both donor and acceptor components are structurally ordered, shows the poorest PCE value, i.e. 3.4%, with a short-circuit current (J_{SC}), open circuit voltage (V_{OC}) and a fill factor (FF) of 8.26 mA·cm^{-2}, 0.90 V and 46.2 % respectively. This results suggest a strong microphase separation in this system. This interpretation was previously reported in literature for P3HT:ITIC system where the excessive degree of crystallinity of ITIC was proven detrimental for the device performance.[289] Moreover, Wang et al.[279] quantify that binaries of PBDB-T:ITIC with 1%DIO content caused serious gradient ITIC concentration vertical distribution and overcrystallization of ITIC.

On the other hand, the PBDB-T:ITIC specimen processed from CF (i.e. the system were both components are in their most disorder state) which depicted weaker GISAXS scattering and strong PL quenching, showed greatly improved device parameters, leading to a PCE value of 9.8% with J_{sc}, V_{oc}, and FF being 16.1 mA·cm^{-2}, 0.90 V, and 67.9% respectively. Interestingly, the device parameters are more sensitive to the crystallisation of the acceptor than to the enhancement of the paracrystalline order of the donor. Indeed, while the device processed from o-Xy resulted in a PCE value comparable to that of the CF device, being 8.65%, with J_{sc}, V_{oc}, and

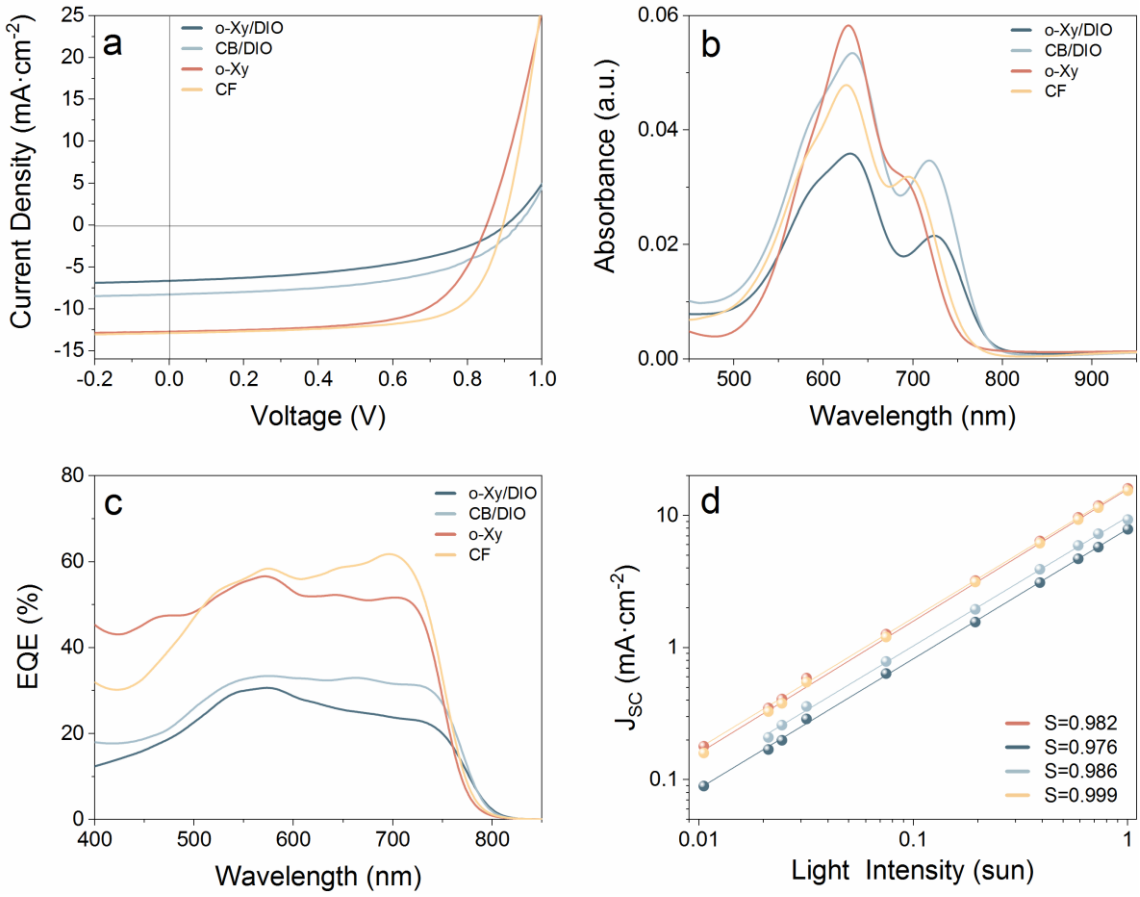

Figure 6.7 Representative current density–voltage (J–V) curves under the illumination of 1 sun (a), UV-Vis absorption spectra corrected by the film thickness (b), external quantum efficiency (EQE) spectra (c) and J_{SC} versus light intensity (d) of the PSCs based on PBDB-T:ITIC cast from different solvents.

Table 6.2 Photovoltaic Parameters of OSCs under AM 1.5G Illumination, 100 mW·cm^{-2} blends

Blend	**Solvent**	Thickness [nm]	E_g [eV]	V_{OC} [V]	J_{SC} [mA·cm^{-2}]	FF [%]	PCE [%]
PBDB-T:ITIC	**o-Xy/DIO**	52	1.59	0.90	-8.26	46.19	3.45
PBDB-T:ITIC	**CB/DIO**	43	1.59	0.92	-10.80	55.31	5.49
PBDB-T:ITIC	**o-Xy**	75	1.63	0.85	-15.85	64.40	8.65
PBDB-T:ITIC	**CF**	43	1.65	0.90	-16.06	67.87	9.76

FF being 15.6 mA·cm^{-2}, 0.85 V, and 64.4% respectively; the device blade coated from CB/DIO yielded much reduced device parameters showing a PCE of 5.5% with J_{sc}, V_{oc}, and FF being 10.8

$mA \cdot cm^{-2}$, 0.92 V, and 55.3% respectively. The loss in efficiency is due to the significant decrease in J_{sc} from 15.6 to 10.8 $mA \cdot cm^{-2}$. Therefore, devices in which the acceptor was vitrified offer significantly better performance – driven by an enhancement of the higher J_{SC} and FF values, due to a more optimize blend morphology with presumably smaller nanodomains (**Figure 6.7**c). Moreover, we found that the impact of the DIO additive is strongly dependent of the solvent used (we found a different of PCE ~2% in o-Xy/DIO blend comping with CB/DIO). The small changes in V_{OC} are connected to variations at molecular level such as crystalline behaviour, morphology and absorption edge.

The UV-Vis absorption spectra (corrected by film thickness) of the champion devices are plotted in **Figure 6.7**b. All four systems reveal the characteristic strong absorption peaks associated with PBDB-T and ITIC.[31,183,290] The maximum absorption peak of ITIC red-shifts after the addition of DIO, regardless of the solvent used, suggesting increased acceptor self-organisation.[290] Furthermore, while the o-Xy/DIO, CB/DIO and CF samples show strong absorption peaks of both PBDB-T and ITIC in the visible wavelength range, the film processed from o-Xy, displays a higher absorption intensity of the 0-0 polymer vibronic peak compared to the ITIC contribution, again suggesting higher polymer aggregation compatible with enhanced paracrystallinity.[278]

The external quantum efficiency (EQE) curves of the optimized devices are shown in **Figure 6.7**c. Although having processing solvent as the only different variable, the four systems showed substantially different photoresponses in the range of 400 and 800 nm. The spectral range of each binary revels the vibronic peaks of both PBDB-T and ITIC. However, shows photoresponses with average of almost 60% for the blend without DIO while nearly half is obtained for the mixtures containing DIO. Consistently, the devices possessing a significantly higher photoresponse exhibited the best FF (i.e. o-Xy 64.4% and CF 67.9%) plus enhanced J_{SC}.

To understand the differences in device FF induced by the effect of microstructural and morphological variations, we studied the extent of bimolecular recombination. It is of great importance to bear in mind that once free charge carriers have been generated in the active layer,

charge recombination plays an important role in whether or not charges can be extracted, and therefore we measure the photocurrent as a function of the light intensity (**Figure 6.7**d).[291] J_{SC} of the best device was plot against light intensity in a double-logarithm scale which can be expressed as Jsc $\propto$ (Plight)^{S} in organic solar cells, where S is the exponential factor (i.e. slope), and weak bimolecular recombination in the device would result in a S value close to unity.[292,293] Thus, the best device processed from CF possess an S value of 0.999 very close to unity suggesting very weak bimolecular recombination, while the device processed from o-Xy/DIO exhibits the lowest S value (0.976) indicating stronger molecular recombination. In general, the obtained S values are in agreement with the J_{SC}, FF and V_{OC} values extracted from J-V curves.

6.3.3.2. Interplay between thickness and performance

Taking advantage of the high throughput technique using gradients of thickness,[16] we developed a device parameter thickness sensitivity study. Data points represent average values of measurements done for minimum 3 pixels every 50 nm thickness and the average was calculated among different substrates.

6.3.3.2.1. Device parameters

Considering that PCE improvements are mostly attributed to the increases in J_{SC} and FF parameters, and these two show strong correlation with the film thickness,[229] detailed investigations on the performance as a function of thickness of the four systems were conducted. The thickness-gradient devices were prepared as summarized in 2.3.5.1. **Figure 6.8** depicts the active layer thickness dependence of PCE, FF, J_{SC} and V_{OC}. All the devices displayed the optimum thickness within a relatively wide range approximately between 50 and 250 nm. Although, the main differences are found between the systems were the NFA is highly crystalline (i.e. presenting the poorest device performance) and the scenarios characterized by the absence of ITIC crystal domain. In the systems were the SMA is highly crystalline, the PCE, FF and J_{sc} have a milder

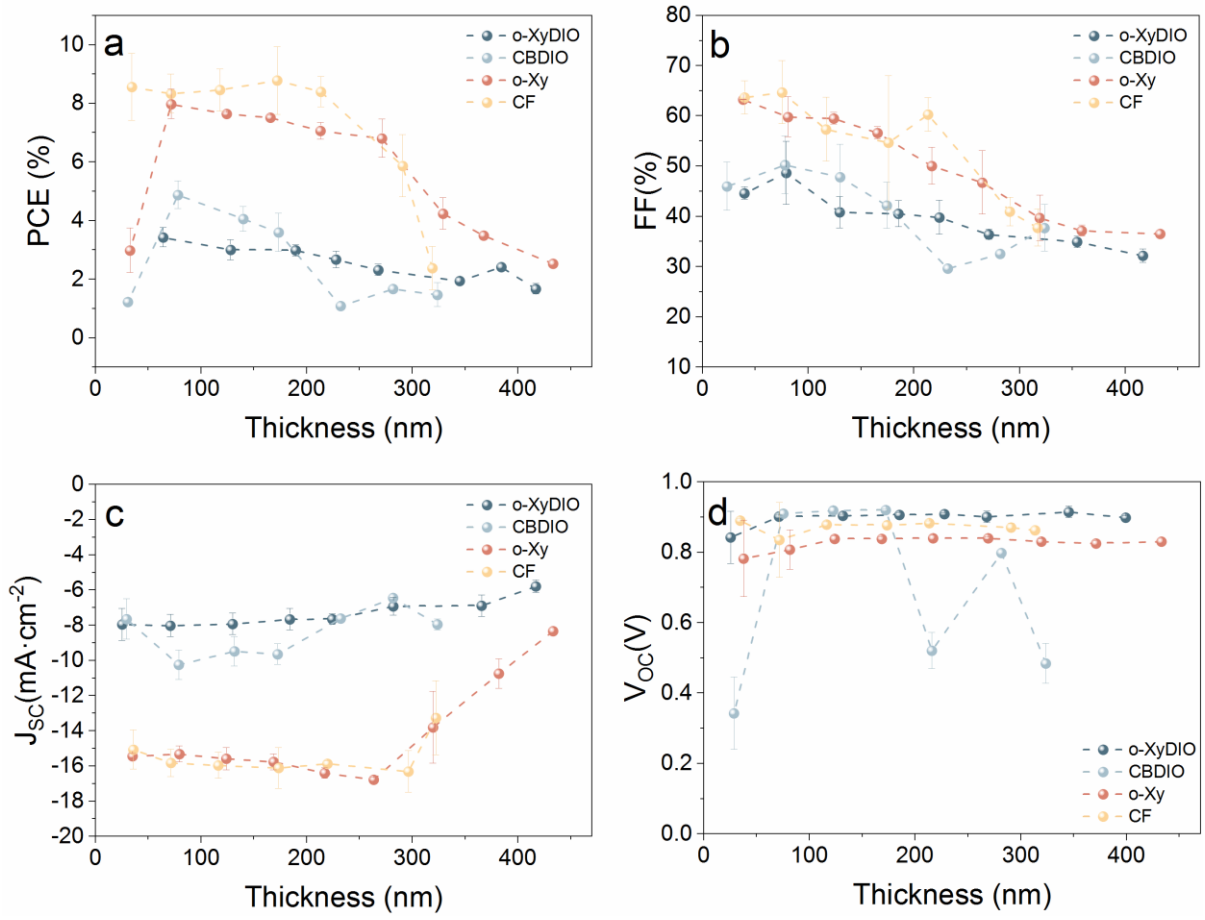

Figure 6.8 Power conversion efficiency (PCE) (a), fill factor (FF) (b), short-circuit current density (J_{SC}) (c) and open-circuit voltage (V_{OC}) (d) of devices as a function of active layer thickness; data points represent average values of measurements for of 2-3 pixels for 300-400 pixels and minimum 6 pixels for the rest of the thickness.

thickness dependence with a slight reduction with increasing device thickness. In the other two scenarios, we observe a dramatic decrease of the PCE which in general seems to be related to sharp decrease of the J_{SC} when the film thickness increases from 250 to 300 nm. Moreover, although progressive, the FF experiments a strong reduction of almost 30%. It is noteworthy that Voc barely changes with thickness in any of the systems, which means that the main source of efficiency deterioration comes from changes in vertical morphology of the BHJs. The threshold thickness or strong drop-off found in J_{SC} and FF respectively, may be related to increased bimolecular recombination,[294,295] changes in the domain size or purity and/or aggravated percolation pathways for charge transport due to changes in vertical segregation.[171]

6.3.3.2.2. Absorption

The thickness dependence of the absorption spectra of each system was followed. **Figure 6.9** shows thickness normalized absorption spectra measured for films with thicknesses between ~50-450 nm. An important aspect is that the curves show the same optical spectrum without wavelength shifts independent of thickness. The thickness seems to affect the absorption intensity and the intensity ratio between the components. The thick layers are governed by the strong absorption of the polymer being higher especially in the film where the donor is more ordered with respect to the acceptor. As the optimum thickness is approached, the absorption intensity decreases due to the reduction of the thickness and amount of material, and the ratio between the vibronic peaks of the polymer and the acceptor get sharper.

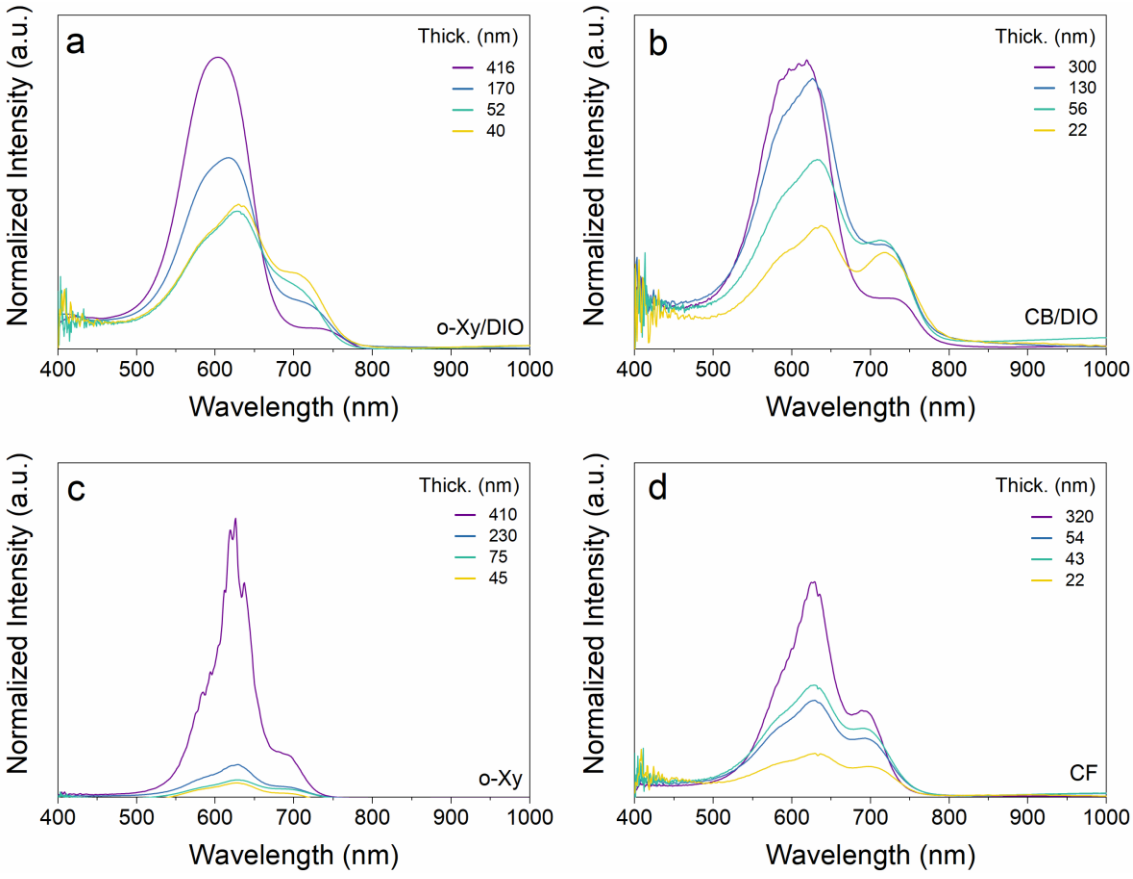

Figure 6.9 UV-Vis absorption spectra as a function of thickness for PBDB-T-ITIC cast from o-Xy/DIO (a), CB/DIO (b), o-Xy (c), and CF (d).

6.3.3.2.3. Photoresponse

We now consider the photoresponse as a function of thickness. Again, the thicknesses do not correspond to these devices but are estimated to be similar to other devices prepared from the same batch. Parameters such as junction thickness and blend composition directly impact the optical field distribution via the optical constants and, hence, the efficiency of carrier photogeneration and the shape of the spectral response.[296] Leaving aside the average percentage of photoresponse which has already been analysed previously, **Figure 6.10** shows the effect of the thickness of the active film as a function of photoresponse. With the exception of the system deposited from o-Xy, we observe that in the other three scenarios there is a limiting thickness at which the photoresponse is steadily diminishes. This explains the decrease of the J_{SC} value due to a lower photon absorption in thinner absorber layers. Moreover, the shape of the EQE spectrum changes in thinner layers with a strong drop-off of whole spectrum intensity and remarkably in the blue response. This reduction is in line with the decrease of J_{SC} and FF.

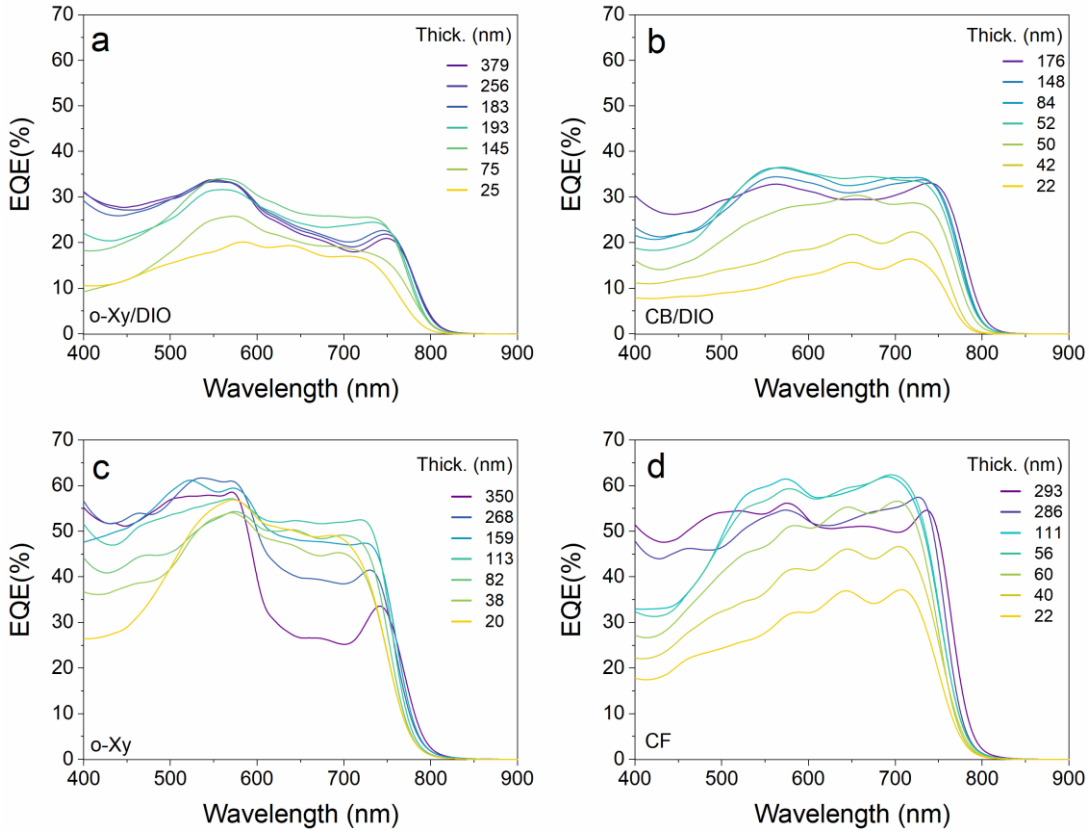

Figure 6.10 External quantum efficiency (EQE) spectra as a function of thickness for PBDB-T-ITIC cast from o-Xy/DIO (a), CB/DIO (b), o-Xy (c), and CF (d).

Interestingly, the system cast from o-Xy (i.e. the one in which we have a mixture consisting of a polymer with an improved paracrystallinity and an amorphous NFA) shows a change in the shape of EQE spectrum depending on the film thickness. **Figure 6.10**c shows the EQE spectra over a range of thicknesses. Thick junctions result in high average photoresponses of the individual components in their specific absorption range, meaning that each component contributes strongly to the absorbed photons (note that the polymer contributes more than the acceptor), thus filtering out the other wavelengths. Intermediate thicknesses, which are close to the optimum, show a higher external quantum efficiency over the solar spectral window with a noticeable increase in the 600-700 nm range. The thinner absorber layers are again characterised by a drop in the EQE spectrum in the blue region, mainly due to surface recombination effects.[297]

6.3.3.2.4. Bimolecular and trap assisted recombination

As stated above, the drop off in FF can be understood in terms of increased bimolecular recombination losses during charge transport. The strong dependence of the FF on the thickness of the active layer indicates that the electric field applied to thicker devices is not strong enough to effectively sweep the charge carriers out of the devices before they recombine.[298] To increase device performance it is of particular interest to enhance light-harvesting which usually is performed via active layer thickness increase to harvest more photons. However, the charge carriers formed in thicker active layer have to travel longer distances to reach the electrodes and are likely to recombine.[299–301] Charges may recombine by the recombination of opposite free charge carriers which in nanocrystalline semiconductors is often described by the Langevin theory[302] (non-geminate (bimolecular) recombination) or via trap-assisted recombination, that is, through available states for charge carriers within the energy gap where trapped electron combine with free-holes.[303]

Firstly, it should be noted that these measurements were performed on encapsulated devices for which thickness values were not measured. However, for comparison purposes, we have used the thicknesses obtained for non-encapsulated devices prepared from the same batch.

In general, depicted in **Figure 6.11** we show that very thin active layers show a reduction in J_{SC}, which we attribute to a decrease in photon absorption in thinner absorber layers.[304–306] In the case of the DIO-containing devices, we cannot extract a thickness-dependent bimolecular recombination trend, as no clear tendency is observed. However, in the devices where we find the absence of acceptor crystalline domains (i.e. those deposited from o-Xy and CF), the drastic reduction of S, more pronounced in the device deposited from o-Xy, suggests a drastic increase of bimolecular recombination with increasing thickness.

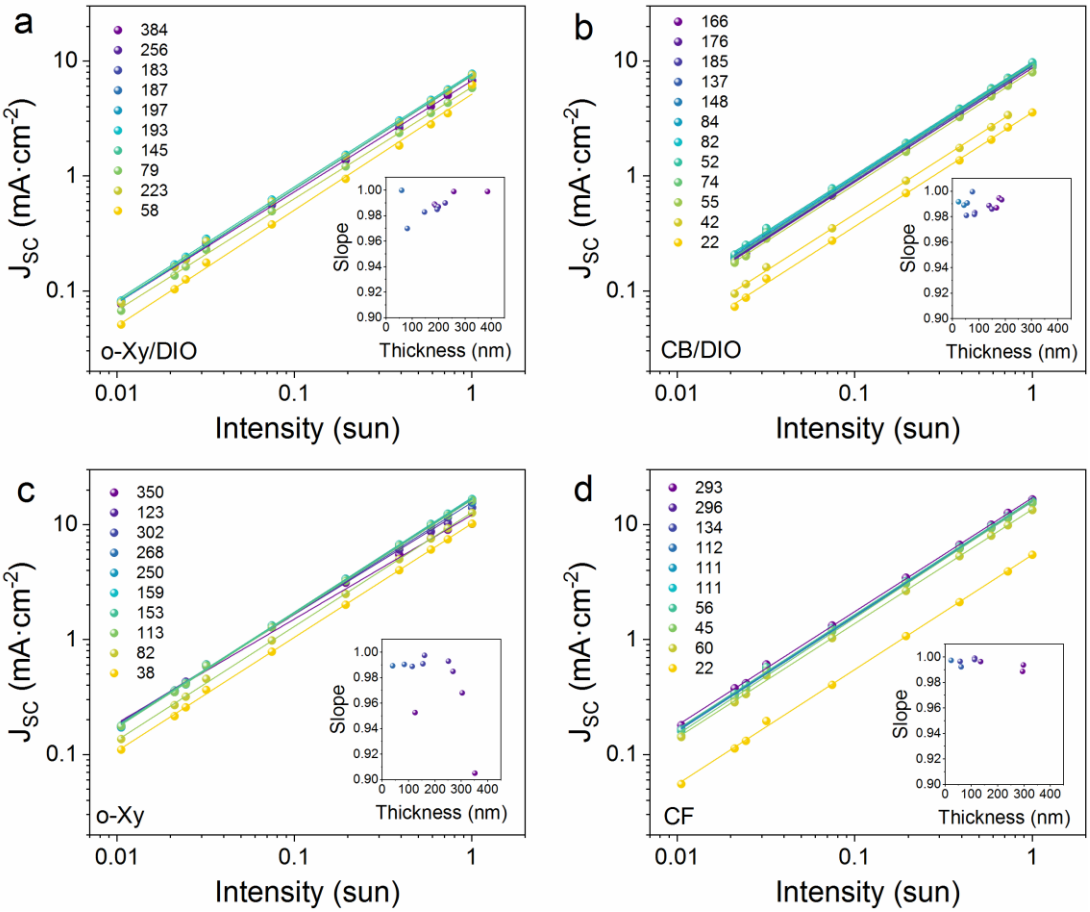

Figure 6.11 J_{SC} versus light intensity as a function of thickness for PBDB-T:ITIC cast from different o-Xy/DIO (a), CB/DIO (b), o-Xy (c), and CF (d).

The classical method to analyse trap-assisted recombination is the light intensity-dependent J-V measurements, where V_{OC} is represented as a function of the natural logarithm of the light intensity. A slope close to k_BT/q indicates the dominant mechanism is bimolecular

recombination and trap-induced recombination is suppressed,[307] while a slope close to $2k_BT/q$ represents a system dominated by trap-assisted recombination, where k_B, T and q are the Boltzmann constant, temperature and elementary charge, respectively.[292,308] **Figure 6.12** displays the V_{OC} versus the logarithm light intensity plot for each scenario as a function of thickness. In general, we found that trap-assisted recombination is found even at light intensities equivalent to 1 sun, being less pronounced in the system where we have an enhanced polymer paracrystalline blended with a vitrified acceptor (i.e. cast from o-Xy). An apparent switch in recombination-loss mechanisms in response to light intensity was represented by the two-segment feature,[301] however, due to lack of expertise, we cannot give further explanations of such matter which is still a debate.[303,309]

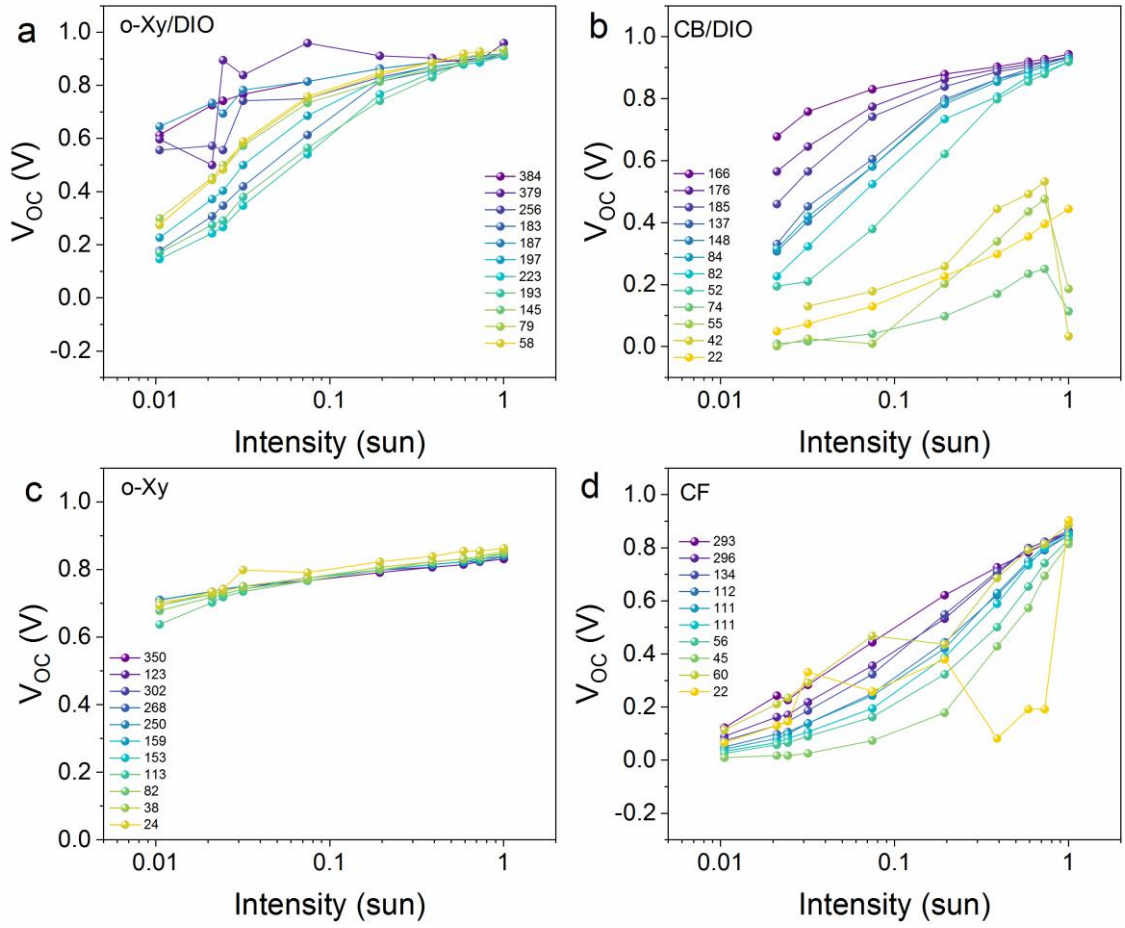

Figure 6.12 V_{OC} versus light intensity as a function of thickness for PBDB-T:ITIC cast from different o-Xy/DIO (a), CB/DIO (b), o-Xy (c), and CF (d).

6.4. Conclusions

In this preliminary study, we confirmed that both solvents and additive play a critical role in determining the microstructure of individual components and we have bridged these aspects with the active layer morphology and the current –voltage characteristics. By a judicious selection of solvents, we developed a system composed of four scenarios in which the microstructures of the individual components is tailored. We, thus, have delineated the microstructural features that control morphology and performance in non-fullerene organic solar cells. Our work underlines the importance of considering the impact of polymer paracrystals on morphology stability and device-relevant studies. We learned the importance of thoughtful selection of processing variables, since, for example, solution in the non-halogenated ortho-xylene solvent results in a binary mixture with enhanced polymer paracrystals comparing with other casting solvents such as CB or CF. Moreover, the resulting single junction showed better device response comparing with blends where both components presented highly order domains or simply acceptor crystalline regions. Interestingly, this blend depicted comparable device parameters to the highest values obtained for the blend cast from CF, in which both components where poorly ordered. Importantly, our results refine and extend the prior morphology-function relation finding that consider this polymer as amorphous materials. It was argued that systems with enhanced polymer paracrystallinity can yield high performances with reduced bimolecular and trap-assisted recombination and thickness-tunable photoresponses. We considered it would be useful to establish novel models for OPV that could integrate the impact polymer paracrystallinity, feature that was recently reported, providing novel and more complete guidelines to understand stability from a microstructural and morphological viewpoint.

4

In the CONCLUSIONS I briefly summarise the most relevant points of the dissertation. Furthermore, I emphasise the findings of this thesis and the importance of the study for the field of organic electronics.

7. Conclusions

This thesis is a comprehensive microstructural study of the materials that comprise the state-of-the-art polymer/non-fullerene acceptor bulk heterojunction model system PBDB-T:ITIC. In addition, throughout the chapters, the microstructural and morphological concepts have been related to relevant optoelectronic properties by knowledge-based fabrication protocols of OPV and OFET devices, thus offering a more cross-disciplinary view of the work.

We demonstrated that all the non-fullerene acceptors based on indacenodithienothiophene present a very rich polymorphism and specifically, arrange into a low-temperature metastable phase that is readily promoted via solution processing and leads to the highest device efficiencies. While these low-temperature forms feature large unit cells in the molecular plane and poor order along the π-π stacking direction, we found they led to electron mobilities comparable to that in the highly ordered high-temperature polymorphs and stronger optical absorptions. Thus, these results indicate that these large-cell packing structures, also found in the benchmark Y6 acceptor, may be an important feature for reaching highest device efficiency.

In addition, we have introduced a new structural model called the "*semi-paracrystalline model*" which solve the conundrum about structural order for high-performance polymeric materials. Using advanced thermal characterisation, among other methods, we uncovered that these polymers are remarkably ordered, as evidenced by order-disorder (melt) transitions. This model rationalises, by seemingly contradictory data, that these semiconducting polymers are underpinned by a dense arrangement of very small paracrystallites coexisting with non-paracrystalline sites. To fully characterise these materials, we have introduce the concept of degree of semi-paracrystallinity which must be estimated in addition to the ordering quality (*g*-parameter) to avoid misconceptions. We furthermore have established the interplay between electrical charge transport of semi-paracrystalline materials and key structural features of the model. That is, thermal aging at intermediate temperatures results in the grown of new paracrystallites within non-ordered regions between preexisting paracrystals, improving their interconnection pathways, and thereby the charge transport.

Then, after having thoroughly investigated the individual components of the active layer, we developed a novel methodology based on fast scanning calorimetry to characterise the intermixed amorphous domains and quantify their absolute composition in bulk heterojunction (BHJ). We found that measuring the glass transition temperature of fully vitrified blends to study the T_g dependence of the blend composition is a simple yet effective method. However, we could not apply the methodology to the PBDB-T:ITIC mixture, because PBDB-T and its congeners revealed a dense arrangement of paracrystallites that made the determination of the glass transition overly challenging.

Finally, we discovered that processing solvents strongly influence the microstructure of the PBDB-T:ITIC blend and we succeeded in developing a set-up consisting of four different scenarios in which we selectively adjusted the microstructure of the individual components and thus the overall morphology. We continue to study the impact of the selective ordering of the individual components on the device performance. Regarding the results achieved, we found that the morphology of the blend is highly sensitive to the crystallisation of the acceptor, while the refinement of the paracrystallinity of the polymer may be beneficial for the overall performance of the device.

In summary, our results present a comprehensive characterisation of the structure-process-function relationship of a model non-fullerene polymer/acceptor blend and emphasise the importance of pursuing in-depth structural studies to move from combinatorial approaches to knowledge-based morphology-function models that will push the field of OPV forward.

5

Here you can find some additional experiments that support the results and conclusions drawn.

A. APPENDIX

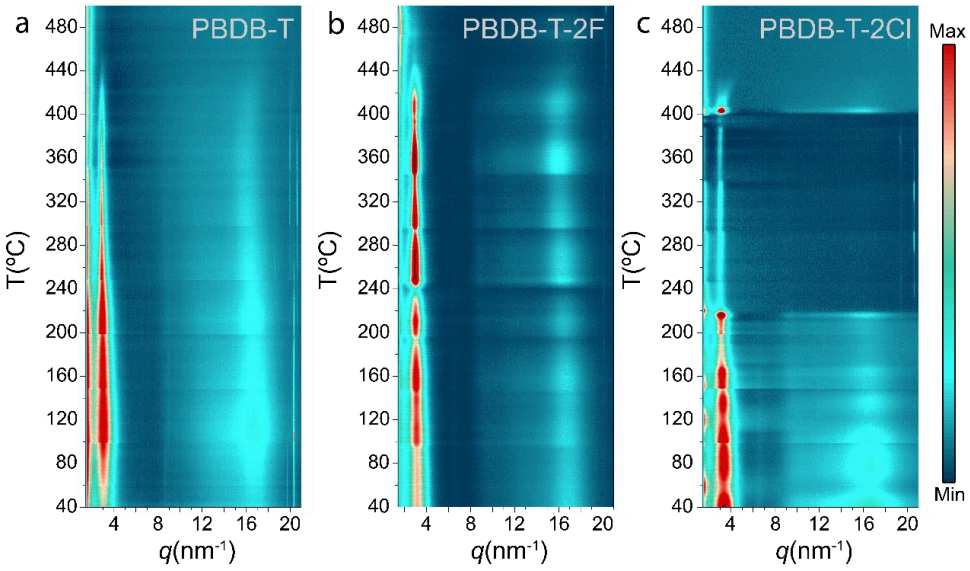

Figure A-1 Contour plot of azimuthal integrations 2D GIWAXS patterns collected during a heating ramp from 30 °C up to 500 °C at 20 °C·min^{-1} **(a)** PBDB-T, and **(b)** PBDB-T-2F and **(c)** PBDB-T-2Cl.

Figure A-2 shows several cycles of a PBDB-T film between -90 and 450 ºC at heating and cooling rates of 4000 °C·s^{-1} (i.e. above the endothermic peak) and recorded heating traces were compared. Because the heat flow values measured are exactly equal in all those heatings, we conclude that (i) the mass of material does not change during the experiment and (ii) the specific heat capacity (cp) of the material does not change during the experiment; thus confirming the absence of any thermal degradation.

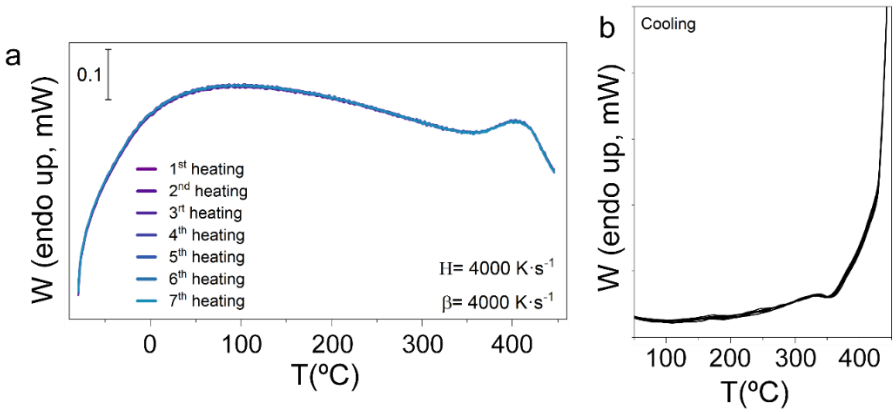

Figure A-2 Representative heating (a) and cooling (b) scans after several heating-cooling runs.

Figure A-3 shows the second FSC thermogram of PEO after cooling the sample at 2000 °C $s^{-1}$and a thermogram in which an annealing process above the glass transition temperature has been applied. The clear glass step-like signal of the glass transition is clearly seen in the second heating scan (black line), which means that -at least a significant fraction of the material did not crystallize during cooling. For comparison, a heating scan (at 2000 °C s^{-1}) of a crystalline PEO sample is also shown.

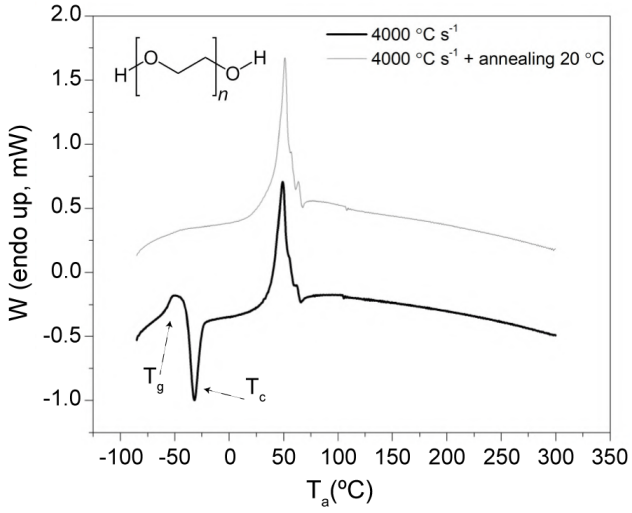

Figure A-3 FSC heating scans for poly(ethylene oxide) (at 2000 °C s^{-1}) after being cooled down from 300 °C to -90 °C at 4000 °C s^{-1} (black line).

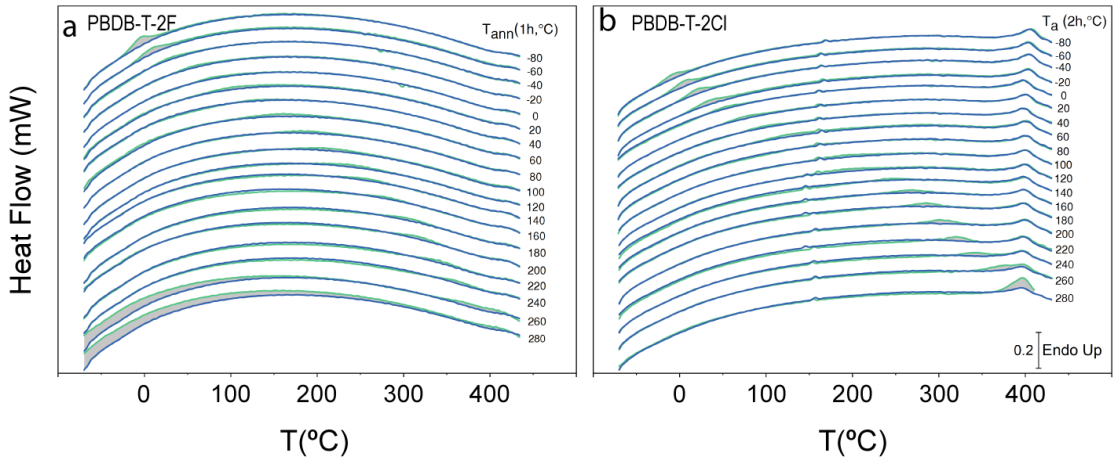

Figure A-4 Isochronous aging experiments conducted by FSC. Green curves correspond to the heating traces (at 4000 ºC·s^{-1}) after ageing samples for 2 h at the temperatures indicated on the right-hand side of each curve. Cooling and heating rates were 4000 ºC·s^{-1}.

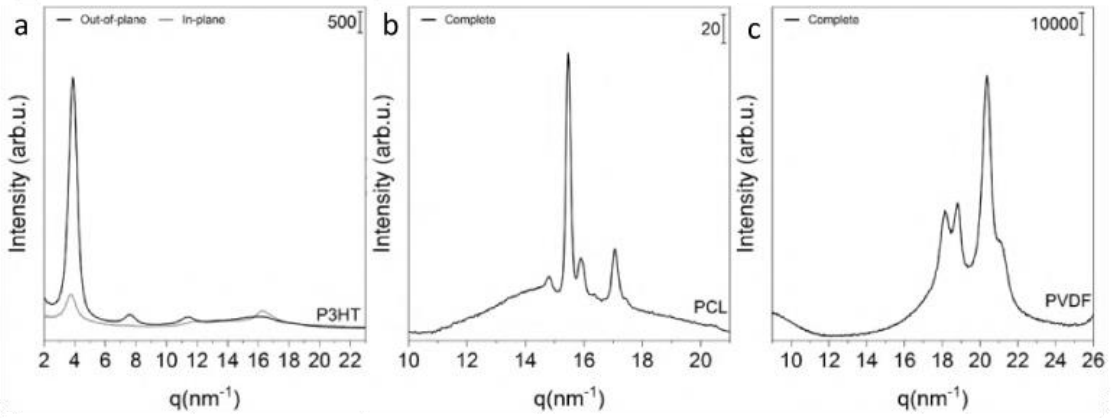

Figure A-5 GIWAXS 1D out-of-plane and in-plane profiles for P3HT (a), PCL (b) and PVDF (c).

For ex-situ temperature-dependent GIWAXS measurements (**Figure A-6**, **Figure A-7** and **Figure A-8**) independent films were cast from the same solution and annealed during 10 minutes at respective temperature. The, films were quenched to room temperature by cooling at 50 ºC·min^{-1}.

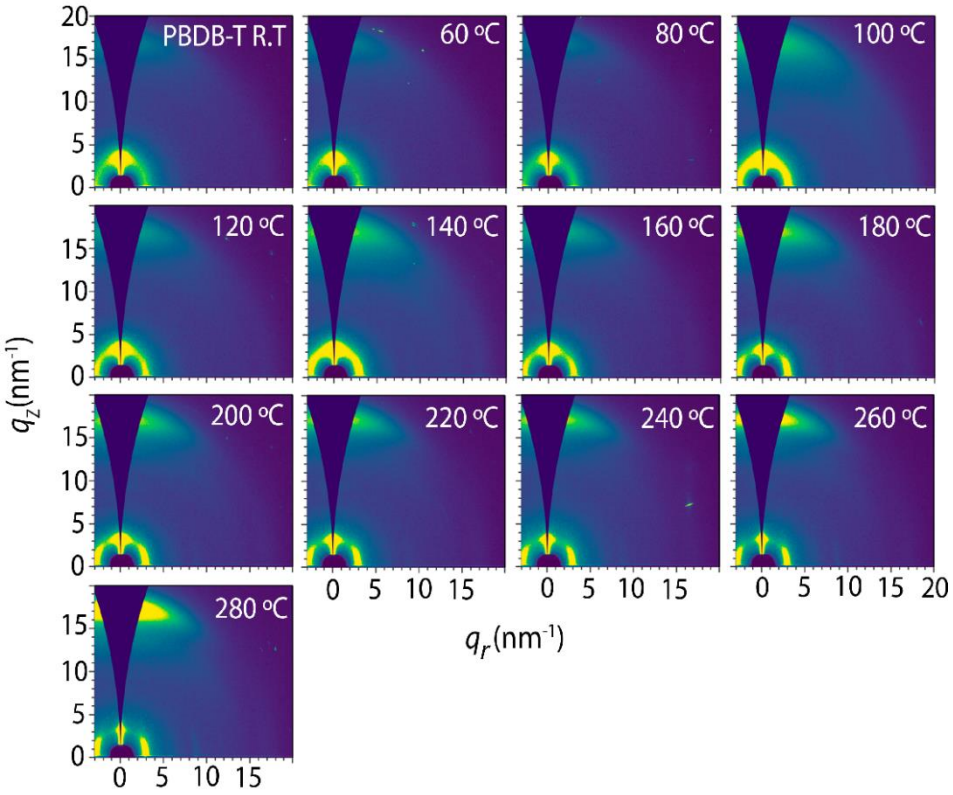

Figure A-6 2D ex-situ GIWAXS patterns after annealing PBDB-T films at specified temperature during 10 minutes.

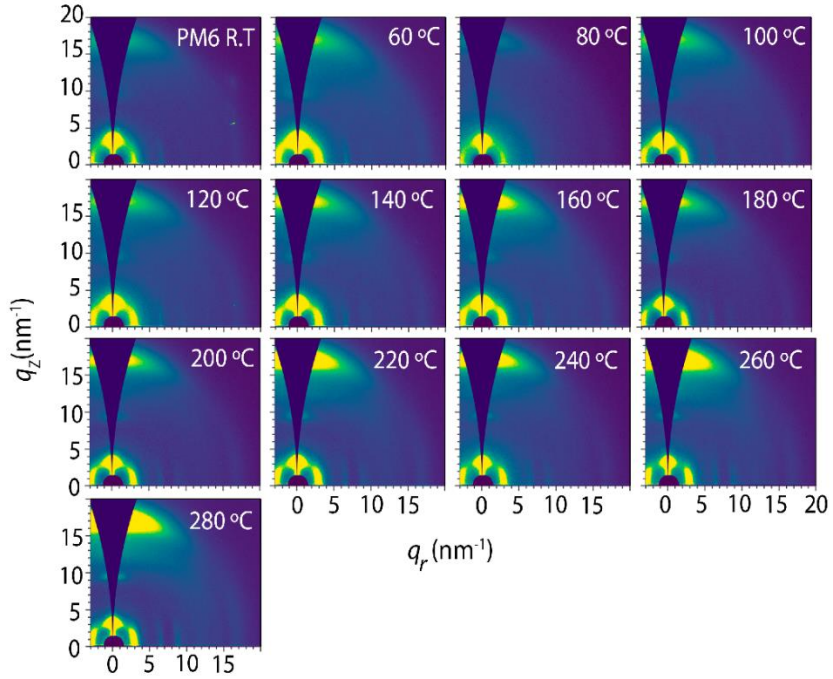

Figure A-7 2D ex-situ GIWAXS patterns after annealing PBDB-T-2F films at specified temperature during 10 minutes.

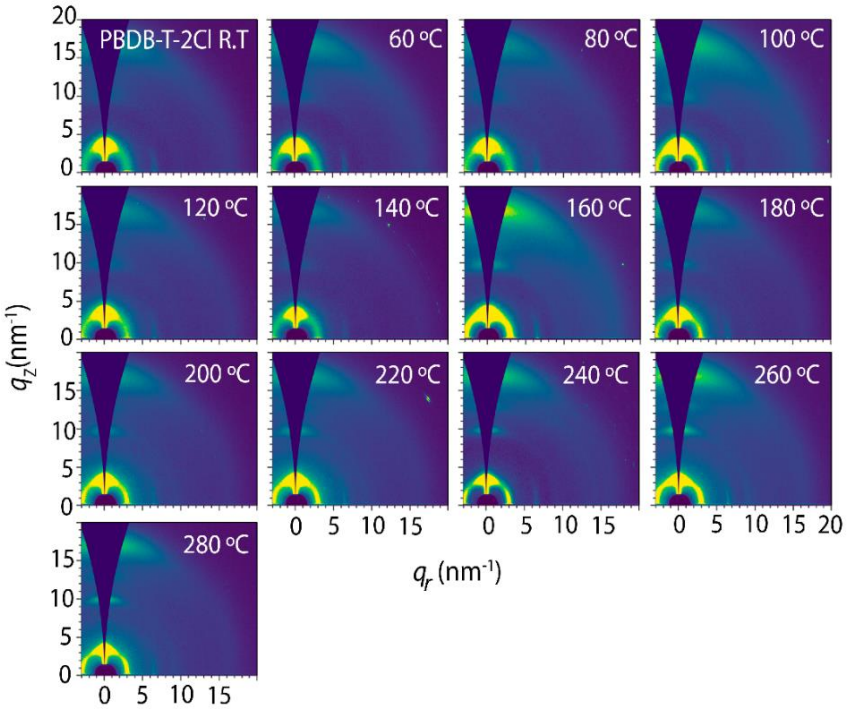

Figure A-8 2D ex-situ GIWAXS patterns after annealing PBDB-T-2Cl films at specified temperature during 10 minutes.

B. APPENDIX

Figure B-1 shows the Raman spectra of Raman spectra of were measured on the freshly prepared film spin cast from chlorobenzene (black solid line) and on a thin film annealed at 270 °C, i.e. a temperature well-above the boiling point of the solvent, for 20 min (grey solid line). The region of interest (between 200 cm^{-1} and 800 cm^{-1}) is highlighted in the inset, which corresponds to the region where modes involving the C-Cl bond show up [C-Cl stretching at 650-850 cm^{-1} (strong); C-Cl symmetrical stretching at 377 cm^{-1}; and C-Cl antisymmetrical stretching at 326 cm^{-1}). We do not see any of the bands above in our spectra, indicating that even our as-cast films are free of trapped solvent.

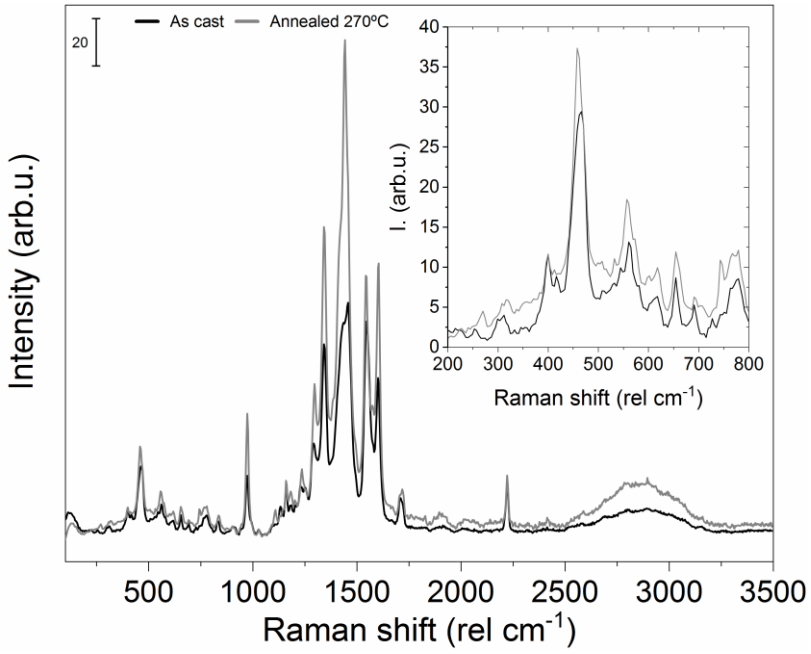

Figure B-1 Raman spectra of as-cast and annealed ITIC thin films.

Figure B-2 shows the TGA degradation curves of ITIC and its derivatives. The results show that ITIC-Th develops an earlier degradation comparing with its counterparts, being ~300ºC for ITIC-Th and higher than 320ºC for the rest of the SMAs.

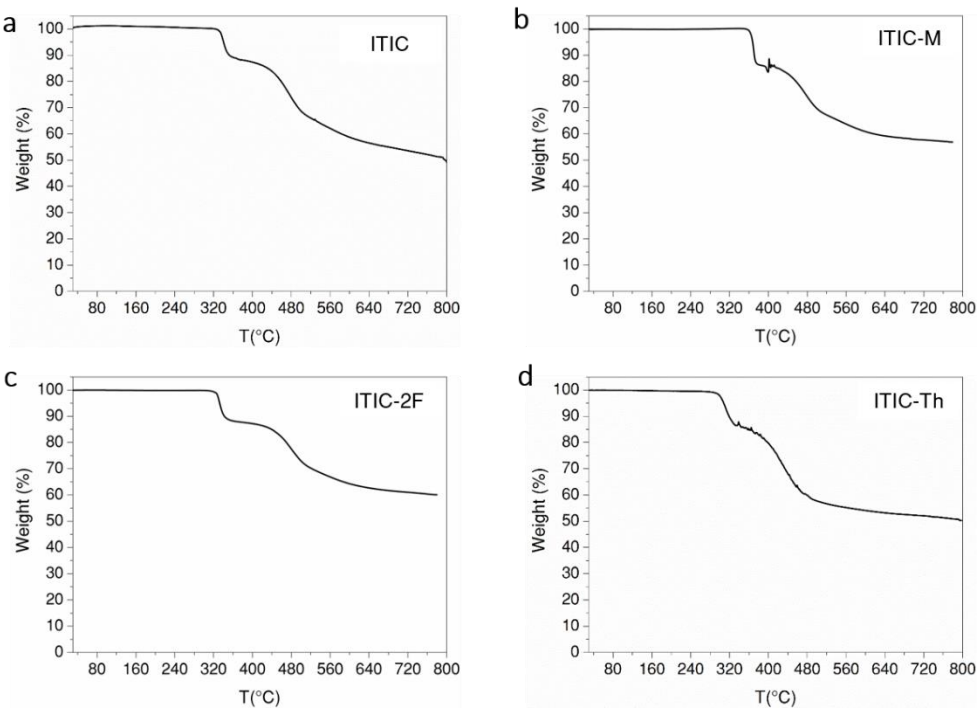

Figure B-2 TGA degradation curves of (a) ITIC, (b) ITIC-M, (c) ITIC-2F, and (d) ITIC-Th, under N_2 atmosphere.

The thermal protocol depicted in **Figure B-3** was employed to probe that both Phase II and Phase III of ITIC are thermodynamically stable in their respective range of temperatures. The result of the experiment is shown in **Figure B-4**.

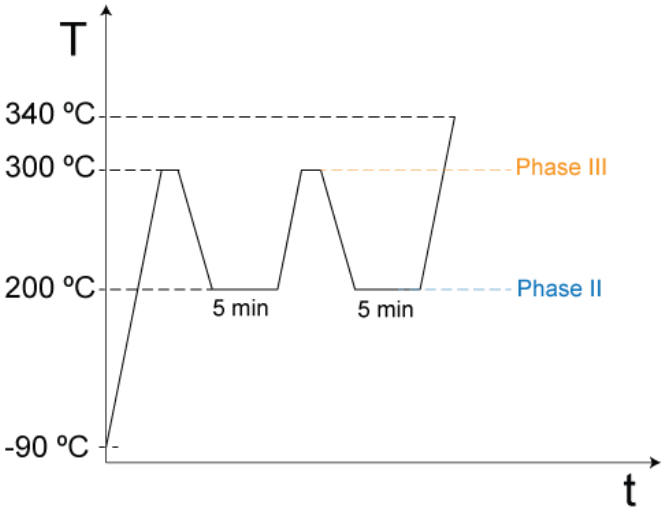

Figure B-3 Thermal protocol applied in DSC to analyse reversibility of phase II.

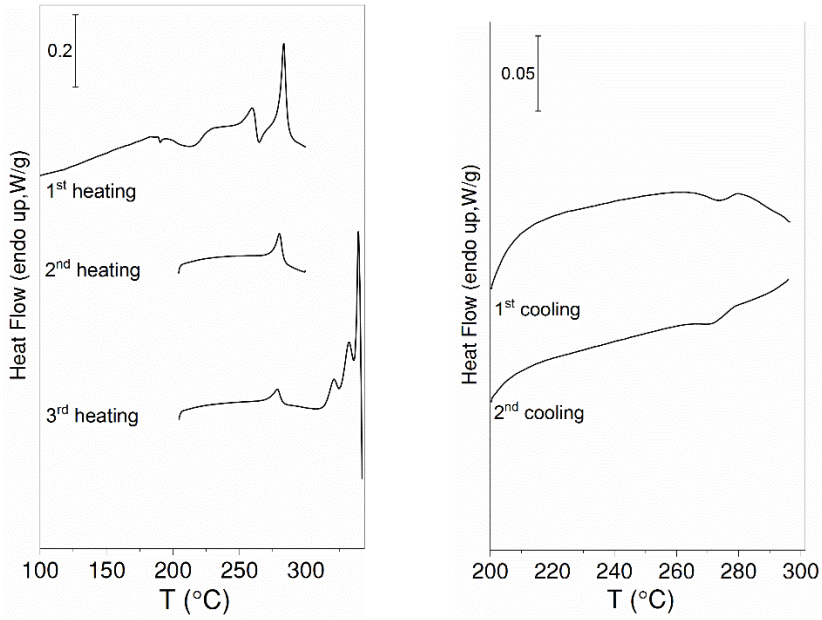

Figure B-4 DSC heating anf cooling thermograms of ITIC to probe the phase II reversibility.

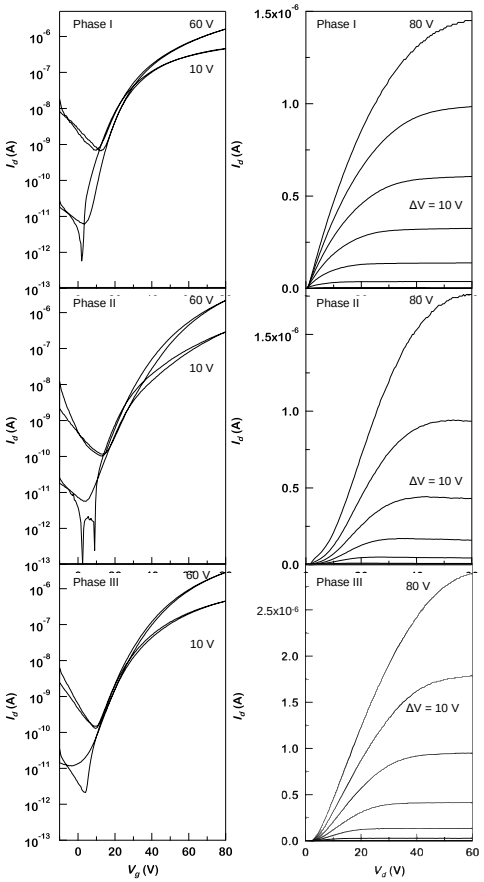

Figure B-5 Left panels: representative transfer characteristics of ITIC Phase I, II and III. V_d for linear and saturation regime. Right panel: corresponding output characteristics with V_g ranging from 0 V to 80 V with a 10 V step.

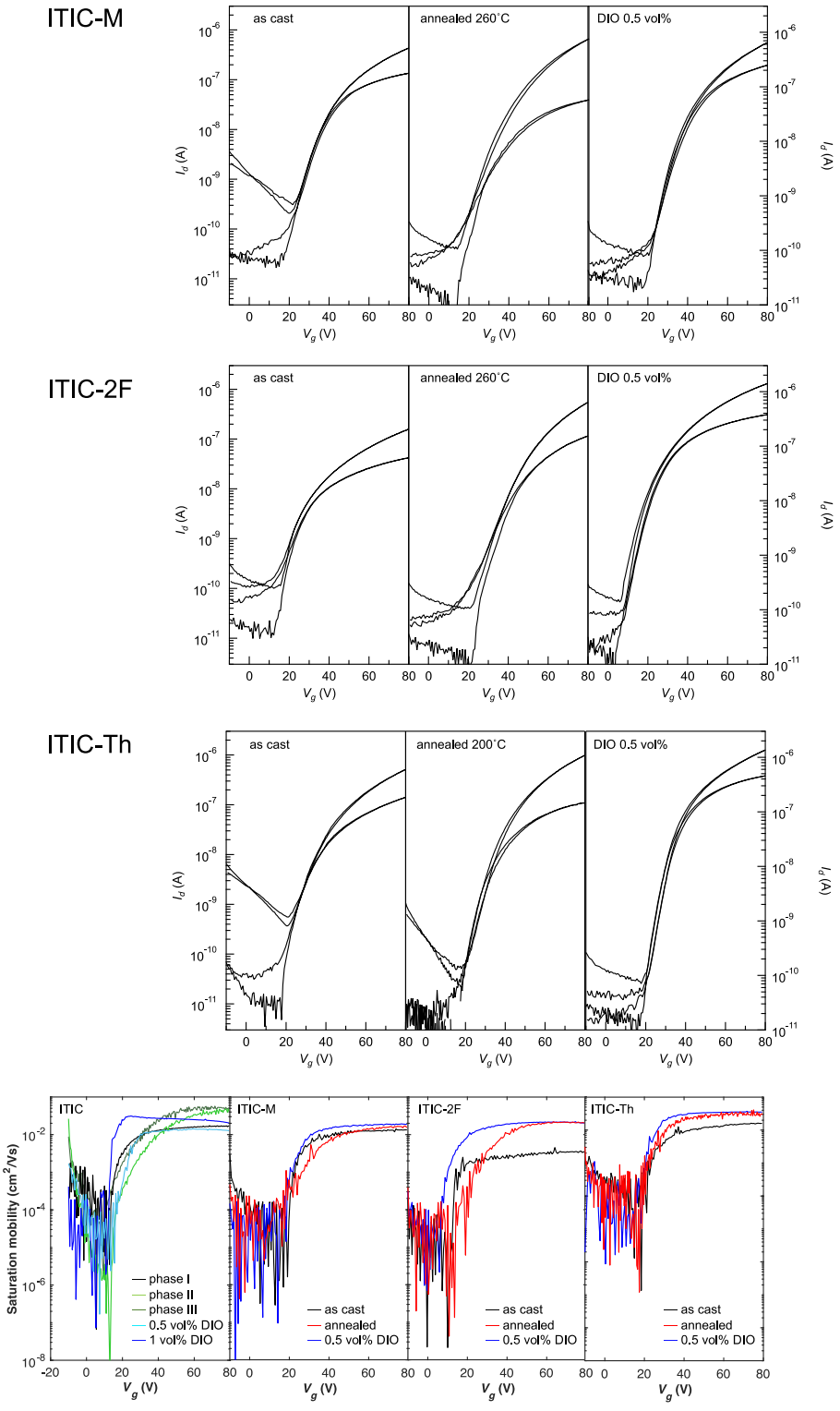

Figure B-6 Representative transfer characteristics of ITIC-M, ITIC-2F and ITIC-Th as cast, annealed and upon DIO addition. V_d for linear and saturation regime is 10 V and 60 V. Bottom panels: Field-effect mobility in saturation as a function of gate voltage for ITIC and derivatives.

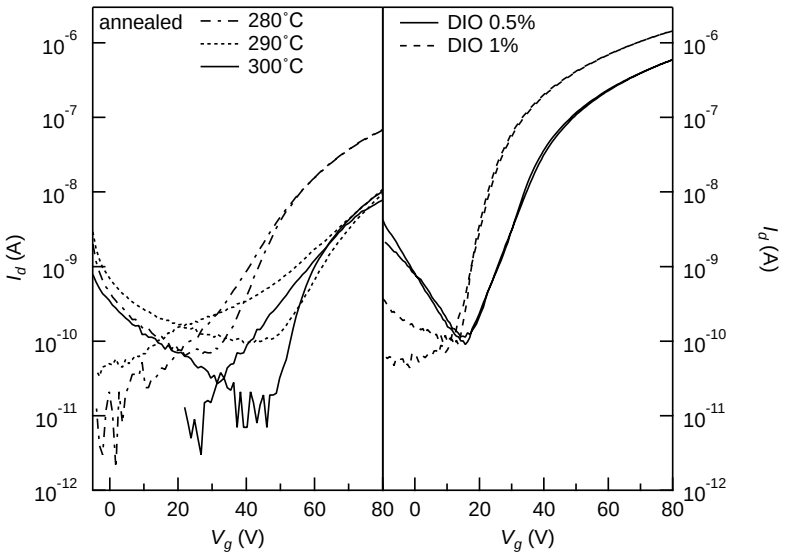

Figure B-7 Left panel: representative transfer characteristics in saturation regime for ITIC annealed at temperatures, as indicated. Right panel: ITIC transfer characteristics in saturation regime upon DIO solvent addition. $V_d = 60$ V.

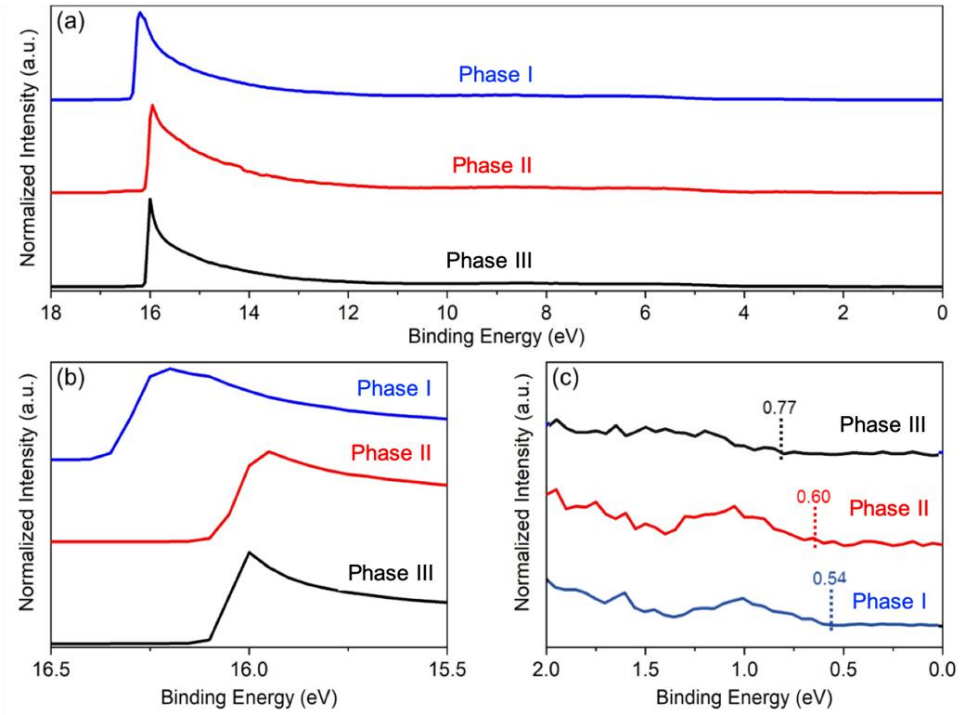

Figure B-8 The three phases of ITIC show similar energy levels according to ultraviolet photoelectron spectroscopy (UPS) measurements. (a) Normalized intensity of the full UPS spectrum. (b) High binding energy portion of UPS spectrum that shows the ITIC film's workfunctions. c) Low binding energy portion of UPS spectrum from which the HOMO level cutoff can be deduced.

C. APPENDIX

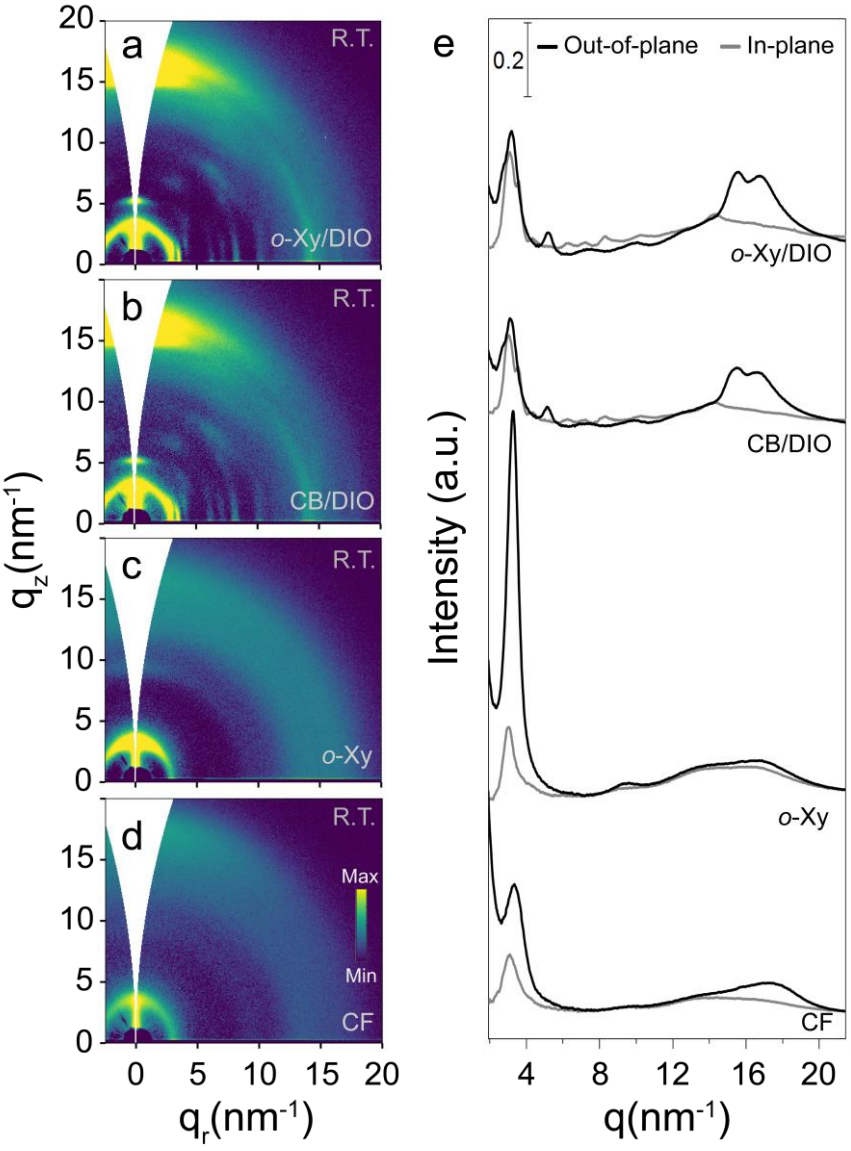

Figure C-1 2D-GIWAXS patterns of PBDB-T:ITIC 50:50 blend blade-coat from orto-xylene and 1 v/v% diiodoctane [o-Xy/DIO] (a), chlorobencene and 1 v/v% DIO [CB/DIO] (b), orto-xylene [o-Xy] (c) and chloroform [CF] (d). Out-of-plane and in-plane profiles (e).

BIBLIOGRAPHY

(1) Ravishankar, E.; Charles, M.; Xiong, Y.; Henry, R.; Swift, J.; Rech, J.; Calero, J.; Cho, S.; Booth, R. E.; Kim, T.; Balzer, A. H.; Qin, Y.; Hoi Yi Ho, C.; So, F.; Stingelin, N.; Amassian, A.; Saravitz, C.; You, W.; Ade, H.; Sederoff, H.; O'Connor, B. T. Balancing Crop Production and Energy Harvesting in Organic Solar-Powered Greenhouses. *Cell Reports Phys. Sci.* **2021**, *2* (3), 100381. https://doi.org/10.1016/j.xcrp.2021.100381.

(2) Cui, Y.; Xu, Y.; Yao, H.; Bi, P.; Hong, L.; Zhang, J.; Zu, Y.; Zhang, T.; Qin, J.; Ren, J.; Chen, Z.; He, C.; Hao, X.; Wei, Z.; Hou, J. Single-Junction Organic Photovoltaic Cell with 19% Efficiency. *Adv. Mater.* **2021**, 2102420. https://doi.org/10.1002/ADMA.202102420.

(3) Li, Y.; Huang, X.; Ding, K.; Sheriff, H. K. M.; Ye, L.; Liu, H.; Li, C.-Z.; Ade, H.; Forrest, S. R. Non-Fullerene Acceptor Organic Photovoltaics with Intrinsic Operational Lifetimes over 30 Years. *Nat. Commun.* **2021**, *12* (5419), 1–9. https://doi.org/10.1038/s41467-021-25718-w.

(4) Shirakawa, H.; Louis, E. J.; MacDiarmid, A. G.; Chiang, C. K.; Heeger, A. J. Synthesis of Electrically Conducting Organic Polymers: Halogen Derivatives of Polyacetylene, (CH)X. *J. Chem. Soc. Chem. Commun.* **1977**, No. 16, 578–580. https://doi.org/10.1039/C39770000578.

(5) Someya, T.; Bao, Z.; Malliaras, G. G. The Rise of Plastic Bioelectronics. *Nature* **2016**, *540* (7633), 379–385. https://doi.org/10.1038/nature21004.

(6) Baran, D.; Corzo, D.; Blazquez, G. T. Flexible Electronics: Status, Challenges and Opportunities. *Front. Electron.* **2020**, *1* (594003), 1–13. https://doi.org/10.3389/FELEC.2020.594003.

(7) Elschner, A.; Kirchmeyer, S.; Lövenich, W.; Merker, U.; Reuter, K. *PEDOT : Principles and Applications of an Intrinsically Conductive Polymer*; CRC Press, 2010. https://doi.org/10.1201/B10318.

(8) Strobl, G. *The Physics of Polymers: Concepts for Understanding Their Structures and Behavior*; Springer Berlin Heidelberg, 2007. https://doi.org/10.1007/978-3-540-68411-4.

(9) Scharber, M. C.; Sariciftci, N. S. Low Band Gap Conjugated Semiconducting Polymers. *Adv. Mater. Technol.* **2021**, *6* (4), 2000857. https://doi.org/10.1002/ADMT.202000857.

(10) Coakley, K. M.; McGehee, M. D. Conjugated Polymer Photovoltaic Cells. *Chem. Mater.* **2004**, *16* (23), 4533–4542. https://doi.org/10.1021/CM049654N.

(11) Yu, G.; Gao, J.; Hummelen, J. C.; Wudl, F.; Heeger, A. J. Polymer Photovoltaic Cells: Enhanced Efficiencies via a Network of Internal Donor-Acceptor Heterojunctions. *Science (80-.).* **1995**, *270* (5243), 1789. https://doi.org/10.1126/SCIENCE.270.5243.1789.

(12) Salleo, A. Charge Transport in Polymeric Transistors. *Mater. Today* **2007**, *10* (3), 38–45. https://doi.org/10.1016/S1369-7021(07)70018-4.

(13) Sirringhaus, H.; Brown, P. J.; Friend, R. H.; Nielsen, M. M.; Bechgaard, K.; Langeveld-Voss, B. M. W.; Spiering, A. J. H.; Janssen, R. A. J.; Meijer, E. W.; Herwig, P.; de Leeuw, D. M. Two-Dimensional Charge Transport in Self-Organized, High-Mobility Conjugated

Polymers. *Nature* **1999**, *401* (6754), 685–688. https://doi.org/10.1038/44359.

(14) Noriega, R.; Rivnay, J.; Vandewal, K.; Koch, F. P. V; Stingelin, N.; Smith, P.; Toney, M. F.; Salleo, A. A General Relationship between Disorder, Aggregation and Charge Transport in Conjugated Polymers. *Nat. Mater.* **2013**, *12*, 1038–1044. https://doi.org/10.1038/NMAT3722.

(15) Bredas, J.-L.; Marder, S. R. *The WSPC Reference on Organic Electronics: Organic Semiconductors. Materials and Energy Series.*; Bredas, J.-L., Marder, S. R., Eds.; John Wiley & Sons, Ltd, 2016; Vol. 2. https://doi.org/10.1002/ANIE.201701913.

(16) Pascual-San-José, E.; Rodríguez-Martínez, X.; Adel-Abdelaleim, R.; Stella, M.; Martínez-Ferrero, E.; Campoy-Quiles, M. Blade Coated P3HT:Non-Fullerene Acceptor Solar Cells: A High-Throughput Parameter Study with a Focus on up-Scalability. *J. Mater. Chem. A* **2019**, *7* (35), 20369–20382. https://doi.org/10.1039/C9TA07361B.

(17) Bernardo, G.; Lopes, T.; Lidzey, D. G.; Mendes, A. Progress in Upscaling Organic Photovoltaic Devices. *Adv. Energy Mater.* **2021**, *11* (23), 2100342. https://doi.org/10.1002/AENM.202100342.

(18) Ma, W.; Yang, C.; Gong, X.; Lee, K.; Heeger, A. J. Thermally Stable, Efficient Polymer Solar Cells with Nanoscale Control of the Interpenetrating Network Morphology. *Adv. Funct. Mater.* **2005**, *15* (10), 1617–1622. https://doi.org/10.1002/ADFM.200500211.

(19) Zhao, G.; He, Y.; Li, Y. 6.5% Efficiency of Polymer Solar Cells Based on Poly(3-Hexylthiophene) and Indene-C60 Bisadduct by Device Optimization. *Adv. Mater.* **2010**, *22* (39), 4355–4358. https://doi.org/10.1002/ADMA.201001339.

(20) Xu, X.; Zhang, G.; Yu, L.; Li, R.; Peng, Q. P3HT-Based Polymer Solar Cells with 8.25% Efficiency Enabled by a Matched Molecular Acceptor and Smart Green-Solvent Processing Technology. *Adv. Mater.* **2019**, *31* (52), 1906045. https://doi.org/10.1002/ADMA.201906045.

(21) Dang, M. T.; Hirsch, L.; Wantz, G.; Wuest, J. D. Controlling the Morphology and Performance of Bulk Heterojunctions in Solar Cells. Lessons Learned from the Benchmark Poly(3-Hexylthiophene):[6,6]-Phenyl-C61-Butyric Acid Methyl Ester System. *Chem. Rev.* **2013**, *113* (5), 3734–3765. https://doi.org/10.1021/CR300005U.

(22) Yang, C.; Zhang, S.; Ren, J.; Gao, M.; Bi, P.; Ye, L.; Hou, J. Molecular Design of a Non-Fullerene Acceptor Enables a P3HT-Based Organic Solar Cell with 9.46% Efficiency. *Energy Environ. Sci.* **2020**, *13* (9), 2864–2869. https://doi.org/10.1039/D0EE01763A.

(23) Wadsworth, A.; Hamid, Z.; Bidwell, M.; Ashraf, R. S.; Khan, J. I.; Anjum, D. H.; Cendra, C.; Yan, J.; Rezasoltani, E.; Guilbert, A. A. Y.; Azzouzi, M.; Gasparini, N.; Bannock, J. H.; Baran, D.; Wu, H.; de Mello, J. C.; Brabec, C. J.; Salleo, A.; Nelson, J.; Laquai, F.; McCulloch, I. Progress in Poly (3-Hexylthiophene) Organic Solar Cells and the Influence of Its Molecular Weight on Device Performance. *Adv. Energy Mater.* **2018**, *8* (28), 1801001. https://doi.org/10.1002/aenm.201801001.

(24) Havinga, E.; Ten Hoeve, W.; Wynberg, H. A New Class of Small Band Gap Organic Polymer Conductors. *Polym. Bull.* **1992**, *29*, 119–126.

(25) Nelson, J. Polymer:Fullerene Bulk Heterojunction Solar Cells. *Mater. Today* **2011**, *14*

(10), 462–470. https://doi.org/10.1016/S1369-7021(11)70210-3.

(26) Ebenhoch, B.; Thomson, S. A. J.; Genevičius, K.; Juška, G.; Samuel, I. D. W. Charge Carrier Mobility of the Organic Photovoltaic Materials PTB7 and PC71BM and Its Influence on Device Performance. *Org. Electron.* **2015**, *22*, 62–68. https://doi.org/10.1016/J.ORGEL.2015.03.013.

(27) Lu, L.; Zheng, T.; Wu, Q.; Schneider, A. M.; Zhao, D.; Yu, L. Recent Advances in Bulk Heterojunction Polymer Solar Cells. **2015**. https://doi.org/10.1021/acs.chemrev.5b00098.

(28) Qian, D.; Ye, L.; Zhang, M.; Liang, Y.; Li, L.; Huang, Y.; Guo, X.; Zhang, S.; Tan, Z.; Hou, J. Design, Application, and Morphology Study of a New Photovoltaic Polymer with Strong Aggregation in Solution State. *Macromolecules* **2012**, *45* (24), 9611–9617. https://doi.org/10.1021/ma301900h.

(29) Nguyen, T.-Q.; Doan, V.; Schwartz, B. J. Conjugated Polymer Aggregates in Solution: Control of Interchain Interactions. *J. Chem. Phys.* **1999**, *110* (8), 4068–4078.

(30) Huang, Y.; Cheng, H.; Han, C. C. Temperature Induced Structure Evolution of Regioregular Poly(3-Hexylthiophene) in Dilute Solution and Its Influence on Thin Film Morphology. *Macromolecules* **2010**, *43* (23), 10031–10037. https://doi.org/10.1021/ma102168a.

(31) Zheng, Z.; Yao, H.; Ye, L.; Xu, Y.; Zhang, S.; Hou, J. PBDB-T and Its Derivatives : A Family of Polymer Donors Enables over 17 % Efficiency in Organic Photovoltaics. *Mater. Today* **2019**, *35*, 115–130.

(32) Zhao, W.; Li, S.; Yao, H.; Zhang, S.; Zhang, Y.; Yang, B.; Hou, J. Molecular Optimization Enables over 13% Efficiency in Organic Solar Cells. *JACS* **2017**, *139*, 7148–7151. https://doi.org/10.1021/jacs.7b02677.

(33) Zhang, S.; Qin, Y.; Zhu, J.; Hou, J. Over 14% Efficiency in Polymer Solar Cells Enabled by a Chlorinated Polymer Donor. *Adv. Mater.* **2018**, *30*, 1800868. https://doi.org/10.1002/adma.201800868.

(34) Zhao, W.; Qian, D.; Zhang, S.; Li, S.; Inganäs, O.; Gao, F.; Hou, J. Fullerene-Free Polymer Solar Cells with over 11% Efficiency and Excellent Thermal Stability. *Adv. Mater.* **2016**, *28*, 4734–4739. https://doi.org/10.1002/adma.201600281.

(35) Lin, Y.; Wang, J.; Zhang, Z.-G.; Bai, H.; Li, Y.; Zhu, D.; Zhan, X. An Electron Acceptor Challenging Fullerenes for Efficient Polymer Solar Cells. *Adv. Mater.* **2015**, *27*, 1170–1174. https://doi.org/10.1002/adma.201404317.

(36) Zhang, Q.; Kelly, M. A.; Bauer, N.; You, W. The Curious Case of Fluorination of Conjugated Polymers for Solar Cells. *Acc. Chem. Res.* **2017**, *50* (9), 2401–2409. https://doi.org/10.1021/ACS.ACCOUNTS.7B00326.

(37) Li, S.; Ye, L.; Zhao, W.; Yan, H.; Yang, B.; Liu, D.; Li, W.; Ade, H.; Hou, J. A Wide Band Gap Polymer with a Deep Highest Occupied Molecular Orbital Level Enables 14.2% Efficiency in Polymer Solar Cells. *J. Am. Chem. Soc.* **2018**, *140*, 7159–7167. https://doi.org/10.1021/jacs.8b02695.

(38) Bronstein, H.; Frost, J. M.; Hadipour, A.; Kim, Y.; Nielsen, C. B.; Ashraf, R. S.; Rand, B. P.; Watkins, S.; McCulloch, I. Effect of Fluorination on the Properties of a Donor–

Acceptor Copolymer for Use in Photovoltaic Cells and Transistors. *Chem. Mater.* **2013**, *25* (3), 277–285. https://doi.org/10.1021/CM301910T.

(39) Wang, Q.; Li, M.; Zhang, X.; Qin, Y.; Wang, J.; Zhang, J.; Hou, J.; Renéa, ‖; Janssen, R. J.; Geng, Y. Carboxylate-Substituted Polythiophenes for Efficient Fullerene-Free Polymer Solar Cells: The Effect of Chlorination on Their Properties. *Macromolecules* **2019**, *52*, 4464–4474. https://doi.org/10.1021/acs.macromol.9b00793.

(40) Qu, S.; Wang, H.; Mo, D.; Chao, P.; Yang, Z.; Li, L.; Tian, L.; Chen, W.; He, F. Fine Tuning of Open-Circuit Voltage by Chlorination in Thieno[3,4-b]Thiophene–Benzodithiophene Terpolymers toward Enhanced Solar Energy Conversion. *Macromolecules* **2017**, *50* (13), 4962–4971. https://doi.org/10.1021/ACS.MACROMOL.7B00785.

(41) Zhang, Y.; Yao, H.; Zhang, S.; Qin, Y.; Zhang, J.; Yang, L.; Li, W.; Wei, Z.; Gao, F.; Hou, J. Fluorination vs. Chlorination: A Case Study on High Performance Organic Photovoltaic Materials. *Sci. China Chem. 2018 6110* **2018**, *61* (10), 1328–1337. https://doi.org/10.1007/S11426-018-9260-2.

(42) Liu, Q.; Jiang, Y.; Jin, K.; Qin, J.; Xu, J.; Li, W.; Xiong, J.; Liu, J.; Xiao, Z.; Sun, K.; Yang, S.; Zhang, X.; Ding, L. 18% Efficiency Organic Solar Cells. *Sci. Bull.* **2020**, *65* (4), 272–275. https://doi.org/10.1016/j.scib.2020.01.001.

(43) Kim, Y.; Cook, S.; Tuladhar, S. M.; Choulis, S. A.; Nelson, J.; Durrant, J. R.; Bradley, D. D. C.; Giles, M.; McCulloch, I.; Ha, C. S.; Ree, M. A Strong Regioregularity Effect in Self-Organizing Conjugated Polymer Films and High-Efficiency Polythiophene:Fullerene Solar Cells. *Nat. Mater.* **2006**, *5* (3), 197–203. https://doi.org/10.1038/nmat1574.

(44) Yin, W.; Dadmun, M. A New Model for the Morphology of P3HT/PCBM Organic Photovoltaics from Small-Angle Neutron Scattering: Rivers and Streams. *ACS Nano* **2011**, *5* (6), 4756–4768. https://doi.org/10.1021/nn200744q.

(45) DeLongchamp, D. M.; Kline, R. J.; Jung, Y.; Lin, E. K.; Fischer, D. A.; Gundlach, D. J.; Cotts, S. K.; Moad, A. J.; Richter, L. J.; Toney, M. F.; Heeney, M.; McCulloch, I. Molecular Basis of Mesophase Ordering in a Thiophene-Based Copolymer. *Macromolecules* **2008**, *41* (15), 5709–5715. https://doi.org/10.1021/MA800440F.

(46) Rivnay, J.; Toney, M. F.; Zheng, Y.; Kauvar, I. V.; Chen, Z.; Wagner, V.; Facchetti, A.; Salleo, A. Unconventional Face-On Texture and Exceptional In-Plane Order of a High Mobility n-Type Polymer. *Adv. Mater.* **2010**, *22* (39), 4359–4363. https://doi.org/10.1002/ADMA.201001202.

(47) Ghasemi, M.; Balar, N.; Peng, Z.; Hu, H.; Qin, Y.; Kim, T.; Rech, J. J.; Bidwell, M.; Mask, W.; McCulloch, I.; You, W.; Amassian, A.; Risko, C.; O'Connor, B. T.; Ade, H. A Molecular Interaction–Diffusion Framework for Predicting Organic Solar Cell Stability. *Nat. Mater. 2021 204* **2021**, *20* (4), 525–532. https://doi.org/10.1038/s41563-020-00872-6.

(48) Hu, H.; Ghasemi, M.; Peng, Z.; Zhang, J.; Rech, J. J.; You, W.; Yan, H.; Ade, H. The Role of Demixing and Crystallization Kinetics on the Stability of Non-Fullerene Organic Solar Cells. *Adv. Mater.* **2020**, 2005348. https://doi.org/10.1002/adma.202005348.

(49) Yu, L.; Qian, D.; Marina, S.; A Nugroho, F. A.; Sharma, A.; Hultmark, S.; Hofmann, A.

I.; Kroon, R.; Benduhn, J.; Smilgies, D.-M.; Vandewal, K.; Andersson, M. R.; Langhammer, C.; Martín, J.; Gao, F.; Mu, C. Diffusion-Limited Crystallization: A Rationale for the Thermal Stability of Non-Fullerene Solar Cells. *ACS Appl. Mater. Interfaces* **2019**, *11* (24), 21766–21774. https://doi.org/10.1021/acsami.9b04554.

(50) Zhang, W.; Smith, J.; Watkins, S. E.; Gysel, R.; McGehee, M.; Salleo, A.; Kirkpatrick, J.; Ashraf, S.; Anthopoulos, T.; Heeney, M.; McCulloch, I. Indacenodithiophene Semiconducting Polymers for High-Performance, Air-Stable Transistors. *J. Am. Chem. Soc.* **2010**, *132* (33), 11437–11439. https://doi.org/10.1021/ja1049324.

(51) Root, S. E.; Alkhadra, M. A.; Rodriquez, D.; Printz, A. D.; Lipomi, D. J. Measuring the Glass Transition Temperature of Conjugated Polymer Films with Ultraviolet−Visible Spectroscopy. *Chem. Mater* **2017**, *29*, 2646–2654. https://doi.org/10.1021/acs.chemmater.7b00242.

(52) Sharma, A.; Pan, X.; Bjuggren, J. M.; Gedefaw, D.; Xu, X.; Kroon, R.; Wang, E.; Campbell, J. A.; Lewis, D. A.; Andersson, M. R. Probing the Relationship between Molecular Structures, Thermal Transitions, and Morphology in Polymer Semiconductors Using a Woven Glass-Mesh-Based DMTA Technique. *Chem. Mater.* **2019**, *31* (17), 6740–6749.

(53) Cendra, C.; Balhorn, L.; Zhang, W.; O'Hara, K.; Bruening, K.; Tassone, C. J.; Steinrück, H.-G.; Liang, M.; Toney, M. F.; McCulloch, I.; Chabinyc, M. L.; Salleo, A.; Takacs, C. J. *Unraveling the Unconventional Order of a High-Mobility Indacenodithiophene-Benzothiadiazole Copolymer*; 2021.

(54) Tanya Kumari; Myeon Lee, S.; So-Huei Kang; Shanshan Chen; Changduk Yang. Ternary Solar Cells with a Mixed Face-on and Edge-on Orientation Enable an Unprecedented Efficiency of 12.1%. *Energy Environ. Sci.* **2017**, *10* (1), 258–265. https://doi.org/10.1039/C6EE02851A.

(55) Park, Y.; Fuentes-Hernandez, C.; Jia, X.; Larrain, F. A.; Zhang, J.; Marder, S. R.; Kippelen, B. Measurements of the Field-Effect Electron Mobility of the Acceptor ITIC. *Org. Electron.* **2018**, *58*, 290–293. https://doi.org/10.1016/J.ORGEL.2018.04.028.

(56) Scharber, M. C.; Mühlbacher, D.; Koppe, M.; Denk, P.; Waldauf, C.; Heeger, A. J.; Brabec, C. J. Design Rules for Donors in Bulk-Heterojunction Solar Cells—Towards 10 % Energy-Conversion Efficiency. *Adv. Mater.* **2006**, *18* (6), 789–794. https://doi.org/10.1002/ADMA.200501717.

(57) Dennler, G.; Scharber, M. C.; Brabec, C. J. Polymer-Fullerene Bulk-Heterojunction Solar Cells. *Adv. Mater.* **2009**, *21* (13), 1323–1338. https://doi.org/10.1002/ADMA.200801283.

(58) Doumon, N. Y.; Dryzhov, M. V.; Houard, F. V.; Corre, V. M. Le; Chatri, A. R.; Christodoulis, P.; Koster, L. J. A. Photostability of Fullerene and Non-Fullerene Polymer Solar Cells: The Role of the Acceptor. *ACS Appl. Mater. Interfaces* **2019**, *11* (8), 8310–8318. https://doi.org/10.1021/ACSAMI.8B20493.

(59) Zhang, G.; Zhao, J.; Chow, P. C. Y.; Jiang, K.; Zhang, J.; Zhu, Z.; Zhang, J.; Huang, F.; Yan, H. Nonfullerene Acceptor Molecules for Bulk Heterojunction Organic Solar Cells. *Chemical Reviews*. 2018, pp 3447–3507. https://doi.org/10.1021/acs.chemrev.7b00535.

(60) Wadsworth, A.; Moser, M.; Marks, A.; Little, M. S.; Gasparini, N.; Brabec, C. J.; Baran,

D.; Mcculloch, I. Critical Review of the Molecular Design Progress in Non-Fullerene Electron Acceptors towards Commercially Viable Organic Solar Cells †. *Chem. Soc. Rev* **2019**, *48*, 1596–1625. https://doi.org/10.1039/c7cs00892a.

(61) Stoltzfus, D. M.; Donaghey, J. E.; Armin, A.; Shaw, P. E.; Burn, P. L.; Meredith, P. Charge Generation Pathways in Organic Solar Cells: Assessing the Contribution from the Electron Acceptor. *Chem. Rev.* **2016**, *116* (21), 12920–12955. https://doi.org/10.1021/ACS.CHEMREV.6B00126.

(62) Hou, J.; Inganäs, O.; Friend, R. H.; Gao, F. Organic Solar Cells Based on Non-Fullerene Acceptors. *Nat. Mater.* **2018**, *17*, 119–128. https://doi.org/10.1038/nmat5063.

(63) Yan, C.; Barlow, S.; Wang, Z.; Yan, H.; Jen, A. K. Y.; Marder, S. R.; Zhan, X. Non-Fullerene Acceptors for Organic Solar Cells. *Nat. Rev. Mater.* **2018**, *3*, 18003.

(64) Schmidt-Mende, L.; Fechtenkötter, A.; Müllen, K.; Moons, E.; Friend, R. H.; MacKenzie, J. D. Self-Organized Discotic Liquid Crystals for High-Efficiency Organic Photovoltaics. *Science (80-.).* **2001**, *293* (5532), 1119–1122. https://doi.org/10.1126/SCIENCE.293.5532.1119.

(65) Han, G.; Guo, Y.; Song, X.; Wang, Y.; Yi, Y. Terminal π–π Stacking Determines Three-Dimensional Molecular Packing and Isotropic Charge Transport in an A–π–A Electron Acceptor for Non-Fullerene Organic Solar Cells. *J. Mater. Chem. C* **2017**, *5*, 4852–4857. https://doi.org/10.1039/C7TC01310H.

(66) Li, S.; Ye, L.; Zhao, W.; Zhang, S.; Mukherjee, S.; Ade, H.; Hou, J. Energy-Level Modulation of Small-Molecule Electron Acceptors to Achieve over 12% Efficiency in Polymer Solar Cells. *Adv. Mater.* **2016**, *28*, 9423–9429. https://doi.org/10.1002/adma.201602776.

(67) Zhang, H.; Yao, H.; Hou, J.; Zhu, J.; Zhang, J.; Li, W.; Yu, R.; Gao, B.; Zhang, S.; Hou, J. Over 14% Efficiency in Organic Solar Cells Enabled by Chlorinated Nonfullerene Small-Molecule Acceptors. *Adv. Mater.* **2018**, *30*, 1800613. https://doi.org/10.1002/adma.201800613.

(68) Lin, Y.; Zhao, F.; He, Q.; Huo, L.; Wu, Y.; Parker, T. C.; Ma, W.; Sun, Y.; Wang, C.; Zhu, D.; Heeger, A. J.; Marder, S. R.; Zhan, X. High-Performance Electron Acceptor with Thienyl Side Chains for Organic Photovoltaics. *JACS* **2016**, *138*, 4955–4961. https://doi.org/10.1021/jacs.6b02004.

(69) Cheng, P.; Li, G.; Zhan, X.; Yang, Y. Next-Generation Organic Photovoltaics Based on Non-Fullerene Acceptors. *Nat. Photonics 2018 123* **2018**, *12* (3), 131–142. https://doi.org/10.1038/s41566-018-0104-9.

(70) Yang, Y.; Zhang, Z.-G.; Bin, H.; Chen, S.; Gao, L.; Xue, L.; Yang, C.; Li, Y. Side-Chain Isomerization on an n-Type Organic Semiconductor ITIC Acceptor Makes 11.77% High Efficiency Polymer Solar Cells. *JACS* **2016**, *138*, 15011–15018. https://doi.org/10.1021/jacs.6b09110.

(71) Gao, F. A New Acceptor for Highly Efficient Organic Solar Cells. *Joule* **2019**, *3*, 908–909. https://doi.org/10.1016/J.JOULE.2019.03.027.

(72) Yuan, J.; Zhang, Y.; Zhou, L.; Zhang, G.; Yip, H. L.; Lau, T. K.; Lu, X.; Zhu, C.; Peng,

H.; Johnson, P. A.; Leclerc, M.; Cao, Y.; Ulanski, J.; Li, Y.; Zou, Y. Single-Junction Organic Solar Cell with over 15% Efficiency Using Fused-Ring Acceptor with Electron-Deficient Core. *Joule* **2019**, *3* (4), 1140–1151. https://doi.org/10.1016/j.joule.2019.01.004.

(73) Philipps, S.; Fraunhofer ISE and Werner Warmuth; PSE Projects GmbH. *Photovoltaics Report*; 2021.

(74) Sproul, A. Understanding the P-n Junction. *Sol. Cells Resour. Second. Sci. Teach.* **2003**.

(75) Ushasree, P. M.; Bora, B. Chapter 1: Silicon Solar Cells. In *Solar Energy Capture Materials*; Royal Society of Chemistry, 2019; pp 1–55. https://doi.org/10.1039/9781788013512-00001.

(76) Tang, C. W. Two-Layer Organic Photovoltaic Cell. *Appl. Phys. Lett.* **1986**, *48* (2), 183–185. https://doi.org/https://doi.org/10.1063/1.96937.

(77) Wöhrle, D.; Meissner, D. Organic Solar Cells. *Adv. Mater.* **1991**, *3* (3), 129–138. https://doi.org/10.1002/ADMA.19910030303.

(78) Winder, C.; Sariciftci, N. S. Low Bandgap Polymers for Photon Harvesting in Bulk Heterojunction Solar Cells. *J. Mater. Chem.* **2004**, *14* (7), 1077–1086. https://doi.org/10.1039/B306630D.

(79) Serap Günes, *; Helmut Neugebauer, and; Sariciftci, N. S. Conjugated Polymer-Based Organic Solar Cells. *Chem. Rev.* **2007**, *107* (4), 1324–1338. https://doi.org/10.1021/CR050149Z.

(80) Maniloff, E. S.; Vacar, D.; McBranch, D. W.; Wang, H.-L.; Mattes, B. R.; Gao, J.; Heeger, A. J. Ultrafast Holography Using Charge-Transfer Polymers. *Opt. Commun.* **1997**, *141*, 243–246. https://doi.org/https://doi.org/10.1016/S0030-4018(97)00241-1.

(81) Lee, C. H.; Yu, G.; Moses, D.; Pakbaz, K.; Zhang, C.; Sariciftci, N. S.; Heeger, A. J.; Wudl, F. Sensitization of the Photoconductivity of Conducting Polymers by C 60 : Photoinduced Electron Transfer. *Phys. Rev. B* **1993**, *48* (20), 15425. https://doi.org/10.1103/PhysRevB.48.15425.

(82) Halls, J. J. M.; Pichler, K.; Friend, R. H.; Moratti, S. C.; Holmes, A. B. Exciton Diffusion and Dissociation in a Poly(P-phenylenevinylene)/C60 Heterojunction Photovoltaic Cell. *Appl. Phys. Lett.* **1998**, *68* (22), 3120. https://doi.org/10.1063/1.115797.

(83) Sariciftci, N. S.; Braun, D.; Zhang, C.; Srdanov, V. I.; Heeger, A. J.; Stucky, G.; Wudl, F. Semiconducting Polymer-buckminsterfullerene Heterojunctions: Diodes, Photodiodes, and Photovoltaic Cells. *Appl. Phys. Lett.* **1998**, *62* (6), 585. https://doi.org/10.1063/1.108863.

(84) Halls, J. J. M.; Walsh, C. A.; Greenham, N. C.; Marseglia, E. A.; Friend, R. H.; Moratti, S. C.; Holmes, A. B. Efficient Photodiodes from Interpenetrating Polymer Networks. *Nature* **1995**, *376* (3), 498–500. https://doi.org/10.1038/376498A0.

(85) Liao, C. Y.; Chen, Y.; Lee, C. C.; Wang, G.; Teng, N. W.; Lee, C. H.; Li, W. L.; Chen, Y. K.; Li, C. H.; Ho, H. L.; Tan, P. H. S.; Wang, B.; Huang, Y. C.; Young, R. M.; Wasielewski, M. R.; Marks, T. J.; Chang, Y. M.; Facchetti, A. Processing Strategies for an Organic Photovoltaic Module with over 10% Efficiency. *Joule* **2020**, *4* (1), 189–206.

https://doi.org/10.1016/J.JOULE.2019.11.006.

(86) Huang, Y.; Kramer, E. J.; Heeger, A. J.; Bazan, G. C. Bulk Heterojunction Solar Cells: Morphology and Performance Relationships. *Chem. Rev.* **2014**, *114*, 7006–7043. https://doi.org/10.1021/cr400353v.

(87) Peet, J.; Kim, J. Y.; Coates, N. E.; Ma, W. L.; Moses, D.; Heeger, A. J.; Bazan, G. C. Efficiency Enhancement in Low-Bandgap Polymer Solar Cells by Processing with Alkane Dithiols. *Nat. Mater.* **2007**, *6* (7), 497–500. https://doi.org/10.1038/nmat1928.

(88) Lee, J. K.; Ma, W. L.; Brabec, C. J.; Yuen, J.; Sun Moon, J.; Young Kim, J.; Lee, K.; Bazan, G. C.; Heeger, A. J. Processing Additives for Improved Efficiency from Bulk Heterojunction Solar Cells. *J. Am. Chem. Soc.* **2008**, *130* (11), 3619–3623. https://doi.org/10.1021/JA710079W.

(89) Ye, L.; Hu, H.; Ghasemi, M.; Wang, T.; Collins, B. A.; Kim, J.-H.; Jiang, K.; Carpenter, J. H.; Li, H.; Li, Z.; McAfee, T.; Zhao, J.; Chen, X.; Lai, J. L. Y.; Ma, T.; Bredas, J.-L.; Yan, H.; Ade, H. Quantitative Relations between Interaction Parameter, Miscibility and Function in Organic Solar Cells. *Nat. Mater.* **2018**, *17* (3), 253–260. https://doi.org/10.1038/s41563-017-0005-1.

(90) Westacott, P.; Tumbleston, J. R.; Shoaee, S.; Fearn, S.; Bannock, J. H.; Gilchrist, J. B.; Heutz, S.; deMello, J.; Heeney, M.; Ade, H.; Durrant, J.; McPhail, D. S.; Stingelin, N. On the Role of Intermixed Phases in Organic Photovoltaic Blends. *Energy Environ. Sci.* **2013**, *6* (9), 2756–2764. https://doi.org/10.1039/C3EE41821A.

(91) Collins, B. A.; Gann, E.; Guignard, L.; He, X.; Mcneill, C. R.; Ade, H. Molecular Miscibility of Polymer-Fullerene Blends. *J. Phys. Chem. Lett* **2010**, *1*, 3160–3166. https://doi.org/10.1021/jz101276h.

(92) Kim, M.-S.; Kim, B.-G.; Kim, J. Effective Variables To Control the Fill Factor of Organic Photovoltaic Cells. *ACS Appl. Mater. Interfaces* **2009**, *1* (6), 1264–1269. https://doi.org/10.1021/AM900155Y.

(93) Ye, L.; Jiao, X.; Zhang, S.; Yao, H.; Qin, Y.; Ade, H.; Hou, J. Control of Mesoscale Morphology and Photovoltaic Performance in Diketopyrrolopyrrole-Based Small Band Gap Terpolymers. *Adv. Energy Mater.* **2017**, *7* (3), 1601138. https://doi.org/10.1002/aenm.201601138.

(94) Liu, Y.; Zhao, J.; Li, Z.; Mu, C.; Ma, W.; Hu, H.; Jiang, K.; Lin, H.; Ade, H.; Yan, H. Aggregation and Morphology Control Enables Multiple Cases of High-Efficiency Polymer Solar Cells. *Nat. Commun.* **2014**, *5* (5293), 1–8. https://doi.org/10.1038/ncomms6293.

(95) Mukherjee, S.; Proctor, C. M.; Bazan, G. C.; Nguyen, T.-Q.; Ade, H. Significance of Average Domain Purity and Mixed Domains on the Photovoltaic Performance of High-Efficiency Solution-Processed Small-Molecule BHJ Solar Cells. *Adv. Energy Mater.* **2015**, *5* (21), 1500877. https://doi.org/10.1002/aenm.201500877.

(96) Hong, L.; Yao, H.; Wu, Z.; Cui, Y.; Zhang, T.; Xu, Y.; Yu, R.; Liao, Q.; Gao, B.; Xian, K.; Woo, H. Y.; Ge, Z.; Hou, J. Eco-Compatible Solvent-Processed Organic Photovoltaic Cells with Over 16% Efficiency. *Adv. Mater.* **2019**, *31* (39), 1903441. https://doi.org/https://doi.org/10.1002/adma.201903441.

(97) Xu, X.; Yu, T.; Bi, Z.; Ma, W.; Li, Y.; Peng, Q. Realizing Over 13% Efficiency in Green-Solvent-Processed Nonfullerene Organic Solar Cells Enabled by 1,3,4-Thiadiazole-Based Wide-Bandgap Copolymers. *Adv. Mater.* **2018**, *30* (3), 1703973. https://doi.org/https://doi.org/10.1002/adma.201703973.

(98) Yu, Y.-Y.; Tsai, T.-W.; Yang, C.-C.; Chen, C.-P. Highly Efficient Non-Fullerene Organic Photovoltaics Processed from o-Xylene without Using Additives. *J. Phys. Chem. C* **2017**, *121*, 121–21969. https://doi.org/10.1021/acs.jpcc.7b07867.

(99) Lee, S.; Jeong, D.; Kim, C.; Lee, C.; Kang, H.; Woo, H. Y.; Kim, B. J. Eco-Friendly Polymer Solar Cells: Advances in Green-Solvent Processing and Material Design. *ACS Nano* **2020**, *14* (11), 14493–14527. https://doi.org/10.1021/ACSNANO.0C07488.

(100) Li, W.; Chen, M.; Cai, J.; Spooner, E. L. K.; Zhang, H.; Gurney, R. S.; Liu, D.; Xiao, Z.; Lidzey, D. G.; Ding, L.; Wang, T. Molecular Order Control of Non-Fullerene Acceptors for High-Efficiency Polymer Solar Cells. *Joule* **2019**, *3* (3), 819–833. https://doi.org/10.1016/j.joule.2018.11.023.

(101) Li, W.; Yang, L.; Tumbleston, J. R.; Yan, L.; Ade, H.; You, W. Controlling Molecular Weight of a High Efficiency Donor-Acceptor Conjugated Polymer and Understanding Its Significant Impact on Photovoltaic Properties. *Adv. Mater.* **2014**, *26* (26), 4456–4462. https://doi.org/10.1002/adma.201305251.

(102) Lee, T.; Oh, S.; Rasool, S.; Chang, B.; Song, E.; Kim, D.; Lee, S. K.; Won, B.; Shin, S.; Lim, E. Non-Halogenated Solvent-Processed Ternary-Blend Solar Cells via Alkyl-Side-Chain Engineering of a Non-Fullerene Acceptor and Their Application in Large-Area Devices. *J. Mater. Chem. A* **2020**, *8*, 10318–10330. https://doi.org/10.1039/D0TA00947D.

(103) Chen, Z.; Yan, L.; Rech, J. J.; Hu, J.; Zhang, Q.; You, W. Green-Solvent-Processed Conjugated Polymers for Organic Solar Cells: The Impact of Oligoethylene Glycol Side Chains. *ACS Appl. Polym. Mater.* **2019**, *1* (4), 804–814. https://doi.org/10.1021/ACSAPM.9B00044.

(104) Ma, Z.; Zhao, B.; Gong, Y.; Deng, J.; Ao Tan, Z. Green-Solvent-Processable Strategies for Achieving Large-Scale Manufacture of Organic Photovoltaics. *J. Mater. Chem. A* **2019**, *7*, 22826–22847. https://doi.org/10.1039/C9TA09277C.

(105) Zhang, S.; Ye, L.; Zhang, H.; Hou, J. Green-Solvent-Processable Organic Solar Cells. *Mater. Today* **2016**, *19* (9), 533–543. https://doi.org/10.1016/J.MATTOD.2016.02.019.

(106) Zhang, L.; Lin, B.; Hu, B.; Xu, X.; Ma, W. Blade-Cast Nonfullerene Organic Solar Cells in Air with Excellent Morphology, Efficiency, and Stability. *Adv. Mater.* **2018**, *30* (22), 1800343. https://doi.org/10.1002/ADMA.201800343.

(107) Cui, Y.; Yao, H.; Zhang, J.; Zhang, T.; Wang, Y.; Hong, L.; Xian, K.; Xu, B.; Zhang, S.; Peng, J.; Wei, Z.; Gao, F.; Hou, J. Over 16% Efficiency Organic Photovoltaic Cells Enabled by a Chlorinated Acceptor with Increased Open-Circuit Voltages. *Nat. Commun.* **2019**, *10* (2515), 1–8. https://doi.org/10.1038/s41467-019-10351-5.

(108) Günther, M.; Blätte, D.; Oechsle, A. L.; Rivas, S. S.; Amin, A. A. Y.; Müller-Buschbaum, P.; Bein, T.; Ameri, T. Increasing Photostability of Inverted Nonfullerene Organic Solar Cells by Using Fullerene Derivative Additives. *ACS Appl. Mater. Interfaces* **2021**, *13* (16),

19072–19084. https://doi.org/10.1021/ACSAMI.1C00700.

(109) He, Q.; Sheng, W.; Zhang, M.; Xu, G.; Zhu, P.; Zhang, H.; Yao, Z.; Gao, F.; Liu, F.; Liao, X.; Chen, Y. Revealing Morphology Evolution in Highly Efficient Bulk Heterojunction and Pseudo-Planar Heterojunction Solar Cells by Additives Treatment. *Adv. Energy Mater.* **2021**, *11* (7), 2003390. https://doi.org/10.1002/AENM.202003390.

(110) Lou, S. J.; Szarko, J. M.; Xu, T.; Yu, L.; Marks, T. J.; Chen, L. X. Effects of Additives on the Morphology of Solution Phase Aggregates Formed by Active Layer Components of High-Efficiency Organic Solar Cells. *J. Am. Chem. Soc.* **2011**, *133* (51), 20661–20663. https://doi.org/10.1021/JA2085564.

(111) Ye, L.; Zhao, W.; Li, S.; Mukherjee, S.; Carpenter, J. H.; Awartani, O.; Jiao, X.; Hou, J.; Ade, H. High-Efficiency Nonfullerene Organic Solar Cells: Critical Factors That Affect Complex Multi-Length Scale Morphology and Device Performance. *Adv. Energy Mater.* **2017**, *7* (7), 1602000. https://doi.org/10.1002/AENM.201602000.

(112) Lin, Y.; Zhao, F.; Wu, Y.; Chen, K.; Xia, Y.; Li, G.; Prasad, S. K. K.; Zhu, J.; Huo, L.; Bin, H.; Zhang, Z.-G.; Guo, X.; Zhang, M.; Sun, Y.; Gao, F.; Wei, Z.; Ma, W.; Wang, C.; Hodgkiss, J.; Bo, Z.; Inganäs, O.; Li, Y.; Zhan, X. Mapping Polymer Donors toward High-Efficiency Fullerene Free Organic Solar Cells. *Adv. Mater.* **2017**, *29* (3), 1604155. https://doi.org/10.1002/ADMA.201604155.

(113) Liao, H. C.; Ho, C. C.; Chang, C. Y.; Jao, M. H.; Darling, S. B.; Su, W. F. Additives for Morphology Control in High-Efficiency Organic Solar Cells. *Mater. Today* **2013**, *16* (9), 326–336. https://doi.org/10.1016/J.MATTOD.2013.08.013.

(114) Perez, L. A.; Rogers, J. T.; Brady, M. A.; Sun, Y.; Welch, G. C.; Schmidt, K.; Toney, M. F.; Jinnai, H.; Heeger, A. J.; Chabinyc, M. L.; Bazan, G. C.; Kramer, E. J. The Role of Solvent Additive Processing in High Performance Small Molecule Solar Cells. *Chem. Mater.* **2014**, *26*, 6531–6541. https://doi.org/10.1021/cm5031987.

(115) Song, X.; Gasparini, N.; Baran, D. The Influence of Solvent Additive on Polymer Solar Cells Employing Fullerene and Non-Fullerene Acceptors. *Adv. Electron. Mater.* **2018**, *4* (10), 1700358. https://doi.org/https://doi.org/10.1002/aelm.201700358.

(116) Radford, C. L.; Pettipas, R. D.; Kelly, T. L. Watching Paint Dry: Operando Solvent Vapor Annealing of Organic Solar Cells. *J. Phys. Chem. Lett.* **2020**, *11* (15), 6450–6455. https://doi.org/10.1021/ACS.JPCLETT.0C01934.

(117) Ye, L.; Collins, B. A.; Jiao, X.; Zhao, J.; Yan, H.; Ade, H. Miscibility–Function Relations in Organic Solar Cells: Significance of Optimal Miscibility in Relation to Percolation. *Adv. Energy Mater.* **2018**, *8* (28), 1703058. https://doi.org/10.1002/AENM.201703058.

(118) Liu, Y.; Zhao, J.; Li, Z.; Mu, C.; Ma, W.; Hu, H.; Jiang, K.; Lin, H.; Ade, H.; Yan, H. Aggregation and Morphology Control Enables Multiple Cases of High-Efficiency Polymer Solar Cells. *Nat. Commun.* **2014**, *5* (5293), 1–8. https://doi.org/10.1038/ncomms6293.

(119) Ye, L.; Li, S.; Liu, X.; Zhang, S.; Ghasemi, M.; Xiong, Y.; Hou, J.; Ade, H. Quenching to the Percolation Threshold in Organic Solar Cells. *Joule* **2019**, *3* (2), 443–458. https://doi.org/10.1016/J.JOULE.2018.11.006.

(120) Ghasemi, M.; Hu, H.; Peng, Z.; Rech, J. J.; Angunawela, I.; Carpenter, J. H.; Stuard, S. J.; Wadsworth, A.; McCulloch, I.; You, W.; Ade, H. Delineation of Thermodynamic and Kinetic Factors That Control Stability in Non-Fullerene Organic Solar Cells. *Joule* **2019**, *3* (5), 1328–1348. https://doi.org/10.1016/j.joule.2019.03.020.

(121) Li, N.; Perea, J. D.; Kassar, T.; Richter, M.; Heumueller, T.; Matt, G. J.; Hou, Y.; Güldal, N. S.; Chen, H.; Chen, S.; Langner, S.; Berlinghof, M.; Unruh, T.; Brabec, C. J. Abnormal Strong Burn-in Degradation of Highly Efficient Polymer Solar Cells Caused by Spinodal Donor-Acceptor Demixing. *Nat. Commun.* **2017**, *8* (14541), 1–9. https://doi.org/10.1038/ncomms14541.

(122) Binder, K.; Fratzl, P. Spinodal Decomposition. In *Phase Transformations in Material*; 2001; pp 411–474.

(123) Isichenko, M. B. Percolation, Statistical Topography, and Transport in Random Media. *Rev. Mod. Phys.* **1992**, *64* (4), 961. https://doi.org/10.1103/RevModPhys.64.961.

(124) Wang, Z.; Peng, Z.; Xiao, Z.; Seyitliyev, D.; Gundogdu, K.; Ding, L.; Ade, H. Thermodynamic Properties and Molecular Packing Explain Performance and Processing Procedures of Three D18:NFA Organic Solar Cells. *Adv. Mater.* **2020**, 2005386. https://doi.org/10.1002/adma.202005386.

(125) Kleinschmidt, A. T.; Lipomi, D. J. Unfavourable Interactions Enable Stability. *Nat. Mater. 2021 204* **2021**, *20* (4), 447–448. https://doi.org/10.1038/s41563-020-00889-x.

(126) McDowell, C.; Abdelsamie, M.; Toney, M. F.; Bazan, G. C. Solvent Additives: Key Morphology-Directing Agents for Solution-Processed Organic Solar Cells. *Adv. Mater.* **2018**, *30* (33), 1707114. https://doi.org/10.1002/ADMA.201707114.

(127) Scharber, M. C.; Sariciftci, N. S. Efficiency of Bulk-Heterojunction Organic Solar Cells. *Prog. Polym. Sci.* **2013**, *38*, 1929–1940. https://doi.org/10.1016/j.progpolymsci.2013.05.001.

(128) Vandewal, K.; Widmer, J.; Heumueller, T.; Brabec, C. J.; McGehee, M. D.; Leo, K.; Riede, M.; Salleo, A. Increased Open-Circuit Voltage of Organic Solar Cells by Reduced Donor-Acceptor Interface Area. *Adv. Mater.* **2014**, *26* (23), 3839–3843. https://doi.org/10.1002/ADMA.201400114.

(129) Bartesaghi, D.; Pérez, I. del C.; Kniepert, J.; Roland, S.; Turbiez, M.; Neher, D.; Koster, L. J. A. Competition between Recombination and Extraction of Free Charges Determines the Fill Factor of Organic Solar Cells. *Nat. Commun.* **2015**, *6* (7083), 1–10. https://doi.org/10.1038/ncomms8083.

(130) Firdaus, Y.; Le Corre, V. M.; Karuthedath, S.; Liu, W.; Markina, A.; Huang, W.; Chattopadhyay, S.; Nahid, M. M.; Nugraha, M. I.; Lin, Y.; Seitkhan, A.; Basu, A.; Zhang, W.; McCulloch, I.; Ade, H.; Labram, J.; Laquai, F.; Andrienko, D.; Koster, L. J. A.; Anthopoulos, T. D. Long-Range Exciton Diffusion in Molecular Non-Fullerene Acceptors. *Nat. Commun.* **2020**, *11* (5220), 1–10. https://doi.org/10.1038/s41467-020-19029-9.

(131) Du, X.; Heumueller, T.; Gruber, W.; Classen, A.; Unruh, T.; Li, N.; Brabec, C. J. Efficient Polymer Solar Cells Based on Non-Fullerene Acceptors with Potential Device Lifetime Approaching 10 Years. *Joule* **2019**, *3* (1), 215–226.

https://doi.org/10.1016/J.JOULE.2018.09.001.

(132) Ciammaruchi, L.; Zapata-Arteaga, O.; Gutiérrez-Fernández, E.; Martin, J.; Campoy-Quiles, M. Structure Dependent Photostability of ITIC and ITIC-4F. *Mater. Adv.* **2020**, *1* (8), 2846–2861. https://doi.org/10.1039/d0ma00458h.

(133) Yamilova, O. R.; Martynov, I. V.; Brandvold, A. S.; Klimovich, I. V.; Balzer, A. H.; Akkuratov, A. V.; Kusnetsov, I. E.; Stingelin, N.; Troshin, P. A. What Is Killing Organic Photovoltaics: Light-Induced Crosslinking as a General Degradation Pathway of Organic Conjugated Molecules. *Adv. Energy Mater.* **2020**, *10* (7), 1903163. https://doi.org/10.1002/aenm.201903163.

(134) Zhuohan Zhang; Xin Liu; Jiangsheng Yu; Hongtao Wang; Ming Zhang; Linqiang Yang; Renyong Geng; Jinru Cao; Fuqiang Du; Feng Liu; Weihua Tang. Enhancing Phase Separation with a Conformation-Locked Nonfullerene Acceptor for over 14.4% Efficiency Solar Cells. *J. Mater. Chem. C* **2019**, *7* (42), 13279–13286. https://doi.org/10.1039/C9TC04798K.

(135) Cangliosi, D.; Alegría, A.; Colmenero, J. Fast Scanning Calorimetry. In *Fast scanning calorimetry*; Schick, Chritoph, Mathot, V., Ed.; Springer, 2016; p 801.

(136) Martín, J.; Stingelin, N.; Cangialosi, D. Direct Calorimetric Observation of the Rigid Amorphous Fraction in a Semiconducting Polymer. *J. Phys. Chem. Lett.* **2018**, *9*, 990–995. https://doi.org/10.1021/acs.jpclett.7b03110.

(137) Marina, S.; Kaufmann, N. P.; Karki, A.; Gutiérrez-Meza, E.; Gutiérrez-Fernández, E.; Vollbrecht, J.; Solano, E.; Walker, B.; Bannock, J. H.; de Mello, J.; Silva, C.; Nguyen, T.; Cangialosi, D.; Stingelin, N.; Martín, J. The Importance of Quantifying the Composition of the Amorphous Intermixed Phase in Organic Solar Cells. *Adv. Mater.* **2020**, *32* (47), 2005241. https://doi.org/https://doi.org/10.1002/adma.202005241.

(138) Luzio, A.; Nübling, F.; Martin, J.; Fazzi, D.; Selter, P.; Gann, E.; McNeill, C. R.; Brinkmann, M.; Hansen, M. R.; Stingelin, N.; Sommer, M.; Caironi, M. Microstructural Control Suppresses Thermal Activation of Electron Transport at Room Temperature in Polymer Transistors. *Nat. Commun.* **2019**, *10* (3365), 1–13. https://doi.org/10.1038/s41467-019-11125-9.

(139) Schmelzer, J. W. P.; Gutzow, I. S. Generic Theory of Vitrification of Glass-Forming Melts. In *Glasses and the Glass Transition*; Wiley-VCH Verlag GmbH & Co. KGaA: Weinheim, Germany, 2011; pp 91–164. https://doi.org/10.1002/9783527636532.ch3.

(140) Schmelzer JWP, Gutzow IS, Mazurin OV, Priven AI, Todorova SV, P. B. *Glasses and the Glass Transition*; Wiley-VCH Verlag: Weinheim, Germany, 2011.

(141) Cangialosi, D. Physical Aging of Polymers. In *Encyclopedia of Polymer Science and Technology*; Wiley, 2018; pp 1–36. https://doi.org/10.1002/0471440264.pst015.pub2.

(142) Martin, J.; Davidson, E. C.; Greco, C.; Xu, W.; Bannock, J. H.; Agirre, A.; Mello, J. de; Segalman, R. A.; Stingelin, N.; Daoulas, K. C. Temperature-Dependence of Persistence Length Affects Phenomenological Descriptions of Aligning Interactions in Nematic Semiconducting Polymers. *Chem. Mater.* **2018**, *30* (3), 748–761. https://doi.org/10.1021/ACS.CHEMMATER.7B04194.

(143) Nogales, A.; Gutiérrez, E. Grazing incidence Wide Angle X Ray Scattering Representation.

(144) Rivnay, J.; Mannsfeld, S. C. B.; Miller, C. E.; Salleo, A.; Toney, M. F. Quantitative Determination of Organic Semiconductor Microstructure from the Molecular to Device Scale. *Chem. Rev.* **2012**, *112*, 5488–5519. https://doi.org/10.1021/cr3001109.

(145) Rivnay, J.; Noriega, R.; Kline, R. J.; Salleo, A.; Toney, M. F. Quantitative Analysis of Lattice Disorder and Crystallite Size in Organic Semiconductor Thin Films. *Phys. Rev. B - Condens. Matter Mater. Phys.* **2011**, *84* (4), 045203. https://doi.org/10.1103/PhysRevB.84.045203.

(146) Kang, H.; Kim, G.; Kim, J.; Kwon, S.; Kim, H.; Lee, K. Bulk-Heterojunction Organic Solar Cells: Five Core Technologies for Their Commercialization. *Adv. Mater.* **2016**, *28*, 7821–7861. https://doi.org/10.1002/adma.201601197.

(147) Lin, Y.; Adilbekova, B.; Firdaus, Y.; Yengel, E.; Faber, H.; Sajjad, M.; Zheng, X.; Yarali, E.; Seitkhan, A.; Bakr, O. M.; El-Labban, A.; Schwingenschlögl, U.; Tung, V.; McCulloch, I.; Laquai, F.; Anthopoulos, T. D. 17% Efficient Organic Solar Cells Based on Liquid Exfoliated WS 2 as a Replacement for PEDOT:PSS. *Adv. Mater.* **2019**, *31*, 1902965. https://doi.org/10.1002/adma.201902965.

(148) Meng, L.; Zhang, Y.; Wan, X.; Li, C.; Zhang, X.; Wang, Y.; Ke, X.; Xiao, Z.; Ding, L.; Xia, R.; Yip, H. L.; Cao, Y.; Chen, Y. Organic and Solution-Processed Tandem Solar Cells with 17.3% Efficiency. *Science (80-.).* **2018**, *361* (6407), 1094–1098. https://doi.org/10.1126/science.aat2612.

(149) Firdaus, Y.; Le Corre, V. M.; Khan, J. I.; Kan, Z.; Laquai, F.; Beaujuge, P. M.; Anthopoulos, T. D. Key Parameters Requirements for Non-Fullerene-Based Organic Solar Cells with Power Conversion Efficiency >20%. *Adv. Sci.* **2019**, *6* (9), 1802028. https://doi.org/10.1002/advs.201802028.

(150) Wang, T.; Kupgan, G.; Brédas, J. L. Organic Photovoltaics: Relating Chemical Structure, Local Morphology, and Electronic Properties. *Trends Chem.* **2020**, *2* (6), 535–554. https://doi.org/https://doi.org/10.1016/j.trechm.2020.03.006.

(151) Wadsworth, A.; Hamid, Z.; Kosco, J.; Gasparini, N.; McCulloch, I. The Bulk Heterojunction in Organic Photovoltaic, Photodetector, and Photocatalytic Applications. *Adv. Mater.* **2020**, *32*, 2001763. https://doi.org/10.1002/adma.202001763.

(152) Yan, C.; Tang, H.; Ma, R.; Zhang, M.; Liu, T.; Lv, J.; Huang, J.; Yang, Y.; Xu, T.; Kan, Z.; Yan, H.; Liu, F.; Lu, S.; Li, G. Synergy of Liquid-Crystalline Small-Molecule and Polymeric Donors Delivers Uncommon Morphology Evolution and 16.6% Efficiency Organic Photovoltaics. *Adv. Sci.* **2020**, *7* (15), 2000149. https://doi.org/10.1002/advs.202000149.

(153) Karki, A.; Vollbrecht, J.; Dixon, A. L.; Schopp, N.; Schrock, M.; Reddy, G. N. M.; Nguyen, T. Q. Understanding the High Performance of over 15% Efficiency in Single-Junction Bulk Heterojunction Organic Solar Cells. *Adv. Mater.* **2019**, *31* (48), 1903868. https://doi.org/10.1002/adma.201903868.

(154) Fratini, S.; Nikolka, M.; Salleo, A.; Schweicher, G.; Sirringhaus, H. Charge Transport in High-Mobility Conjugated Polymers and Molecular Semiconductors. *Nat. Mater.* **2020**,

19, 491–502. https://doi.org/10.1038/s41563-020-0647-2.

(155) Stingelin, N. On the Phase Behaviour of Organic Semiconductors. *Polym. Int.* **2012**, *61*, 866–873. https://doi.org/10.1002/pi.4214.

(156) Hermann, K.; Gerngross, O.; Abitz, W. Zur Rontgenographischem Strukturforschung Des Delatinemicells. *Z. Phys. Chem.* **1930**, *10*.

(157) Van Antwerpen, F.; Van Krevelen, D. W. Light-Scattering Method for Investigation of the Kinetics of Crystallization of Spherulites. *J. Polym. Sci. Part A-2 Polym. Phys.* **1972**, *10* (12), 2409–2421. https://doi.org/10.1002/pol.1972.180101210.

(158) Martín, J.; Iturrospe, A.; Cavallaro, A.; Arbe, A.; Stingelin, N.; Ezquerra, T. A.; Mijangos, C.; Nogales, A. Relaxations and Relaxor-Ferroelectric-Like Response of Nanotubularly Confined Poly(Vinylidene Fluoride). *Chem. Mater.* **2017**, *29* (8), 3515–3525. https://doi.org/10.1021/acs.chemmater.6b05391.

(159) Dobb, M. G.; Johnson, D. J.; Saville, B. P. SUPRAMOLECULAR STRUCTURE OF A HIGH-MODULUS POLYAROMATIC FIBER (KEVLAR 49). *J Polym Sci Polym Phys Ed* **1977**, *15* (12), 2201–2211. https://doi.org/10.1002/pol.1977.180151212.

(160) Magat, E. E.; Watt, W.; Harris, B.; Ham, A. C. Paracrystalline State of Synthetic Polymers. *Philos. Trans. R. Soc. London. Ser. A, Math. Phys. Sci.* **1980**, *294* (1411), 463–472. https://doi.org/10.1002/polc.5070500116.

(161) Hosemann, R. Crystallinity in High Polymers, Especially Fibres. *Polymer (Guildf).* **1962**, *3*, 349–392. https://doi.org/https://doi.org/10.1016/0032-3861(62)90093-9.

(162) Zapata-Arteaga, O.; Perevedentsev, A.; Marina, S.; Martin, J.; Reparaz, J. S.; Campoy-Quiles, M. Reduction of the Lattice Thermal Conductivity of Polymer Semiconductors by Molecular Doping. *ACS Energy Lett.* **2020**, *5* (9), 2972–2978. https://doi.org/https://doi.org/10.1021/acsenergylett.0c01410.

(163) Snyder, C. R.; Nieuwendaal, R. C.; Delongchamp, D. M.; Luscombe, C. K.; Sista, P.; Boyd, S. D. Quantifying Crystallinity in High Molar Mass Poly(3-Hexylthiophene). *Macromolecules* **2014**, *47* (12), 3942–3950. https://doi.org/10.1021/ma500136d.

(164) Balko, J.; Lohwasser, R. H.; Sommer, M.; Thelakkat, M.; Thurn-Albrecht, T. Determination of the Crystallinity of Semicrystalline Poly(3- Hexylthiophene) by Means of Wide-Angle X-Ray Scattering. *Macromolecules* **2013**, *46* (24), 9642–9651. https://doi.org/10.1021/ma401946w.

(165) Ghasemi, M.; Balar, N.; Peng, Z.; Hu, H.; Qin, Y.; Kim, T.; Rech, J. J.; Bidwell, M.; Mask, W.; McCulloch, I.; You, W.; Amassian, A.; Risko, C.; O'Connor, B. T.; Ade, H. A Molecular Interaction–Diffusion Framework for Predicting Organic Solar Cell Stability. *Nat. Mater.* **2021**, *20* (4), 525–532. https://doi.org/10.1038/s41563-020-00872-6.

(166) Ye, L.; Hu, H.; Ghasemi, M.; Wang, T.; Collins, B. A.; Kim, J. H.; Jiang, K.; Carpenter, J. H.; Li, H.; Li, Z.; McAfee, T.; Zhao, J.; Chen, X.; Lai, J. L. Y.; Ma, T.; Bredas, J. L.; Yan, H.; Ade, H. Quantitative Relations between Interaction Parameter, Miscibility and Function in Organic Solar Cells. *Nat. Mater.* **2018**, *17* (3), 253–260. https://doi.org/10.1038/s41563-017-0005-1.

(167) Köntges, W.; Perkhun, P.; Kammerer, J.; Alkarsifi, R.; Würfel, U.; Margeat, O.; Videlot-

Ackermann, C.; Simon, J. J.; Schröder, R. R.; Schröder, R. R.; Pfannmöller, M. Visualizing Morphological Principles for Efficient Photocurrent Generation in Organic Non-Fullerene Acceptor Blends. *Energy Environ. Sci.* **2020**, *13* (4), 1259–1268. https://doi.org/10.1039/c9ee03535d.

(168) Collins, B. A.; Li, Z.; Tumbleston, J. R.; Gann, E.; McNeill, C. R.; Ade, H. Absolute Measurement of Domain Composition and Nanoscale Size Distribution Explains Performance in PTB7:PC 71 BM Solar Cells. *Adv. Energy Mater.* **2013**, *3*, 65–74. https://doi.org/10.1002/aenm.201200377.

(169) Bartelt, J. A.; Beiley, Z. M.; Hoke, E. T.; Mateker, W. R.; Douglas, J. D.; Collins, B. A.; Tumbleston, J. R.; Graham, K. R.; Amassian, A.; Ade, H.; J Fréchet, J. M.; Toney, M. F.; McGehee, M. D.; Bartelt, J. A.; Beiley, Z. M.; Mateker, W. R.; Graham, K. R.; McGehee, M. D.; Hoke, E. T.; Douglas, J. D.; J Fréchet, J. M. The Importance of Fullerene Percolation in the Mixed Regions of Polymer-Fullerene Bulk Heterojunction Solar Cells. *Adv. Energy Mater.* **2013**, *3*, 364–374. https://doi.org/10.1002/aenm.201200637.

(170) Mukherjee, S.; Proctor, C. M.; Tumbleston, J. R.; Bazan, G. C.; Nguyen, T. Q.; Ade, H. Importance of Domain Purity and Molecular Packing in Effi Cient Solution-Processed Small-Molecule Solar Cells. *Adv. Mater.* **2015**, *27* (6), 1105–1111. https://doi.org/10.1002/adma.201404388.

(171) Ye, L.; Li, S.; Liu, X.; Zhang, S.; Ghasemi, M.; Xiong, Y.; Hou, J.; Ade, H. Quenching to the Percolation Threshold in Organic Solar Cells. *Joule* **2019**, *3* (2), 443–458. https://doi.org/10.1016/j.joule.2018.11.006.

(172) Li, S.; Ye, L.; Zhao, W.; Zhang, S.; Mukherjee, S.; Ade, H.; Hou, J. Energy-Level Modulation of Small-Molecule Electron Acceptors to Achieve over 12% Efficiency in Polymer Solar Cells. *Adv. Mater.* **2016**, *28*, 9423–9429. https://doi.org/10.1002/adma.201602776.

(173) Sommerville, P. J. W.; Li, Y.; Dong, X.; Zhang, Y.; Onorato, J. W.; Tatum, W. K.; Balzer, A. H.; Stingelin, N.; Patel, S. N.; Nealey, P. F.; Luscombe, C. K. Elucidating the Influence of Side-Chain Circular Distribution on the Crack Onset Strain and Hole Mobility of Near-Amorphous Indacenodithiophene Copolymers. *Macromolecules* **2020**, *53* (17), 7511–7518. https://doi.org/https://doi.org/10.1021/acs.macromol.0c00512.

(174) Xiao, M.; Sadhanala, A.; Abdi-Jalebi, M.; Thomas, T. H.; Ren, X.; Zhang, T.; Chen, H.; Carey, R. L.; Wang, Q.; Senanayak, S. P.; Jellett, C.; Onwubiko, A.; Moser, M.; Liao, H.; Yue, W.; McCulloch, I.; Nikolka, M.; Sirringhaus, H. Linking Glass-Transition Behavior to Photophysical and Charge Transport Properties of High-Mobility Conjugated Polymers. *Adv. Funct. Mater.* **2021**, *31* (7), 2007359. https://doi.org/10.1002/adfm.202007359.

(175) Beaucage, G. Approximations Leading to a Unified Exponential/Power-Law Approach to Small-Angle Scattering. *J. Appl. Crystallogr.* **1995**, *28* (6), 717–728. https://doi.org/10.1107/s0021889895005292.

(176) Snyder, C. R.; DeLongchamp, D. M. Glassy Phases in Organic Semiconductors. *Curr. Opin. Solid State Mater. Sci.* **2018**, *22*, 41–48. https://doi.org/10.1016/J.COSSMS.2018.03.001.

(177) Van Krevelen, D. W.; Te Nijenhuis, K. *Properties of Polymers*, Elsevier.; 2009.

https://doi.org/10.1016/B978-0-08-054819-7.X0001-5.

(178) Wang, Z.; Peng, Z.; Xiao, Z.; Seyitliyev, D.; Gundogdu, K.; Ding, L.; Ade, H. Thermodynamic Properties and Molecular Packing Explain Performance and Processing Procedures of Three D18:NFA Organic Solar Cells. *Adv. Mater.* **2020**, *32* (49), 2005386. https://doi.org/10.1002/adma.202005386.

(179) Chen, W.; Xu, T.; He, F.; Wang, W.; Wang, C.; Strzalka, J.; Liu, Y.; Wen, J.; Miller, D. J.; Chen, J.; Hong, K.; Yu, L.; Darling, S. B. Hierarchical Nanomorphologies Promote Exciton Dissociation in Polymer/Fullerene Bulk Heterojunction Solar Cells. *Nano Lett.* **2011**, *11* (9), 3707–3713. https://doi.org/10.1021/nl201715q.

(180) Zhang, X.; Bronstein, H.; Kronemeijer, A. J.; Smith, J.; Kim, Y.; Kline, R. J.; Richter, L. J.; Anthopoulos, T. D.; Sirringhaus, H.; Song, K.; Heeney, M.; Zhang, W.; McCulloch, I.; Delongchamp, D. M. Molecular Origin of High Field-Effect Mobility in an Indacenodithiophene- Benzothiadiazole Copolymer. *Nat. Commun.* **2013**, *4* (2238), 1–9. https://doi.org/10.1038/ncomms3238.

(181) McCulloch, I.; Heeney, M.; Bailey, C.; Genevicius, K.; MacDonald, I.; Shkunov, M.; Sparrowe, D.; Tierney, S.; Wagner, R.; Zhang, W.; Chabinyc, M. L.; Kline, R. J.; McGehee, M. D.; Toney, M. F. Liquid-Crystalline Semiconducting Polymers with High Charge-Carrier Mobility. *Nat. Mater.* **2006**, *5* (4), 328–333. https://doi.org/10.1038/nmat1612.

(182) Jiao, X.; Wang, C.; Mcneill, C. R. Detecting the Onset of Molecular Reorganization in Conjugated Polymer Thin Films Using an Easily Accessible Optical Method. *Macromolecules* **2019**, *52* (12), 4646–4654. https://doi.org/10.1021/acs.macromol.9b00606.

(183) Marina, S.; Scaccabarozzi, A. D.; Gutierrez-Fernandez, E.; Solano, E.; Khirbat, A.; Ciammaruchi, L.; Iturrospe, A.; Balzer, A.; Yu, L.; Gabirondo, E.; Monnier, X.; Sardon, H.; Anthopoulos, T. D.; Caironi, M.; Campoy-Quiles, M.; Müller, C.; Cangialosi, D.; Stingelin, N.; Martin, J. Polymorphism in Non-Fullerene Acceptors Based on Indacenodithienothiophene. *Adv. Funct. Mater.* **2021**, *31*, 2103784. https://doi.org/10.1002/adfm.202103784.

(184) Brabec, C. J.; Gowrisanker, S.; Halls, J. J. M.; Laird, D.; Jia, S.; Williams, S. P. Polymer-Fullerene Bulk-Heterojunction Solar Cells. *Adv. Mater.* **2010**, *22* (34), 3839–3856. https://doi.org/10.1002/adma.200903697.

(185) Feng, L.; Yuan, J.; Zhang, Z.; Peng, H.; Zhang, Z. G.; Xu, S.; Liu, Y.; Li, Y.; Zou, Y. Thieno[3,2-b]Pyrrolo-Fused Pentacyclic Benzotriazole-Based Acceptor for Efficient Organic Photovoltaics. *ACS Appl. Mater. Interfaces* **2017**, *9* (37), 31985–31992. https://doi.org/10.1021/acsami.7b10995.

(186) Zhao, J.; Swinnen, A.; Van Assche, G.; Manca, J.; Vanderzande, D.; Van Mele, B. Phase Diagram of P3HT/PCBM Blends and Its Implication for the Stability of Morphology. *J. Phys. Chem. B* **2009**, *113* (6), 1587–1591. https://doi.org/10.1021/jp804151a.

(187) Müller, C.; Bergqvist, J.; Vandewal, K.; Tvingstedt, K.; Anselmo, A. S.; Magnusson, R.; Alonso, M. I.; Moons, E.; Arwin, H.; Campoy-Quiles, M.; Inganäs, O. Phase Behaviour of Liquid-Crystalline Polymer/Fullerene Organic Photovoltaic Blends: Thermal Stability

and Miscibility. *J. Mater. Chem.* **2011**, *21* (29), 10676–10684. https://doi.org/10.1039/c1jm11239b.

(188) Lindqvist, C.; Sanz-Velasco, A.; Wang, E.; Bäcke, O.; Gustafsson, S.; Olsson, E.; Andersson, M. R.; Müller, C. Nucleation-Limited Fullerene Crystallisation in a Polymer-Fullerene Bulk-Heterojunction Blend. *J. Mater. Chem. A* **2013**, *1* (24), 7174–7180. https://doi.org/10.1039/c3ta11018d.

(189) Yu, L.; Davidson, E.; Sharma, A.; Andersson, M. R.; Segalman, R.; Mü, C. Isothermal Crystallization Kinetics and Time−Temperature− Transformation of the Conjugated Polymer: Poly(3-(2′-Ethyl)Hexylthiophene). *Chem. Mater* **2017**, *29*, 5662. https://doi.org/10.1021/acs.chemmater.7b01393.

(190) Müller, C. On the Glass Transition of Polymer Semiconductors and Its Impact on Polymer Solar Cell Stability. *Chem. Mater.* **2015**, *27* (8), 2740–2754. https://doi.org/10.1021/acs.chemmater.5b00024.

(191) Cha, H.; Fish, G.; Luke, J.; Alraddadi, A.; Lee, H. H.; Zhang, W.; Dong, Y.; Limbu, S.; Wadsworth, A.; Maria, I. P.; Francàs, L.; Sou, H. L.; Du, T.; Kim, J.; McLachlan, M. A.; McCulloch, I.; Durrant, J. R. Suppression of Recombination Losses in Polymer:Nonfullerene Acceptor Organic Solar Cells Due to Aggregation Dependence of Acceptor Electron Affinity. *Adv. Energy Mater.* **2019**, *9*, 1901254. https://doi.org/10.1002/aenm.201901254.

(192) Du, X.; Heumueller, T.; Gruber, W.; Almora, O.; Classen, A.; Qu, J.; He, F.; Unruh, T.; Li, N.; Brabec, C. J. Unraveling the Microstructure-Related Device Stability for Polymer Solar Cells Based on Nonfullerene Small-Molecular Acceptors. *Adv. Mater.* **2020**, *32*, 1908305. https://doi.org/10.1002/adma.201908305.

(193) Zhu, W.; Spencer, A. P.; Mukherjee, S.; Alzola, J. M.; Sangwan, V. K.; Amsterdam, S. H.; Swick, S. M.; Jones, L. O.; Heiber, M. C.; Herzing, A. A.; Li, G.; Stern, C. L.; DeLongchamp, D. M.; Kohlstedt, K. L.; Hersam, M. C.; Schatz, G. C.; Wasielewski, M. R.; Chen, L. X.; Facchetti, A.; Marks, T. J. Crystallography, Morphology, Electronic Structure, and Transport in Non-Fullerene/Non-Indacenodithienothiophene Polymer:Y6 Solar Cells. *J. Am. Chem. Soc.* **2020**, *142* (34), 14532–14547. https://doi.org/https://doi.org/10.1021/jacs.0c05560.

(194) Liang, Q.; Han, J.; Song, C.; Yu, X.; Smilgies, D.-M.; Zhao, K.; Liu, J.; Han, Y. Reducing the Confinement of PBDB-T to ITIC to Improve the Crystallinity of PBDB-T/ITIC Blends †. *J. Mater. Chem. A* **2018**, *6*, 15610–15620. https://doi.org/10.1039/c8ta05892j.

(195) Mai, J.; Xiao, Y.; Zhou, G.; Wang, J.; Zhu, J.; Zhao, N.; Zhan, X.; Lu, X. Hidden Structure Ordering Along Backbone of Fused-Ring Electron Acceptors Enhanced by Ternary Bulk Heterojunction. *Adv. Mater.* **2018**, *30* (34), 1802888. https://doi.org/10.1002/adma.201802888.

(196) Kissi, E. O.; Grohganz, H.; Löbmann, K.; Ruggiero, M. T.; Zeitler, J. A.; Rades, T. Glass-Transition Temperature of the β-Relaxation as the Major Predictive Parameter for Recrystallization of Neat Amorphous Drugs. *J. Phys. Chem. B* **2018**, *122* (10), 2803–2808. https://doi.org/10.1021/acs.jpcb.7b10105.

(197) Dudognon, E.; Danède, F.; Descamps, M.; Correia, N. T. Evidence for a New Crystalline

Phase of Racemic Ibuprofen. In *Pharmaceutical Research*; Springer New York, 2008; Vol. 25, pp 2853–2858. https://doi.org/10.1007/s11095-008-9655-7.

(198) Chen, J.; Shao, M.; Xiao, K.; Rondinone, A. J.; Loo, Y. L.; Kent, P. R. C.; Sumpter, B. G.; Li, D.; Keum, J. K.; Diemer, P. J.; Anthony, J. E.; Jurchescu, O. D.; Huang, J. Solvent-Type-Dependent Polymorphism and Charge Transport in a Long Fused-Ring Organic Semiconductor. *Nanoscale* **2014**, *6* (1), 449–456. https://doi.org/10.1039/c3nr04341j.

(199) Giri, G.; Li, R.; Smilgies, D. M.; Li, E. Q.; Diao, Y.; Lenn, K. M.; Chiu, M.; Lin, D. W.; Allen, R.; Reinspach, J.; Mannsfeld, S. C. B.; Thoroddsen, S. T.; Clancy, P.; Bao, Z.; Amassian, A. One-Dimensional Self-Confinement Promotes Polymorph Selection in Large-Area Organic Semiconductor Thin Films. *Nat. Commun.* **2014**, *5* (3573), 1–8. https://doi.org/10.1038/ncomms4573.

(200) Luk, J. C. Solubility and Pseudo-Polymorphic Transition of L-Serine in Water-Methanol Systems, Georgia Institute of Technology, 2005.

(201) Ostwald, W. Studien Über Die Bildung Und Umwandlung Fester Körper. *Z. Phys. Chem.* **1897**, *22* (1).

(202) Chung, H.; Diao, Y. Polymorphism as an Emerging Design Strategy for High Performance Organic Electronics. *J. Mater. Chem. C* **2016**, *4* (18), 3915–3933. https://doi.org/10.1039/c5tc04390e.

(203) Giri, G.; Verploegen, E.; Mannsfeld, S. C. B.; Atahan-Evrenk, S.; Kim, D. H.; Lee, S. Y.; Becerril, H. A.; Aspuru-Guzik, A.; Toney, M. F.; Bao, Z. Tuning Charge Transport in Solution-Sheared Organic Semiconductors Using Lattice Strain. *Nature* **2011**, *480* (7378), 504–508. https://doi.org/10.1038/nature10683.

(204) Giri, G.; Park, S.; Vosgueritchian, M.; Shulaker, M. M.; Bao, Z. High-Mobility, Aligned Crystalline Domains of Tips-Pentacene with Metastable Polymorphs through Lateral Confinement of Crystal Growth. *Adv. Mater.* **2014**, *26* (3), 487–493. https://doi.org/10.1002/adma.201302439.

(205) Davies, D. W.; Park, S. K.; Kafle, P.; Chung, H.; Yuan, D.; Strzalka, J. W.; Mannsfeld, S. C. B.; Wang, S. G.; Chen, Y. S.; Gray, D. L.; Zhu, X.; Diao, Y. Radically Tunable N-Type Organic Semiconductor via Polymorph Control. *Chem. Mater.* **2021**, *33* (7), 2466–2477. https://doi.org/https://doi.org/10.1021/acs.chemmater.0c04678.

(206) Wu, Y.; Zou, Y.; Yang, H.; Li, Y.; Li, H.; Cui, C.; Li, Y. Achieving over 9.8% Efficiency in Nonfullerene Polymer Solar Cells by Environmentally Friendly Solvent Processing. *ACS Appl. Mater. Interfaces* **2017**, *9* (42), 37078–37086. https://doi.org/10.1021/acsami.7b11488.

(207) Eastham, N. D.; Logsdon, J. L.; Manley, E. F.; Aldrich, T. J.; Leonardi, M. J.; Wang, G.; Powers-Riggs, N. E.; Young, R. M.; Chen, L. X.; Wasielewski, M. R.; Melkonyan, F. S.; Chang, R. P. H.; Marks, T. J. Hole-Transfer Dependence on Blend Morphology and Energy Level Alignment in Polymer: ITIC Photovoltaic Materials. *Adv. Mater.* **2018**, *30* (3), 1704263. https://doi.org/10.1002/adma.201704263.

(208) Pan, Q.-Q.; Li, S.-B.; Duan, Y.-C.; Wu, Y.; Zhang, J.; Geng, Y.; Zhao, L.; Su, Z.-M. Exploring What Prompts ITIC to Become a Superior Acceptor in Organic Solar Cell by Combining Molecular Dynamics Simulation with Quantum Chemistry Calculation. *Phys.*

Chem. Chem. Phys. **2017**, *19*, 31227–31235. https://doi.org/10.1039/C7CP05938H.

(209) Jiao, X.; Statz, M.; Lai, L.; Schott, S.; Jellett, C.; McCulloch, I.; Sirringhaus, H.; McNeill, C. R. Resolving Different Physical Origins toward Crystallite Imperfection in Semiconducting Polymers: Crystallite Size vs Paracrystallinity. *J. Phys. Chem. B* **2020**, *124* (46), 10529–10538. https://doi.org/10.1021/acs.jpcb.0c06763.

(210) Bin, H.; Gao, L.; Zhang, Z. G.; Yang, Y.; Zhang, Y.; Zhang, C.; Chen, S.; Xue, L.; Yang, C.; Xiao, M.; Li, Y. 11.4% Efficiency Non-Fullerene Polymer Solar Cells with Trialkylsilyl Substituted 2D-Conjugated Polymer as Donor. *Nat. Commun.* **2016**, *7* (13651), 1–11. https://doi.org/10.1038/ncomms13651.

(211) Li, X.; Yao, J.; Angunawela, I.; Sun, C.; Xue, L.; Liebman-Pelaez, A.; Zhu, C.; Yang, C.; Zhang, Z.-G.; Ade, H.; Li, Y. Improvement of Photovoltaic Performance of Polymer Solar Cells by Rational Molecular Optimization of Organic Molecule Acceptors. *Adv. Energy Mater.* **2018**, *8* (23), 1800815. https://doi.org/10.1002/aenm.201800815.

(212) Liu, Y.; Zhang, C.; Hao, D.; Zhang, Z.; Wu, L.; Li, M.; Feng, S.; Xu, X.; Liu, F.; Chen, X.; Bo, Z. Enhancing the Performance of Organic Solar Cells by Hierarchically Supramolecular Self-Assembly of Fused-Ring Electron Acceptors. *Chem. Mater.* **2018**, *30* (13), 4307–4312. https://doi.org/10.1021/acs.chemmater.8b01319.

(213) Chen, H.; Qu, J.; Liu, L.; Chen, W.; He, F. Carrier Dynamics and Morphology Regulated by 1,8-Diiodooctane in Chlorinated Nonfullerene Polymer Solar Cells. *J. Phys. Chem. Lett.* **2019**, *10* (5), 936–942. https://doi.org/10.1021/acs.jpclett.9b00063.

(214) Ciammaruchi, L.; Zapata-Arteaga, O.; Gutiérrez-Fernández, E.; Martin, J.; Campoy-Quiles, M. Structure Dependent Photostability of ITIC and ITIC-4F. *Mater. Adv.* **2020**, *1* (8), 2846–2861. https://doi.org/10.1039/d0ma00458h.

(215) Zhu, L.; Zhang, M.; Zhou, G.; Hao, T.; Xu, J.; Wang, J.; Qiu, C.; Prine, N.; Ali, J.; Feng, W.; Gu, X.; Ma, Z.; Tang, Z.; Zhu, H.; Ying, L.; Zhang, Y.; Liu, F. Efficient Organic Solar Cell with 16.88% Efficiency Enabled by Refined Acceptor Crystallization and Morphology with Improved Charge Transfer and Transport Properties. *Adv. Energy Mater.* **2020**, *10* (18), 1904234. https://doi.org/10.1002/aenm.201904234.

(216) Aldrich, T. J.; Matta, M.; Zhu, W.; Swick, S. M.; Stern, C. L.; Schatz, G. C.; Facchetti, A.; Melkonyan, F. S.; Marks, T. J. Fluorination Effects on Indacenodithienothiophene Acceptor Packing and Electronic Structure, End-Group Redistribution, and Solar Cell Photovoltaic Response. *J. Am. Chem. Soc.* **2019**, *141* (7), 3274–3287. https://doi.org/10.1021/jacs.8b13653.

(217) Bristow, H.; Thorley, K. J.; White, A. J. P.; Wadsworth, A.; Babics, M.; Hamid, Z.; Zhang, W.; Paterson, A. F.; Kosco, J.; Panidi, J.; Anthopoulos, T. D.; McCulloch, I. Impact of Nonfullerene Acceptor Side Chain Variation on Transistor Mobility. *Adv. Electron. Mater.* **2019**, *5* (10), 1900344. https://doi.org/10.1002/aelm.201900344.

(218) Halaby, S.; Martynowycz, M. W.; Zhu, Z.; Tretiak, S.; Zhugayevych, A.; Gonen, T.; Seifrid, M. Microcrystal Electron Diffraction for Molecular Design of Functional Non-Fullerene Acceptor Structures. **2021**, *16*, 2021. https://doi.org/10.1021/acs.chemmater.0c04111.

(219) Lai, H.; Chen, H.; Zhou, J.; Qu, J.; Wang, M.; Xie, W.; Xie, Z.; He, F. 3D Interpenetrating

Network for High-Performance Nonfullerene Acceptors via Asymmetric Chlorine Substitution. *J. Phys. Chem. Lett.* **2019**, *10* (16), 4737–4743. https://doi.org/10.1021/acs.jpclett.9b01931.

(220) Lai, H.; Chen, H.; Zhou, J.; Qu, J.; Chao, P.; Liu, T.; Chang, X.; Zheng, N.; Xie, Z.; He, F. Isomer-Free: Precise Positioning of Chlorine-Induced Interpenetrating Charge Transfer for Elevated Solar Conversion. *iScience* **2019**, *17*, 302–314. https://doi.org/10.1016/j.isci.2019.06.033.

(221) Yan, D.; Liu, W.; Yao, J.; Zhan, C. Fused-Ring Nonfullerene Acceptor Forming Interpenetrating J-Architecture for Fullerene-Free Polymer Solar Cells. *Adv. Energy Mater.* **2018**, *8* (31), 1800204. https://doi.org/10.1002/aenm.201800204.

(222) Qu, J.; Chen, H.; Zhou, J.; Lai, H.; Liu, T.; Chao, P.; Li, D.; Xie, Z.; He, F.; Ma, Y. Chlorine Atom-Induced Molecular Interlocked Network in a Non-Fullerene Acceptor. *ACS Appl. Mater. Interfaces* **2018**, *10* (46), 39992–40000. https://doi.org/10.1021/acsami.8b15923.

(223) Swick, S. M.; Gebraad, T.; Jones, L.; Fu, B.; Aldrich, T. J.; Kohlstedt, K. L.; Schatz, G. C.; Facchetti, A.; Marks, T. J. Building Blocks for High-Efficiency Organic Photovoltaics: Interplay of Molecular, Crystal, and Electronic Properties in Post-Fullerene ITIC Ensembles. *ChemPhysChem* **2019**, *20* (20), 2608–2626. https://doi.org/10.1002/cphc.201900793.

(224) Williams, G.; Watts, D. C. Non-Symmetrical Dielectric Relaxation Behaviour Arising from a Simple Empirical Decay Function. *Trans. Faraday Soc.* **1970**, *66* (0), 80–85. https://doi.org/10.1039/TF9706600080.

(225) Cangialosi, D. Dynamics and Thermodynamics of Polymer Glasses. *Journal of Physics Condensed Matter*. IOP Publishing April 16, 2014, p 153101. https://doi.org/10.1088/0953-8984/26/15/153101.

(226) Lin, Y.; Adilbekova, B.; Firdaus, Y.; Yengel, E.; Faber, H.; Sajjad, M.; Zheng, X.; Yarali, E.; Seitkhan, A.; Bakr, O. M.; El-Labban, A.; Schwingenschlögl, U.; Tung, V.; McCulloch, I.; Laquai, F.; Anthopoulos, T. D. 17% Efficient Organic Solar Cells Based on Liquid Exfoliated WS2 as a Replacement for PEDOT:PSS. *Adv. Mater.* **2019**, *31*, 1902965. https://doi.org/10.1002/adma.201902965.

(227) Brédas, J. L.; Norton, J. E.; Cornil, J.; Coropceanu, V. Molecular Understanding of Organic Solar Cells: The Challenges. *Acc. Chem. Res.* **2009**, *42* (11), 1691–1699. https://doi.org/10.1021/ar900099h.

(228) Zhao, J.; Li, Y.; Yang, G.; Jiang, K.; Lin, H.; Ade, H.; Ma, W.; Yan, H. Efficient Organic Solar Cells Processed from Hydrocarbon Solvents. *Nat. Energy* **2016**, *1* (2), 15027. https://doi.org/10.1038/NENERGY.2015.27.

(229) Ye, L.; Zhao, W.; Li, S.; Mukherjee, S.; Carpenter, J. H.; Awartani, O.; Jiao, X.; Hou, J.; Ade, H. High-Efficiency Nonfullerene Organic Solar Cells: Critical Factors That Affect Complex Multi-Length Scale Morphology and Device Performance. *Adv. Energy Mater.* **2017**, *7* (7), 1602000. https://doi.org/10.1002/aenm.201602000.

(230) Baran, D.; Ashraf, R. S.; Hanifi, D. A.; Abdelsamie, M.; Gasparini, N.; Röhr, J. A.; Holliday, S.; Wadsworth, A.; Lockett, S.; Neophytou, M.; Emmott, C. J. M.; Nelson, J.;

Brabec, C. J.; Amassian, A.; Salleo, A.; Kirchartz, T.; Durrant, J. R.; McCulloch, I. Reducing the Efficiency-Stability-Cost Gap of Organic Photovoltaics with Highly Efficient and Stable Small Molecule Acceptor Ternary Solar Cells. *Nat. Mater.* **2017**, *16* (3), 363–369. https://doi.org/10.1038/nmat4797.

(231) Moon, J. S.; Lee, J. K.; Cho, S.; Byun, J.; Heeger, A. J. "Columnlike" Structure of the Cross-Sectional Morphology of Bulk Heterojunction Materials. *Nano Lett.* **2009**, *9* (1), 230–234. https://doi.org/10.1021/nl802821h.

(232) Sun, Y.; Welch, G. C.; Leong, W. L.; Takacs, C. J.; Bazan, G. C.; Heeger, A. J. Solution-Processed Small-Molecule Solar Cells with 6.7% Efficiency. *Nat. Mater.* **2012**, *11* (1), 44–48. https://doi.org/10.1038/nmat3160.

(233) Westacott, P.; Tumbleston, J. R.; Shoaee, S.; Fearn, S.; Bannock, J. H.; Gilchrist, J. B.; Heutz, S.; Demello, J.; Heeney, M.; Ade, H.; Durrant, J.; McPhail, D. S.; Stingelin, N. On the Role of Intermixed Phases in Organic Photovoltaic Blends. *Energy Environ. Sci.* **2013**, *6* (9), 2756–2764. https://doi.org/10.1039/c3ee41821a.

(234) Collins, B. A.; Gann, E.; Guignard, L.; He, X.; Mcneill, C. R.; Ade, H. Molecular Miscibility of Polymer-Fullerene Blends. *J. Phys. Chem. Lett* **2010**, *1*, 3160–3166. https://doi.org/10.1021/jz101276h.

(235) Watts, B.; Belcher, W. J.; Thomsen, L.; Ade, H.; Dastoor, P. C. A Quantitative Study of PCBM Diffusion during Annealing of P3HT: PCBM Blend Films. *Macromolecules* **2009**, *42*, 8392–8397. https://doi.org/10.1021/ma901444u.

(236) Treat, N. D.; Varotto, A.; Takacs, C. J.; Batara, N.; Al-Hashimi, M.; Heeney, M. J.; Heeger, A. J.; Wudl, F.; Hawker, C. J.; Chabinyc, M. L. Polymer-Fullerene Miscibility: A Metric for Screening New Materials for High-Performance Organic Solar Cells. *J. Am. Chem. Soc.* **2012**, *134* (38), 15869–15879. https://doi.org/10.1021/ja305875u.

(237) Leman, D.; Kelly, M. A.; Ness, S.; Engmann, S.; Herzing, A.; Snyder, C.; Ro, H. W.; Kline, R. J.; DeLongchamp, D. M.; Richter, L. J. In Situ Characterization of Polymer-Fullerene Bilayer Stability. *Macromolecules* **2015**, *48* (2), 383–392. https://doi.org/10.1021/ma5021227.

(238) Guo, X.; Zhang, M.; Ma, W.; Ye, L.; Zhang, S.; Liu, S.; Ade, H.; Huang, F.; Hou, J. Enhanced Photovoltaic Performance by Modulating Surface Composition in Bulk Heterojunction Polymer Solar Cells Based on PBDTTT-C-T/PC $_{71}$ BM. *Adv. Mater.* **2014**, *26* (24), 4043–4049. https://doi.org/10.1002/adma.201400411.

(239) Zhao, J.; Li, Y.; Yang, G.; Jiang, K.; Lin, H.; Ade, H.; Ma, W.; Yan, H. Efficient Organic Solar Cells Processed from Hydrocarbon Solvents. *Nat. Energy* **2016**, *1* (2), 15027. https://doi.org/10.1038/NENERGY.2015.27.

(240) Lan, L.; Chen, Z.; Hu, Q.; Ying, L.; Zhu, R.; Liu, F.; Russell, T. P.; Huang, F.; Cao, Y. High-Performance Polymer Solar Cells Based on a Wide-Bandgap Polymer Containing Pyrrolo[3,4-*f*]Benzotriazole-5,7-Dione with a Power Conversion Efficiency of 8.63%. *Adv. Sci.* **2016**, *3* (9), 1600032. https://doi.org/10.1002/advs.201600032.

(241) Bartelt, J. A.; Beiley, Z. M.; Hoke, E. T.; Mateker, W. R.; Douglas, J. D.; Collins, B. A.; Tumbleston, J. R.; Graham, K. R.; Amassian, A.; Ade, H.; Fréchet, J. M. J.; Toney, M. F.; Mcgehee, M. D. The Importance of Fullerene Percolation in the Mixed Regions of

Polymer-Fullerene Bulk Heterojunction Solar Cells. *Adv. Energy Mater.* **2013**, *3* (3), 364–374. https://doi.org/10.1002/aenm.201200637.

(242) Roland, S.; Schubert, M.; Collins, B. A.; Kurpiers, J.; Chen, Z.; Facchetti, A.; Ade, H.; Neher, D. Fullerene-Free Polymer Solar Cells with Highly Reduced Bimolecular Recombination and Field-Independent Charge Carrier Generation. *J. Phys. Chem. Lett.* **2014**, *5* (16), 2815–2822. https://doi.org/10.1021/jz501506z.

(243) Pfannmöller, M.; Flügge, H.; Benner, G.; Wacker, I.; Sommer, C.; Hanselmann, M.; Schmale, S.; Schmidt, H.; Hamprecht, F. A.; Rabe, T.; Kowalsky, W.; Schröder, R. R. Visualizing a Homogeneous Blend in Bulk Heterojunction Polymer Solar Cells by Analytical Electron Microscopy. *Nano Lett.* **2011**, *11* (8), 3099–3107. https://doi.org/10.1021/nl201078t.

(244) Kozub, D. R.; Vakhshouri, K.; Orme, L. M.; Wang, C.; Hexemer, A.; Gomez, E. D. Polymer Crystallization of Partially Miscible Polythiophene/Fullerene Mixtures Controls Morphology. *Macromolecules* **2011**, *44*, 5722–5726. https://doi.org/10.1021/ma200855r.

(245) Huang, W.; Gann, E.; Chandrasekaran, N.; Thomsen, L.; Prasad, S. K. K.; Hodgkiss, J. M.; Kabra, D.; Cheng, Y. B.; McNeill, C. R. Isolating and Quantifying the Impact of Domain Purity on the Performance of Bulk Heterojunction Solar Cells. *Energy Environ. Sci.* **2017**, *10* (8), 1843–1853. https://doi.org/10.1039/c7ee01387f.

(246) Collins, B. A.; Tumbleston, J. R.; Ade, H. Miscibility, Crystallinity, and Phase Development in P3HT/PCBM Solar Cells: Toward an Enlightened Understanding of Device Morphology and Stability. *J. Phys. Chem. Lett.* **2011**, *2* (24), 3135–3145. https://doi.org/10.1021/jz2014902.

(247) McNeill, C. R.; Ade, H. Soft X-Ray Characterisation of Organic Semiconductor Films. *Journal of Materials Chemistry C*. The Royal Society of Chemistry January 14, 2013, pp 187–201. https://doi.org/10.1039/c2tc00001f.

(248) Jiao, X.; Ye, L.; Ade, H.; Jiao, X.; Ye, L.; Ade, H. Quantitative Morphology–Performance Correlations in Organic Solar Cells: Insights from Soft X-Ray Scattering Organic Photovoltaics. *Adv. Energy Mater.* **2017**, *7*, 1700084. https://doi.org/10.1002/aenm.201700084.

(249) Jiao, X.; Ye, L.; Ade, H. Quantitative Morphology-Performance Correlations in Organic Solar Cells: Insights from Soft X-Ray Scattering. *Adv. Energy Mater.* **2017**, *7* (18), 1700084. https://doi.org/10.1002/aenm.201700084.

(250) Kalogeras, I. M. Glass-Transition Phenomena in Polymer Blends. *Encyclopedia of Polymer Blends: Volume 3*; Wiley-VCH Verlag GmbH & Co. KGaA, 2016; p 1.

(251) Gordon, M.; Taylor, J. S. Ideal Copolymers and the Second-Order Transitions of Synthetic Rubbers. i. Non-Crystalline Copolymers. *J. Appl. Chem.* **2007**, *2* (9), 493–500. https://doi.org/10.1002/jctb.5010020901.

(252) I. M. Kalogeras. Encyclopedia of Polymer Blends. *Encyclopedia of Polymer Blends: Volume 3*; 2011.

(253) Bannock, J. H.; Treat, N. D.; Chabinyc, M.; Stingelin, N.; Heeney, M.; De Mello, J. C. The Influence of Polymer Purification on the Efficiency of Poly(3-

Hexylthiophene):Fullerene Organic Solar Cells. *Sci. Rep.* **2016**, *6*, 23651. https://doi.org/https://doi.org/10.1038/srep23651.

(254) Walker, B. E.; Bannock, J. H.; Nightingale, A. M.; Demello, J. C. Tuning Reaction Products by Constrained Optimisation. *React. Chem. Eng.* **2017**, *2* (5), 785–798. https://doi.org/10.1039/c7re00123a.

(255) Meng, X.; Zhao, G.; Xu, Q.; Tan, Z.; Zhang, Z.; Jiang, L.; Shu, C.; Wang, C.; Li, Y. Effects of Fullerene Bisadduct Regioisomers on Photovoltaic Performance. *Adv. Funct. Mater.* **2014**, *24* (1), 158–163. https://doi.org/10.1002/adfm.201301411.

(256) Tremel, K.; Ludwigs, S. Morphology of P3HT in Thin Films in Relation to Optical and Electrical Properties. *Adv. Polym. Sci.* **2014**, *265*, 39–82. https://doi.org/10.1007/12_2014_288.

(257) Boucher, V. M.; Cangialosi, D.; Alegría, A.; Colmenero, J. Enthalpy Recovery in Nanometer to Micrometer Thick Polystyrene Films. *Macromolecules* **2012**, *45* (12), 5296–5306. https://doi.org/10.1021/ma300622k.

(258) Abdulrazzaq, O.; Bourdo, S. E.; Woo, M.; Saini, V.; Berry, B. C.; Ghosh, A.; Biris, A. S. Comparative Aging Study of Organic Solar Cells Utilizing Polyaniline and PEDOT:PSS as Hole Transport Layers. *ACS Appl. Mater. Interfaces* **2015**, *7* (50), 27667–27675. https://doi.org/10.1021/acsami.5b08000.

(259) Albrecht, S.; Tumbleston, J. R.; Janietz, S.; Dumsch, I.; Allard, S.; Scherf, U.; Ade, H.; Neher, D. Quantifying Charge Extraction in Organic Solar Cells: The Case of Fluorinated PCPDTBT. *J. Phys. Chem. Lett.* **2014**, *5* (7), 1131–1138. https://doi.org/10.1021/jz500457b.

(260) Brus, V. V.; Proctor, C. M.; Ran, N. A.; Nguyen, T.-Q. Capacitance Spectroscopy for Quantifying Recombination Losses in Nonfullerene Small-Molecule Bulk Heterojunction Solar Cells. *Adv. Energy Mater.* **2016**, *6* (11), 1502250. https://doi.org/10.1002/aenm.201502250.

(261) Vollbrecht, J.; Wiebeler, C.; Bock, H.; Schumacher, S.; Kitzerow, H. S. Curved Polar Dibenzocoronene Esters and Imides versus Their Planar Centrosymmetric Homologs: Photophysical and Optoelectronic Analysis. *J. Phys. Chem. C* **2019**, *123* (7), 4483–4492. https://doi.org/10.1021/acs.jpcc.8b10730.

(262) Vollbrecht, J.; Brus, V. V.; Ko, S. J.; Lee, J.; Karki, A.; Cao, D. X.; Cho, K.; Bazan, G. C.; Nguyen, T. Q. Quantifying the Nongeminate Recombination Dynamics in Nonfullerene Bulk Heterojunction Organic Solar Cells. *Adv. Energy Mater.* **2019**, *9* (32), 1901438. https://doi.org/10.1002/aenm.201901438.

(263) Paquin, F.; Latini, G.; Sakowicz, M.; Karsenti, P. L.; Wang, L.; Beljonne, D.; Stingelin, N.; Silva, C. Charge Separation in Semicrystalline Polymeric Semiconductors by Photoexcitation: Is the Mechanism Intrinsic or Extrinsic? *Phys. Rev. Lett.* **2011**, *106* (19), 197401. https://doi.org/10.1103/PhysRevLett.106.197401.

(264) Kozub, D. R.; Vakhshouri, K.; Orme, L. M.; Wang, C.; Hexemer, A.; Gomez, E. D. Polymer Crystallization of Partially Miscible Polythiophene/Fullerene Mixtures Controls Morphology. *Macromolecules* **2011**, *44*, 5722–5729. https://doi.org/10.1021/ma200855r.

(265) Monnier, X.; Cavallo, D.; Righetti, M. C.; Di Lorenzo, M. L.; Marina, S.; Martin, J.; Cangialosi, D. Physical Aging and Glass Transition of the Rigid Amorphous Fraction in Poly(l -Lactic Acid). *Macromolecules* **2020**, *53* (20), 8741–8750. https://doi.org/10.1021/acs.macromol.0c01182.

(266) Xu, J.; Feng, H.; Liang, Y.; Tang, H.; Tang, Y.; Du, Z.; Hu, Z.; Huang, F.; Cao, Y. N-Alkyl Chain Modification in Dithienobenzotriazole Unit Enabled Efficient Polymer Donor for High-Performance Non-Fullerene Solar Cells. *J. Energy Chem.* **2021**, *66*, 382–389. https://doi.org/https://doi.org/10.1016/j.jechem.2021.08.033.

(267) Cao, J.; Wang, H.; Yang, L.; Du, F.; Yu, J.; Tang, W. Chlorinated Unfused Acceptor Enabling 13.57% Efficiency and 73.39% Fill Factor Organic Solar Cells via Fine-Tuning Alkoxyl Chains on Benzene Core. *Chem. Eng. J.* **2022**, *427*, 131828. https://doi.org/10.1016/J.CEJ.2021.131828.

(268) Wang, K.; Li, W.; Guo, X.; Zhu, Q.; Fan, Q.; Guo, Q.; Ma, W.; Zhang, M. Optimizing the Alkyl Side-Chain Design of a Wide Band-Gap Polymer Donor for Attaining Nonfullerene Organic Solar Cells with High Efficiency Using a Nonhalogenated Solvent. *Chem. Mater.* **2021**, *33* (15), 5981–5990. https://doi.org/10.1021/ACS.CHEMMATER.1C01307.

(269) Liu, Q.; Fang, J.; Wu, J.; Zhu, L.; Guo, X.; Liu, F.; Zhang, M. Tuning Aggregation Behavior of Polymer Donor via Molecular-Weight Control for Achieving 17.1% Efficiency Inverted Polymer Solar Cells. *Chinese J. Chem.* **2021**, *39* (7), 1941–1947. https://doi.org/10.1002/CJOC.202100112.

(270) Bi, P.; Zhang, S.; Wang, J.; Ren, J.; Hou, J. Progress in Organic Solar Cells: Materials, Physics and Device Engineering. *Chinese J. Chem.* **2021**, *39* (9), 2607–2625. https://doi.org/10.1002/CJOC.202000666.

(271) Xiao, X.; Yi, N.; Yao, G.; Lu, J.; Leng, S.; Liu, F.; Hu, M.; Yuan, Z.; Zhou, W. Preaggregation Matching of Donors and Acceptors in Solution Accounting for Thermally Stable Non-Fullerene Solar Cells. *Cite This ACS Appl. Mater. Interfaces* **2020**, *12*, 58093. https://doi.org/10.1021/acsami.0c17049.

(272) Wang, Y.; Lan, W.; Li, N.; Lan, Z.; Li, Z.; Jia, J.; Zhu, F. Stability of Nonfullerene Organic Solar Cells: From Built-in Potential and Interfacial Passivation Perspectives. *Adv. Energy Mater.* **2019**, *9* (19), 1900157. https://doi.org/10.1002/AENM.201900157.

(273) Cheng, P.; Zhan, X. Stability of Organic Solar Cells: Challenges and Strategies. *Chem. Soc. Rev.* **2016**, *45* (9), 2544–2582. https://doi.org/10.1039/C5CS00593K.

(274) Zhu, Y.; Gadisa, A.; Peng, Z.; Ghasemi, M.; Ye, L.; Xu, Z.; Zhao, S.; Ade, H. Rational Strategy to Stabilize an Unstable High-Efficiency Binary Nonfullerene Organic Solar Cells with a Third Component. *Adv. Energy Mater.* **2019**, *9* (20), 1900376. https://doi.org/10.1002/AENM.201900376.

(275) Marina, S.; Gutierrez-Fernandez, E.; Gutierrez, J.; Gobbi, M.; Solano, E.; Rech, J.; You, W.; Hueso, L.; Tercjak, A.; Ade, H.; Martin, J. *Common High-Performance Semiconducting Polymers Are Not Amorphous but Semi-Para-Crystalline*; 2021.

(276) Venkateshvaran, D.; Nikolka, M.; Sadhanala, A.; Lemaur, V.; Zelazny, M.; Kepa, M.; Hurhangee, M.; Kronemeijer, A. J.; Pecunia, V.; Nasrallah, I.; Romanov, I.; Broch, K.; McCulloch, I.; Emin, D.; Olivier, Y.; Cornil, J.; Beljonne, D.; Sirringhaus, H.

Approaching Disorder-Free Transport in High-Mobility Conjugated Polymers. *Nature* **2014**, *515*, 384–388. https://doi.org/10.1038/nature13854.

(277) Guo, C.; Li, D.; Wang, L.; Du, B.; Liu, Z.-X.; Shen, Z.; Wang, P.; Zhang, X.; Cai, J.; Cheng, S.; Yu, C.; Wang, H.; Liu, D.; Li, C.-Z.; Wang, T. Cold-Aging and Solvent Vapor Mediated Aggregation Control toward 18% Efficiency Binary Organic Solar Cells. *Adv. Energy Mater.* **2021**, 2102000. https://doi.org/10.1002/AENM.202102000.

(278) Zhao, H.; Naveed, H. B.; Lin, B.; Zhou, X.; Yuan, J.; Zhou, K.; Wu, H.; Guo, R.; Scheel, M. A.; Chumakov, A.; Roth, S. V.; Tang, Z.; Müller-Buschbaum, P.; Ma, W. Hot Hydrocarbon-Solvent Slot-Die Coating Enables High-Efficiency Organic Solar Cells with Temperature-Dependent Aggregation Behavior. *Adv. Mater.* **2020**, *32* (39), 2002302. https://doi.org/10.1002/ADMA.202002302.

(279) Wang, L.; Li, Q.; Liu, S.; Cao, Z.; Cai, Y.; Jiao, X.; Lai, H.; Xie, W.; Zhan, X.; Zhu, T. Quantitative Determination of the Vertical Segregation and Molecular Ordering of PBDB-T/ITIC Blend Films with Solvent Additives. *ACS Appl. Mater. Interfaces* **2020**, *12* (21), 24165–24173. https://doi.org/10.1021/acsami.0c02843.

(280) Xiao, Z.; Yuan, Y.; Yang, B.; VanDerslice, J.; Chen, J.; Dyck, O.; Duscher, G.; Huang, J. Universal Formation of Compositionally Graded Bulk Heterojunction for Efficiency Enhancement in Organic Photovoltaics. *Adv. Mater.* **2014**, *26* (19), 3068–3075. https://doi.org/10.1002/ADMA.201305196.

(281) Zhang, Q.; Chen, Z.; Ma, W.; Xie, Z.; Han, Y. Optimizing Domain Size and Phase Purity in All-Polymer Solar Cells by Solution Ordered Aggregation and Confinement Effect of the Acceptor. *J. Mater. Chem. C* **2019**, *7* (40), 12560–12571. https://doi.org/10.1039/C9TC03697K.

(282) Wang, T.; Brédas, J.-L. Organic Photovoltaics: Understanding the Preaggregation of Polymer Donors in Solution and Its Morphological Impact. *J. Am. Chem. Soc.* **2021**, *143* (4), 1822–1835. https://doi.org/10.1021/JACS.0C09542.

(283) Fan Chen; Guodong Ding; Ailing Tang; Bo Xiao; Jianfeng Li; Erjun Zhou. A Perylenediimide Dimer Containing an Asymmetric π-Bridge and Its Fused Derivative for Fullerene-Free Organic Solar Cells. *J. Mater. Chem. C* **2018**, *6* (10), 2580–2587. https://doi.org/10.1039/C8TC00089A.

(284) Mao, Y.; Li, W.; Chen, M.; Chen, X.; Gurney, R. S.; Liu, D.; Wang, T. Evolution of Molecular Aggregation in Bar-Coated Non-Fullerene Organic Solar Cells. *Mater. Chem. Front.* **2019**, *3* (6), 1062–1070. https://doi.org/10.1039/c9qm00078j.

(285) Todor-Boer, O.; Petrovai, I.; Tarcan, R.; Vulpoi, A.; David, L.; Astilean, S.; Botiz, I. Enhancing Photoluminescence Quenching in Donor–Acceptor PCE11:PPCBMB Films through the Optimization of Film Microstructure. *Nanomaterials* **2019**, *9*, 1757. https://doi.org/10.3390/NANO9121757.

(286) Hultmark, S.; Paleti, S. H. K.; Harillo, A.; Marina, S.; Nugroho, F. A. A.; Liu, Y.; Ericsson, L. K. E.; Li, R.; Martín, J.; Bergqvist, J.; Langhammer, C.; Zhang, F.; Yu, L.; Campoy-Quiles, M.; Moons, E.; Baran, D.; Müller, C. Suppressing Co-Crystallization of Halogenated Non-Fullerene Acceptors for Thermally Stable Ternary Solar Cells. *Adv. Funct. Mater.* **2020**, *30*, 2005462. https://doi.org/10.1002/adfm.202005462.

(287) Otieno, F.; Kotane, L.; Airo, M.; Billing, C.; Erasmus, R. M.; Wamwangi, D.; Billing, D. G. Probing the Properties of Polymer/Non-Fullerene/Fullerene Bulk Heterojunction Ternary Blend Solar Cells, Study of Varied Blend Ratios of PBDB-T:ITIC-Th:PC71BM. *Eur. Phys. J. Plus* **2021**, *136* (171), 1–17. https://doi.org/10.1140/EPJP/S13360-021-01129-0.

(288) Schaffer, C. J.; Schlipf, J.; Dwi Indari, E.; Su, B.; Bernstorff, S.; Müller-Buschbaum, P. Effect of Blend Composition and Additives on the Morphology of PCPDTBT:PC 71 BM Thin Films for Organic Photovoltaics. *ACS Appl. Mater. Interfaces* **2015**, *7* (38), 21347–21355. https://doi.org/10.1021/acsami.5b05939.

(289) Qin, Y.; Afsar Uddin, M.; Chen, Y.; Jang, B.; Zhao, K.; Zheng, Z.; Yu, R.; Joo Shin, T.; Young Woo, H.; Hou, J.; Qin, Y. P.; Chen, Y.; Zhao, K.; Zheng, Z.; Yu, R. N.; Hou, J. H.; Uddin, M. A.; Jang, B.; Woo, H. Y.; Shin, T. J. Highly Efficient Fullerene-Free Polymer Solar Cells Fabricated with Polythiophene Derivative. *Adv. Mater.* **2016**, *28*, 9416–9422. https://doi.org/10.1002/adma.201601803.

(290) Mao, Y.; Li, W.; Chen, M.; Chen, X.; Gurney, R. S.; Liu, D.; Wang, T. Evolution of Molecular Aggregation in Bar-Coated Non-Fullerene Organic Solar Cells. *Mater. Chem. Front.* **2019**, *3* (6), 1062–1070. https://doi.org/10.1039/C9QM00078J.

(291) Hou, L.; Lv, J.; Wobben, F.; Corre, V. M. Le; Tang, H.; Singh, R.; Kim, M.; Wang, F.; Sun, H.; Chen, W.; Xiao, Z.; Kumar, M.; Xu, T.; Zhang, W.; McCulloch, I.; Duan, T.; Xie, H.; Koster, L. J. A.; Lu, S.; Kan, Z. Effects of Fluorination on Fused Ring Electron Acceptor for Active Layer Morphology, Exciton Dissociation, and Charge Recombination in Organic Solar Cells. *ACS Appl. Mater. Interfaces* **2020**, *12* (50), 56231–56239. https://doi.org/10.1021/ACSAMI.0C16411.

(292) Proctor, C. M.; Nguyen, T.-Q. Effect of Leakage Current and Shunt Resistance on the Light Intensity Dependence of Organic Solar Cells. *Appl. Phys. Lett.* **2015**, *106* (8), 083301. https://doi.org/10.1063/1.4913589.

(293) Shi, H.; Xia, R.; Zhang, G.; Yip, H.-L.; Cao, Y. Spectral Engineering of Semitransparent Polymer Solar Cells for Greenhouse Applications. *Adv. Energy Mater.* **2019**, *9* (5), 1803438. https://doi.org/10.1002/AENM.201803438.

(294) Juška, G.; Arlauskas, K.; Stuchlik, J.; Österbacka, R. Non-Langevin Bimolecular Recombination in Low-Mobility Materials. *J. Non. Cryst. Solids* **2006**, *352* (9–20), 1167–1171. https://doi.org/10.1016/J.JNONCRYSOL.2005.11.099.

(295) Clarke, T. M.; Lungenschmied, C.; Peet, J.; Drolet, N.; Mozer, A. J. Tuning Non-Langevin Recombination in an Organic Photovoltaic Blend Using a Processing Additive. *J. Phys. Chem. C* **2015**, *119* (13), 7016–7021. https://doi.org/10.1021/JP5129707.

(296) Armin, A.; Velusamy, M.; Wolfer, P.; Zhang, Y.; Burn, P. L.; Meredith, P.; Pivrikas, A. Quantum Efficiency of Organic Solar Cells: Electro-Optical Cavity Considerations. **2021**, *12*, 27. https://doi.org/10.1021/ph400044k.

(297) Honsberg, C.; Bowden, S. Quantum Efficiency https://www.pveducation.org/pvcdrom/solar-cell-operation/quantum-efficiency (accessed Aug 23, 2021).

(298) Heumueller, T.; Mateker, W. R.; Sachs-Quintana, I. T.; Vandewal, K.; Bartelt, J. A.;

Burke, T. M.; Ameri, T.; Brabec, C. J.; McGehee, M. D. Reducing Burn-in Voltage Loss in Polymer Solar Cells by Increasing the Polymer Crystallinity. *Energy Environ. Sci.* **2014**, *7* (9), 2974–2980. https://doi.org/10.1039/C4EE01842G.

(299) Fukuhara, T.; Tamai, Y.; Ohkita, H. Nongeminate Charge Recombination in Organic Photovoltaics. *Sustain. Energy Fuels* **2020**, *4* (9), 4321–4351. https://doi.org/10.1039/D0SE00310G.

(300) Zhang, X.; Zuo, X.; Xie, S.; Yuan, J.; Zhou, H.; Zhang, Y. Understanding Charge Transport and Recombination Losses in High Performance Polymer Solar Cells with Non-Fullerene Acceptors. *J. Mater. Chem. A* **2017**, *5*, 17230–17239. https://doi.org/10.1039/C7TA05865A.

(301) Tian Du; Weidong Xu; Shengda Xu; R. Ratnasingham, S.; Chieh-Ting Lin; Jinhyun Kim; Joe Briscoe; A. McLachlan, M.; R. Durrant, J. Light-Intensity and Thickness Dependent Efficiency of Planar Perovskite Solar Cells: Charge Recombination versus Extraction. *J. Mater. Chem. C* **2020**, *8* (36), 12648–12655. https://doi.org/10.1039/D0TC03390A.

(302) Gutierrez-Fernandez, E. Nanostructuring of Soft Matter for Organic Electronics, 2019, Vol. 28.

(303) Zeiske, S.; Sandberg, O. J.; Zarrabi, N.; Li, W.; Meredith, P.; Armin, A. Direct Observation of Trap-Assisted Recombination in Organic Photovoltaic Devices. *Nat. Commun.* **2021**, *12* (3603), 1–7. https://doi.org/10.1038/s41467-021-23870-x.

(304) Wu, J.; Luke, J.; Lee, H. K. H.; Shakya Tuladhar, P.; Cha, H.; Jang, S.-Y.; Tsoi, W. C.; Heeney, M.; Kang, H.; Lee, K.; Kirchartz, T.; Kim, J.-S.; Durrant, J. R. Tail State Limited Photocurrent Collection of Thick Photoactive Layers in Organic Solar Cells. *Nat. Commun.* **2019**, *10* (5159), 1–10. https://doi.org/10.1038/s41467-019-12951-7.

(305) Kotlarski, J. D.; Blom, P. W. M.; Koster, L. J. A.; Lenes, M.; Slooff, L. H. Combined Optical and Electrical Modeling of Polymer:Fullerene Bulk Heterojunction Solar Cells. *J. Appl. Phys.* **2008**, *103* (8), 084502. https://doi.org/10.1063/1.2905243.

(306) Lenes, M.; Koster, L. J. A.; Mihailetchi, V. D.; Blom, P. W. M. Thickness Dependence of the Efficiency of Polymer:Fullerene Bulk Heterojunction Solar Cells. *Appl. Phys. Lett.* **2006**, *88* (24), 243502. https://doi.org/10.1063/1.2211189.

(307) Kyaw, A. K. K.; Wang, D. H.; Gupta, V.; Leong, W. L.; Ke, L.; Bazan, G. C.; Heeger, A. J. Intensity Dependence of Current–Voltage Characteristics and Recombination in High-Efficiency Solution-Processed Small-Molecule Solar Cells. *ACS Nano* **2013**, *7* (5), 4569–4577. https://doi.org/10.1021/NN401267S.

(308) Ryu, S.; Ha, N. Y.; Ahn, Y. H.; Park, J.-Y.; Lee, S. Light Intensity Dependence of Organic Solar Cell Operation and Dominance Switching between Shockley–Read–Hall and Bimolecular Recombination Losses. *Sci. Reports 2021 111* **2021**, *11* (1), 1–10. https://doi.org/10.1038/s41598-021-96222-w.

(309) Chen, Z.; Wang, T.; Wen, Z.; Lu, P.; Qin, W.; Yin, H.; Hao, X.-T. Trap State Induced Recombination Effects on Indoor Organic Photovoltaic Cells. *ACS Energy Lett.* **2021**, *6*, 3203–3211. https://doi.org/10.1021/ACSENERGYLETT.1C01336.

eman ta zabal zazu

Universidad del País Vasco

Euskal Herriko Unibertsitatea